Lead halide perovskite solar cells

Document Version:
Publisher's PDF, also known as Version of Record (includes final page, issue and volume numbers)

Please check the document version of this publication:

• A submitted manuscript is the version of the article upon submission and before peer-review. There can be important differences between the submitted version and the official published version of record. People interested in the research are advised to contact the author for the final version of the publication, or visit the DOI to the publisher's website.
• The final author version and the galley proof are versions of the publication after peer review.
• The final published version features the final layout of the paper including the volume, issue and page numbers.

Link to publication

Download date: 16. Nov. 2023

Lead Halide Perovskite Solar Cells

PROEFSCHRIFT

ter verkrijging van de graad van doctor aan de Technische Universiteit Eindhoven, op gezag van de rector magnificus prof.dr.ir. F.P.T. Baaijens, voor een commissie aangewezen door het College voor Promoties, in het openbaar te verdedigen op donderdag 28 juni 2018 om 13:30 uur

door

Bernardo Joseph Bruijnaers

Geboren te Weert

Dit proefschrift is goedgekeurd door de promotoren en de samenstelling van de promotiecomissie is als volgt:

voorzitter:	prof. dr. E. W. Meijer
1^e promotor:	prof. dr. ir. R. A. J. Janssen
copromotor:	dr. ir. M. M. Wienk
leden:	prof. dr. M. A. Loi (Rijksuniversiteit Groningen)
	prof. dr. ir. A. H. M. Smets (Technische Universiteit Delft)
	dr. M. Creatore
	prof. dr. E. P. A. M. Bakkers
adviseur:	dr. Y. Galagan (Solliance – TNO)

Het onderzoek of ontwerp dat in dit proefschrift wordt beschreven is uitgevoerd in overeenstemming met de TU/e Gedragscode Wetenschapsbeoefening.

Lead Halide Perovskite Solar Cells

Bardo Bruijnaers

Table of Contents

Chapter 1
Introduction

Abstract

In this chapter, a short introduction about the necessity of using solar power is followed by explanation of basic solar cell operation. Perovskite solar cells are discussed in more detail by first giving an overview of the historic development of this relatively new technology, after which the possibilities with the variation in composition of the perovskite semiconductor are presented. Perovskite solar cell architectures and processing methods are explained and advantages and challenges of the technology are commented on. At the end of this chapter, the aim and outline of this thesis are clarified.

1.1 Introduction

With the growing global population and economy, the energy demand is increasing substantially, with a projected increase of energy consumption of ~28% from 169 PWh in 2015 to 216 PWh in 2040.[1] Especially countries with strong growing economies like China and India contribute to this increase.[1] Although renewable energy is the world's fastest growing energy source, the majority (77%) of energy is still expected to be generated by burning fossil fuels in 2040.[1]

Even though the burning of fossil fuels is an easy way to generate energy, the effects this has on our planet are serious. Looking at results from simulations and comparing them to observed temperature changes (Figure 1.1) clearly shows that the emission of greenhouse gasses (like CO_2) due to human activity is responsible for the increase in the global average temperature.[2,3]
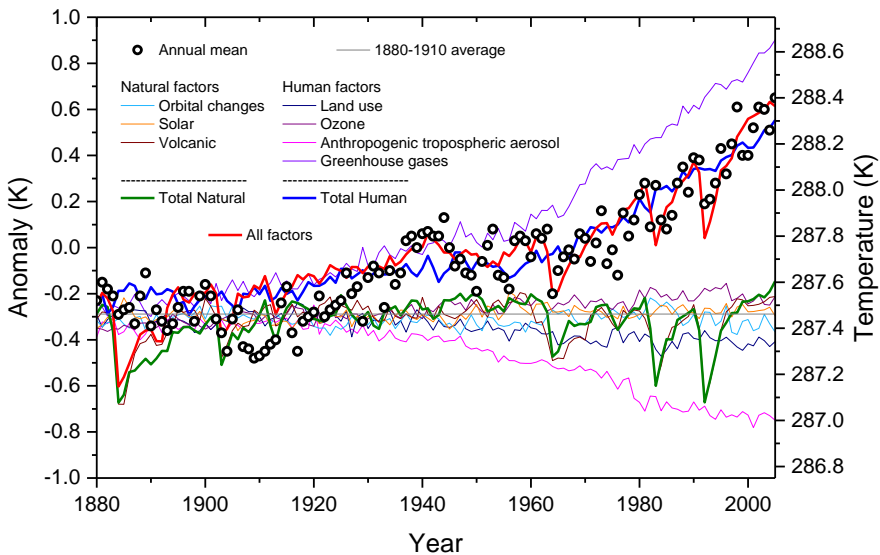
Figure 1.1 Observed land-ocean temperature plotted with simulated data that takes several different factors (like the orbital changes of the earth, varying temperature of the sun, CO_2 emission from volcanoes, deforestation and paving of the earth's surface, Ozone pollution, sulphate aerosols from coal burning and the emission of greenhouse gasses like CO_2 by humans) into account.[2,3]

Although a temperature increase of 1 to 2 K does not seem like much at first, recent research has suggested that most of the generated heat is being stored in the western Pacific Ocean due to an unprecedented strengthening of the equatorial trade winds (Figure 1.2).[4–6] This heat uptake is masking the actual surface temperature

increase, making it appear less severe than it really is. Additionally, concerns have been expressed about the potential release of methane (a much stronger greenhouse gas than CO_2) into the atmosphere from hydrate decomposition in these warming oceans.[7]
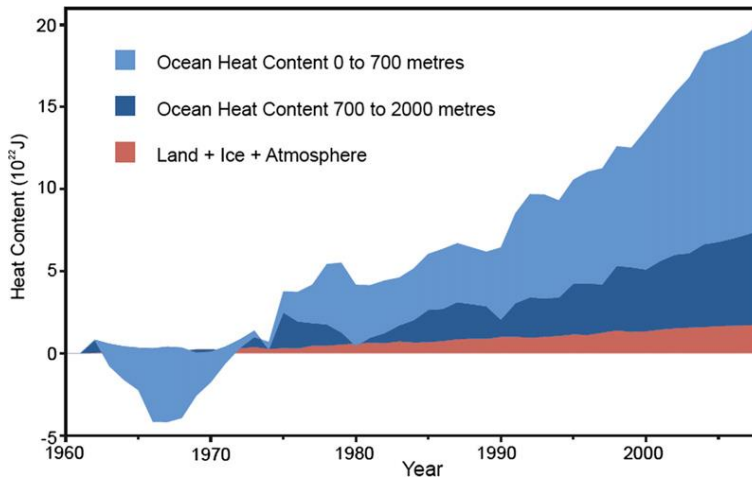
Figure 1.2 Land, atmosphere, and ice heating, 0–700 meter ocean heat content and 700–2000 meter ocean heat content. Reprinted with permission from reference [5]

It is evident that generating the energy we require from renewable energy sources is paramount if we want to mitigate climate change. The only source of energy that reaches the earth's surface is solar irradiation. The amount of solar energy delivered to the earth is enormous and one hour of solar irradiation equals the amount of energy that humanity consumes annually.[8] The potential of solar energy therefore appears almost limitless and converting the solar energy (photons) into energy that is useful to us (electricity) is extremely appealing. The direct conversion of sunlight in to electrical power is called the photovoltaic effect and was first described by Becquerel in 1839 who used silver chloride or silver bromide covered platinum electrodes in an acidic solution.[9] After the discovery of a naturally formed p-n junction in silicon ingots by Ohl in 1941[10] and the improvement of the production process,[11] the first "modern" silicon solar cell was developed by Chapin, Fuller and Pearson in 1954 and could convert 6% of sunlight energy into electrical energy.[12] Due to the initial immaturity of the silicon manufacturing industry, the major application until the early 1970's was for satellites used in space.[13] Since then, the research effort and efficiencies of these solar cells has grown steadily and nowadays, conversion efficiencies of >25% have been achieved.[14,15] This is already approaching the

3

theoretical thermodynamic power conversion efficiency limit in sunlight calculated by Shockley and Queisser in 1961 of 33.7% for a single p-n junction solar cell with a bandgap of 1.4 eV.[16,17]

Nowadays, the crystalline silicon solar cells are completely dominating the commercial and private photovoltaic (PV) markets. The high production cost of crystalline silicon solar cells due to the requirement of extremely high purity of raw materials and high temperature processing has traditionally been used as an argument for the inability of large scale application of this technology. However, the upscaling of silicon solar panel production and maturing of the technology has in fact drastically reduced the production costs in recent years, making it a much more competitive technology.[18] The fact that crystalline silicon is an indirect bandgap material however requires the semiconductor layer to be relatively thick (~200 μm), making the panels comparably heavy and making flexible applications nearly impossible.

Thin film photovoltaics aim to reduce the weight and material cost by applying a thin active layer (< 5 μm), which is made possible by the use of a direct bandgap semiconductor absorber. The currently leading thin film PV technologies include amorphous silicon (a-Si), cadmium telluride (CdTe), copper indium gallium selenide (CIGS) and gallium arsenide (GaAs) thin film solar cells which have reached efficiencies of up to 14.0%, 22.1%, 22.6%, and 28.8% respectively.[15] The drawback of these thin film technologies however, is that highest efficiency devices require the use of highly toxic or very costly materials or production methods. Recently, metal halide perovskites have emerged as a new thin film PV technology. Promising initial results and an impressive increase in power conversion efficiency (PCE) in only a few years have characterized this technology. What is making this thin film technology potentially so competitive is the combination of solution processability, high efficiency and low cost.

1.2 Solar cell operation

The operation of a solar cell relies on the absorption of light and the subsequent generation and collection of charges. For this purpose, a semiconductor material is used to form the active layer of the solar cell. Semiconductor materials are characterized by a bandgap, which is the energy gap that separates the valence band (VB, the highest energy band occupied by electrons) from the conduction band (CB, the lowest energy band where no states are occupied). The magnitude of the bandgap determines which photons can be absorbed by the material, where photons with an energy less that the bandgap will not be absorbed. When the photon energy is higher than, or equal to bandgap, an electron is excited from the VB to the CB, and any excess energy is lost through thermalization. The negatively charged electron (e^-) in the CB leaves behind a positively charged hole (h^+) in the VB. In most inorganic semiconductors the electron and hole can be considered as free charges at room temperature. When the electron and hole are strongly bound by coulomb interaction, e.g. due to a low permittivity as commonly found in organic semiconductors, the electron-hole pair is referred to as an exciton. For a photovoltaic effect the exciton must be separated into free charges (one e^- and one h^+) that can move freely through the active material. After generation and separation, the electrons are collected by an electrode into an external circuit, where they dissipate energy and produce power before returning to the solar cell at the opposite electrode, where it recombines with the hole, closing the cycle. If the electron is not extracted from the solar cell, it will eventually recombine with the hole and the light generated electron-hole pair and the accompanying energy are lost.

1.3 Metal halide perovskite semiconductors

The name perovskite was originally given to the mineral calcium titanate ($CaTiO_3$) in 1839 and now lends its name to a class of materials that crystallize in the same structure as $CaTiO_3$ (ABX_3, Figure 1.3).
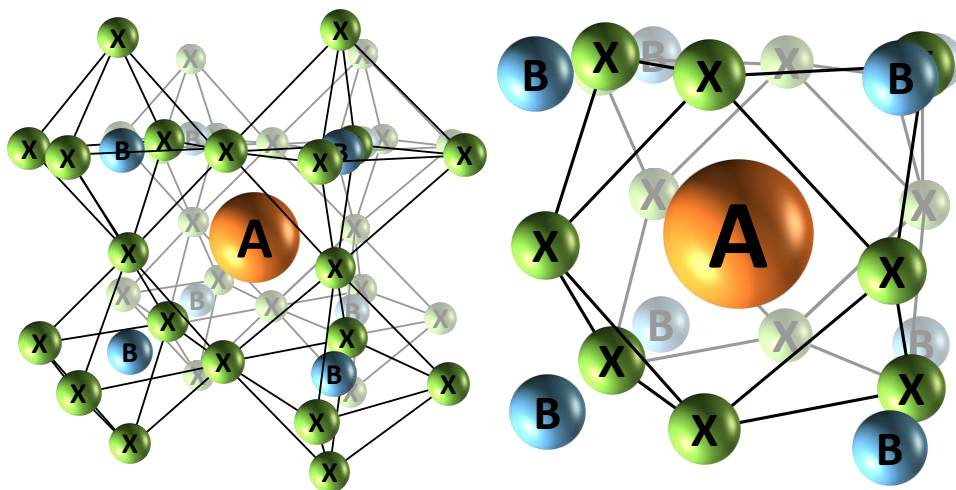
Figure 1.3 Schematic representations of the cubic perovskite crystal structure ABX_3.

In 2009, Kojima *et al.* found that a specific class of perovskite materials, i.e. metal halide perovskite semiconductors can function as a sensitizer in a dye sensitized solar cell (DSSC), providing a short lived efficiency of 3.8%.[19] In these metal halide perovskites, A^+ is a (larger) (in)organic cation, B^{2+} is a (smaller) divalent metal cation and X^- is a halide anion. After the initial discovery the research on metal halide perovskites for solar cell applications has grown enormously. Especially after a breakthrough efficiency of ~10% was reached for solid-state solar cells in 2012 by two different research groups simultaneously, the research efforts skyrocketed.[20,21] This is evidenced by the number of publications on the subject of perovskite solar cells in the following years (Figure 1.4).
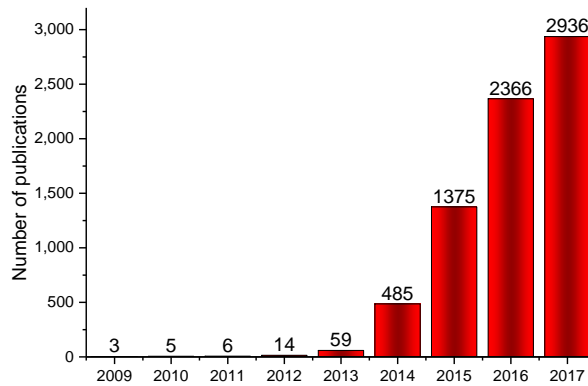
Figure 1.4 Annual number of publications complying with the search criteria "perovskite solar cell" from 2009 to 2017.[22]

Along with this increasing research effort, came an increase in efficiency and better understanding of these devices. Looking at the graph of record solar cell efficiencies (Figure 1.5) it is clear that the perovskite solar cells have made an incredibly strong climb from first discovery in 2009 to solar cells with efficiencies of up to 22.7%, approaching to that of silicon, in only a few years.[15] What makes perovskite solar cells especially attractive is the fact they combine the high efficiency of silicon solar cells with the solution processability of thin film organic photovoltaics, making future low-cost production of highly efficient solar panels a possibility.
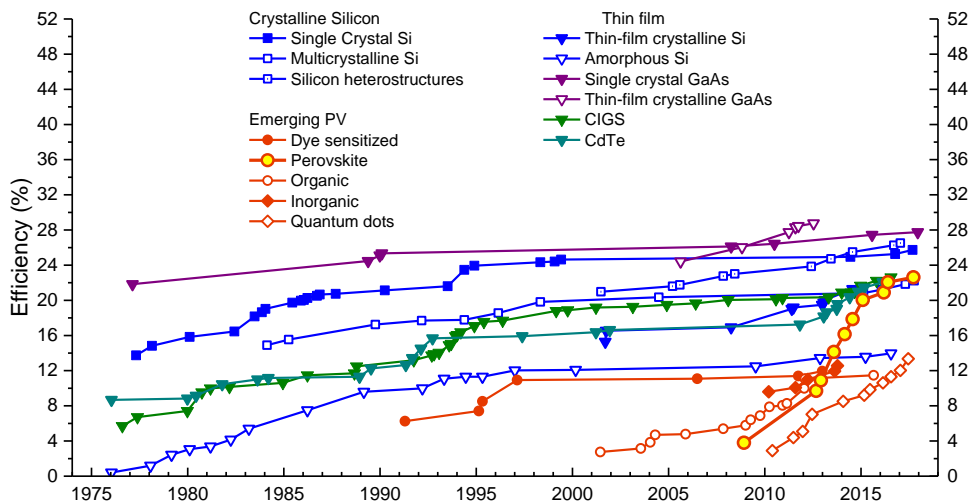
Figure 1.5 Record efficiencies of different solar cell technologies over the past 4 decades.[15,19–21]

1.4 Metal halide perovskite composition

As described in paragraph 1.3, the perovskites possess an ABX_3 crystal structure (Figure 1.3). Since the discovery of the perovskite structure in 1839, the material has been investigated extensively and in 1962, the Goldschmidt tolerance factor was described by Victor M. Goldschmidt.[23] This tolerance factor uses the ionic radii of the atoms in the perovskite structure and can be used to indicate the stability of a certain perovskite composition. It is defined as:

$$t = \frac{r_A + r_X}{\sqrt{2}\,(r_B + r_X)}$$

with tolerance factor (t), r_A and r_B the ionic radii of the A and B cations respectively and r_X the ionic radius of the anion. The tolerance factor assesses if the A cation can fit inside the cavities of the BX_3 framework. Where a tolerance factor of $t = 1$ indicates a perfect fit resulting in the formation of a perfect cubic perovskite structure. For metal halide perovskites, the perovskite structure is generally formed with calculated tolerance factors of $0.81 \geq t \leq 1.11$, although tilting of the BX_6 octahedra can occur in the lower range. In the narrower range of $0.89 \geq t \leq 1.00$, the cubic perovskite structure can be expected. If $t > 1.1$ or $t < 0.8$, the A site cation is either too large or too small respectively and the perovskite structure will generally not be formed.[24,25] For metal halide perovskites, alternative methods for the determination of the ionic radii have been proposed for several reasons. The A cation is often a molecule with a non-spherical shape and a dipole moment instead of a spherical single atom. Due to the low decomposition temperatures of the A molecules, processing is often done at low temperature, which can result in the kinetic trapping of the material in a thermodynamically less stable state. The tolerance factor equation is designed for use with oxides and fluorides which can be interpreted as non-polarizable hard spheres, which might not be valid for the halogen anions used in metal halide perovskites.[24,26,27] Besides the tolerance factor, the stability of the perovskite is also determined by the octahedral factor μ, which is defined as:

$$\mu = \frac{r_B}{r_X}$$

and should lie between 0.44 and 0.90 for stable perovskite structures.[24,25,28] The relatively broad ranges for stable perovskite structures in tolerance factor and octahedral factor already suggest that the perovskite structure is quite tolerant towards changes in composition. Consequently, many different compositions of metal halide perovskites have been produced and studied as will be discussed later.

In the original publication of Kojima *et al.* the studied perovskite consisted of methylammonium ($CH_3NH_3^+$ (MA^+)) as the large organic cation (A^+), lead(II) (Pb^{2+}) as the divalent metal cation (B^{2+}) and iodide (I^-) or bromide (Br^-) as the halide (X^-) and remains the most extensively studied compositions for use in photovoltaic applications to date.[19] These structures are referred to as methylammonium lead triiodide ($MAPbI_3$) and methylammonium lead tribromide ($MAPbBr_3$) respectively. In general, the metal halide perovskite structures used for photovoltaic applications are considered to be relatively soft and malleable crystal structures. Consequently, sensitivity of the material to ambient conditions and thermal instability of the structures have been widely reported.[29–32] Additionally, the materials undergo several phase transitions as a function of a changing temperature.[33]

One of the main advantages and an attractive aspect of the perovskite material is its tolerance to the (partial) exchange of one or more of its three compounds (A, B and X) with different molecules or atoms. This change of the perovskite composition has been found to influence the materials' physical properties significantly and many different compositions have been reported. Potentially allowing the tuning of the perovskites' physical properties towards application specific requirements.

Replacing the large organic cation (A)

In the $MAPbI_3$ composition (bandgap ~1.55 eV), the A cation (MA^+) has been replaced with the larger formamidinium ($CH(NH_2)_2^+$, FA^+), as well as with the smaller cesium (Cs^+) or rubidium (Rb^+). Both MA^+ and FA^+ are organic molecules with a dipole moment while Cs^+ and Rb^+ are inorganic atoms without a permanent dipole moment. The cation size difference causes the lattice to expand (FA^+) or contract (Cs^+ and Rb^+), changing the B-X bond length and has been found to have a small effect on the bandgap of the material.[34–40] Complete replacement of MA^+ with FA^+ ($FAPbI_3$) results in a photo-inactive, yellow non perovskite (δ) phase at room temperature which can be turned into the dark perovskite (α) phase at elevated temperatures (125 – 165°C).[38,41–43] Upon storage at room temperature however, a slow phase transition back to the δ phase has been reported, making device performance unstable over time.[41,43–47] Mixing FA^+ into the $MAPbI_3$ (resulting in a mixed $FA_xMA_{1-x}PbI_3$ perovskite) however, allows a moderate reduction of the bandgap (higher FA^+ fraction results in a lower bandgap) and results in more stable compounds.[34,45,46,48] Partial replacement of MA^+ with Cs^+ has shown to moderately increase the bandgap of the perovskite and improve its ambient thermal stability.[49,50] Similar to the $MAPbI_3$ case, partially

replacing FA^+ with Cs^+ in $FAPbI_3$ results in a moderate increase in the bandgap and increased stability of the formed perovskite.[38,39,51-53] The complete replacement of MA^+/FA^+ with Cs^+, gives $CsPbI_3$ which exhibits polymorphism, similar to $FAPbI_3$, with a phase transition above 300 °C and also suffers from instability at room temperature due to a favourable α to δ phase transition at room temperature.[49,54] Partial replacement of FA^+ with Rb^+ is possible but only with very low fractions of Rb^+ before phase segregation occurs.[40,55] With a Rb^+ fraction of 0.05 ($Rb_{0.05}FA_{0.95}PbI_3$), the α perovskite phase is formed around 120 – 150 °C which is stable at room temperature, while pure $RbPbI_3$ only shows a δ phase that is photo-inactive. Even with only this small amount of incorporated Rb^+, the stability towards moisture exposure at room temperature is greatly enhanced.[40,55] Due to the low Rb^+ fraction that can be incorporated, a change in the bandgap was not observed.[40,55]

With the mixing of organic cations to form new perovskite structures, a method for calculating the effective tolerance factor (t_{eff}) was proposed which employs the atomic-ratio weighted average of the two different cations for calculating the effective ionic radius (r_{eff}). With the best performing perovskite devices exhibiting a t_{eff} between $t_{eff} = 0.94$ and $t_{eff} = 0.98$.[38]

$$t_{eff} = \frac{r_{eff} + r_X}{\sqrt{2}(r_B + r_X)}$$
$$r_{eff} = x r_{A_1} + (1-x) r_{A_2}$$

Replacing the halogen ion (X)

The substitution of I^- by Cl^- in the $MAPbI_3$ composition has been studied extensively in the earlier years of perovskite solar cell research since it produced the highest efficiency devices at that time. The incorporation of Cl^- into the $MAPbI_3$ crystal has however been subject of substantial debate. With many studies showing some degree of Cl^- incorporation in the MAPbI structure,[56-71] but just as many showing there is no incorporated Cl^- in the final perovskite structure.[72-86] This makes it difficult to ascribe any changes in physical properties to the incorporation of Cl^- into the perovskite structure. The general consensus is however that Cl^- incorporation is very small if any and that the reported changes in the physical properties (like improved electron and hole diffusion lengths, are related more closely to the changes in morphology and crystallite quality than to the incorporation of Cl^-.[34,47,70,87-90]

In contrast to the Cl^- incorporation, the substitution of I^- with Br^- in the $MAPbI_3$ and $FAPbI_3$ structures has been widely demonstrated and compounds have been produced with values of x ranging from $x = 0$ to $x = 1$ in $MAPb(I_{1-x}Br_x)_3$ and

FAPb(I$_{1-x}$Br$_x$)$_3$.[34,91-93] The incorporation of Br$^-$ into the MAPbI$_3$ and FAPbI$_3$ allows modification of the perovskite material bandgap much more effectively than by changing the organic cation. With increasing Br$^-$ content, the bandgap increases as much as ~0.7 eV and ~0.8 eV for the MA and FA compositions, respectively (versus a bandgap change of ~0.1 eV for changing the organic A cation) upon complete substitution of I$^-$ with Br$^-$.[91-94] With the increasing Br$^-$ content up to $x > 0.2$ an increase in stability towards moisture exposure has also been reported for MAPb(I$_{1-x}$Br$_x$)$_3$.[93] Under accelerated stress tests, using extremely strong illumination conditions (~100 suns), MAPbBr$_3$ turns out to be the most stable composition.[95] Although mixed MAPb(I$_{1-x}$Br$_x$)$_3$ compounds are stable under storage conditions, the materials phase segregate over time under illumination (1 sun) into iodine-rich and bromide-rich phases.[94-97] This phase segregation has been shown to be reversible by storage in the dark at room temperature. Additional experiments have shown that this phase segregation is caused solely by illumination and is not an effect of temperature increase, nevertheless, the phase segregation rate is strongly temperature dependent.[94,98] By replacing MA$^+$ with Cs$^+$ in the MAPb(I$_{1-x}$Br$_x$)$_3$ structure, the thermal and illuminated stability of the material is enhanced and the phase segregation is minimal for values of $x < 0.4$. For values of $x > 0.4$ phase segregation does occur.[99,100]

Contrary to the MAPb(I/Cl) mixtures, the incorporation of Cl$^-$ in MAPb(Br/Cl) mixtures has been demonstrated and single crystals have been grown for the full range of MAP(Br$_{1-x}$Cl$_x$)$_3$ mixtures.[94,101-103] The smaller difference in ionic radius of Cl$^-$ (1.67 Å) and Br$^-$ (1.84 Å) versus I$^-$ (2.07 Å) is probably the reason for the compatibility of Cl$^-$ with Br$^-$ but not with I$^-$.[90,104] The bandgap of the MAPb(Br$_{1-x}$Cl$_x$)$_3$ mixtures (~2.3 eV – ~3.05 eV) is much larger than that of the MAPb(I$_{1-x}$Cl$_x$)$_3$ and MAPb(I$_{1-x}$Br$_x$)$_3$ mixtures.[103] Due to this high bandgap, the material is less interesting for PV applications and therefore, most studies on this material focus on light emitting devices where the emitted color can be tuned from yellow towards blue.[103,105-108]

Ternary mixtures that contain all three halogen ions described above (I$^-$, Cl$^-$, and Br$^-$) have also been reported. The results from these studies are very similar to the ones from the binary mixtures. The Cl$^-$ incorporation was found to be minimal again but does have influence on device performance through improved crystal quality or morphology. An increase in Br$^-$ incorporation again strongly increases the bandgap of the material and improves the stability of the formed compound.[109-111]

Replacing the divalent metal cation (B)

The main reason for replacing the divalent metal cation lead(II) (Pb^{2+}) in metal halide perovskites is to reduce the materials' toxicity. The ionic radius of the less toxic tin(II) (Sn^{2+}, 1.35Å) is similar to that of Pb^{2+} (1.49Å) and complete substitution of Pb^{2+} with Sn^{2+} in the $MAPbI_3$ compound has been accomplished.[109–111] The formed compound turns to dark perovskite at room temperature and this complete substitution reduces the bandgap to ~1.3 eV.[112,113] The complete substitution of Pb^{2+} with Sn^{2+} in the $FAPbI_3$ compound has also been achieved, resulting in a perovskite phase with no known polymorphs and a reduction in the bandgap from 1.48 eV ($FAPbI_3$) to 1,41 eV ($FASnI_3$).[112,114]

A disadvantage of the substitution of Pb^{2+} with Sn^{2+} in perovskite compositions is that Sn^{2+} oxidizes easily to Sn^{4+}, whereby the perovskite structure and its functionality are lost.[113,115–117] Moreover, at least up to now, the efficiency of Sn^{2+} based perovskite solar cells has been less than that of Pb^{2+} based devices.[113,115,117–119]

As in the $MAPbI_3$ case, the bandgap of the tin based perovskite can also be tuned by the partial substitution of I^- by Br^- ($MASn(I_{1-x}Br_x)_3$) where bandgaps between 1.3 eV ($x = 0$) and 2.15 eV ($x = 1$) can be reached, where again the efficiency lacks considerably compared to its lead based counterpart.[112]

Mixtures of Pb^{2+} and Sn^{2+} ($MASn_{1-x}Pb_xI_3$) have also been produced where interestingly the calculated bandgap of the mixture is smaller than that of both pristine compounds for values of $x < 0.8$.[120–122]

Theoretical calculations show that Pb^{2+} can also be replaced with germanium (Ge^{2+}) and provide stable compounds. The ionic radius of Ge^{2+} is smaller than that of Sn^{2+} and Pb^{2+} and with an increasing ionic radius of the A cation (Cs < MA < FA) the bandgap of the Ge^{2+}-based perovskites increases (1.63 eV for $CsGeI_3$, 2.0 eV for $MAGeI_3$ and 2.35 eV for $FAGeI_3$), which is opposite to the results of its lead counterpart.[118] So far, the efficiency of Ge^{2+} based perovskite solar cells is very low and as with Sn^{2+}, Ge^{2+} is easily oxidized to Ge^{4+} whereby the perovskite structure and its functional properties are lost.[119,123]

Perovskite materials in which Pb^{2+} has been substituted with magnesium (Mg), thallium (Tl) in combination with bismuth (Bi), sulfur (S) and selenium (Se) have also been investigated. These structures have however only resulted in devices with very low efficiencies (< 1%) and some of these compounds are even more toxic than the lead they replace, invalidating the original purpose of the lead replacement.[118,119]

In the search for a lead(II) substitute in perovskite materials to reduce or even completely eliminate their toxicity, Sn^{2+} and Ge^{2+} seem the most likely candidate to date. However, the low efficiency of the devices and instability of the perovskite due to the oxidation of the Sn^{2+} to Sn^{4+} and Ge^{2+} to Ge^{4+} limits the implementation of these materials.

Complex mixtures

More complex mixtures containing multiple cations in combination with multiple halogens have also been used often. As a matter of fact the best performing devices (in efficiency as well as stability) are currently being produced using these highly complex mixtures.[42,124,125] Since the physical properties of these mixtures are altered in a multitude of ways simultaneously, it is challenging to ascribe them to anything specific. Although, it can be expected that substitution of the cation or halogen will have a similar effect in these complex mixtures as they do in the binary and ternary mixtures.

1.5 Perovskite solar cell architectures and processing methods

For the fabrication of solid state perovskite solar cells, mainly four different solar cell architectures are used. These architectures are termed mesoporous, capping-layer, planar n-i-p and planar p-i-n. Examples of these four are displayed in Figure 1.6. The mesoporous perovskite solar cell is a remainder of its first use as a sensitizer in a dye sensitized solar cells (DSSC). On top of the glass substrate and transparent electrode a compact electron transport layer (ETL), usually TiO_2, is deposited. On top of this, a mesoporous ETL (usually TiO_2 or Al_2O_3) is produced by sintering small particles together at high temperature (>400 °C). This porous mesoscopic structure is then filled with the perovskite active layer on top of which the solid hole transport layer (HTL), usually doped 2,2',7,7'-tetrakis-(*N*,*N*-di-4-methoxyphenylamino)-9,9'-spirobifluorene (Spiro-OMeTAD), and an opaque back contact (usually gold (Au)) are deposited (Figure 1.6a). From this mesoscopic configuration, the capping-layer structure has evolved. Since it was found that the perovskite does not need the ETL/perovskite interface to separate photo-generated excitons into free charges and the perovskite material is capable of efficient ambipolar charge transport, the thickness of the mesoscopic structure was significantly reduced

and a thick capping-layer of pure perovskite is produced on top (Figure 1.6b).[21] By completely excluding the mesoporous structure, the planar n-i-p structure is formed which therefore does not necessarily require the high temperature sintering step (Figure 1.6c). The planar p-i-n architecture is produced by depositing the HTL (usually poly(3,4-ethylenedioxythiophene):polystyrene sulfonate (PEDOT:PSS)) on top of the transparent electrode covered glass substrate. Then the perovskite layer is deposited followed by the deposition of the ETL (usually [6,6]-phenyl-C_{61}-butyric acid methyl ester (PCBM)) and an opaque back contact (usually aluminum (Al) or silver (Ag)) (Figure 1.6d).
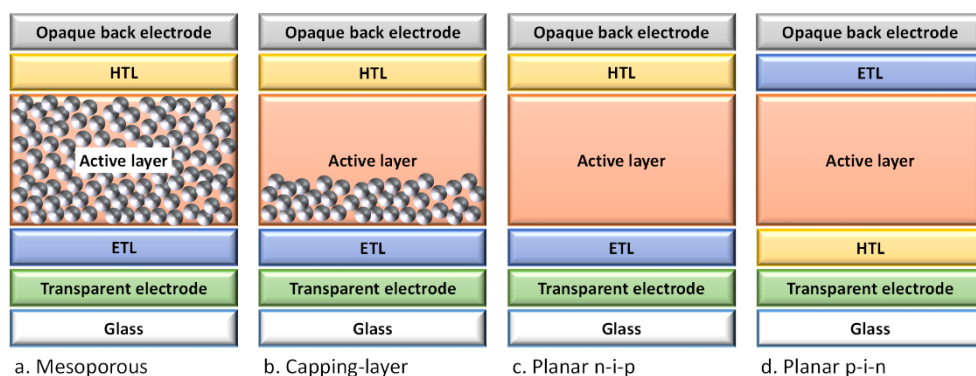
Figure 1.6 Four device architectures most used in perovskite solar cells.

Besides the development of these different device architectures, much research effort has been spent on developing different perovskite deposition methods. The aim being the production of dense, homogeneous and pinhole free perovskite layers, since controlling the perovskite morphology relates strongly to controlling the solar cell efficiency.

Because the perovskite precursor materials are quite soluble in a number of different solvents the simplest and most used deposition technique to produce a thin perovskite film is one-step spin coating. Where all precursor materials (PbI_2 and MAI in the simplest recipe) are dissolved in one solvent (usually *N,N*-dimethylformamide (DMF)) and are deposited onto the substrate in one spin coating step. In the one step spin coating deposition, changing the solvent strongly affects the produced morphology and has been used to optimize the perovskite morphology for different compositions.[126–134] Besides the solvent, changing the precursor materials from which the perovskite layer is formed can also drastically alter the crystallization process. Especially changes in the lead source have a large

effect on the crystallization kinetics. It has been shown that (partial) replacement of lead(II) iodide (PbI$_2$) with lead(II) chloride (PbCl$_2$) retards the crystallization process, allowing the perovskites crystallites to grow bigger, while (partial) replacement of PbI$_2$ with lead(II) acetate (Pb(OAc)$_2$) speeds up the crystallization process.[135–139] The chloride and acetate do however not incorporate into the perovskite structure like Br does; they mainly affect the crystallization speed and are released out of the perovskite along with the excess organics.[59,62,65,73,77,78] An excess of one of the precursor materials in the mixture or the addition of an acid or inert filler is also often used to influence the morphology and conversion of the perovskite layer.[91,125,140–148] Application of an anti-solvent on top of the wet perovskite film during spin coating drives away the excess solvent, forcing fast nucleation and crystallization to happen.[133,149–152]

In order to gain more control of the crystallization process, the crystallization of PbI$_2$ and conversion to the perovskite material can be separated by sequential processing. With this method the lead precursor is usually deposited first by spin coating and converted into perovskite by exposure of the formed (PbI$_2$) film to the organic compound (usually MAI). Where deposition of the PbI$_2$ from DMF results in crystalline layers, deposition from the strongly coordinating solvents *e.g.* dimethyl sulfoxide (DMSO) results in amorphous PbI$_2$ layers.[128,133,153–159] This PbI$_2$ layer can also be thermally or solvent annealed to optimize its morphology for incorporation of the organic compound in the second processing step.[157,158,160–164] The organic compound can be introduced to the completed PbI$_2$ layer in a variety of ways. A solution containing the organic compound can be spin coated on top of the PbI$_2$ covered substrate,[159,162–167] the PbI$_2$ covered substrate can be immersed into a MAI (or MAI/MACl) containing solution (usually in 2-propanol).[67,73,128,157,158,160,161,168–172] For these two-step deposition techniques, two competing crystallization mechanisms have been proposed as the conversion process. The first being *in-situ* conversion, where the organic compound incorporates into the PbI$_2$ crystals and the morphology formed in the first step remains and the second being dissolution-recrystallization, where the PbI$_2$ layer (partially) dissolves in the solvent used in the second step and the perovskite material crystallizes forming a new morphology.[173,174] All the solution processed films usually require some post deposition thermal annealing to evaporate solvent and promote crystallization. A great variety of annealing schemes has been proposed in the search for the most efficient devices including solvent annealing, exposure to moisture and methods that eliminate thermal annealing altogether.[72,139,175–183]

The organic compound can also be supplied from the vapor phase, which can be done using expensive high vacuum equipment but can also be done in cheaper and simpler low vacuum or atmospheric conditions.[184–187] Completely thermally evaporated perovskite films have also been produced in which different techniques have also been used.[187–191] Using co-evaporation it is challenging to keep the evaporation rate of both materials constant to avoid inhomogeneity in the perovskite layer. (Co-) evaporation could however potentially allow the production of perovskite layers with gradual changes in doping level or composition. Single crystals of different perovskite materials have also been fabricated, often using the inverse thermal solubility that some perovskite precursor-solvent combinations exhibit.[192–194] Some large area deposition techniques that have been explored successfully include doctor blading, roll to roll processing, slot dye coating, soft cover deposition and press-peel techniques.[41,195–200]

Throughout the development of ever more efficient perovskite solar cells, it appears like the efficiency increases when the perovskite composition and production procedure become more and more complex. Illustrated by the two published highest efficiency perovskite solar cells (22.1% and 21.1%, respectively) that are currently being produced as follows. In the first, the precursor solution consists of PbI_2 and $PbBr_2$ in a mixture of DMF and DMSO, which is deposited onto mesoporous TiO_2 on top of a compact TiO_2 layer on fluorinated tin oxide (FTO). A mixture of FAI, and MABr in 2-propanol (IPA) containing hydrogen triiodide is then spin coated onto the wet layer after which the perovskite layer is annealed. After this, the perovskite layers is washed with pure IPA and annealed again. A doped poly(triaryl amine) (PTAA) semiconductor layer is deposited as HTL and a gold electrode completes the device.[124] In the second, the precursor solution consists of FAI, PbI_2, MABr, $PbBr_2$ and CsI in a mixture of DMF and DMSO, which is deposited onto doped mesoporous TiO_2 on top of a compact TiO_2 layer on FTO. During spin coating, the anti-solvent chlorobenzene is deposited on top of the still wet film. A doped Spiro-OMeTAD layer is deposited as HTL and a gold electrode completes the device.[42]

The perovskite solar cells produced for the work described in this thesis have a planar p-i-n architecture, with a device stack consisting of a patterned indium tin oxide (ITO) transparent electrode on top of a glass slide. On top of which the PEDOT:PSS HTL is deposited. A $MAPbI_3$ perovskite material is deposited on top and the devices are completed by application of a PCBM ETL and a LiF/Al top contact.

1.6 Advantages and challenges

Beyond doubt, the perovskite material is suitable for use as an active material in solar cells. The high absorption coefficient, low exciton binding energy and efficient ambipolar charge transport capabilities of the material make the production of highly efficient thin film devices possible. Due to the high solubility of the precursor materials, low cost solution processing of the perovskite layer is an attractive option. Even though the record efficiency of perovskite solar cells is approaching that of the industry giant silicon, the price of silicon solar panels has dropped so significantly due to the development and maturing of the fabrication processes, that the low material costs of perovskite solar cells is no longer a strong selling point for the technology. The high defect tolerance and ability to change the composition of the material and with that tune its physical properties towards specific applications is however a unique advantage of perovskite materials. Combining this with the large number of diverse processing methods that have been developed, the way is paved for application of perovskite solar cells in large area applications as well as niche markets like flexible and tandem solar cells. The main challenges that remain for the technology are the toxicity of the lead that is used in the material. Although calculations and studies have shown that the amount of lead in perovskite solar panels is far from catastrophic for the environment or the public, recycling seems a viable option and alternatives like tin might be more toxic to the aquatic environment than lead, avoiding possible exposure to toxic materials is always preferable.[201–207] Furthermore, the long term stability of the material under operating conditions still deserves attention.

1.7 Aim and outline of this thesis

The research described in this thesis aims to introduce the perovskite material as a semiconductor for solar cell applications within the research group. Furthermore, the aim is to optimize the device performance and gain a better understanding of the material properties and photophysical processes inside the perovskite solar cells.

The correct characterization of perovskite solar cells can be challenging due to the typical response these cells can have towards the traditional measurement protocols. Especially sub-optimal perovskite solar cells can show misleading results in efficiency measurements. Therefore, measurement protocols specifically for perovskite solar cells were developed which provide correct and reliable data. The development process of these measurement protocols and the response of the perovskite solar cells towards these and the traditional measurement protocols are discussed in Chapter 2 of this thesis.

Chapter 3 describes the use of different perovskite precursor materials and the effect they have on the perovskite layer morphology. When using $PbCl_2$ as the only lead source in combination with MAI dissolved in DMF, the resulting perovskite layers are rough and show large voids in between the perovskite crystals. By combining $PbCl_2$ and $Pb(OAc)_2$ as the lead source, the ration between the two can be used to finely tune the layer morphology and improve the device performance. Further optimization of the production procedure resulted in the reproducible production of solar cells with a PCE of ~14%.

In Chapter 4 the influence of the processing atmosphere on the optimized perovskite solar cell performance is described. It was found that the influence of the atmosphere during spin coating is negligible, while the influence of the atmosphere during annealing is critical. Further investigation shows that it is specifically exposure to oxygen (O_2) during annealing that is crucial for high efficiency devices. This is because the application of the perovskite precursor solution on top of the poly(3,4-ethylenedioxythiophene):polystyrene sulfonate (PEDOT:PSS) HTL chemically reduces the oxidation state of the HTL. This changes the work function of the PEDOT:PSS that in turn alters that of the perovskite layer on top of it, resulting in lower efficiency solar cells, mainly due to reductions in open-circuit voltage and short-circuit current density. The exposure to O_2 during the annealing step (partially) re-oxidizes the PEDOT:PSS, restoring its function in the solar cell and yielding highly efficiency devices.

In chapter 5, a sequential deposition method is introduced, in which a layer of the metal halide (PbI_2) is spin coated first, that is converted into perovskite subsequently by introducing the organic compound (MAI) from the vapor phase. This method has been termed vapor assisted solution processing (VASP) in literature. In this chapter, initial experiments using a commercial thermal gradient sublimer confirm the possibility of conversion of PbI_2 layers into perovskite layers with this method. After determining the most critical parameters in the deposition process, using this setup, a dedicated VASP reactor is designed and built. This reactor provides more control over the parameters that were found highly influential in the deposition process. Experiments in which the deposition profile of MAI onto glass slides is assessed show that the carrier gas flow rate strongly influences the homogeneity of the deposition profile, while the temperature (difference) of the crucible and sample stage mainly determine the amount of deposition. When converting PbI_2 layers on glass slides, it is found that a proper balance between the deposition and the conversion reaction is much more important than heavy MAI deposition. Finally when producing solar cells using this sequential deposition method, it is found that the flow rate of the heated carrier gas is crucial for obtaining decent perovskite layers for application in a solar cell. A low flow rate is essential for gentle MAI deposition and providing sufficient time for the conversion reaction to occur. Furthermore, it is found that the purity of the PbI_2 that is used has a significant influence on the conversion and therefore the solar cell performance. The highest solar cell efficiency that was achieved using this equipment is 11.7%.

1.8 References

1   EIA, U.S. Energy Inf. Adm., 2017, **IEO2017**.

2   Bloomberg, What's Really Warming the World, https://www.bloomberg.com/graphics/2015-whats-warming-the-world/, (accessed 3 January 2018).

3   R. L. Miller, G. A. Schmidt, L. S. Nazarenko, N. Tausnev, S. E. Bauer, A. D. DelGenio, M. Kelley, K. K. Lo, R. Ruedy, D. T. Shindell, I. Aleinov, M. Bauer, R. Bleck, V. Canuto, Y. Chen, Y. Cheng, T. L. Clune, G. Faluvegi, J. E. Hansen, R. J. Healy, N. Y. Kiang, D. Koch, A. A. Lacis, A. N. LeGrande, J. Lerner, S. Menon, V. Oinas, C. Pérez García-Pando, J. P. Perlwitz, M. J. Puma, D. Rind, A. Romanou, G. L. Russell, M Sato, S Sun, K. Tsigaridis, N. Unger, A. Voulgarakis, M.-S. Yao, and J. Zhang, *J. Adv. Model. Earth Syst.*, 2014, **6**, 441–477.

4   M. H. England, S. Mcgregor, P. Spence, G. A. Meehl, A. Timmermann, W. Cai, A. S. Gupta, M. J. McPhaden, A. Purich and A. Santoso, *Nat. Clim. Chang.*, 2014, **4**, 222–227.

5   D. Nuccitelli, R. Way, R. Painting, J. Church and J. Cook, *Phys. Lett. A*, 2012, **376**, 3466–3468.

6   D. H. Douglass and R. S. Knox, *Phys. Lett. A*, 2012, **376**, 3673–3675.

7   S. L. Hautala, E. A. Solomon, H. P. Johnson, R. N. Harris and U. K. Miller, *Geophys. Res. Lett.*, 2014, **41**, 8486–8494.

8   G. W. Crabtree and N. S. Lewis, *Phys. Today*, 2007, **60**, 37.

9   A. E. Becquerel, *Comptes Rendus L´Academie des Sciences*, 1839, **9**, 145–149.

10   R. S. Ohl, *US patent*, 1941, **2**, 402, 602.

11   R. S. Ohl and E. F. Kingsbury, *Bell Syst. Tech. J.*, 1952, **31**, 802–815.

12   D. M. Chapin, C. S. Fuller and G. L. Pearson, *J. Appl. Phys.*, **1954**, 25, 676–677.

13   C. Honsberg and S. Bowden, Early silicon solar cells, http://www.pveducation.org/pvcdrom/manufacturing/early-silicon-solar-cells, (accessed 3 January 2018).

14   Fraunhofer ISE, Press-release, Fraunhofer ISE Achieves New World Record for Both Sides-Contacted Silicon Solar Cells, Freiburg, 2015. https://www.ise.fraunhofer.de/en/press-media/press-releases/2015/fraunhofer-ise-achieves-new-world-record-for-both-sides-contacted-silicon-solar-cells.html (accessed 30 January 2018)

15   National Renewable Energy Laboratory, NREL efficiency chart, https://www.nrel.gov/pv/assets/images/efficiency-chart.png, (accessed 3 January 2018).

16   W. Shockley and H. J. Queisser, *J. Appl. Phys.*, 1961, **32**, 510–519.

17   S. Rühle, *Sol. Energy*, 2016, **130**, 139–147.

18   Fraunhofer ISE (2015): Current and Future Cost of Photovoltaics. Long-term Scenarios for Market Development, System Prices and LCOE of Utility-Scale PV Systems. Study on behalf of Agora Energiewende

19   A. Kojima, K. Teshima, Y. Shirai and T. Miyasaka, *J. Am. Chem. Soc.*, 2009, **131**, 6050–6051.

20   H.-S. Kim, C.-R. Lee, J.-H. Im, K.-B. Lee, T. Moehl, A. Marchioro, S.-J. Moon, R. Humphry-Baker, J.-H. Yum, J. E. Moser, M. Grätzel and N.-G. Park, *Sci. Rep.*, 2012, **2**, 591.

21   M. M. Lee, J. Teuscher, T. Miyasaka, T. N. Murakami and H. J. Snaith, *Science*, 2012, **338**, 643–647.

22   Web of Science, Annual number of publications, https://apps.webofknowledge.com/RAMore.do?product=WOS&search_mode=General Search&SID=E1rYWp3nndHncVdBATq&qid=1&ra_mode=more&ra_name=Publication Year&colName=WOS&viewType=raMore&more_sort_order=alpha, (accessed 3 January 2018).

23   V. M. Goldschmidt, *Naturwissenschaften*, 1926, **14**, 477–485.

24   W. Travis, E. N. K. Glover, H. Bronstein, D. O. Scanlon and R. G. Palgrave, *Chem. Sci.*, 2016, **7**, 4548–4556.

25   M. A. Green, A. Ho-Baillie and H. J. Snaith, *Nat. Photonics*, 2014, **8**, 506–514.

26   G. Kieslich, S. Sun and A. K. Cheetham, *Chem. Sci.*, 2014, **5**, 4712–4715.

27   G. Kieslich, S. Sun and A. K. Cheetham, *Chem. Sci.*, 2015, **6**, 3430–3433.

28   N. Ashurov, B. L. Oksengendler, S. Maksimov, S. Rashiodva, A. R. Ishteev, D. S. Saranin, I. N. Burmistrov, D. V. Kuznetsov and A. A. Zakhisov, *Mod. Electron. Mater.*, 2017, **3**, 1–25.

29   D. Wang, M. Wright, N. K. Elumalai and A. Uddin, *Sol. Energy Mater. Sol. Cells*, 2016, **147**, 255–275.

30   M. I. Asghar, J. Zhang, H. Wang and P. D. Lund, *Renew. Sustain. Energy Rev.*, 2017, **77**, 131–146.

31   T. A. Berhe, W.-N. Su, C.-H. Chen, C.-J. Pan, J.-H. Cheng, H.-M. Chen, M.-C. Tsai, L.-Y. Chen, A. A. Dubale and B.-J. Hwang, *Energy Environ. Sci.*, 2016, **9**, 323–356.

32   W. R. Mateker and M. D. McGehee, *Adv. Mater.*, 2017, **29**, 1603940

33   A. M. A. Leguy, A. R. Goñi, J. M. Frost, J. Skelton, F. Brivio, X. Rodríguez-Martínez, O. J. Weber, A. Pallipurath, M. I. Alonso, M. Campoy-Quiles, M. T. Weller, J. Nelson, A. Walsh and P. R. F. Barnes, *Phys. Chem. Chem. Phys.*, 2016, **18**, 27051–27066.

34   L. K. Ono, E. J. Juarez-Perez and Y. Qi, *ACS Appl. Mater. Interfaces*, 2017, **9**, 30197-30246

35   J.-P. Correa-Baena, A. Abate, M. Saliba, W. Tress, T. Jesper Jacobsson, M. Grätzel and A. Hagfeldt, *Energy Environ. Sci.*, 2017, **10**, 710–727.

36   N. Pellet, P. Gao, G. Gregori, T.-Y. Yang, M. K. Nazeeruddin, J. Maier and M. Grätzel, *Angew. Chemie - Int. Ed.*, 2014, **53**, 3151–3157.

37   H. Choi, J. Jeong, H.-B. Kim, S. Kim, B. Walker, G.-H. Kim and J. Y. Kim, *Nano Energy*, 2014, **7**, 80–85.

38   Z. Li, M. Yang, J.-S. Park, S.-H. Wei, J. J. Berry and K. Zhu, *Chem. Mater.*, 2016, **28**, 284–292.

39   J.-W. Lee, D.-H. Kim, H.-S. Kim, S.-W. Seo, S. M. Cho and N.-G. Park, *Adv. Energy Mater.*, 2015, **5**, 1501310.

40   Y. H. Park, I. Jeong, S. Bae, H. J. Son, P. Lee, J. Lee, C.-H. Lee and M. J. Ko, *Adv. Funct. Mater.*, 2017, **27**, 1605988.

41   Y. Deng, Q. Dong, C. Bi, Y. Yuan and J. Huang, *Adv. Energy Mater.*, 2016, **6**, 1600372.

42   M. Saliba, T. Matsui, J.-Y. Seo, K. Domanski, J.-P. Correa-Baena, M. K. Nazeeruddin, S. M. Zakeeruddin, W. Tress, A. Abate, A. Hagfeldt and M. Grätzel, *Energy Environ. Sci.*, 2016, **9**, 1989–1997.

43   C. C. Stoumpos, C. D. Malliakas and M. G. Kanatzidis, *Inorg. Chem.*, 2013, **52**, 9019–9038.

44   A. Binek, F. C. Hanusch, P. Docampo and T. Bein, *J. Phys. Chem. Lett.*, 2015, **6**, 1249–1253.

45   B. Slimi, M. Mollar, I. B. Assaker, I. Kriaa, R. Chtourou and B. Marí, *Energy Procedia*, 2016, **102**, 87–95.

46   J. Dai, Y. Fu, L. H. Manger, M. T. Rea, L. Hwang, R. H. Goldsmith and S. Jin, *J.-Phys. Chem. Lett.*, 2016, **7**, 5036-5043.

47   Y. Zhou, Z. Zhou, M. Chen, Y. Zong, J. Huang, S. Pang and N. P. Padture, *J. Mater. Chem. A*, 2016, **4**, 17623–17635.

48   O. J. Weber, B. Charles and M. T. Weller, *J. Mater. Chem. A*, 2016, **4**, 15375–15382.

49   G. E. Eperon, G. M. Paternò, R. J. Sutton, A. Zampetti, A. A. Haghighirad, F. Cacialli and H. J. Snaith, *J. Mater. Chem. A*, 2015, **3**, 19688–19695.

50   G. Niu, W. Li, J. Li, X. Liang and L. Wang, *RSC Adv.*, 2017, **7**, 17473–17479.

51   J. Huang, P. Xu, J. Liu and X. Z. You, *Small*, 2017, **13**, 1603225.

52   T. Liu, Y. Zong, Y. Zhou, M. Yang, Z. Li, O. S. Game, K. Zhu, R. Zhu, Q. Gong and N. P. Padture, *Chem. Mater.*, 2017, **29**, 3246–3250.

53   Y. Yu, C. Wang, C. R. Grice, N. Shrestha, J. Chen, D. Zhao, W. Liao, A. J. Cimaroli, P. J. Roland, R. J. Ellingson and Y. Yan, *ChemSusChem*, 2016, **9**, 3288–3297.

54   M. C. Neuburger, *Z. Kristallogr.*, 1936, **93**, 314

55   M. Zhang, J. S. Yun, Q. Ma, J. Zheng, C. F. J. Lau, X. Deng, J. Kim, D. Kim, J. Seidel, M. A. Green, S. Huang and A. W. Y. Ho-Baillie, *ACS Energy Lett.*, 2017, **2**, 438–444.

56   S. Colella, E. Mosconi, P. Fedeli, A. Listorti, F. Gazza, F. Orlandi, P. Ferro, T. Besagni, A. Rizzo, G. Calestani, G. Gigli, F. De Angelis and R. Mosca, *Chem. Mater.*, 2013, **25**, 4613–4618.

57   B. Conings, L. Baeten, C. De Dobbelaere, J. D'Haen, J. Manca and H. G. Boyen, *Adv. Mater.*, 2014, **26**, 2041–2046.

58   J. You, Z. Hong, Y. Yang, Q. Chen, M. Cai, T.-B. Song and C.-Chen, S. Lu, Y. Liu, H. Zhou and Y. Yang, *ACS Nano*, 2014, **8**, 1674–1680.

59   H. Yu, F. Wang, F. Xie, W. Li, J. Chen and N. Zhao, *Adv. Funct. Mater.*, 2014, **24**, 7102–7108.

60   N. Yantara, F. Yanan, C. Shi, H. A. Dewi, P. P. Boix, S. G. Mhaisalkar and N. Mathews, *Chem. Mater.*, 2015, **27**, 2309–2314.

61   P. Pistor, J. Borchert, W. Fränzel, R. Csuk and R. Scheer, *J. Phys. Chem. Lett.*, 2014, **5**, 3308–3312.

62   S. Colella, E. Mosconi, G. Pellegrino, A. Alberti, V. L. P. Guerra, S. Masi, A. Listorti, A. Rizzo, G. G. Condorelli, F. De Angelis and G. Gigli, *J. Phys. Chem. Lett.*, 2014, **5**, 3532–3538.

63   Y. Chen, T. Chen and L. Dai, *Adv. Mater.*, 2015, **27**, 1053–1059.

64   E. L. Unger, A. R. Bowring, C. J. Tassone, V. L. Pool, A. Gold-Parker, R. Cheacharoen, K. H. Stone, E. T. Hoke, M. F. Toney and M. D. McGehee, *Chem. Mater.*, 2014, **26**, 7158–7165.

65   Q. Chen, H. Zhou, Y. Fang, A. Z. Stieg, T.-B. Song, H.-H. Wang, X. Xu, Y. Liu, S. Lu, J. You, P. Sun, J. McKay, M. S. Goorsky and Y. Yang, *Nat. Commun.*, 2015, **6**, 7269.

66   D. E. Starr, G. Sadoughi, E. Handick, R. G. Wilks, J. H. Alsmeier, L. Köhler, M. Gorgoi, H. J. Snaith and M. Bär, *Energy Environ. Sci.*, 2015, **8**, 1609–1615.

67   Y. Li, W. Sun, W. Yan, S. Ye, H. Peng, Z. Liu, Z. Bian and C. Huang, *Adv. Funct. Mater.*, 2015, **25**, 4867–4873.

68   L. Cojocaru, S. Uchida, A. K. Jena, T. Miyasaka, J. Nakazaki, T. Kubo and H. Segawa, *Chem. Lett.*, 2015, **44**, 1089–1091.

69   J. Chae, Q. Dong, J. Huang and A. Centrone, *Nano Lett.*, 2015, **15**, 8114–8121.

70   V. L. Pool, A. Gold-Parker, M. D. McGehee and M. F. Toney, *Chem. Mater.*, 2015, **27**, 7240–7243.

71   M. Ralaiarisoa, Y. Busby, J. Frisch, I. Salzmann, J.-J. Pireaux and N. Koch, *Phys. Chem. Chem. Phys.*, 2017, **19**, 828–836.

72   A. Dualeh, N. Tétreault, T. Moehl, P. Gao, M. K. Nazeeruddin and M. Grätzel, *Adv. Funct. Mater.*, 2014, **24**, 3250–3258.

73   P. Docampo, F. C. Hanusch, S. D. Stranks, M. Döblinger, J. M. Feckl, M. Ehrensperger, N. K. Minar, M. B. Johnston, H. J. Snaith and T. Bein, *Adv. Energy Mater.*, 2014, **4**, 1400355.

74   Y. Zhao and K. Zhu, *J. Phys. Chem. C*, 2014, **118**, 9412–9418.

75   B.-W. Park, B. Philippe and T. Gustafsson, K. Sveinbjörnsson, A Hagfeldt, E. M. J. Johansson and G. Boschloo, *Chem. Mater.*, 2014, **26**, 4466-4471.

76   Y. Tidhar, E. Edri, H. Weissman, D. Zohar, G. Hodes, D. Cahen, B. Rybtchinski and S. Kirmayer, *J. Am. Chem. Soc.*, 2014, **136**, 13249-13256.

77   S. T. Williams, F. Zuo, C.-C. Chueh, C.-Y. Liao, P.-W. Liang and A. K.-Y. Jen, *ACS Nano*, 2014, **8**, 10640–10654.

78   M. I. Dar, N. Arora, P. Gao, S. Ahmad, M. Grätzel and M. K. Nazeeruddin, *Nano Lett.*, 2014, **14**, 6991–6996.

79   F. X. Xie, D. Zhang, H. Su, X. Ren, K. S. Wong, M. Grätzel and W. C. H. Choy, *ACS Nano*, 2015, **9**, 639–646.

80   P. Luo, Z. Liu, W. Xia, C. Yuan, J. Cheng, C. Xu and Y. Lu, *J. Mater. Chem. A*, 2015, **3**, 22949–22959.

81   T.-W. Ng, C.-Y. Chan, M.-F. Lo, Z. Q. Guan and C.-S. Lee, *J. Mater. Chem. A*, 2015, **3**, 9081–9085.

82   A. Binek, I. Grill, N. Huber, K. Peters, A. G. Hufnagel, M. Handloser, P. Docampo, A. Hartschuh and T. Bein, *Chem. Asian J.*, 2016, **11**, 1199–1204.

83   B. Yang, J. Keum, O. S. Ovchinnikova, A. Belianinov, S. Chen, M.-H. Du, I. N. Ivanov, C. M. Rouleau, D. B. Geohegan and K. Xiao, *J. Am. Chem. Soc.*, 2016, **138**, 5028–5035.

84   X. Zhang, C. Liu, Y. Ma, Y. Shen, H. Li, R. Chen and Y. Mai, *Sol. Energy*, 2017, **148**, 70–77.

85   L. Fan, Y. Ding, J. Luo, B. Shi, X. Yao, C. Wei, D. Zhang, G. Wang, Y. Sheng, Y. Chen, A. Hagfeldt, Y. Zhao and X. Zhang, *J. Mater. Chem. A*, 2017, **5**, 7423–7432.

86   M. Jiang, J. Wu, F. Lan, Q. Tao, D. Gao and G. Li, *J. Mater. Chem. A*, 2015, **3**, 963–967.

87   S. D. Stranks, G. E. Eperon, G. Grancini, C. Menelaou, M. J. P. Alcocer, T. Leijtens, L. M. Herz, A. Petrozza and H. J. Snaith, *Science*, 2013, **342**, 341–344.

88   G. Xing, N. Mathews, S. Sun, S. S. Lim, Y. M. Lam, M. Grätzel, S. Mhaisalkar, T. C. Sum, *Science*, 2013, **342**, 344–347.

89   W.-J. Yin, J.-H. Yang, J. Kang, Y. Yan and S.-H. Wei, *J. Mater. Chem. A*, 2015, **3**, 8926–8942.

90   Q. Chen, N. De Marco, Y. Yang, T.-B. Song, C.-C. Chen, H. Zhao, Z. Hong, H. Zhou and Y. Yang, *Nano Today*, 2015, **10**, 355–396.

91   G. E. Eperon, S. D. Stranks, C. Menelaou, M. B. Johnston, L. M. Herz and H. J. Snaith, *Energy Environ. Sci.*, 2014, **7**, 982.

92   P. Fedeli, F. Gazza, D. Calestani, P. Ferro, T. Besagni, A. Zappettini, G. Calestani, E. Marchi, P. Ceroni and R. Mosca, *J. Phys. Chem. C*, 2015, **119**, 21304–21313.

93   J. H. Noh, S. H. Im, J. H. Heo, T. N. Mandal and S. Il Seok, *Nano Lett.*, 2013, **13**, 1764–1769.

94   E. T. Hoke, D. J. Slotcavage, E. R. Dohner, A. R. Bowring, H. I. Karunadasa and M. D. McGehee, *Chem. Sci.*, 2015, **6**, 613–617.

95   R. K. Misra, L. Ciammaruchi, S. Aharon, D. Mogilyansky, L. Etgar, I. Visoly-Fisher and E. A. Katz, *ChemSusChem*, 2016, **9**, 2572–2577.

96   C. G. Bischak, C. L. Hetherington, H. Wu, S. Aloni, D. F. Ogletree, D. T. Limmer and N. S. Ginsberg, *Nano Lett.*, 2017, **17**, 1028–1033.

97   Y. Yuan and J. Huang, *Acc. Chem. Res.*, 2016, **49**, 286–293.

98   F. Brivio, C. Caetano and A. Walsh, *J. Phys. Chem. Lett.*, 2016, **7**, 1083–1087.

99   R. E. Beal, D. J. Slotcavage, T. Leijtens, A. R. Bowring, R. A. Belisle, W. H. Nguyen, G. F. Burkhard, E. T. Hoke and M. D. McGehee, *J. Phys. Chem. Lett.*, 2016, **7**, 746–751.

100   R. J. Sutton, G. E. Eperon, L. Miranda, E. S. Parrott, B. A. Kamino, J. B. Patel, M. T. Hörantner, M. B. Johnston, A. A. Haghighirad, D. T. Moore and H. J. Snaith, *Adv. Energy Mater.*, 2016, **6**, 1502458.

101   N. Kitazawa, Y. Watanabe and Y. Nakamura, *J. Mater. Sci.*, 2002, 3**7**, 3585–3587.

102   T. Zhang, M. Yang, E. E. Benson, Z. Li, J. van de Lagemaat, J. M. Luther, Y. Yan, K. Zhu and Y. Zhao, *Chem. Commun.*, 2015, **51**, 7820–7823.

103   Y. Fang, Q. Dong, Y. Shao, Y. Yuan and J. Huang, *Nat. Photonics*, 2015, **9**, 679–686.

104   W.-J. Yin, Y. Yan and S.-H. Wei, *J. Phys. Chem. Lett.*, 2014, **5**, 3625–3631.

105   Y.-H. Kim, H. Cho, J. H. Heo, T.-S. Kim, N. S. Myoung, C.-L. Lee, S. H. Im and T.-W. Lee, *Adv. Mater.*, 2015, **27**, 1248–1254.

106   F. Zhang, H. Zhong, C. Chen, X.-G. Wu, X. Hu, H. Huang, J. Han, B. Zou and Y. Dong, *ACS Nano*, 2015, **9**, 4533–4542.

107   Z.-K. Tan, R. S. Moghaddam, M. L. Lai, P. Docampo, R. Higler, F. Deschler, M. Price, A. Sadhanala, L. M. Pazos, D. Credgington, F. Hanusch, T. Bein, H. J. Snaith and R. H. Friend, *Nat. Nanotechnol.*, 2014, **9**, 687–692.

108   M. Wei, Y.-H. Chung, Y. Xiao and Z. Chen, *Org. Electron.*, 2015, **26**, 260–264.

109   C.-H. Chiang, J.-W. Lin and C.-G. Wu, *J. Mater. Chem. A*, 2016, **4**, 13525–13533.

110   Y. Zhao and K. Zhu, *J. Am. Chem. Soc.*, 2014, **136**, 12241–12244.

111   B. Suarez, V. Gonzalez-Pedro, T. S. Ripolles, R. S. Sanchez, L. Otero and I. Mora-Sero, *J. Phys. Chem. Lett.*, 2014, **5**, 1628–1635.

112   F. Hao, C. C. Stoumpos, D. H. Cao, R. P. H. Chang and M. G. Kanatzidis, *Nat. Photonics*, 2014, **8**, 489–494.

113   N. K. Noel, S. D. Stranks, A. Abate, C. Wehrenfennig, S. Guarnera, A.-A. Haghighirad, A. Sadhanala, G. E. Eperon, S. K. Pathak, M. B. Johnston, A. Petrozza, L. M. Herz and H. J. Snaith, *Energy Environ. Sci.*, 2014, **7**, 3061–3068.

114   Y.-Y. Sun, J. Shi, J. Lian, W. Gao, M. L. Agiorgousis, P. Zhang and S. Zhang, *Nanoscale*, 2016, **8**, 6284–6289.

115   W. Liao, D. Zhao, Y. Yu, C. R. Grice, C. Wang, A. J. Cimaroli, P. Schulz, W. Meng, K. Zhu, R.-G. Xiong and Y. Yan, *Adv. Mater.*, 2016, **28**, 9333–9340.

116   T. Yokoyama, D. H. Cao, C. C. Stoumpos, T.-B. Song, Y. Sato, S. Aramaki and M. G. Kanatzidis, *J. Phys. Chem. Lett.*, 2016, **7**, 776–782.

117   F. Hao, C. C. Stoumpos, P. Guo, N. Zhou, T. J. Marks, R. P. H. Chang and M. G. Kanatzidis, *J. Am. Chem. Soc.*, 2015, **137**, 11445–11452.

118   S. Yang, W. Fu, Z. Zhang, H. Chen and C.-Z. Li, *J. Mater. Chem. A*, 2017, **5**, 11462–11482.

119   Z. Shi, J. Guo, Y. Chen, Q. Li, Y. Pan, H. Zhang, Y. Xia and W. Huang, *Adv. Mater.*, 2017, **29**, 1605005.

120   F. Hao, C. C. Stoumpos, R. P. H. Chang and M. G. Kanatzidis, *J. Am. Chem. Soc.*, 2014, **136**, 8094–8099.

121   F. Zuo, S. T. Williams, P.-W. Liang, C.-C. Chueh, C.-Y. Liao and A. K.-Y. Jen, *Adv. Mater.*, 2014, **26**, 6454–6460.

122   J. Im, C. C. Stoumpos, H. Jin, A. J. Freeman and M. G. Kanatzidis, *J. Phys. Chem. Lett.*, 2015, **6**, 3503–3509.

123   T. Krishnamoorthy, H. Ding, C. Yan, W. L. Leong, T. Baikie, Z. Zhang, M. Sherburne, S. Li, M. Asta, N. Mathews and S. G. Mhaisalkar, *J. Mater. Chem. A*, 2015, **3**, 23829–23832.

124   W. S. Yang, B.-W. Park, E. H. Jung and N. J. Jeon, Y. C. Kim, D. U. Lee, S. S. Shin, J. Seo, E. K. Kim, J. H. Noh, S. I. Seok, *Science*, 2017, **356**, 1376–1379.

125   D. Bi, W. Tress, M. I. Dar, P. Gao, J. Luo, C. Renevier, K. Schenk, A. Abate, F. Giordano, J.-P. Correa Baena, J.-D. Decoppet, S. M. Zakeeruddin, M. K. Nazeeruddin, M. Grätzel and A. Hagfeldt, *Sci. Adv.*, 2016, **2**, 1501170.

126   N. K. Noel, S. N. Habisreutinger, B. Wenger, M. T. Klug, M. T. Hörantner, M. B. Johnston, R. J. Nicholas, D. T. Moore and H. J. Snaith, *Energy Environ. Sci.*, 2017, **10**, 145-152.

127   K. H. Hendriks, J. J. van Franeker, B. J. Bruijnaers, J. A. Anta, M. M. Wienk and R. A. J. Janssen, *J. Mater. Chem. A*, 2017, **5**, 2346–2354.

128   Y. Wu, A. Islam, X. Yang, C. Qin, J. Liu, K. Zhang, W. Peng and L. Han, *Energy Environ. Sci.*, 2014, **7**, 2934–2938.

129   N. Ahn, D.-Y. Son, I.-H. Jang, S. M. Kang, M. Choi and N.-G. Park, *J. Am. Chem. Soc.*, 2015, **137**, 8696–8699.

130   K. L. Gardner, J. G. Tait, T. Merckx, W. Qiu, U. W. Paetzold, L. Kootstra, M. Jaysankar, R. Gehlhaar, D. Cheyns, P. Heremans and J. Poortmans, *Adv. Energy Mater.*, 2016, **6**, 1600386.

131   S. Bae, S. J. Han, T. J. Shin and W. H. Jo, *J. Mater. Chem. A*, 2015, **3**, 23964–23972.

132   N. J. Jeon, J. H. Noh, Y. C. Kim, W. S. Yang, S. Ryu and S. Il Seok, *Nat. Mater.*, 2014, **13**, 897–903.

133   Y. Jo, K. S. Oh, M. Kim, K.-H. Kim, H. Lee, C.-W. Lee and D. S. Kim, *Adv. Mater. Interfaces*, 2016, **3**, 1500768.

134   G. E. Eperon, V. M. Burlakov, P. Docampo, A. Goriely and H. J. Snaith, *Adv. Funct. Mater.*, 2014, **24**, 151–157.

135   W. Qiu, T. Merckx, M. Jaysankar, C. Masse de la Huerta, L. Rakocevic, W. Zhang, U. W. Paetzold, R. Gehlhaar, L. Froyen, J. Poortmans, D. Cheyns, H. J. Snaith and P. Heremans, *Energy Environ. Sci.*, 2016, **9**, 484–489.

136   F. K. Aldibaja, L. Badia, E. Mas-Marzá, R. S. Sánchez, E. M. Barea and I. Mora-Sero, *J. Mater. Chem. A*, 2015, **3**, 9194–9200.

137   D. T. Moore, H. Sai, K. W. Tan, L. A. Estroff and U. Wiesner, *APL Mater.*, 2014, **2**, 081802.

138   D. T. Moore, H. Sai, K. W. Tan, D.-M. Smilgies, W. Zhang, H. J. Snaith, U. Wiesner and L. A. Estroff, *J. Am. Chem. Soc.*, 2015, **137**, 2350–2358.

139   W. Zhang, M. Saliba, D. T. Moore, S. K. Pathak, M. T. Hörantner, T. Stergiopoulos, S. D. Stranks, G. E. Eperon, J. A. Alexander-Webber, A. Abate, A. Sadhanala, S. Yao, Y. Chen, R. H. Friend, L. A. Estroff, U. Wiesner and H. J. Snaith, *Nat. Commun.*, 2015, **6**, 6142.

140   H. Yu, H. Lu, F. Xie, S. Zhou and N. Zhao, *Adv. Funct. Mater.*, 2016, **26**, 1411–1419.

141   C. Roldán-Carmona, P. Gratia, I. Zimmermann, G. Grancini, P. Gao, M. Graetzel and M. K. Nazeeruddin, *Energy Environ. Sci.*, 2015, **8**, 3550–3556.

142   Y. C. Kim, N. J. Jeon, J. H. Noh, W. S. Yang, J. Seo, J. S. Yun, A. Ho-Baillie, S. Huang, M. A. Green, J. Seidel, T. K. Ahn and S. I. Seok, *Adv. Energy Mater.*, 2016, **6**, 1502104.

143   M. Yang, Y. Zhou, Y. Zeng, C.-S. Jiang, N. P. Padture and K. Zhu, *Adv. Mater.*, 2015, **27**, 6363–6370.

144   J. H. Heo, D. H. Song, H. J. Han, S. Y. Kim, J. H. Kim, D. Kim, H. W. Shin, T. K. Ahn, C. Wolf, T.-W. Lee and S. H. Im, *Adv. Mater.*, 2015, **27**, 3424–3430.

145   T. Zhang, N. Guo, G. Li, X. Qian, L. Li and Y. Zhao, *J. Mater. Chem. A*, 2016, **4**, 3245–3248.

146   G. Li, T. Zhang and Y. Zhao, *J. Mater. Chem. A*, 2015, **3**, 19674–19678.

147   X. Li, M. Ibrahim Dar, C. Yi, J. Luo, M. Tschumi, S. M. Zakeeruddin, M. K. Nazeeruddin, H. Han and M. Grätzel, *Nat. Chem.*, 2015, **7**, 703–711.

148   Y. Zhao, J. Wei, H. Li, Y. Yan, W. Zhou, D. Yu and Q. Zhao, *Nat. Commun.*, 2016, **7**, 10228.

149   J. Xiong, B. Yang, R. Wu, C. Cao, Y. Huang, C. Liu, Z. Hu, H. Huang, Y. Gao and J. Yang, *Org. Electron.*, 2015, **24**, 106–112.

150   Y. Zhou, M. Yang, W. Wu, A. L. Vasiliev, K. Zhu and N. P. Padture, *J. Mater. Chem. A*, 2015, **3**, 8178–8184.

151   H. D. Kim, H. Ohkita, H. Benten and S. Ito, *Adv. Mater.*, 2016, **28**, 917–922.

152   M. Xiao, F. Huang, W. Huang, Y. Dkhissi, Y. Zhu, J. Etheridge, A. Gray-Weale, U. Bach, Y.-B. Cheng and L. Spiccia, *Angew. Chemie*, 2014, **126**, 10056-10061.

153   J. W. Lee, H.-S. Kim and N.-G. Park, *Acc. Chem. Res.*, 2016, **49**, 311–319.

154   B. J. Foley, J. Girard, B. A. Sorenson, A. Z. Chen, J. Scott Niezgoda, M. R. Alpert, A. F. Harper, D.-M. Smilgies, P. Clancy, W. A. Saidi and J. J. Choi, *J. Mater. Chem. A*, 2017, **5**, 113–123.

155   A. Wakamiya, M. Endo, T. Sasamori, N. Tokitoh, Y. Ogomi, S. Hayase and Y. Murata, *Chem. Lett.*, 2014, **43**, 711–713.

156   H. Miyamae, Y. Numahata and M. Nagata, *Chem. Lett.*, 1980, 663–664.

157   H. Zhang, J. Mao, H. He, D. Zhang, H. L. Zhu, F. Xie, K. S. Wong, M. Grätzel and W. C. H. Choy, *Adv. Energy Mater.*, 2015, **5**, 1501354.

158   W. Li, H. Dong, L. Wang, N. Li, X. Guo, J. Li and Y. Qiu, *J. Mater. Chem. A*, 2014, **2**, 13587–13592.

159   W. Li, J. Fan, J. Li, Y. Mai and L. Wang, *J. Am. Chem. Soc.*, 2015, **137**, 10399–10405.

160   Y. H. Lee, J. Luo, R. Humphry-Baker, P. Gao, M. Grätzel and M. K. Nazeeruddin, *Adv. Funct. Mater.*, 2015, **25**, 3925–3933.

161   Y. Xie, F. Shao, Y. Wang, T. Xu, D. Wang and F. Huang, *ACS Appl. Mater. Interfaces*, 2015, **7**, 12937–12942.

162   Z. Zhang, D. Wei, B. Xie, X. Yue, M. Li, D. Song and Y. Li, *Sol. Energy*, 2015, **122**, 97–103.

163   K. Wang, C. Liu, C. Yi, L. Chen, J. Zhu, R. A. Weiss and X. Gong, *Adv. Funct. Mater.*, 2015, **25**, 6875–6884.

164   Y. Zhou, M. Yang, A. L. Vasiliev, H. F. Garces, Y. Zhao, D. Wang, S. Pang, K. Zhu and N. P. Padture, *J. Mater. Chem. A*, 2015, **3**, 9249–9256.

165   C.-H. Chiang, Z.-L. Tseng and C.-G. Wu, *J. Mater. Chem. A*, 2014, **2**, 15897–15903.

166   X. Huang, K. Wang, C. Yi, T. Meng and X. Gong, *Adv. Energy Mater.*, 2015, **6**, 1501773.

167   Q. Dong, Y. Yuan, Y. Shao, Y. Fang, Q. Wang and J. Huang, *Energy Environ. Sci.*, 2015, **8**, 2464–2470.

168   K. Liang, D. B. Mitzi and M. T. Prikas, *Chem. Mater.*, 1998, **10**, 403–411.

169   J. Burschka, N. Pellet, S.-J. Moon, R. Humphry-Baker, P. Gao, M. K. Nazeeruddin and M. Grätzel, *Nature*, 2013, **499**, 316–319.

170   T. Zhang, M. Yang, Y. Zhao and K. Zhu, *Nano Lett.*, 2015, **15**, 3959–3963.

171   D. Liu and T. L. Kelly, *Nat. Photonics*, 2014, **8**, 133–138.

172   Y. Jin and G. Chumanov, *Chem. Lett.*, 2014, **43**, 1722–1724.

173   Y. Fu, F. Meng, M. B. Rowley, B. J. Thompson, M. J. Shearer, D. Ma, R. J. Hamers, J. C. Wright and S. Jin, *J. Am. Chem. Soc.*, 2015, **137**, 5810–5818.

174   S. Yang, Y. C. Zheng, Y. Hou, X. Chen, Y. Chen, Y. Wang, H. Zhao and H. G. Yang, *Chem. Mater.*, 2014, **26**, 6705–6710.

175   S. R. Raga, M.-C. Jung, M. V. Lee, M. R. Leyden, Y. Kato and Y. Qi, *Chem. Mater.*, 2015, **27**, 1597–1603.

176   M.-F. Xu, H. Zhang, S. Zhang, H. L. Zhu, H.-M. Su, J. Liu, K. S. Wong, L.-S. Liao and W. C. H. Choy, *J. Mater. Chem. A*, 2015, **3**, 14424–14430.

177   B. Conings, A. Babayigit, M. T. Klug, S. Bai, N. Gauquelin, N. Sakai, J. T.-W. Wang, J. Verbeeck, H.-G. Boyen and H. J. Snaith, *Adv. Mater.*, 2016, **28**, 10701–10709.

178   Z. Zhou, Z. Wang, Y. Zhou, S. Pang, D. Wang, H. Xu, Z. Liu, N. P. Padture and G. Cui, *Angew. Chemie Int. Ed.*, 2015, **54**, 9705–9709.

179   Z. Xiao, Q. Dong, C. Bi, Y. Shao, Y. Yuan and J. Huang, *Adv. Mater.*, 2014, **26**, 6503–6509.

180   H. Yu, X. Liu, Y. Xia, Q. Dong, K. Zhang, Z. Wang, Y. Zhou, B. Song and Y. Li, *J. Mater. Chem. A*, 2016, **4**, 321–326.

181   Q. Liang, J. Liu, Z. Cheng, Y. Li, L. Chen, R. Zhang, J. Zhang and Y. Han, *J. Mater. Chem. A*, 2016, **4**, 223–232.

182   Y. Chen, Y. Zhao and Z. Liang, *Chem. Mater.*, 2015, **27**, 1448–1451.

183   J. Liu, C. Gao, X. He, Q. Ye, L. Ouyang, D. Zhuang, C. Liao, J. Mei and W. Lau, *ACS Appl. Mater. Interfaces*, 2015, **7**, 24008–24015.

184   Q. Chen, H. Zhou, Z. Hong, S. Luo, H.-S. Duan, H.-H. Wang, Y. Liu, G. Li and Y. Yang, *J. Am. Chem. Soc.*, 2014, **136**, 622–625.

185   F. Huang, Y. Dkhissi, W. Huang, M. Xiao, I. Benesperi, S. Rubanov, Y. Zhu, X. Lin, L. Jiang, Y. Zhou, A. Gray-Weale, J. Etheridge, C. R. McNeill, R. A. Caruso, U. Bach, L. Spiccia and Y.-B. Cheng, *Nano Energy*, 2014, **10**, 10–18.

186   M. M. Tavakoli, L. Gu, Y. Gao, C. Reckmeier, J. He, A. L. Rogach, Y. Yao and Z. Fan, *Sci. Rep.*, 2015, **5**, 14083.

187   L. K. Ono, M. R. Leyden, S. Wang and Y. Qi, *J. Mater. Chem. A*, 2016, **4**, 6693–6713.

188   M. Liu, M. B. Johnston and H. J. Snaith, *Nature*, 2013, **501**, 395–398.

189   C. Roldán-Carmona, O. Malinkiewicz, A. Soriano, G. Mínguez Espallargas, A. Garcia, P. Reinecke, T. Kroyer, M. I. Dar, M. K. Nazeeruddin and H. J. Bolink, *Energy Environ. Sci.*, 2014, **7**, 994-997.

190   O. Malinkiewicz, A. Yella, Y. H. Lee, G. M. Espallargas, M. Graetzel, M. K. Nazeeruddin and H. J. Bolink, *Nat. Photonics*, 2014, **8**, 128–132.

191   P. Fan, D. Gu, G.-X. Liang, J.-T. Luo, J.-L. Chen, Z.-H. Zheng and D.-P. Zhang, *Sci. Rep.*, 2016, **6**, 29910.

192   G. Maculan, A. D. Sheikh, A. L. Abdelhady, M. I. Saidaminov, M. A. Haque, B. Murali, E. Alarousu, O. F. Mohammed, T. Wu and O. M. Bakr, *J. Phys. Chem. Lett.*, 2015, **6**, 3781–3786.

193   M. I. Saidaminov, A. L. Abdelhady, B. Murali, E. Alarousu, V. M. Burlakov, W. Peng, I. Dursun, L. Wang, Y. He, G. Maculan, A. Goriely, T. Wu, O. F. Mohammed and O. M. Bakr, *Nat. Commun.*, 2015, **6**, 7586.

194   H.-H. Fang, R. Raissa, M. Abdu-Aguye, S. Adjokatse, G. R. Blake, J. Even and M. A. Loi, *Adv. Funct. Mater.*, 2015, **25**, 2378–2385.

195   K. Hwang, Y.-S. Jung, Y.-J. Heo, F. H. Scholes, S. E. Watkins, J. Subbiah, D. J. Jones, D.-Y. Kim and D. Vak, *Adv. Mater.*, 2015, **27**, 1241–1247.

196   H. Chen, F. Ye, W. Tang, J. He, M. Yin, Y. Wang, F. Xie, E. Bi, X. Yang, M. Grätzel and L. Han, *Nature*, 2017, **550**, 92–95.

197   Z. Gu, L. Zuo, T. T. Larsen-Olsen, T. Ye, G. Wu, F. C. Krebs and H. Chen, *J. Mater. Chem. A*, 2015, **3**, 24254–24260.

198   T. M. Schmidt, T. T. Larsen-Olsen, J. E. Carlé, D. Angmo and F. C. Krebs, *Adv. Energy Mater.*, 2015, **5**, 1500569.

199   F. Ye, H. Chen, F. Xie, W. Tang, M. Yin, J. He, E. Bi, Y. Wang, X. Yang and L. Han, *Energy Environ. Sci.*, 2016, **9**, 2295–2301.

200   Y. Galagan, E. W. C. Coenen, W. J. H. Verhees and R. Andriessen, *J. Mater. Chem. A*, 2016, **4**, 5700–5705.

201   A. Binek, M. L. Petrus, N. Huber, H. Bristow, Y. Hu, T. Bein and P. Docampo, *ACS Appl. Mater. Interfaces*, 2016, **8**, 12881–12886.

202   D. Fabini, *J. Phys. Chem. Lett.*, 2015, **6**, 3546–3548.

203   A. Babayigit, D. D. Thanh, A. Ethirajan, J. Manca, M. Muller, H.-G. Boyen and B. Conings, *Sci. Rep.*, 2016, **6**, 18721.

204   A. Babayigit, A. Ethirajan, M. Muller and B. Conings, *Nat. Mater.*, 2016, **15**, 247–251.

205   B. Hailegnaw, S. Kirmayer, E. Edri, G. Hodes and D. Cahen, *J. Phys. Chem. Lett.*, 2015, **6**, 1543–1547.

206   J. M. Kadro, N. Pellet, F. Giordano, A. Ulianov, O. Müntener, J. Maier, M. Grätzel and A. Hagfeldt, *Energy Environ. Sci.*, 2016, **9**, 3172–3179.

207   B. J. Kim, D. H. Kim, S. L. Kwon, S. Y. Park, Z. Li, K. Zhu and H. S. Jung, *Nat. Commun.*, 2016, **7**, 11735.

Chapter 2

Correct characterization of metal halide perovskite solar cells

Abstract

The research effort on metal halide perovskite solar cells has been growing incredibly fast in the past few years with many groups that were focused on other types of solar cells making the switch to perovskite solar cell research. This has led to a variety of processing methods and perovskite compositions and has pushed the efficiency of this new class of solar cells to over 22% in a short time period. The fast growth of the field and focus on publishing ever higher efficiencies has however resulted in a lack of research effort on the working principles of this new type of solar cell in the early years of perovskite solar cell research. It is now well known throughout the perovskite community that perovskite solar cells can display behavior that is typical to perovskite cells and has not been seen before in organic- or inorganic solar cells. Especially if the perovskite cells are sub-optimal, the behavior in efficiency measurements can be misleading. Due to the lack of knowledge on how to characterize the perovskite solar cells correctly some unreliable efficiencies have been reported in the early years of perovskite solar cell research. The proper way to characterize perovskite solar cells has been debated extensively and at this point in time a general agreement has been reached on how to properly characterize perovskite solar cells. The characterization methods that we use today, their development and the reasoning behind the methods are discussed in this chapter.

2.1 Introduction

Since the discovery of a metal halide perovskite that functions well as an absorber material in a dye sensitized solar cell (DSSC),[1] an immense research effort has been triggered, especially when breakthrough efficiencies of 10% were reached only a few years later.[2,3] The latest reported efficiencies are even exceeding 20%,[4–6] making this material an interesting option for thin-film photovoltaic application and an inexpensive alternative for conventional inorganic solar cells.

High quality perovskite layers are currently being produced using a variety of precursor components, processing procedures and pre- and post-deposition treatments of the perovskite layer. The most used perovskite material for solar cell application is the methylammonium (MA) lead triiodide (PbI_3) ($MAPbI_3$),[2,7–10] but this is certainly not the only combination of the perovskite structure that has been studied in the field. The organic monovalent cation MA has been replaced by formamidinium (FA) and cesium (Cs) resulting in a slight decrease and increase of the bandgap of the material, respectively.[5,11–15] Cs has been reported to also stabilize the perovskite structure itself.[6,16] Replacement of Pb by mainly tin (Sn) has been reported to reduce the potential toxicity problems with the use of lead containing perovskites[17–19], while studies for the replacement of Pb by bismuth (Bi), antimony (Sb), germanium (Ge) and strontium (Sr) have also been conducted.[20,21] The substitution of the iodide (I) by chloride (Cl) and bromide (Br) has also been studied extensively, where it has been found that the Cl is not incorporated into the perovskite structure, but can be used for tuning of the crystallization behavior.[22–29] Br on the other hand can be incorporated into the perovskite structure and allows the tuning of the bandgap by changing the I:Br ratio.[13]

Aside from the different precursor materials that can be used and the influence they have on the properties of the perovskite material, the processing method can also affect the quality of the perovskite layer, which has led to the development of a large variety of processing methods. The perovskite layer can be deposited from a single precursor solution that can consist of different perovskite precursor materials dissolved in (a combination of) different solvents, with or without additives, or an excess of certain compounds.[5,11,13,30–36] Sequential deposition methods have also been reported where usually a lead iodide (PbI_2) layer is deposited from solution and methylammonium iodide (MAI) is deposited on top of this layer *via* either spin coating[37–41] or dipping[42,43] of a solution containing MIA or *via* evaporation of MAI.[27,44–51] Non-solvent treatments on the deposited precursor solution[52–55] and

solvent vapor treatments are also broadly applied.[52–55] Even fully evaporated perovskite layers have been reported.[56–58] The crystallization behavior is generally influenced by the use of different solvents or solvent combinations and precursor materials to achieve the desired smoothness and dense perovskite layers.[5,32,53,59,60] The applied perovskite layer generally requires some post deposition annealing in order to produce the best performing perovskite layers. The sensitivity of the perovskite towards atmospheric conditions[61–64] and annealing times and temperatures[65–68] have given rise to complex annealing schemes including ramp annealing procedures.[69–72] On top of this versatility in composition and processing methods, the perovskite material can be used in different solar cell architectures like any other absorber material.[73,74]

Independent of the cell architecture, perovskite composition, production procedure and pre- and post-deposition treatments that are required to produce the high quality perovskite layers for efficient solar cells, the characterization of the solar cell efficiency after completion of the device is of high importance. The efficiency of a solar cell is usually determined using standardized test methods which were traditionally developed to characterize inorganic and organic solar cells. Since the general operating mechanisms of inorganic and organic solar cells are already quite well understood, these measurement protocols are well suited for the characterization of these types of devices. The perovskite material however can display very atypical behavior when subjected to these standardized efficiency measurements. Here, the standard measurement protocols for organic- and inorganic solar cells are explained and some typical responses of perovskite solar cells to these measurement protocols are demonstrated. The origins of this atypical behavior are discussed and specific measurement protocols for the correct characterization of perovskite solar cells are proposed if the standard methods do not suffice.

2.2 Perovskite solar cell efficiency measurement

J-V measurement

Probably the most important characterization of a solar cell is the determination of the solar cell efficiency. The solar cell's efficiency is typically determined by performing a current density – voltage (*J-V*) measurement. In this characterization, the solar cell's electrodes are connected and while the cell is set to operate at a certain bias voltage, the current flow through the cell is measured. This step is performed at different bias voltages and connecting these measured points

results in a *J-V* curve (Figure 2.1). This procedure is quite fast (a scan spanning 4 V typically consist of 401 voltage steps and takes 15-20 s in total) and can be performed with the cell illuminated or with the cell in the dark. In the dark, the device should show a diode like curve, passing almost no current in reverse bias ($V < 0$) while passing a large amount of current at forward bias ($V \geq V_{bi}$). With the cell under illumination, it produces power and the *J-V* curve shifts down the y-axis due to the generated current flow (Figure 2.1).
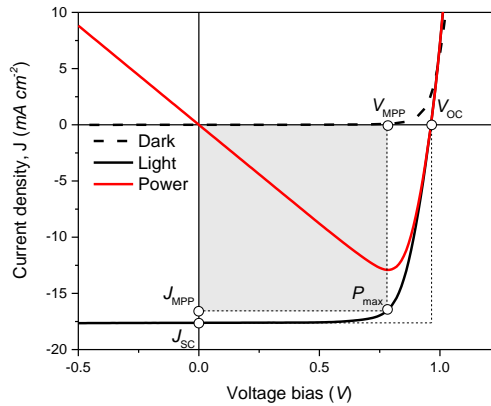
Figure 2.1 Typical *J-V* curve of a solar cell in dark (dashed) and under illumination (solid) showing some characteristic points. The power curve ($P = I \times V$) is displayed in the red solid line.

From the curve with the cell illuminated, a few important parameters can be extracted. The most important being the short-circuit current density (J_{SC}), the open-circuit voltage (V_{OC}), the maximum power (P_{max}) and the fill factor (FF). The J_{SC} being the current density that is produced by the cell at a bias voltage of zero volts and is the maximum amount of current that can be generated by illuminating the solar cell (Figure 2.1). The V_{OC} is the voltage at which no net current flows through the device (photocurrent density equals dark current density) and is dependent on the bandgap of the absorber material and device layout. The power output of the solar cell is the product of the voltage and current ($P = I \times V$) and the *I*, *V* combination for which *P* maximizes (P_{max}) is called the maximum power point (MPP) (Figure 2.1).

$$P_{max} = J_{MPP} \cdot V_{MPP}$$

The fill factor of the solar cell is determined by dividing the product of the current density and voltage at maximum power point by the product of the J_{SC} and V_{OC}.

$$\text{FF} = \frac{J_{MPP} \cdot V_{MPP}}{J_{SC} \cdot V_{OC}}$$

Resulting in the equation for calculating the power generated at the maximum power point.

$$P_{max} = \text{FF} \cdot J_{SC} \cdot V_{OC}$$

Where conventionally, the power (P) is expressed in milliwatts per square centimeter (mW cm^{-2}), the J_{SC} is expressed in milliamperes per square centimeter (mA cm^{-2}) and the V_{OC} is expressed in volts (V).

Upon characterizing perovskite solar cells using these typical J-V measurements, some peculiar behavior can be observed. The measured J-V curve of the perovskite solar cell can change with illumination time, often increasing the cell's performance by an increase in FF and V_{OC} (Figure 2.2). This effect is well known in the field and is referred to as 'light soaking'. In Table 2.1 the parameters extracted from the measured J-V curves at two different illumination times are displayed.
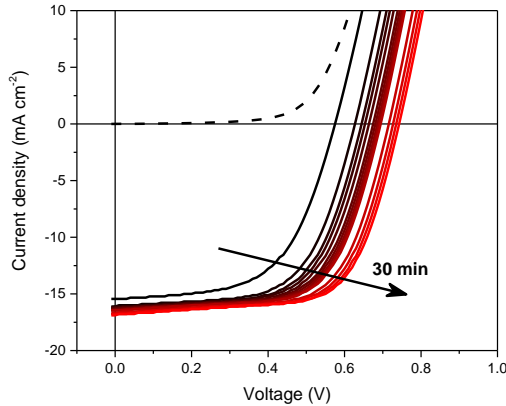
Figure 2.2 J-V curves of a perovskite solar cell in dark (dashed) and under illumination (solid) after different illumination times up to 30 minutes.

Table 2.1 *J-V* parameters extracted from scans with the cell at different illumination times

Illumination time t (min.)	J_{sc} (mA cm^{-2})	V_{oc} (V)	FF	P_{max} (mW cm^{-2})
0	15.4	0.58	0.58	5.2
30	16.9	0.74	0.66	8.3

The origin of the light soaking effect has been investigated abundantly and has been attributed to the redistribution of mobile ions inside the perovskite layer. It has been experimentally confirmed that MA$^+$ ions and I$^-$ vacancies are the most mobile species in the perovskite layer.[75,76] Due to the applied and photogenerated electric field, these mobile ions move towards the (selective) contact interfaces. This facilitates charge accumulation at the interfaces, forming *p-i-n* homo-junctions *in-situ* in the perovskite layer.[77–79] Furthermore, the aggregation of MA$^+$ ions at the interface with [6,6]-phenyl-C$_{61}$-butyric acid methyl ester (PCBM), which is frequently used as electron transport layer, reduces the energy disorder of the interface, improving the V_{OC}. Due to the strong binding energy between PCBM and MA$^+$,[77] the MA$^+$ ion could be trapped at the PCBM interface, reducing the reversibility of the light soaking effect.[77,80]

Another remarkable phenomenon that is observed in the characterization of perovskite solar cells is the difference in their response depending on the scanning direction of the *J-V* measurement. A *J-V* scan can be performed from negative voltage bias to positive voltage bias (up) or in the opposite direction (down). For perovskite solar cells, the resulting *J-V* graphs from scans in different directions on the same device can be different (Figure 2.3). This phenomenon is called hysteresis (a phenomenon in which the value of a physical property lags behind changes in the effect causing it) and has also been encountered in the characterization of dye sensitized solar cells (DSSCs), where it is attributed to the mobility of the ions in the liquid electrolyte that is used in these solar cells.[81] In Table 2.2 the parameters extracted from the measured *J-V* curves using different scan directions are displayed. In the upward scan (starting at -0.5 V) the cell is clearly not in a steady-state situation at the start of the measurement and there is a delay in the response of the cell to the changing voltage, resulting in the strange deviation in the curve at negative voltage bias. This indicates that the hysteresis can be a slow process and that the pre-conditioning of the cell has influence on the measurement. The same effect is seen for the downward measurement at the 1.5 V starting point of the measurement (not shown in Figure 2.3).
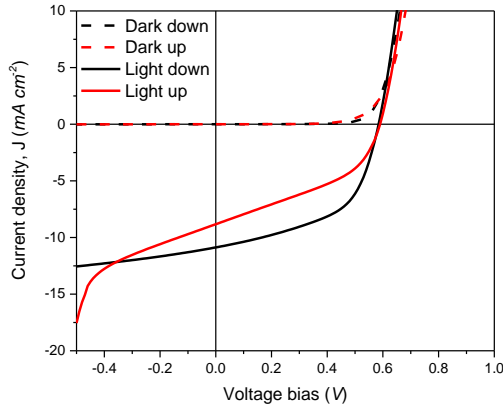
Figure 2.3 *J-V* curves of a perovskite solar cell in dark (dashed) and under illumination (solid) in different scan directions, up (red) and down (black).

Table 2.2 *J-V* parameters extracted from scans using different scan directions

Scan direction	J_{SC} (mA cm^{-2})	V_{OC} (V)	FF	P_{max} (mW cm^{-2})
Up	5.9	0.54	0.38	1.2
Down	7.0	0.53	0.47	1.8

Hysteresis in the *J-V* measurement has been observed in many studies on perovskite solar cells and because of its large effect on the measured efficiency, it has received widespread attention. The response of the perovskite solar cell to a *J-V* measurement and the magnitude of hysteresis are strongly dependent on external parameters like the scan direction,[73,82–85] scan speed,[82–84,86] illumination intensity,[86] perovskite crystal size,[82] pre-scanning conditions,[83,84,86] the solar cell architecture[73,83,85] and the temperature.[87] It is important to note that a hysteresis-free curve can be obtained with both extremely fast and slow voltage sweeps, where only the slow sweep will provide steady state conditions and a valid efficiency.[83] Also, hysteresis is generally recognized to exist more abundantly in perovskite solar cells that employ mesoscopic electrodes compared to planar ones.[73,85]

The origin of hysteresis has also received abundant attention and has also been attributed to ionic movement inside the perovskite layer. This movement of ions can result in charge accumulation at the interfaces and any change in the applied external voltage will result in a redistribution of these charges.[76,83,85,88–91] It has been calculated and proven experimentally that the ionic species that are most likely to move inside the perovskite layer are I$^-$ (vacancies) and the MA$^+$ ions.[76,91] However, if ionic movement would be the only cause of hysteresis, it would be an intrinsic

property of the perovskite layer. Therefore purely ionic movement cannot explain the differences in hysteresis observed with a change of the electron transport layer (ETL), hole transport layer (HTL), or cell architecture (mesoscopic vs planar). Additionally, ionic movement in the perovskite layer has also been observed in solar cells displaying no/minimal hysteresis.[92] It has therefore been proposed that hysteresis is caused by a combination of ionic movement and surface recombination at the interfaces.[92]

Both hysteresis and light soaking can significantly change the measured J-V curve and therefore change the determined efficiency of the solar cell as discussed above. Therefore it is essential to measure the perovskite solar cell correctly in a fully stationary state. To do so, a new measurement protocol for perovskite solar cells was developed which consists of two phases. The first phase is implemented to address the light soaking effect. Since the V_{OC} and FF are most influenced by light soaking (Figure 2.2), the cell is kept at V_{OC} while it is illuminated for typically 10-30 minutes. During this time, the evolution of the V_{OC} is recorded, making the stabilization of V_{OC} visible (Figure 2.4).
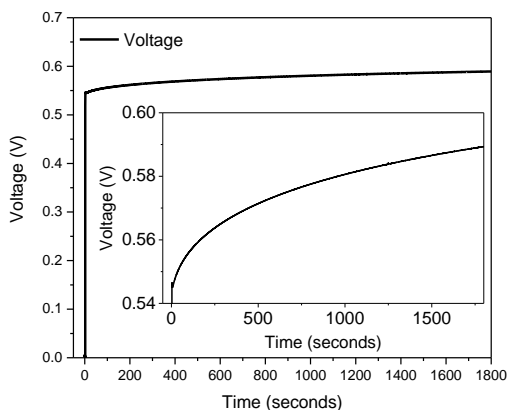
Figure 2.4 Recorded voltage during light soaking for 30 minutes. The first few seconds, the cell was kept in the dark after which the shutter was opened. The inset shows a zoom to illustrate that in this example, the voltage is still increasing slowly, even after 30 minutes of light soaking.

After the initial stabilization at V_{OC}, the second phase of the measurement is initiated where the voltage is increased to a value above V_{OC} that is determined by adding double of the pre-selected voltage step size to the last recorded V_{OC} in the first phase. At this voltage the current flow is recorded for a pre-determined time (typically 15-60 s). After the set time has expired, the voltage is lowered by one step size and the current is recorded again for the pre-determined duration. This procedure is repeated until the voltage has dropped to two step sizes below 0 V. This second phase is the actual stabilized *J-V* measurement and aims to remove the influence of hysteresis. It results in the time dependent current density graph shown in Figure 2.5.
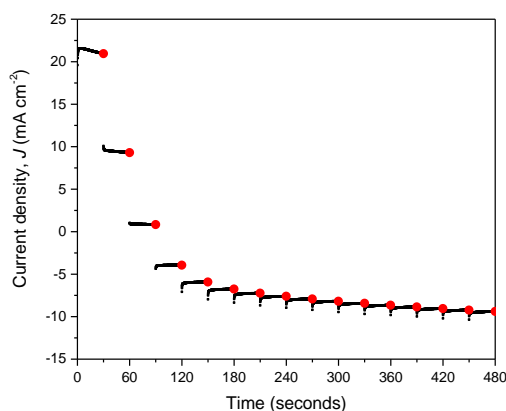
Figure 2.5 Recorded current density during the stabilized *J-V* sweep at which the voltage is changed every 30 seconds with a voltage step size of 0.05 V. In this example, the current flow stabilizes quite quickly. The hysteresis is typically the largest around the MPP.

From this time dependent current density data, the last measured current density at every voltage step is selected (indicated as red dots in Figure 2.5) and plotted versus the applied bias voltage, resulting in a stabilized *J-V* curve (Figure 2.6).
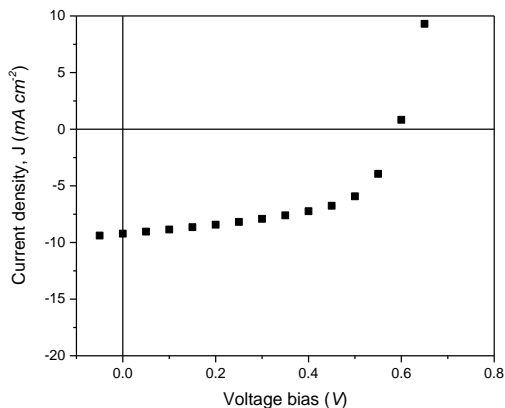
Figure 2.6 Stabilized *J-V* curve, reconstructed from the last points of every voltage step in the time dependent current density graph (indicated in red in figure 2.5).

Upon comparison of the stabilized *J-V* curve with the regular (fast) *J-V* sweeps performed before and after the stabilized measurement, the effects of both light soaking and hysteresis become clear. Comparing the regular (fast) *J-V* measurements performed after the stabilized measurement to the stabilized measurement itself, it becomes clear that the downward sweep overestimates the determined efficiency (mainly through the J_{SC}), while the upward sweep underestimates it (mainly through the FF, Figure 2.7 and Table 2.3). The effect of light soaking is visible by comparing the regular (fast) *J-V* measurements from before (black) and after (red) the stabilized measurement. It is worth noting that in this particular example the current density also increases substantially by the light soaking during the stabilized measurement. This comparison also nicely shows that the effect of light soaking is similar on both the upward and downward sweeps and that the magnitude of the hysteresis is not influenced by the light soaking. The reconstructed, stabilized *J-V* curve (blue) is typically in between the downward and upward sweeps.
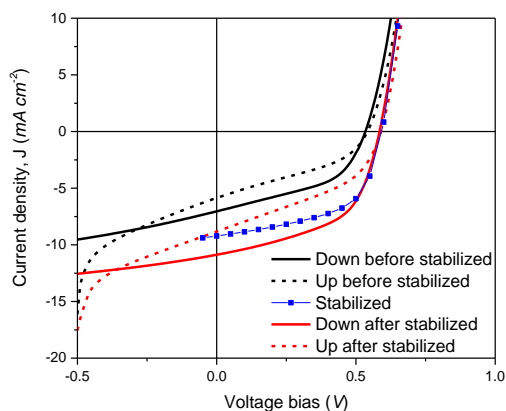
Figure 2.7 Reconstructed *J-V* curve from the stabilized sweep (blue), regular (fast) *J-V* sweeps recorded before (black) and after (red) the stabilized *J-V* measurement in both up (dashed) and down (solid) scan directions.

Table 2.3 *J-V* parameters extracted from the stabilized measurement and regular (fast) *J-V* sweeps in both scan directions recorded before and after the stabilized measurement

	J_{SC} (mA cm^{-2})	V_{OC} (V)	FF	P_{max} (mW cm^{-2})
Up before stabilized	5.9	0.54	0.38	1.2
Down before stabilized	7.0	0.53	0.47	1.8
Stabilized	9.2	0.59	0.56	3.0
Up after stabilized	8.8	0.59	0.41	2.1
Down after stabilized	10.9	0.59	0.53	3.4

Protocols in which the light soaking of the solar cell is performed at J_{SC} instead of V_{OC} conditions have also been explored. The change in J_{SC} is however usually not as significant as that of the V_{OC} and it was found that prolonged light exposure of the cell under short circuit conditions can degrade a sub-optimal perovskite solar cell significantly before the stabilized measurement has started. With the demonstrated method, the light soaking time in the first phase and the voltage step size and the stabilization time at every voltage step in the second phase can be selected as desired, making the method suitable for any kind of perovskite solar cell, independent of the time the cell requires to stabilize.

It must be noted that sub-optimal (low performance) perovskite solar cells in general exhibit stronger light soaking and hysteresis effects compared to their high-performing analogues. This could result in a high performance cell with small hysteresis appearing to be less efficient than a low performance cell that exhibits large

hysteresis in a scan that is performed too fast in a downward direction. When both cells would be measured in the upward direction, it would become clear that the high performance cell will show the exact same *J-V* curve while that of the low performance cell will be shifted severely. Also pre-conditioning of the cell with the application of a (large) forward bias voltage prior to the measurement will usually make a low performance cell appear to be highly efficient.

This correct measurement of the *J-V* curve, although more time consuming, is essential to correctly assess and report the efficiency of perovskite solar cells. It has therefore also been advised and become required in the community to show *J-V* characteristics in both scan directions with additional stabilized measurements. Similar methods to the one described here have also been reported by others.[81,83]

Solar cell area

The area of a solar cell is conventionally determined by the overlap of the indium tin oxide (ITO) bottom and aluminum (Al) top electrode and is 0.09 cm^2 (a) or 0.16 cm^2 (b) in this study (Figure 2.8).
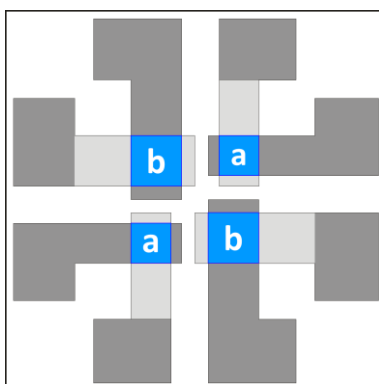
Figure 2.8 Substrate layout with a total of 4 solar cells (2× a and 2× b). The ITO bottom electrodes are shown in light grey and the top Al electrodes are shown in dark grey. The electrode overlap (active device area) is accentuated in blue.

During the *J-V* measurements, one of the four cells on the substrate is illuminated. The size of the circular illumination spot is however larger than the exact cell size. A shadow mask can be used to reduce the illumination spot size to a square that is slightly smaller than the solar cell area (0.0676 cm^2 for a-cells and 0.1296 cm^2 for b-cells). Upon comparison of stabilized *J-V* measurements with and without the

use of a shadow mask, it is clear that the unmasked measurement givers a higher solar cell efficiency (Figure 2.9).
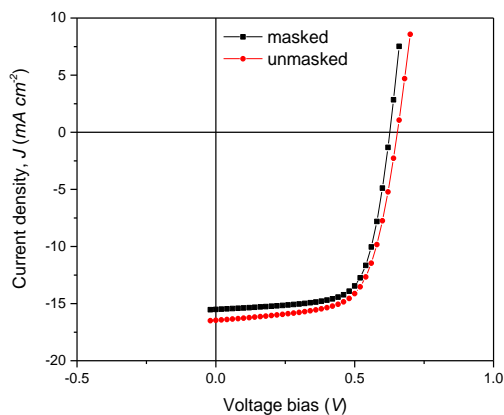
Figure 2.9 Reconstructed *J-V* curves from stabilized *J-V* measurements performed without (red) and with the use of a shadow mask (black).

Table 2.4 *J-V* parameters extracted from the stabilized measurement sweeps with and without the use of a shadow mask.

	J_{SC} (mA cm^{-2})	V_{OC} (V)	FF	P_{max} (mW cm^{-2})
Masked	15.5	0.63	0.69	6.7
No mask	16.5	0.65	0.66	7.1

This indicates that without the use of a shadow mask, the area from which charges are being collected is larger than the electrode overlap, causing an underestimation of the active area resulting in an overestimation of the efficiency. The importance of using a shadow mask when performing *J-V* measurements has been discussed in literature for DSSCs, where the origin of the overestimation of J_{SC} is the absorption of scattered- and diffuse light from outside the cell area.[81,93–95] The necessity of using a shadow mask to avoid overestimation of the J_{SC} has also been discussed in the field of organic photovoltaics (OPV), where the origin of the introduced error is quite different. In OPV, the current generation is overestimated mainly when a highly conductive grade of poly(3,4-ethylenedioxytiophene): poly(styrenesulfonate) (PEDOT:PSS) is used. Due to its high conductivity the PEDOT:PSS can transport charges that are generated outside the solar cell area to the electrode where they can be extracted.[94,96–100] In our perovskite solar cells, the PEDOT:PSS that is used however, is not highly conductive. It has been reported though

that the conductivity of "regular" PEDOT:PSS can be enhanced by mixing in different solvent (mixtures) into the aqueous PEDOT:PSS solution.[99,101–103] Furthermore it has been reported that simply spin coating *N,N*-dimethylformamide (DMF) on top of a deposited non-high conductivity PEDOT:PSS layer also enhances the conductivity and that this enhancement is even stronger when MAI is added to the DMF.[104,105] This enhancement of the conductivity is attributed to the phase segregation of PSSH chains from PEDOT:PSS and the conformational change of PEDOT chains.[104] Since the perovskite layer is produced by depositing a precursor mixture containing MAI amongst others from DMF onto a PEDOT:PSS layer, it is likely that the conductivity of the PEDOT:PSS layer is enhanced, resulting in an overestimation of the efficiency when measuring unmasked.

Constant voltage current tracking

The true efficiency of the perovskite solar cells can be determined by performing a masked, stabilized *J-V* sweep. However the long term stability of the current output of the solar cell at the MPP is still unknown. To measure this, the MPP of the cell is determined from the stabilized *J-V* sweep, and the cell is then forced to operate at the correct voltage (V_{MPP}) under prolonged illumination (typically 1-2 hours), while the current output of the cell is recorded and the power is calculated (Figure 2.10).
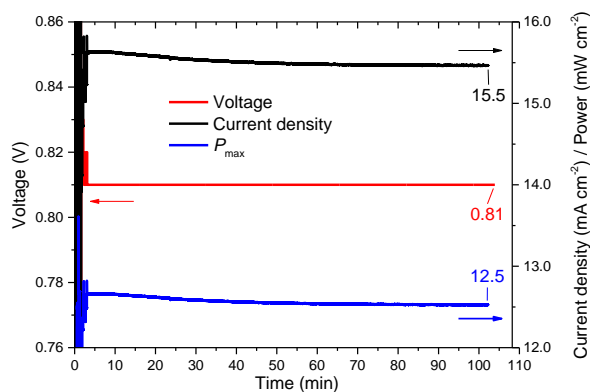
Figure 2.10 Constant voltage - current tracking curve of a perovskite solar cell. The voltage (red) is changed for a few minutes at the start of the measurement in order to find the maximum power point. Current density (black) is recorded and the output power (blue) is calculated.

In Figure 2.10, the cell shows a nice stabilization over time, however cells that stabilize even faster as well as cells that do not reach a stable current output within 2 hours have also been observed. Also in this measurement, there is a strong relation between the overall performance of the solar cell and the stability at the MPP where sub-optimal cells have low stability and good cells exhibit excellent stability.

2.3 Wavelength dependent spectral responsivity

To determine a truly meaningful solar cell efficiency, it should be related to the solar spectrum that is incident on the earth's surface. Upon passing through the earth's atmosphere, the spectrum that is emitted by the sun (extraterrestrial spectrum in Figure 2.11) is significantly modified due to light absorption of compounds that are present in the atmosphere (mainly ozone (O_3), oxygen (O_2), carbon dioxide (CO_2) and water (H_2O)). Since the spectrum changes when traveling through the atmosphere, the distance the light travels through it is also of importance. This distance is dependent on the position on the globe since the angle at which the light travels through the atmosphere changes as illustrated in the inset of Figure 2.11. Therefore the convention is to report the distance the light has traveled through the atmosphere in units of "air mass" (AM), where AM 1.0 is once the thickness of the atmosphere and AM 1.5 is 1.5 times this distance. The letters D and G are often added to this notation to indicate the direct (D) or global (G) spectra, where the global spectrum also takes scattered light into account. In order to make reported solar cell efficiencies comparable, the spectrum that is conventionally used for solar cell measurements is the AM 1.5G spectrum with an overall illumination intensity of 100 mW cm^{-2} and the solar cell at a temperature of 25 °C. The spectrum of the light source used in *J-V* measurements (in our experiments a tungsten-halogen lamp with added filters) resembles the AM 1.5G spectrum quite well but does not match it exactly. Therefore there will always be a small discrepancy in the efficiency determined in the *J-V* setup and the efficiency determined using the accepted standard illumination spectrum.
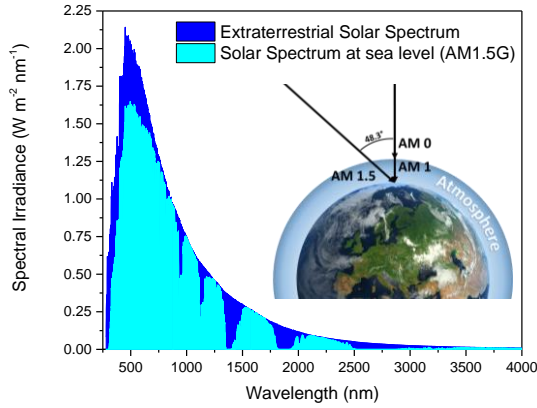
Figure 2.11 Comparison of the solar spectrum above the atmosphere (extraterrestrial) and the commonly used standard at sea level (AM 1.5G). The inset schematically shows the differences between the path length through the atmosphere of the AM 1.0 and AM 1.5 spectra.[106]

The short circuit current density (J_{SC}) is the only parameter that can show a significant difference between the simulated *J-V* parameters and the actual AM1.5 G performance. Therefore the J_{SC} at AM1.5G illumination is determined more accurately using a wavelength dependent spectral responsivity ($S(\lambda)$, expressed in A W^{-1}) measurement. The spectral responsivity relates to the external quantum efficiency (EQE (λ)), which is defined as the ratio of the number of electrons that can be extracted from the device per photon incident on the device as function of the wavelength of the incident light:

$$S(\lambda) = \text{EQE}(\lambda)\frac{q\lambda}{hc}$$

$$\text{EQE}(\lambda) = \frac{number\ of\ electrons\ out\ of\ device}{number\ of\ photons\ incident\ on\ device}$$

Here q is the elementary charge, λ the wavelength of the light, h is Planck's constant, and c is the speed of light. Multiplying the spectral responsivity with the AM 1.5G spectral irradiance and then integrating over the wavelengths yields the J_{SC} that can be expected when the cell is subjected to standard solar illumination.

The correct power conversion efficiency (PCE) can then be calculated using:

$$\text{PCE} = \frac{P_{\max}}{P_{\text{in}}} = \frac{FF \cdot V_{\text{OC}} \cdot J_{\text{SC}}}{P_{\text{in}}} = \frac{FF \cdot V_{\text{OC}}}{P_{\text{in}}} \int S(\lambda) \cdot E_{AM\ 1.5G}(\lambda)\, d\lambda$$

Where P_{in} is the power of the incident light and $E_{\text{AM 1.5G}}(\lambda)$ is spectral irradiance (expressed in W m^{-2} nm^{-1}) of the AM 1.5G spectrum. In addition to the J_{SC} under AM 1.5G illumination of the solar cell, the EQE shows the spectral regions that contribute to photocurrent generation.

The EQE measurement is performed using low intensity modulated monochromatic light in combination with lock-in amplification to determine the response per wavelength. This low light intensity measurement however does not necessarily represent the EQE values of the solar cell at an illumination intensity of approximately 100 mW cm^{-2}. Therefore the EQE is also measured with the use of an additional bias illumination. The bias light intensity is set so that it generates a charge carrier density in the device that is comparable to that of the device under AM 1.5G (1 sun) illumination conditions. An ideal solar cell would exhibit a linear response of current density to the light intensity. For sub-optimal perovskite solar cells however, this response is often sublinear and the EQE at high light intensity is (much) lower than that at low light intensity (Figure 2.12).
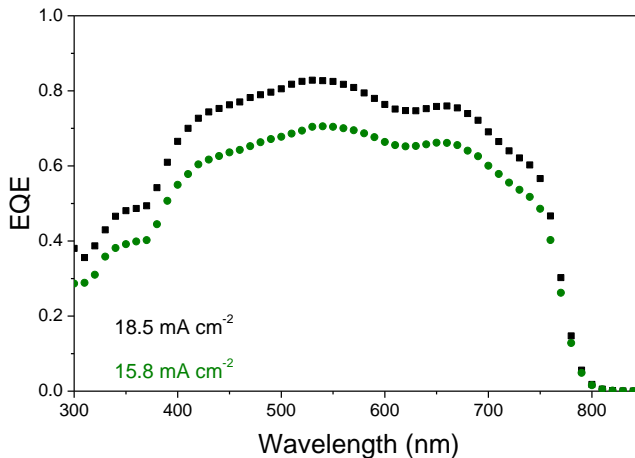
Figure 2.12 EQE at low (black squares) and high (green circles) light intensity of a perovskite solar cell that exhibits a sublinear response of current density to the light intensity. The integrated short circuit current density (J_{SC}) is displayed in black and green for the low and high light intensity respectively.

2.4 Light intensity dependent measurements

Besides *J-V* and EQE measurements that provide the PCE of the measured solar cell, light intensity dependent measurements of the J_{SC} and V_{OC} can give us insight in the recombination mechanisms that are limiting the device performance.

The V_{OC} of a solar cell equals the difference between quasi-Fermi levels for electrons and holes and can be written as:[107]

$$V_{OC} = \frac{E_g}{q} - \frac{kT}{q} ln\left[\frac{N_V N_C}{np}\right]$$

In this equation E_g is the bandgap, k is Boltzmann's constant, T is the temperature, N_v and N_c are the density of states in the valence and conduction bands, and n and p are the electron and hole densities. At open circuit all charges must recombine and hence the charge generation rate (G) must equal the recombination rate (R), $R = G$.

When bimolecular (Langevin) recombination prevails ($R \approx R_{BR}$) this implies that:[108,109]

$$R_{BR} = k_{BR} np = G$$

Here k_{BR} is the bimolecular recombination constant. Because G is proportional to the light intensity I_0 ($G = gI_0$) it follows that:

$$V_{OC} = \frac{E_g}{q} - \frac{kT}{q} ln\left[\frac{k_{BR} N_V N_C}{gI_0}\right]$$

For dominant trap-assisted recombination the recombination rate ($R \approx R_{SRH}$) can be expressed by the Shockley–Read–Hall (SRH) equation:[108,109]

$$R_{SRH} = \frac{C_n C_p N_t}{C_n(n + n_1) + C_p(p + p_1)} np = G$$

In this equation N_t is the trap density, and C_n and C_p are the trap coefficients for electron and holes respectively that denote the probability per unit time that the electron (hole) in the conduction (valence) band will be captured when the trap is filled with a hole (electron). n_1 and p_1 are the thermally occupied trap densities.

Generally $n \gg n_1$ and $p \gg p_1$ when traps act as recombination centers. Assuming that $C_n = C_p$ and $n \approx p$, as in the middle of a *p-i-n* junction solar cell, we can simplify the equation to:

$$np = \frac{4G^2}{C_n C_p N_t^2}$$

The relation between V_{OC} and light intensity (I_0) for dominant Shockley–Read–Hall recombination then becomes:

$$V_{OC} = \frac{E_g}{q} - \frac{2kT}{q} ln\left[\frac{N_t\sqrt{C_n C_p N_v N_c}}{2gI_0}\right]$$

A light intensity dependent V_{OC} measurement can therefore be used to determine the proportionality factor ($\eta kT/q$) by determining the slope of the V_{OC} versus the light intensity plotted on a logarithmic scale (ln(I_0)). In analogy with the common Shockley diode equation describing *p-n* diodes, η, is referred to as the ideality factor.

Hence, an ideality factor of $\eta = 1$ indicates dominant bimolecular (e.g. Langevin) recombination, while an ideality factor of $\eta = 2$ indicates monomolecular, trap-assisted (e.g. Shockley-Read-Hall (SRH)) recombination. An ideality factor higher than 1 therefore indicates an increasingly strong influence of trap-assisted recombination.[110-117] We note that the Shockley equation for *p-n* diodes can phenomenologically describe the characteristics of perovskite cells. The Shockley diode equation, however, was derived considering diffusion currents only. In contrast, *p-i-n* devices should consider both diffusion and drift currents because the intrinsic layer, where the electric field is present, is usually the thickest layer. Such models have been described in the literature.[118]

Figure 2.13 presents an example of a semi-logarithmic plot of V_{OC} vs light intensity (at 730 nm illumination wavelength) from which the ideality factor can be extracted by performing a linear fit in the high light intensity range.
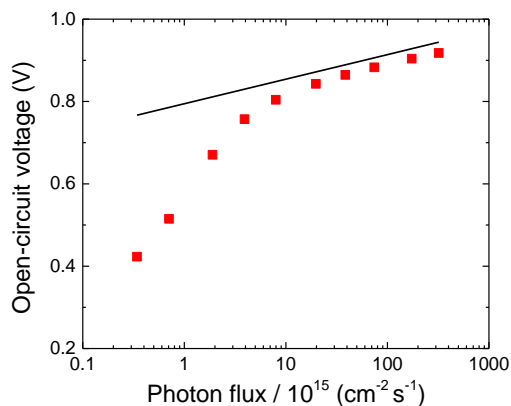
Figure 2.13 Example of light intensity dependent V_{OC} plotted in a logarithmic (ln) scale (red squares). A black line with a slope of 25.9 meV (= kT/q at 300 K) has been added to indicate the slope of a device with an ideality factor of 1.

From this curve it is clear that at high light intensities, the slope is about 25.9 meV (= kT/q), meaning that the ideality factor is (close to) 1 and band-to-band recombination is dominant. However, the slope is much steeper, even $\eta > 2$, for low light intensities, indicating dominant trap-assisted recombination. By performing this measurement on one device using different illumination areas, we see that the slope at low light intensity depends on the illuminated area and is lower when a larger part of the solar cell is illuminated (Figure 2.14).
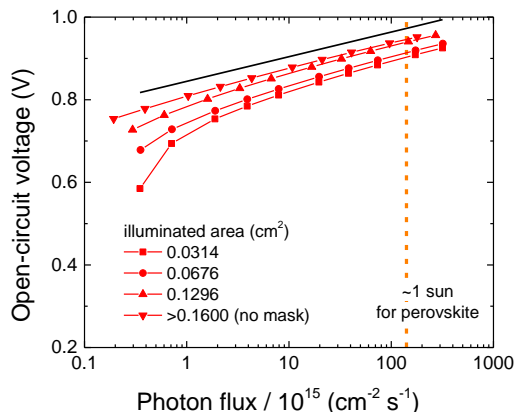
Figure 2.14 Light intensity dependent V_{OC} of a perovskite solar cell using 730 nm illumination wavelength with different illumination areas. The solar cell area (electrode overlap) is 0.16 cm^2, a charge carrier density similar to that of the perovskite solar cell under 1 sun AM1.5G illumination is indicated with the orange dashed line. The black line represents the slope for $\eta = 1$.

The higher ideality factor at low light intensities in Figure 2.14 is an artefact caused by the leakage current as a result of a low shunt resistance. Since the physical device area (0.16 cm^2) of the device remains the same, so do the number of leakage paths. When the illuminated area is increased, the number of charges generated increases proportionally, while the leakage current and voltage loss remain constant in first approximation. Hence, by illuminating the entire cell area the effect of these shunt paths at a lower photon flux are minimized, causing band-to-band recombination to become dominant and the ideality factor to become (close to) 1 at a lower absolute photon flux.

For an ideal solar cell, a linear dependence of the short-circuit current (I_{SC}) on the illumination intensity (I_0) is expected. The resulting graph can be fitted using a power law dependence, ($I_{SC} \propto I_0^{\alpha}$) where the α is 1 for an ideal device and an α of 0.75 has been observed for devices that have a highly unbalanced electron and hole mobility.[119–121] In Figure 2.15, examples of the light intensity dependent I_{SC} and EQE measurements using different illumination wavelengths are shown.
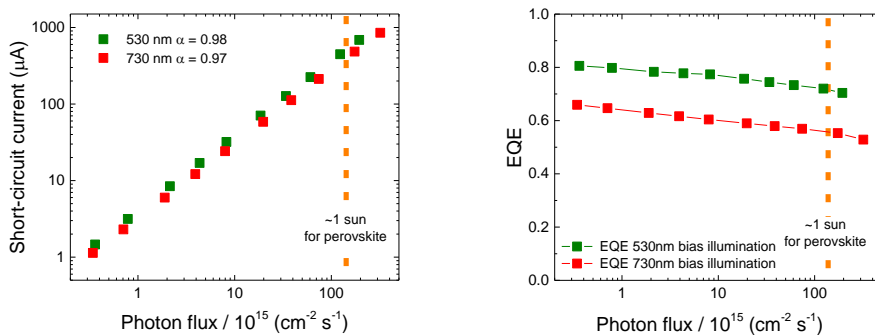
Figure 2.15 Example of light intensity dependent I_{sc} (left) and EQE (right) of a perovskite solar cell using 530 nm (green squares) and 730 nm (red squares) light illumination wavelength. In the left figure, the exponent α value obtained from a power-law fit is displayed and in both figures, a charge carrier density similar to that of the perovskite solar cell under 1 sun AM1.5G illumination is indicated with the orange dashed line.

2.5 Scanning electron microscopy of perovskite layers

Scanning electron microscopy (SEM) is a valuable technique in assessing the morphology of the produced perovskite layers by taking top-view or cross-section images of the deposited layer. However, as with the electrical characterization of perovskite layers, making correct SEM images of perovskite layers requires some additional attention. The most common way to prepare samples for SEM analysis of perovskite layers is to deposit them on top of a glass slide, either with or without the selective contact layer (e.g. PEDOT:PSS) in between the perovskite and the glass. Deposition of a perovskite layer on top of the selective contact will give a better representation of the perovskite layer that is used in a solar cell since the properties of the layer on which the perovskite layer is deposited influence the nucleation and crystal growth of the perovskite layer. The nucleation and crystal growth of the perovskite structure is however even more sensitive than that. It was found that even the layer underneath the selective contact influences the crystallization behavior (Figure 2.16).
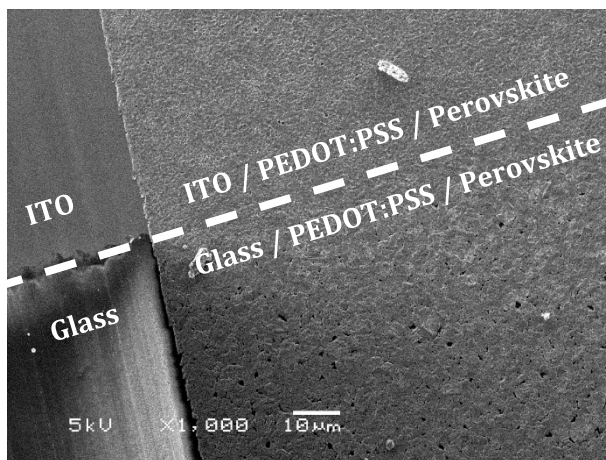
Figure 2.16 SEM image of a 400 nm thick perovskite layer deposited on top of a patterned glass/ITO substrate with a 50 nm PEDOT:PSS layer between the glass/ITO and perovskite layer at 1.000x magnification with a scale bar of 10 μm.

The perovskite layer formed on top of ITO/PEDOT:PSS possesses less pinholes and is much more compact than that formed on top of Glass/PEDOT:PSS. In order to assess the quality and crystallinity of the perovskite layer in a solar cell, it is

therefore vital that the SEM measurement is performed on a section that has an ITO bottom layer. The origin of this strong difference in crystallization of the perovskite structure is still unknown. One obvious cause could be a difference in nucleation and crystal growth due to differences in roughness of the PEDOT:PSS layer on top of ITO or on top of glass. AFM measurements however confirm that the roughness of the PEDOT:PSS is not much different on top of ITO or glass (Figure 2.17) Additionally, grounding the perovskite layer is important to avoid charging of the layer.

| Rq = 1.73 nm   Ra = 1.17 nm | Rq = 1.32 nm   Ra = 1.03 nm | Rq = 2.12 nm   Ra = 1.71 nm | Rq = 5.64 nm   Ra = 4.61 nm |
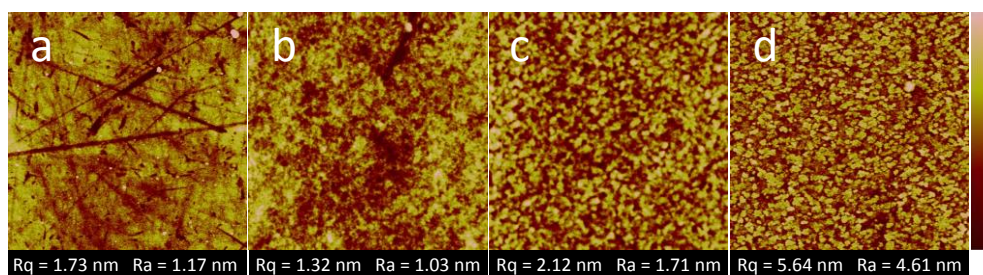
Figure 2.17 AFM height images of the surface of clean glass (a) and ITO (d) and glass and ITO with a PEDOT:PSS layer on top (b and c respectively). Calculated root mean squared (R_q) and arithmetical mean deviation (R_a) surface roughness values are displayed beneath the images. All image sizes are 5 μm × 5 μm and the height bar spans from 0 (dark red) to (a) 10, (b) 8, (c) 12, and (d) 30 nm (light pink).

2.6 References

1   A. Kojima, K. Teshima, Y. Shirai, and T. Miyasaka, *J. Am. Chem. Soc.*, 2009, **131**, 6050–6051.

2   H.-S Kim, C.-R. Lee, J.-H. Im, K.-B. Lee, T. Moehl, A. Marchioro, S.-J. Moon, R. Humphry-baker, J.-H. Yum, J. E. Moser, M. Grätzel and N.-G. Park, *Sci. Rep.*, 2012, **2**, 591.

3   M. M. Lee, J. Teuscher, T. Miyasaka, T. N. Murakami and H. J. Snaith, *Science*, 2012, **338**, 643–647.

4   W. S. Yang, B.-W. Park, E. H. Jung, N. J. Jeon, Y. C. Kim, D. U. Lee, S. S. Shin, J. Seo, E. K. Kim, J. H. Noh and S. I. Seok, *Science*, 2017, **356**, 1376–1379.

5   D. Bi, W. Tress, M. I. Dar, P. Gao, J. Luo, C. Renevier, K. Schenk, A. Abate, F. Giordano, J.-P. Correa Baena, J.-D. Decoppet, S. M. Zakeeruddin, M. K. Nazeeruddin, M. Grätzel and A. Hagfeldt, *Sci. Adv.*, 2016, **2**, 1501170.

6   M. Saliba, T. Matsui, J.-Y. Seo, K. Domanski, J.-P. Correa-Baena, M. K. Nazeeruddin, S. M. Zakeeruddin, W. Tress, A. Abate, A. Hagfeldt and M. Grätzel, *Energy Environ. Sci.*, 2016, **9**, 1989–1997.

7   M. a. Green, A. Ho-Baillie and H. J. Snaith, *Nat. Photonics*, 2014, **8**, 506–514.

8   Y. Zhao and K. Zhu, *J. Phys. Chem. Lett.*, 2014, **5**, 4175–4186.

9   J. Burschka, N. Pellet, S.-J. Moon, R. Humphry-Baker, P. Gao, M. K. Nazeeruddin and M. Grätzel, *Nature*, 2013, **499**, 316–319.

10   N.-G. Park, *J. Phys. Chem. Lett.*, 2013, **4**, 2423–2429.

11   S. Lv, S. Pang, Y. Zhou, N. P. Padture, H. Hu, L. Wang, X. Zhou, H. Zhu, L. Zhang, C. Huang and G. Cui, *Phys. Chem. Chem. Phys.*, 2014, **16**, 19206–19211.

12   J.-W. Lee, D.-J. Seol, A.-N. Cho and N.-G. Park, *Adv. Mater.*, 2014, **26**, 4991–4998.

13   G. E. Eperon, S. D. Stranks, C. Menelaou, M. B. Johnston, L. M. Herz and H. J. Snaith, *Energy Environ. Sci.*, 2014, **7**, 982-988.

14   Y. Zhou, M. Yang, S. Pang, K. Zhu and N. P. Padture, *J. Am. Chem. Soc.*, 2016, **138**, 5535–5538.

15   F. C. Hanusch, E. Wiesenmayer, E. Mankel, A. Binek, P. Angloher, C. Fraunhofer, N. Giesbrecht, J. M. Feckl, W. Jaegermann, D. Johrendt, T. Bein and P. Docampo, *J. Phys. Chem. Lett.*, 2014, **5**, 2791–2795.

16   M. Kulbak, D. Cahen and G. Hodes, *J. Phys. Chem. Lett.*, 2015, **6**, 2452–2456.

17   F. Giustino and H. J. Snaith, *ACS Energy Lett.*, 2016, **1**, 1233–1240.

18   S. Yang, W. Fu, Z. Zhang, H. Chen and C.-Z. Li, *J. Mater. Chem. A*, 2017, **5**, 11462–11482.

19   S. F. Hoefler, G. Trimmel and T. Rath, *Monatshefte für Chemie - Chem. Mon.*, 2017, **148**, 795–826.

20   P. V. Kamat, J. Bisquert and J. Buriak, *ACS Energy Lett.*, 2017, **2**, 904–905.

21   K. Wang, Z. Liang, X. Wang and X. Cui, *Adv. Electron. Mater.*, 2015, **1**, 1500089.

22   H. Yu, F. Wang, F. Xie, W. Li, J. Chen and N. Zhao, *Adv. Funct. Mater.*, 2014, **24**, 7102–7108.

23   Q. Chen, H. Zhou, Y. Fang, A. Z. Stieg, T.-B. Song, H.-H. Wang, X. Xu, Y. Liu, S. Lu, J. You, P. Sun, J. McKay, M. S. Goorsky and Y. Yang, *Nat. Commun.*, 2015, **6**, 7269.

24   Y. Tian, M. Peter, E. Unger, M. Abdellah, K. Zheng, T. Pullerits, A. Yartsev, V. Sundström and I. G. Scheblykin, *Phys. Chem. Chem. Phys.*, 2015, **17**, 24978–24987.

25   S. Colella, E. Mosconi, P. Fedeli, A. Listorti, F. Gazza, F. Orlandi, P. Ferro, T. Besagni, A. Rizzo, G. Calestani, G. Gigli, F. De Angelis and R. Mosca, *Chem. Mater.*, 2013, **25**, 4613–4618.

26   J. H. Heo, M. H. Lee, M. H. Jang and S. H. Im, *J. Mater. Chem. A*, 2016, **4**, 17636–17642.

27   M. M. Tavakoli, L. Gu, Y. Gao, C. Reckmeier, J. He, A. L. Rogach, Y. Yao and Z. Fan, *Sci. Rep.*, 2015, **5**, 14083.

28   S. Colella, E. Mosconi, G. Pellegrino, A. Alberti, V. L. P. Guerra, S. Masi, A. Listorti, A. Rizzo, G. G. Condorelli, F. De Angelis and G. Gigli, *J. Phys. Chem. Lett.*, 2014, **5**, 3532–3538.

29   Y. Tidhar, E. Edri, H. Weissman, D. Zohar, D. Cahen, B. Rybtchinski and S. Kirmayer, *J. Am. Chem. Soc.*, 2014, **136**, 13249–13256.

30   H. Yu, H. Lu, F. Xie, S. Zhou and N. Zhao, *Adv. Funct. Mater.*, 2016, **26**, 1411–1419.

31   M. Yang, Y. Zhou, Y. Zeng, C.-S. Jiang, N. P. Padture and K. Zhu, *Adv. Mater.*, 2015, **27**, 6363–6370.

32   H.-B. Kim, H. Choi, J. Jeong, S. Kim, B. Walker, S. Song and J. Y. Kim, *Nanoscale*, 2014, **6**, 6679.

33   C. Roldán-Carmona, P. Gratia, I. Zimmermann, G. Grancini, P. Gao, M. Graetzel and M. K. Nazeeruddin, *Energy Environ. Sci.*, 2015, **8**, 3550–3556.

34   N. K. Noel, S. N. Habisreutinger, B. Wenger, M. T. Klug, M. T. Hörantner, M. B. Johnston, R. J. Nicholas, D. T. Moore and H. J. Snaith, *Energy Environ. Sci.*, 2017, **10**, 145.

35   P.-W. Liang, C.-Y. Liao, C.-C. Chueh, F. Zuo, S. T. Williams, X.-K. Xin, J. Lin and A. K.-Y. Jen, *Adv. Mater.*, 2014, **26**, 3748–3754.

36   Y. C. Kim, N. J. Jeon, J. H. Noh, W. S. Yang, J. Seo, J. S. Yun, A. Ho-Baillie, S. Huang, M. A. Green, J. Seidel, T. K. Ahn and S. I. Seok, *Adv. Energy Mater.*, 2016, **6**, 1502104.

37   Z. Xiao, C. Bi, Y. Shao, Q. Dong, Q. Wang, Y. Yuan, C. Wang, Y. Gao and J. Huang, *Energy Environ. Sci.*, 2014, **7**, 2619–2623.

38   Y. Wu, A. Islam, X. Yang, C. Qin, J. Liu, K. Zhang, W. Peng and L. Han, *Energy Environ. Sci.*, 2014, **7**, 2934–2938.

39   P. Mao, Q. Zhou, Z. Jin, H. Li and J. Wang, *ACS Appl. Mater. Interfaces*, 2016, **8**, 23837–23843.

40   J.-H. Im, H.-S. Kim and N.-G. Park, *APL Mater.*, 2014, **2**, 081510.

41   C.-H. Chiang, Z.-L. Tseng and C.-G. Wu, *J. Mater. Chem. A*, 2014, **2**, 15897–15903.

42   Y. Zhao and K. Zhu, *J. Mater. Chem. A*, 2015, **3**, 9086–9091.

43   A. Wakamiya, M. Endo, T. Sasamori, N. Tokitoh, Y. Ogomi, S. Hayase and Y. Murata, *Chem. Lett.*, 2014, **43**, 711–713.

44   P. Luo, Z. Liu, W. Xia, C. Yuan, J. Cheng and Y. Lu, *ACS Appl. Mater. Interfaces*, 2015, **7**, 2708–2714.

45   Q. Chen, H. Zhou, Z. Hong, S. Luo, H.-S. Duan, H.-H. Wang, Y. Liu, G. Li and Y. Yang, *J. Am. Chem. Soc.*, 2014, **136**, 622–625.

46   M. R. Leyden, L. K. Ono, S. R. Raga, Y. Kato, S. Wang and Y. Qi, *J. Mater. Chem. A*, 2014, **2**, 18742–18745.

47   L. K. Ono, M. R. Leyden, S. Wang and Y. Qi, *J. Mater. Chem. A*, 2016, **4**, 6693–6713.

48   M. R. Leyden, M. V. Lee, S. R. Raga and Y. Qi, *J. Mater. Chem. A*, 2015, **3**, 16097–16103.

49   F. Hao, C. C. Stoumpos, Z. Liu, R. P. H. Chang and M. G. Kanatzidis, *J. Am. Chem. Soc.*, 2014, **136**, 16411–16419.

50   T. Zhang, N. Guo, G. Li, X. Qian, L. Li and Y. Zhao, *J. Mater. Chem. A*, 2016, **4**, 3245–3248.

51   P. Luo, Z. Liu, W. Xia, C. Yuan, J. Cheng, C. Xu and Y. Lu, *J. Mater. Chem. A*, 2015, **3**, 22949–22959.

52   J. Xiong, B. Yang, R. Wu, C. Cao, Y. Huang, C. Liu, Z. Hu, H. Huang, Y. Gao and J. Yang, *Org. Electron.*, 2015, **24**, 106–112.

53   N. J. Jeon, J. H. Noh, Y. C. Kim, W. S. Yang, S. Ryu and S. I. Seok, *Nat. Mater.*, 2014, **13**, 897–903.

54   H. D. Kim, H. Ohkita, H. Benten and S. Ito, *Adv. Mater.*, 2016, **28**, 917–922.

55   N. Ahn, D.-Y. Son, I.-H. Jang, S. M. Kang, M. Choi and N.-G. Park, *J. Am. Chem. Soc.*, 2015, **137**, 8696–8699.

56   M. Liu, M. B. Johnston and H. J. Snaith, *Nature*, 2013, **501**, 395–398.

57 C. Wehrenfennig, M. Liu, H. J. Snaith, M. B. Johnston and L. M. Herz, *Energy Environ. Sci.*, 2014, **7**, 2269.

58 W. Ke, D. Zhao, C. R. Grice, A. J. Cimaroli, G. Fang and Y. Yan, *J. Mater. Chem. A*, 2015, **3**, 23888–23894.

59 W. Qiu, T. Merckx, M. Jaysankar, C. Masse de la Huerta, L. Rakocevic, W. Zhang, U. W. Paetzold, R. Gehlhaar, L. Froyen, J. Poortmans, D. Cheyns, H. J. Snaith and P. Heremans, *Energy Environ. Sci.*, 2016, **9**, 484–489.

60 W. Zhang, M. Saliba, D. T. Moore, S. K. Pathak, M. T. Hörantner, T. Stergiopoulos, S. D. Stranks, G. E. Eperon, J. A. Alexander-Webber, A. Abate, A. Sadhanala, S. Yao, Y. Chen, R. H. Friend, L. A. Estroff, U. Wiesner and H. J. Snaith, *Nat. Commun.*, 2015, **6**, 6142.

61 M. Salado, L. Contreras-Bernal, L. Caliò, A. Todinova, C. López-Santos, S. Ahmad, A. Borras, J. Idígoras and J. A. Anta, *J. Mater. Chem. A*, 2017, **5**, 10917–10927.

62 F. Li and M. Liu, *J. Mater. Chem. A*, 2017, **5**, 15447–15459.

63 G. E. Eperon, S. N. Habisreutinger, T. Leijtens, B. J. Bruijnaers, J. J. Van Franeker, D. W. Dequilettes, S. Pathak, R. J. Sutton, G. Grancini, D. S. Ginger, R. A. J. Janssen, A. Petrozza and H. J. Snaith, *ACS Nano*, 2015, **9**, 9380–9393.

64 J. J. van Franeker, K. H. Hendriks, B. J. Bruijnaers, M. W. G. M. Verhoeven, M. M. Wienk and R. A. J. Janssen, *Adv. Energy Mater.*, 2017, **7**, 1601822.

65 A. Dualeh, N. Tétreault, T. Moehl, P. Gao, M. K. Nazeeruddin and M. Grätzel, *Adv. Funct. Mater.*, 2014, **24**, 3250–3258.

66 V. L. Pool, B. Dou, D. G. Van Campen, T. R. Klein-Stockert, F. S. Barnes, S. E. Shaheen, M. I. Ahmad, M. F. A. M. van Hest and M. F. Toney, *Nat. Commun.*, 2017, **8**, 14075.

67 C. Bi, Y. Shao, Y. Yuan, Z. Xiao, C. Wang, Y. Gao and J. Huang, *J. Mater. Chem. A*, 2014, **2**, 18508–18514.

68 S. R. Raga, M.-C. Jung, M. V. Lee, M. R. Leyden, Y. Kato and Y. Qi, *Chem. Mater.*, 2015, **27**, 1597–1603.

69 M. Saliba, K. W. Tan, H. Sai, D. T. Moore, T. Scott, W. Zhang, L. A. Estroff, U. Wiesner and H. J. Snaith, *J. Phys. Chem. C*, 2014, **118**, 17171–17177.

70 R. Kang, J.-E. Kim, J.-S. Yeo, S. Lee, Y.-J. Jeon and D.-Y. Kim, *J. Phys. Chem. C*, 2014, **118**, 26513–26520.

71 M.-F. Xu, H. Zhang, S. Zhang, H. L. Zhu, H.-M. Su, J. Liu, K. S. Wong, L.-S. Liao and W. C. H. Choy, *J. Mater. Chem. A*, 2015, **3**, 14424–14430.

72 L. Huang, Z. Hu, J. Xu, K. Zhang, J. Zhang and Y. Zhu, *Sol. Energy Mater. Sol. Cells*, 2015, **141**, 377–382.

73 E. Zimmermann, K. K. Wong, M. Müller, H. Hu, P. Ehrenreich, M. Kohlstädt, U. Würfel, S. Mastroianni, G. Mathiazhagan, A. Hinsch, T. P. Gujar, M. Thelakkat, T. Pfadler and L. Schmidt-Mende, *APL Mater.*, 2016, **4**, 091901.

74 L. K. Ono, E. J. Juárez-Pérez and Y. Qi, *ACS Appl. Mater. Interfaces*, 2017, **9**, 30197-30246.

75 Y. Yuan, Q. Wang, Y. Shao, H. Lu, T. Li, A. Gruverman and J. Huang, *Adv. Energy Mater.*, 2016, **6**, 1501803.

76   Y. Yuan and J. Huang, *Acc. Chem. Res.*, 2016, **49**, 286–293.

77   T. Zhang, S. H. Cheung, X. Meng, L. Zhu, Y. Bai, C. H. Y. Ho, S. Xiao, Q. Xue, S. K. So and S. Yang, *J. Phys. Chem. Lett.*, 2017, **8**, 5069-5076.

78   Y. Deng, Z. Xiao and J. Huang, *Adv. Energy Mater.*, 2015, **5**, 1500721.

79   C. Zhao, B. Chen, X. Qiao, L. Luan, K. Lu and B. Hu, *Adv. Energy Mater.*, 2015, **5**, 1500279.

80   S. Shao, M. Abdu-Aguye, L. Qiu, L.-H. Lai, J. Liu, S. Adjokatse, F. Jahani, M. E. Kamminga, G. H. ten Brink, T. T. M. Palstra, B. J. Kooi, J. C. Hummelen and M. A. Loi, *Energy Environ. Sci.*, 2016, **9**, 2444–2452.

81   X. Yang, M. Yanagida and L. Han, *Energy Environ. Sci.*, 2013, **6**, 54–66.

82   H.-S. Kim and N.-G. Park, *J. Phys. Chem. Lett.*, 2014, **5**, 2927-2934.

83   E. L. Unger, E. T. Hoke, C. D. Bailie, W. H. Nguyen, A. R. Bowring, T. Heumüller, M. G. Christoforo and M. D. McGehee, *Energy Environ. Sci.*, 2014, **7**, 3690–3698.

84   J. A. Christians, J. S. Manser and P. V. Kamat, *J. Phys. Chem. Lett.*, 2015, **6**, 852–857.

85   H. J. Snaith, A. Abate, J. M. Ball, G. E. Eperon, T. Leijtens, N. K. Noel, S. D. Stranks, J. T.-W. Wang, K. Wojciechowski and W. Zhang, *J. Phys. Chem. Lett.*, 2014, **5**, 1511–1515.

86   W. Tress, N. Marinova, T. Moehl, S. M. Zakeeruddin, M. K. Nazeeruddin and M. Grätzel, *Energy Environ. Sci.*, 2015, **8**, 995–1004.

87   L. K. Ono, S. R. Raga, S. Wang, Y. Kato and Y. Qi, *J. Mater. Chem. A*, 2015, **3**, 9074–9080.

88   J.-P. Correa-Baena, A. Abate, M. Saliba, W. Tress, T. Jesper Jacobsson, M. Grätzel and A. Hagfeldt, *Energy Environ. Sci.*, 2017, **10**, 710–727.

89   W. Tress, J. P. Correa Baena, M. Saliba, A. Abate and M. Graetzel, *Adv. Energy Mater.*, 2016, **6**, 1600396.

90   C. Li, S. Tscheuschner, F. Paulus, P. E. Hopkinson, J. Kießling, A. Köhler, Y. Vaynzof and S. Huettner, *Adv. Mater.*, 2016, **28**, 2446–2454.

91   D. A. Egger, A. M. Rappe and L. Kronik, *Acc. Chem. Res.*, 2016, **49**, 573–581.

92   P. Calado, A. M. Telford, D. Bryant, X. Li, J. Nelson, B. C. O'Regan and P. R. F. Barnes, *Nat. Commun.*, 2016, **7**, 13831.

93   S. Ito, M. K. Nazeeruddin, P. Liska, P. Comte, R. Charvet, P. Péchy, M. Jirousek, A. Kay, S. M. Zakeeruddin and M. Grätzel, *Prog. Photovolt. Res. Appl.*, 2006, **14**, 589–601.

94   H. J. Snaith, *Energy Environ. Sci.*, 2012, **5**, 6513-6520.

95   I. Chung, B. Lee, J. He, R. P. H. Chang and M. G. Kanatzidis, *Nature*, 2012, **485**, 486–489.

96   E. Zimmermann, P. Ehrenreich, T. Pfadler, J. A. Dorman, J. Weickert and L. Schmidt-Mende, *Nat. Photonics*, 2014, **8**, 669–672.

97   A. Cravino, P. Schilinsky and C. J. Brabec, *Adv. Funct. Mater.*, 2007, **17**, 3906–3910.

98   S. A. Gevorgyan, J. E. Carlé, R. Søndergaard, T. T. Larsen-Olsen, M. Jørgensen and F. C. Krebs, *Sol. Energy Mater. Sol. Cells*, 2013, **110**, 24–35.

99   W. J. Potscavage Jr., *Adv. Mater.*, 2013, **25**, 4825.

100   H. J. Snaith, *Nat. Photonics*, 2012, **6**, 337–340.

101   O. Bubnova, Z. U. Khan, H. Wang, S. Braun, D. R. Evans, M. Fabretto, P. Hojati-Talemi, D. Dagnelund, J.-B. Arlin, Y. H. Geerts, S. Desbief, D. W. Breiby, J. W. Andreasen, R. Lazzaroni,

W. M. Chen, I. Zozoulenko, M. Fahlman, P. J. Murphy, M. Berggren and X. Crispin, *Nat. Mater.*, 2013, **13**, 190–194.

102   A. M. Nardes, R. A. J. Janssen and M. Kemerink, *Adv. Funct. Mater.*, 2008, **18**, 865–871.

103   S. K. M. Jönsson, J. Birgerson, X. Crispin, G. Greczynski, W. Osikowicz, A. W. Denier van der Gon, W. R. Salaneck and M. Fahlman, *Synth. Met.*, 2003, **139**, 1–10.

104   Y. Xia, K. Sun, J. Chang and J. Ouyang, *J. Mater. Chem. A*, 2015, **3**, 15897–15904.

105   Z. Yu, Y. Xia, D. Du and J. Ouyang, *ACS Appl. Mater. Interfaces*, 2016, **8**, 11629–11638.

106   Solar Spectral Irradiance: ASTM G-173, http://rredc.nrel.gov/solar/spectra/am1.5/ASTMG173/ASTMG173.html, (accessed 3 November 2017).

107   W. Shockley and H. J. H. Queisser, *J. Appl. Phys.*, 1961, **32**, 510–519.

108   T. S. Sherkar, C. Momblona, L. Gil-Escrig, J. Ávila, M. Sessolo, H. J. Bolink and L. J. A. Koster, *ACS Energy Lett.*, 2017, **2**, 1214–1222.

109   T. Kirchartz, B. E. Pieters, J. Kirkpatrick, U. Rau and J. Nelson, *Phys. Rev. B*, 2011, **83**, 115209.

110   G.-J. A. H. Wetzelaer, M. Scheepers, A. M. Sempere, C. Momblona, J. Ávila and H. J. Bolink, *Adv. Mater.*, 2015, **27**, 1837–1841.

111   N. K. Elumalai and A. Uddin, *Energy Environ. Sci.*, 2016, **9**, 391–410.

112   R. N. Hall, *The Institution of Electrical Engineers*, 1960, **3047 E**, 923-931.

113   T. Kirchartz, F. Deledalle, P. S. Tuladhar, J. R. Durrant and J. Nelson, *J. Phys. Chem. Lett.*, 2013, **4**, 2371–2376.

114   K. Tvingstedt, L. Gil-Escrig, C. Momblona, P. Rieder, D. Kiermasch, M. Sessolo, A. Baumann, H. J. Bolink and V. Dyakonov, *ACS Energy Lett.*, 2017, **2**, 424–430.

115   W. Shockley and W. T. Read, *Phys. Rev.*, 1952, **87**, 835–842.

116   N. Marinova, W. Tress, R. Humphry-Baker, M. I. Dar, V. Bojinov, S. M. Zakeeruddin, M. K. Nazeeruddin and M. Grätzel, *ACS Nano*, 2015, **9**, 4200–4209.

117   M. M. Mandoc, F. B. Kooistra, J. C. Hummelen, B. De Boer and P. W. M. Blom, *Appl. Phys. Lett.*, 2007, **91**, 263505.

118   K. Taretto, U. Rau and J. H. Werner, *Appl. Phys. A Mater. Sci. Process.*, 2003, **77**, 865–871.

119   S. R. Cowan, A. Roy and A. J. Heeger, *Phys. Rev. B*, 2010, **82**, 245207.

120   L. J. A. Koster, V. D. Mihailetchi, H. Xie and P. W. M. Blom, *Appl. Phys. Lett.*, 2005, **87**, 203502.

121   P. Schilinsky, C. Waldauf and C. J. Brabec, *Appl. Phys. Lett.*, 2002, **81**, 3885–3887.

Chapter 3

Perovskite layer crystallization tuning for maximizing solar cell efficiency

Abstract

It was found that the reproducible production of efficient planar p-i-n lead halide perovskite solar cells is challenging when using the "mixed halide" precursor mixture consisting of lead(II) chloride ($PbCl_2$) and methylammonium iodide (MAI) in N,N-dimethylformamide (DMF). The main reason for the low performance of the solar cells is the formation of a rough perovskite layer with large voids in between large crystals. By changing the lead source in the mixed halide precursor mixture, the crystallization behavior of the perovskite layer can be significantly modified. By mixing different lead sources ($PbCl_2$ and lead(II) acetate trihydrate ($Pb(OAc)_2·3H_2O$)) and varying the ratio of the two, the crystallization process can be tuned and smooth and compact perovskite layers can be produced. Further optimization of spin coating and annealing procedures resulted in the reproducible production of highly efficient solar cells with a power conversion efficiency (PCE) of around 14%.

3.1 Introduction

The intense research on lead halide perovskite solar cells in recent years has resulted in highly efficient devices as well as an improved understanding of the opportunities for using this material in solar cells. Apart from the attractive physical properties like a high absorption coefficient,[1,2] almost ideal bandgap, high charge mobilities,[3,4] and low exciton binding energy,[5] the most important property of the perovskite material is the tolerance towards composition and processing methods it displays. By changing the composition of the perovskite material, changes can be made to the physical properties like bandgap[6] and higher stability.[7] This allows optimization of the material for specific applications (*e.g.* multi-junction solar cells). More importantly from a processing point of view however, a specific composition of perovskite (*e.g.* $CH_3NH_3PbI_3$) can be produced from different precursor and solvent combinations.[8–12] In such case, a change in the precursor composition and solvent can be used to tune the crystallization behavior.[13–16] This has resulted in the application of a large variety of precursor compositions and deposition techniques that can yield high quality perovskite films.

In the early years of solid state perovskite solar cell research, the two most used perovskite formulations were the 'tri-iodide' and 'mixed halide' precursor mixtures. Where the 'tri-iodide' consists of methylammonium iodide (MAI) and lead(II) iodide (PbI_2) in a 1 : 1 molar ratio and the 'mixed halide' precursor mixture consists of MAI and lead(II) chloride ($PbCl_2$) in a 3 : 1 molar ratio to provide the 3 equivalents of iodide required for the formation of the perovskite structure ($MAPbI_3$).[17–27]

The main differences between these two recipes are the higher charge mobility and larger diffusion length[28] and the overall superior photovoltaic performance of perovskite layers obtained from the mixed halide precursor. Where the initial thought was that the chloride ions intercalate into the perovskite structure (hence the 'mixed halide' name),[18,19,21,25,27] it was later shown that only trace amounts of chloride could be found in the perovskite layer in completed devices.[29–31] Therefore the currently accepted conclusion is that even with the use of the mixed halide precursor solution the regular $MAPbI_3$ perovskite is formed, and that the increased photovoltaic performance is caused by improvement of the perovskite layer quality.[29,30,32] Here, the mixed halide perovskite recipe is used as a starting point for optimization of the perovskite solar cell efficiency. The steps in the optimization procedure are shown and discussed in this chapter.

3.2 Solar cells from a single lead source

To produce a solar cell, first a glass substrate with patterned indium-tin oxide (ITO) electrodes is coated with the hole transport material poly(3,4-ethylenedioxythiophene):poly(styrenesulfonate) (PEDOT:PSS) *via* spin coating. The mixed halide perovskite precursor solution consisting of methylammonium iodide (MAI) and lead(II) chloride (PbCl$_2$) in a 3:1 molar ratio dissolved in *N,N*-dimethylformamide (DMF) is spin cast on top of the PEDOT:PSS layer. After thermal annealing of the perovskite layer, the device is completed by spin coating the electron transport material [6,6]-phenyl-C$_{61}$-butyric acid methyl ester (PCBM) on top of the perovskite layer and the thermal evaporation of lithium fluoride (LiF) and aluminum (Al) under high vacuum. This results in the solar cell stack displayed in Figure 3.1, where typical layer thicknesses are 140 nm for the ITO, 40 nm for the PEDOT:PSS, 50 nm for the PCBM, 1 nm for the LiF, and 100 nm for the Al. The perovskite layer thickness is not fixed as it is optimized as described in section 3.4.

Figure 3.1 The solar cell stack that is used for the optimization of the perovskite layer for high solar cell efficiency as described in this chapter.

It was found that reproducibly producing solar cells in this device configuration with acceptable efficiency is challenging using the mixed halide precursor mixture. The perovskite layer typically consists of large crystals but also large voids in between the crystals that create shunt paths and reduce the cell efficiency. The biggest problem with the use of this precursor mixture however is the irreproducibility of the quality of the produced perovskite layer. When depositing up to 9 perovskite layers sequentially,

typically the first deposited layer performs reasonably well, but the short-circuit current density (J_{SC}) and therefore the solar cell efficiency reduces with every subsequently produced sample (Figure 3.2).
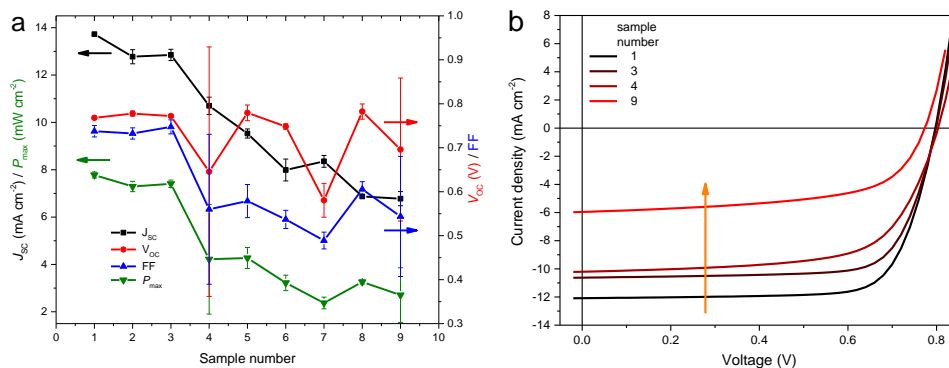
Figure 3.2 a) Graph displaying the short-circuit current density (J_{SC}) in black squares, open-circuit voltage (V_{OC}) in red dots, fill factor (FF) in blue triangles pointing up, and the maximum power (P_{max}) in green triangles pointing down, obtained from regular (fast) J-V measurements of perovskite solar cells produced sequentially using the exact same processing procedure. Symbols are the average and error bars are the standard deviation over 4 cells on the same substrate. b) Accompanying stabilized J-V measurements of 4 of these samples (number 1, 3, 4, and 9).

It is clear from Figure 3.2a that the first three samples perform similarly, while from sample number four on, the open-circuit voltage (V_{OC}) starts fluctuating more, and the fill factor (FF) and J_{SC} drop with every subsequent sample produced. Stabilized J-V measurements (Figure 3.2b) show the same trend in the J_{SC} and overall efficiency of the cells. Upon further investigation using external quantum efficiency (EQE) measurements, it is found that the reduction in J_{SC} is mainly caused by an increase in the sub-linearity of the J_{SC} with light intensity. This can be seen by comparing EQE measurements performed without (Figure 3.3a) and with (Figure 3.3b) bias illumination, where the EQE at higher light intensity drops more and more for sequentially produced samples.
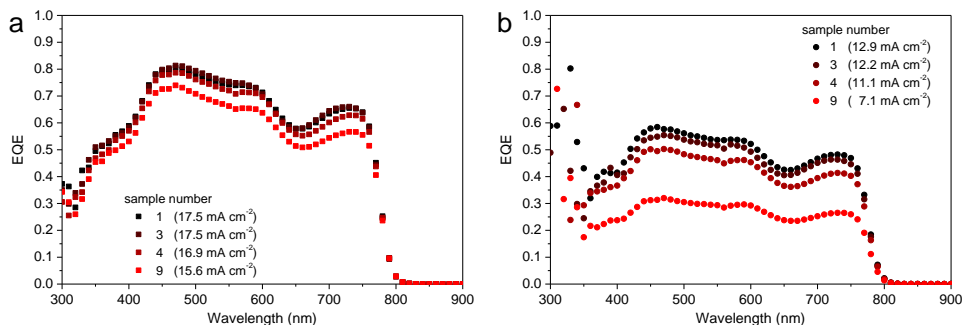
Figure 3.3 External quantum efficiency (EQE) plots of perovskite solar cells produced sequentially measured under low- (a) and high- (b) illumination intensity.

All steps in the processing procedure were investigated and altered extensively aiming to reduce this decrease of performance. The spin coating speed, duration, and atmosphere of the perovskite layer were changed, the annealing time and temperature was changed including complex and lengthy ramp annealing schemes, the hole transport layer (HTL) and electron transport layer (ETL) were changed with several alternatives, the atmosphere in which the layers are stored between spin coating and annealing was changed, and even the precursor solution was changed, all without any improvement in the reproducibility. Although the optimized production procedure produces solar cells with an efficiency up to 8%, the irreproducibility of the perovskite layer quality using this recipe is detrimental for the systematic investigation and improvement of this new type of solar cell. Another approach is therefore required for further increase of solar cell efficiency and systematic investigation of the perovskite material for use in solar cell application.

3.3 Tuning of the crystallization speed using multiple lead sources

As illustrated in section 3.2, the desired high efficiency (>10% PCE) solar cells could not be produced using the mixed halide precursor mixture. During initial experiments employing different lead sources in the mixed halide precursor solution, it was noted that a precursor solution containing MAI and $PbCl_2$ in DMF crystallizes extremely slowly and only during annealing (visible by the color change from yellow to dark brown), and eventually forms a rough perovskite layer. A precursor solution containing MAI and lead(II) acetate trihydrate ($Pb(OAc)_2 \cdot 3H_2O$) on the other hand, crystallizes extremely fast, already turning light brown during spin coating. This is most

likely caused by a more rapid formation and/or evaporation of the decomposition products, contributing to faster crystal growth.[8] Upon annealing of the formed film, the light brown color changes to darker brown and an extremely smooth layer is formed (root mean squared roughness (Rq) of 5 to 10 nm for ~400 nm thick perovskite layers produced from MAI and $Pb(OAc)_2$ versus Rq of ~120 nm for 275 nm thick perovskite layers produced from MAI and $PbCl_2$). The disadvantage of replacing all $PbCl_2$ in the precursor mixture with $Pb(OAc)_2 \cdot 3H_2O$ is that during annealing, the layer formed from MAI and $Pb(OAc)_2 \cdot 3H_2O$ starts to form large cracks.

Upon closer analysis of the formed perovskite layers using scanning electron microscopy (SEM), the crystallites formed from a precursor solution containing MAI and $PbCl_2$ are very large and are accompanied by large voids in between them (Figure 3.4, $PbCl_2$ fraction = 1). The crystallites formed from a precursor solution containing MAI and $Pb(OAc)_2 \cdot 3H_2O$ are extremely small but do form a completely closed layer in between the large cracks that were observed visually (Figure 3.4, $Pb(OAc)_2 \cdot 3H_2O$ fraction = 1). Since the crystallization behavior is so strongly influenced by the lead source that is used in the precursor solution, both lead sources were used together in different ratios in the precursor solution in order to tune the crystallization speed and size of the crystallites, aiming to produce a compact perovskite layer with large crystals to avoid the creation of shunt paths and maximize the charge transport efficiency. During production of these perovskite layers, it was observed that the crystallization speed can actually be controlled very well by changing the ratio of the two lead sources in the precursor solution. Throughout the full range of ratios a higher fraction of $Pb(OAc)_2 \cdot 3H_2O$ leads to faster perovskite formation and smoother perovskite layer after annealing. SEM images of perovskite layers produced from precursor solutions with different ratios of $PbCl_2$ and $Pb(OAc)_2 \cdot 3H_2O$ are shown in Figure 3.4.

PbCl$_2$ fraction								
0	0.1	0.2	0.3	0.4	0.5	0.6	0.7	1

Pb(OAc)$_2$·3H$_2$O fraction								
1	0.9	0.8	0.7	0.6	0.5	0.4	0.3	0
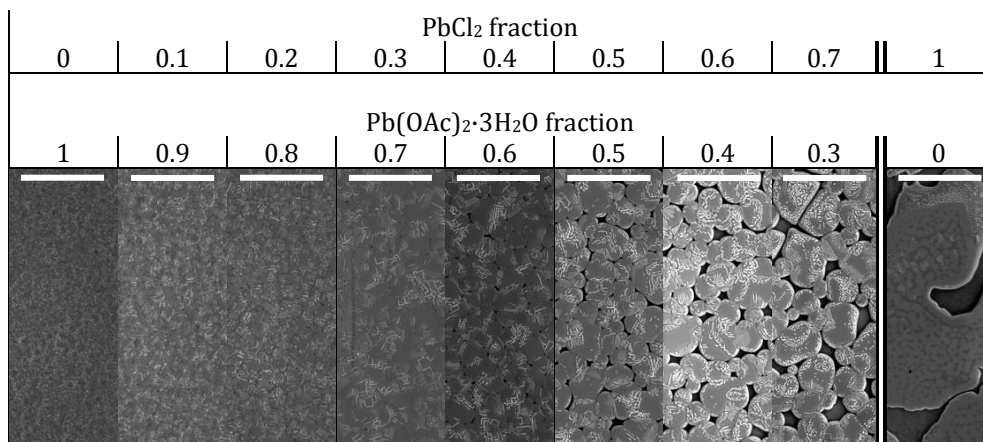
Figure 3.4 Top view SEM images of perovskite layers deposited from a mixture of MAI and both lead sources PbCl$_2$ and Pb(OAc)$_2$·3H$_2$O in different ratios, as indicated above the images. ITO and a PEDOT:PSS are underneath the perovskite film and scale bars are 5 μm.

From these images it is clear that the use of a higher fraction of PbCl$_2$ (slower crystallization) allows the crystallites that are formed to grow larger. Starting from the leftmost image (pure Pb(OAc)$_2$·3H$_2$O), at about a one to one ratio of both lead sources, the perovskite layer starts to show serious voids in between the crystals. Some additional crystallite phase on top of the perovskite crystals is also visible, which is most likely lead(II) iodide (PbI$_2$) that is formed as a degradation product of over-annealing the perovskite layer whereby MAI is evaporated from the perovskite crystal.[33]

X-Ray diffraction patterns of these layers along with the XRD trace of perovskite powder that was collected by scratching off the perovskite layer from several dedicated spin coated substrates (full ITO, fraction PbCl$_2$ = 0.2) are displayed in Figure 3.5. The XRD patterns of the spin cast layers show characteristic perovskite peaks at ~14.1° and ~28.3° corresponding to respectively the 110 and 220 diffraction planes of tetragonal CH$_3$NH$_3$PbI$_3$ (MAPbI$_3$) perovskite.[34] Confirming that the MAPbI$_3$ perovskite can be formed even with the use of MAI and lead sources that do not contain iodide, as long as the correct stoichiometry of precursor materials is used. The perovskite powder trace shows considerably more peaks than the spin cast layers do, indicating a strong preferential orientation of the perovskite crystals in the spin cast layers.[35–41] The perovskite layer produced from a precursor solution containing only Pb(OAc)$_2$·3H$_2$O (fraction PbCl$_2$ = 0) shows a small PbI$_2$ peak at ~12.8° among other additional peaks.[34] Indicating that the precursor materials are not completely converted to perovskite and the crystals in the layer that is formed are not as well

ordered as with the other compositions or additional phases of perovskite alongside the tetragonal phase are formed.
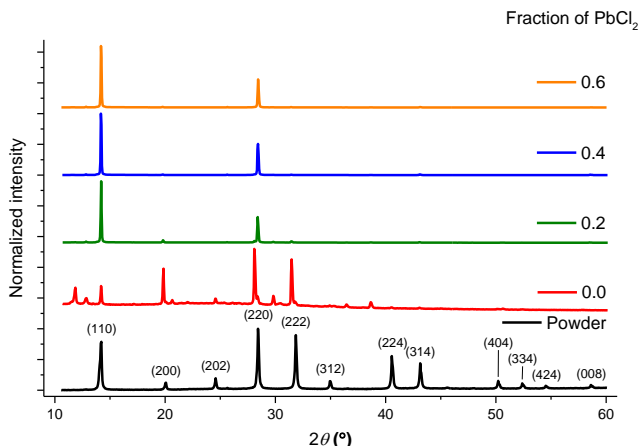
Figure 3.5 X-Ray diffraction (XRD) patterns of perovskite layers produced using different precursor compositions as indicated by the legend. The bottom trace is the XRD pattern of perovskite powder. All traces are normalized to the highest peak.

The results of *J-V* measurements on cells produced with these different lead source ratios are summarized in Figure 3.6. The open circuit voltage (V_{OC}) is quite stable up to a $PbCl_2$ fraction of 0.6, where it clearly starts to drop since the perovskite layer becomes less dense and there are more leakage paths. Both FF and J_{SC} vary slightly by changing the lead source ratio, resulting in a maximum power (P_{max}) that is fairly similar for cells with a $PbCl_2$ fraction from 0 to 0.5. The SEM images show dense layers for perovskite layers with a $PbCl_2$ fraction of up to 0.4. Therefore, a $PbCl_2$ fraction of 0.2 was selected for further optimization of the perovskite layer for use in a solar cell.
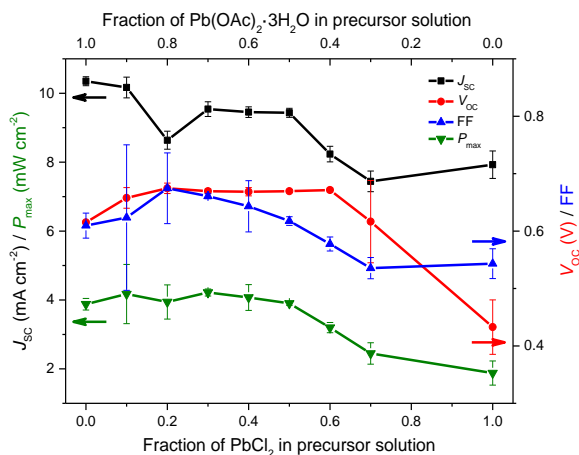
Figure 3.6 Graph displaying the short circuit current density (J_{SC}) in black squares, open circuit voltage (V_{OC}) in red dots, fill factor (FF) in blue triangles pointing up, and maximum power (P_{max}) in green triangles pointing down, obtained from regular (fast) J-V measurements, of perovskite solar cells produced using precursor mixtures containing different ratios of lead sources $PbCl_2$ and $Pb(OAc)_2 \cdot 3H_2O$. Symbols are the average and error bars are the standard deviation over 4 cells on the same substrate.

3.4 Perovskite phase control

Additional crystallites (most likely PbI_2) were observed on top of the perovskite crystals in the SEM images shown in Figure 3.4. As mentioned in section 3.3, the PbI_2 crystals are probably formed as a degradation product by evaporating MAI from the perovskite crystals, leaving PbI_2 behind. Therefore, the effect of annealing temperature and duration on the appearance and performance of the perovskite layer was investigated. Figure 3.7 shows SEM images of the perovskite layers produced from a precursor solution with a $PbCl_2$ fraction of 0.2 that was annealed at different temperatures with different durations. From these SEM images it is clear that the additional crystallites only appear at annealing temperatures of >90 °C when annealing for 10 minutes. When annealing for 30 minutes at 90 °C, the additional crystallites appear to also starting forming, indicating that although the annealing temperature has the strongest influence and should be kept below 110 °C to avoid PbI_2 formation, also the annealing time should be kept below 30 minutes.
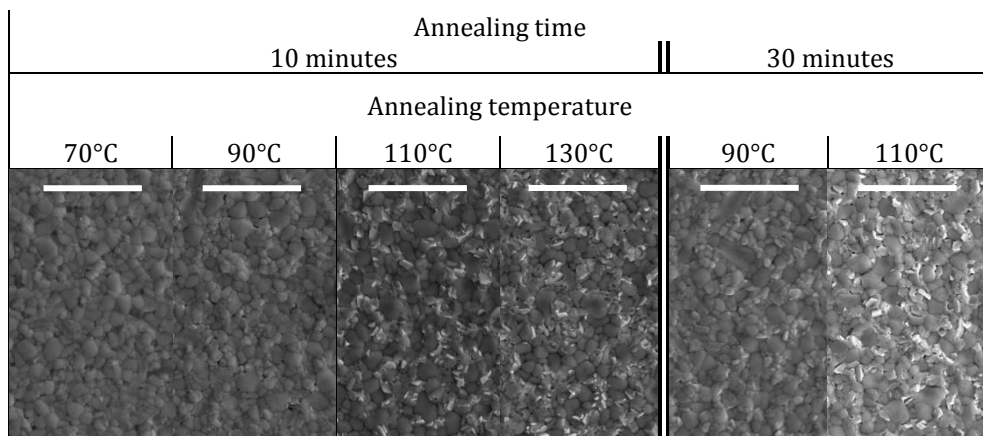
Figure 3.7 Top view SEM images of perovskite layers deposited from a precursor mixture containing a PbCl$_2$ fraction of 0.2, as described in section 3.3, annealed for 10 minutes (left) or 30 minutes (right) using different annealing temperatures. All scale bars are 3 μm.

J-V measurements show an optimum in cell performance for an annealing temperature of 90 °C, both for 10 and 30 minutes annealing (Figure 3.8). Confirming that under- and over-annealing are both detrimental for cell performance. Under-annealing probably causes incomplete conversion to the perovskite and leaves residual solvent and ions in the layer, while over-annealing decomposes the perovskite layer into PbI$_2$ by evaporating MAI from the layer. The efficiency of the perovskite solar cells was improved from about 4% to 8%, measured by regular (fast) *J-V*, by tuning the crystallization speed and optimizing the annealing procedure.
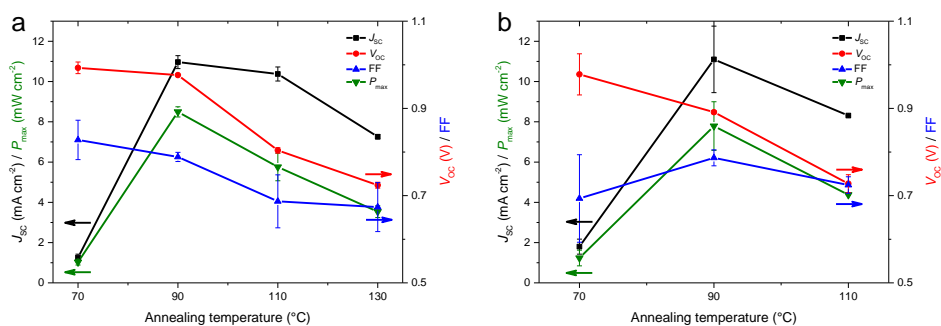
Figure 3.8 Graphs displaying the short circuit current density (J_{SC}) in black squares, open circuit voltage (V_{OC}) in red dots, fill factor (FF) in blue upward facing triangles, and maximum power (P_{max}) in green downward facing triangles, obtained from regular (fast) *J-V* measurements, of cells prepared from a precursor composition with a 0.2 fraction of PbCl$_2$. The perovskite layers are annealed for 10 minutes (a) and 30 minutes (b) using different annealing temperatures. Symbols are the average and error bars are the standard deviation over 4 cells on the same substrate.

3.5 Optimization of photocurrent generation

Up to this point, the best performing device is produced from a precursor solution with a PbCl$_2$ fraction of 0.2 and annealing the formed film at 90 °C for 10 minutes. The completed device has an average V_{OC} of 0.98 V and an average FF of 0.79 which are both good compared to reported values for planar p-i-n devices.[42–44] The J_{SC} of the cell (~11 mA cm^{-2}) however, is substantially lower than reported values for this solar cell configuration[42–44] leading to a P_{max} of only 8.5 mW cm^{-2} in the regular J-V measurement. The amount of current that can be generated in a solar cell's active layer strongly depends on the amount of light that is absorbed and therefore depends on the thickness of the active layer. The measured thickness of the perovskite layer is about 250 nm, which is lower than the reported values (~400 nm) for highly efficient planar p-i-n perovskite solar cells.[44–46] Therefore, increasing the perovskite layer thickness seems to be the way to increase the power conversion efficiency (PCE) of the cells further. The most straightforward ways of increasing the layer thickness when using spin coating as the deposition technique are reducing the spin coating speed or increasing the concentration of the solution that is being applied.

In initial experiments, it was found that the best performing perovskite layers are produced using a high spin speed in combination with a high precursor solution concentrations. Due to the high spin speed, the produced layers are very smooth (Rq < 10nm), while the high concentration of the precursor solution facilitates sufficient layer thickness and compactness. In order to find the optimal perovskite layer thickness for use in the solar cell, the spin coating speed was kept the same (5600 RPM) while the concentration of the precursor solution was varied from 0.6 to 1.4 M of total Pb content, where 1.0 M was used up to this point. This molarity is based on the amount of precursor materials weighed and the amount of pure DMF added and is technically not correct due to the large volume expansion. Although technically not correct it is used to easily indicate different concentrations. This lead to a variation in perovskite layer thickness from about 110 to 360 nm. In Figure 3.9 SEM images of the different layers are shown where it is seen that with the increase in layer thickness, the size of the crystallites also increases.

X-Ray diffraction patterns of these perovskite layers with different thicknesses (Figure 3.10) show the characteristic perovskite peaks at ~14.1° and ~28.3° as expected. Also the absolute signal intensity increases with increasing layer thickness.

Precursor solution concentration				
0.6 M	0.8 M	1.0 M	1.2 M	1.4 M
Perovskite layer thickness				
110 nm	180 nm	240 nm	290 nm	360 nm
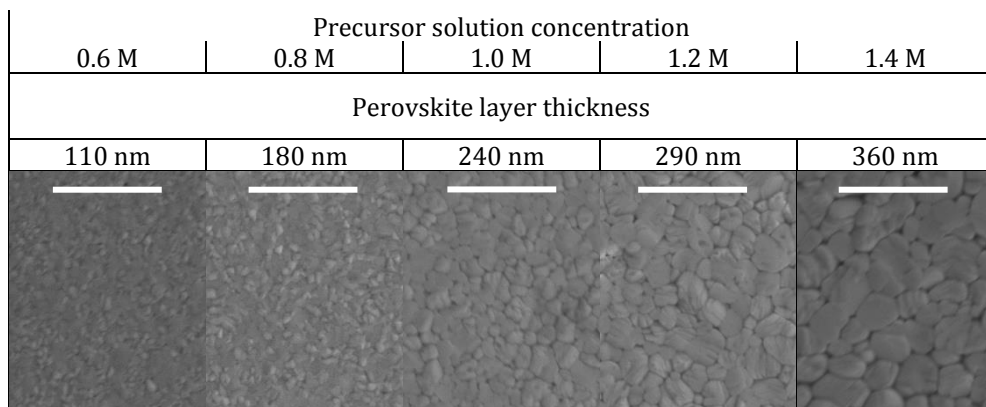
Figure 3.9 Top view SEM images of perovskite layers spin coated at 5600 RPM using different precursor solution concentrations as indicated above the images. The perovskite layer thickness is also displayed above the images and all scale bars are 2 μm.
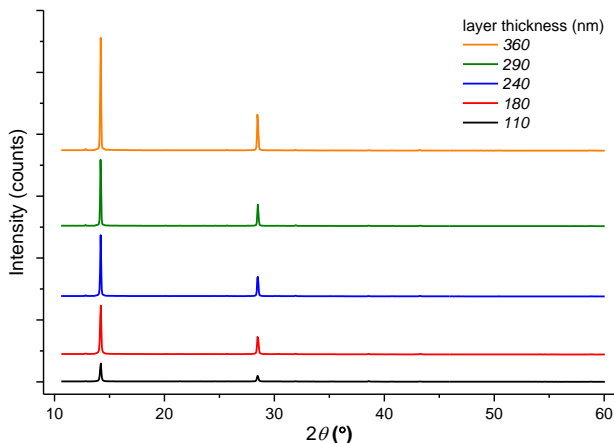
Figure 3.10 X-Ray diffraction (XRD) patterns of perovskite layers with different thicknesses as indicated by the legend.

The regular (fast) *J-V* graphs in Figure 3.11a show an increase of both J_{SC} and V_{OC} with increasing layer thickness. At higher perovskite thicknesses, the *J-V* curve starts showing a "dip" around the maximum power point (MPP) that is most likely caused by slow ion movement, just like hysteresis and light soaking that were discussed in section 2.2. The stabilized *J-V* curves (recorded as described in section 2.2) in Figure 3.11b therefore do not show this effect. Additionally, Figure 3.11a and b show that the J_{SC} does not increase anymore with increasing layer thicknesses above 240nm.
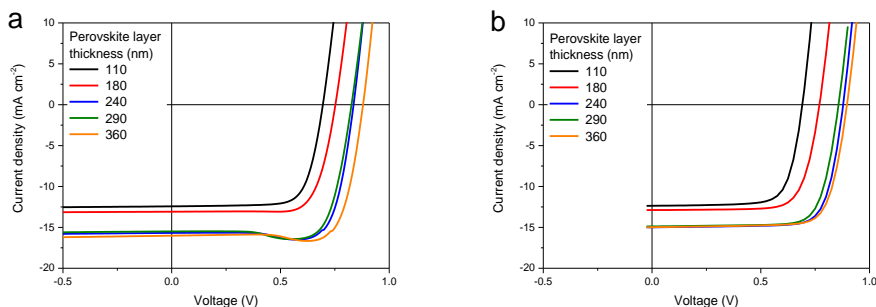
Figure 3.11 *J-V* curves of perovskite solar cells with different layer thicknesses measured using the regular (fast) *J-V* measurement (a) and stabilized *J-V* measurement method as described in section 2.2 (b).

In Figure 3.12 all *J-V* parameters of both the regular and stabilized *J-V* measurements are plotted versus the perovskite layer thickness. Comparing the values obtained from the fast and stabilized *J-V* sweeps, it is evident that the J_{SC} matches very well for all perovskite layer thicknesses, while the V_{OC} is underestimated and the FF is overestimated in the fast sweep due to the dip around the MPP. The V_{OC} and J_{SC} seem to reach a plateau at a perovskite layer thickness of 240 nm, causing the efficiency of the cells to also level off.
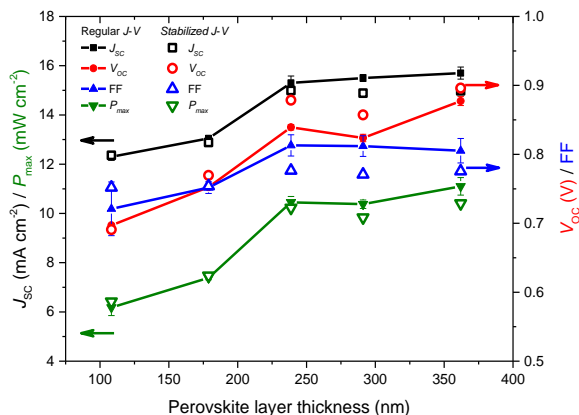
Figure 3.12 Graph displaying the short circuit current (J_{SC}) in black squares, open circuit voltage (V_{OC}) in red dots, fill factor (FF) in blue upward facing triangles, and maximum power (P_{max}) in green downward facing triangles, obtained from regular *J-V* measurements (lines with solid symbols) and stabilized measurements (open symbols, no line) with different perovskite layer thicknesses. Symbols are the average and error bars are the standard deviation over 4 cells on the same substrate.

The extracted current density (<16 mA cm^{-2}) is however still substantially lower than values reported in literature for the highest efficiency devices (~20 mA cm^{-2}).[42–44] The saturation of J_{SC} at higher layer thicknesses therefore suggests a limitation in charge extraction or transport. To study the charge generation and extraction of these cells in more detail, external quantum efficiency (EQE) measurements (as described in section 2.3) were performed under both low and high illumination intensities. The results of these measurements are shown in Figure 3.13a to 3.13e accompanied with a graph showing the simulated fraction of absorbed photons with different perovskite layer thicknesses (Figure 3.13f).

The simulated data (Figure 1.13f) shows that the fraction of absorbed photons does not vary much with a difference in perovskite layer thickness (d) in the lower wavelength range ($\lambda < 550$ nm) due to the strong absorbance there. At higher wavelengths ($\lambda > 550$ nm), due to the strong interference in this cavity region, the fraction of absorbed photons is very sensitive to the perovskite layer thickness.[1] The same trend is also seen in the measured EQEs of solar cells with different perovskite layer thicknesses, indicating that for the thinnest perovskite layers ($d < 240$nm) the lack of absorbance in the higher wavelength range is the cause of the lower current generation.
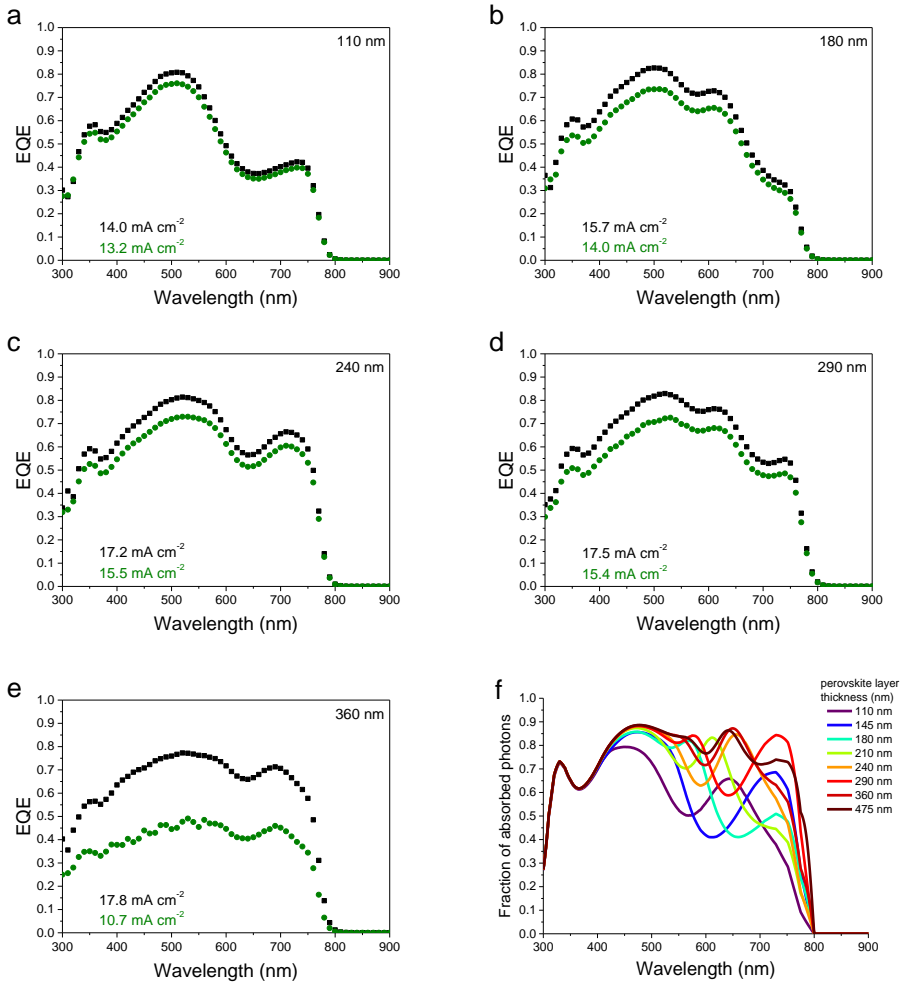
Figure 3.13 a-e) External quantum efficiency (EQE) plots of perovskite solar cells with different perovskite layer thicknesses as indicated in the top right of each graph. Measured under low- (black squares) and high- (green dots) illumination intensity, where the high illumination intensity generates a charge carrier density similar to that of the cell under 1 sun AM 1.5G illumination conditions. The integrated current density is displayed for both measurements in black and green for the low and high illumination intensity measurements respectively. f) Simulated fraction of absorbed photons with different perovskite layer thicknesses.

The EQE and corresponding integrated current density obtained from the EQE measurements at low light intensity increase significantly up to a layer thickness of 240 nm due to the increased absorbance. For thicker perovskite layers it increases only marginally, which matches the results obtained in the stabilized *J-V* measurements. However, the integrated current density from the low light intensity EQE measurements is substantially larger than the one measured in the stabilized *J-V* measurements, especially for the thickest layers. The reason for this difference becomes clear when looking at the EQE of the cells measured at a high light intensity that generates a charge carrier density similar to that of the cell in 1 sun AM 1.5G illumination intensity. All EQEs measured at high light intensity are lower than those measured at low light intensity. The striking observation here is that the difference between the low- and high light intensity EQEs increases with the thickness of the perovskite layer is. Indicating that charge transport and/or extraction is less efficient for the thicker perovskite layers and that with all perovskite layers, the generated photocurrent is increasing sublinear with the light intensity. It must be noted here that only for the thickest perovskite cell (360 nm perovskite layer) the high light intensity EQE measurement was performed using a much higher light intensity than for the others. Explaining the much larger drop in EQE compared to the other samples and showing that the effect is more severe at higher light intensity

In order to investigate this sublinear behavior of the photocurrent with respect to the light intensity, the photocurrent was measured at different light intensities as described in section 2.4. Figure 3.14 shows the I_{SC} and EQE of the cells at a wavelength of 530 nm plotted versus light intensity. The EQE is normalized to 1 at the lowest measured light intensity. The light intensity dependent EQE measurements show that the EQE is stable up to a photon flux of about 10^{16} cm^{-2} s^{-1}, but starts dropping at higher photon fluxes for all perovskite layer thicknesses. This reduction of EQE at high light intensity is more severe with increasing perovskite layer thickness and it is the main cause for the limitation of the solar cell performance.
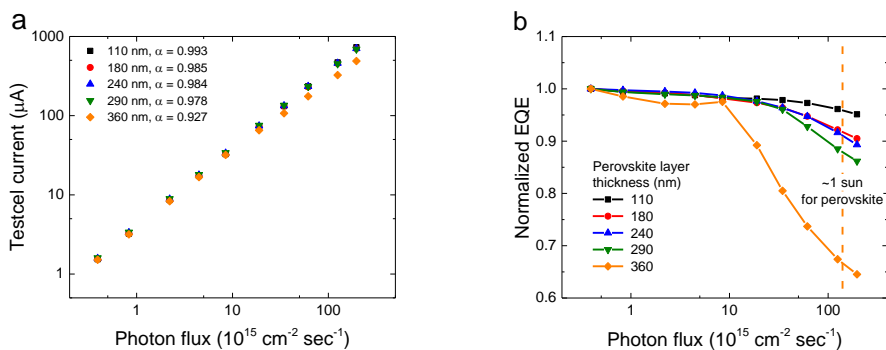
Figure 3.14 Light intensity dependent short circuit current (Isc) (a) and external quantum efficiency (EQE) at 530 nm (b) of solar cells with different perovskite layer thicknesses using a 530 nm LED light source. EQE curves are normalized to the lowest measured light intensity. The orange dashed line indicates the light intensity that corresponds to ~1 sun AM 1.5G light intensity for perovskite solar cells.

By changing the atmosphere in which the perovskite layer is annealed, it was found that this sub-linearity of the EQE versus light intensity is greatly reduced and almost non-existent when the perovskite layer is annealed in air instead of N_2. Therefore, annealing in air allows further increase in the perovskite layer thickness without suffering from a reduction in charge extraction efficiency. In Figure 3.15 the EQEs of solar cells with different perovskite layer thicknesses annealed in air are displayed. In contrast to the previously produced cells that were annealed in a nitrogen atmosphere, these solar cells do not display the sub-linearity of the current generation with increasing light intensity. Therefore, the perovskite layer thickness can be increased further and the plateau efficiency of ~11% of the solar cells annealed in N_2 can be surpassed. Figure 3.16 shows the fast and stabilized J-V graphs of the cells with different perovskite layer thicknesses that are annealed in air.
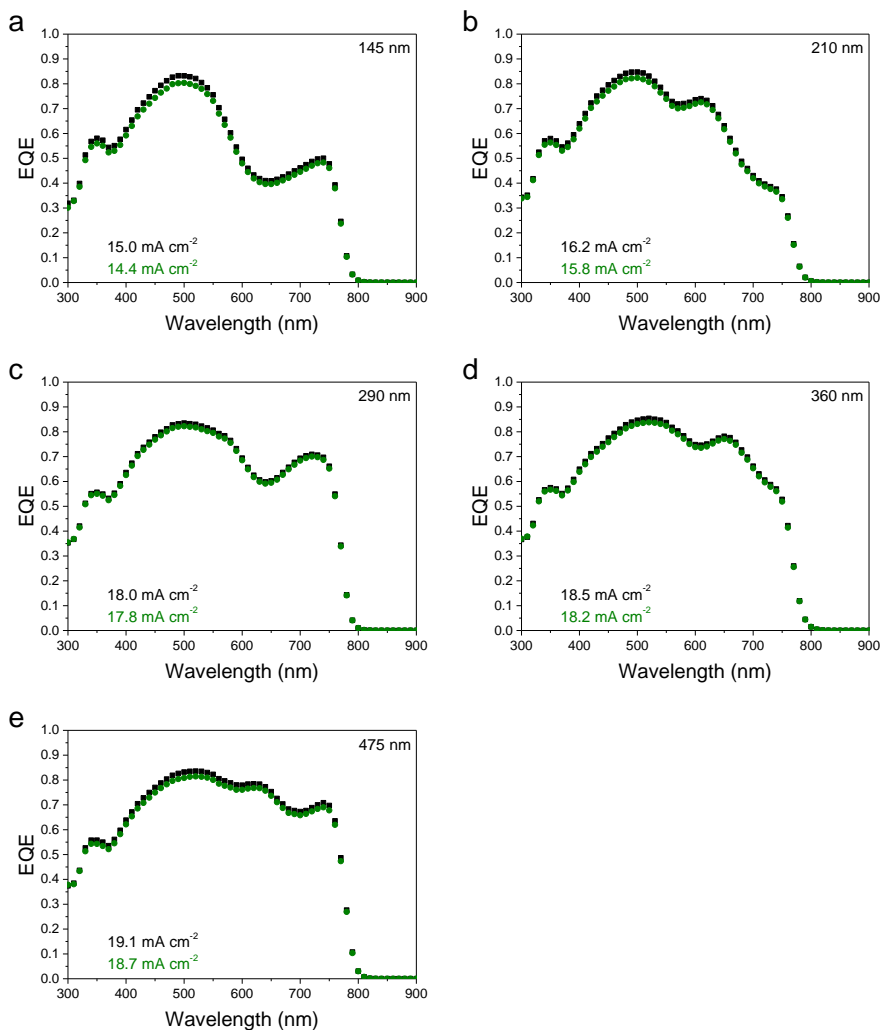
Figure 3.15 External quantum efficiency (EQE) plots of perovskite solar cells with air annealed perovskite layers that have different thicknesses as indicated in the top right of each graph. Measured under low- (black squares) and high- (green dots) illumination intensity. The integrated current density is displayed for both measurements in black and green for the low and high illumination intensity measurements respectively.
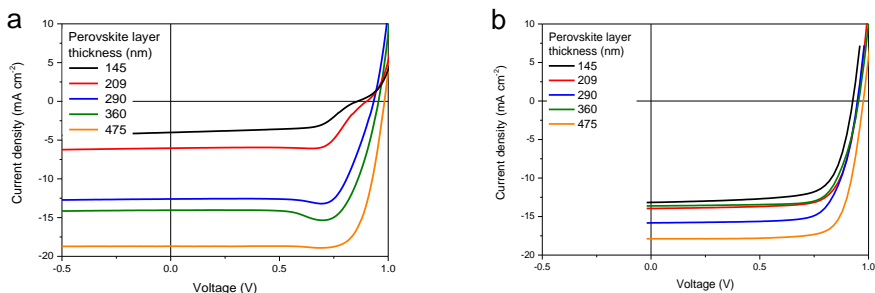
Figure 3.16 *J-V* curves of solar cells with different perovskite layer thicknesses annealed in air measured using the regular (fast) *J-V* measurement (a) and stabilized *J-V* measurement method as described in section 2.2 (b).

As expected, the regular (fast) *J-V* graphs in Figure 3.16a show an increase of both J_{SC} and V_{OC} with increasing layer thickness. Also the "dip" around the MPP is seen just as in the cells with perovskite layers annealed in N_2. The thinnest perovskite layers show a severe S-shaped *J-V* curve near V_{OC}, indicating some interface issue, which was not seen in the N_2 annealed perovskite layers. Also the overall performance of these cells is lower than N_2 annealed perovskite layers with similar layer thicknesses. The stabilized *J-V* measurements (Figure 3.16b) however, show more reasonable results where the J_{SC} and V_{OC} increase with increasing perovskite layer thickness and the "dip" around MPP is not present. The only outlying result in the stabilized measurements is that of the 360 nm thick perovskite layer that shows a lower J_{SC} than it should comparing it to the regular (fast) *J-V* measurements and EQE measurement at high illumination intensity. There is no clear explanation for this lower photocurrent generation since the measurement was conducted on the same day as the regular (fast) *J-V* measurements. One day after the stabilized measurement, a regular *J-V* scan and the EQE measurements were performed where the cell behaved correctly again. Unfortunately no stabilized measurement was performed on the cell with a perovskite layer thickness of 360 nm on that day.

All *J-V* parameters of both the regular and stabilized *J-V* measurements are plotted versus the perovskite layer thickness in Figure 3.17. As was already discussed, the match between the fast- and stabilized *J-V* measurements is substantially worse than with annealing in N_2, once more illustrating the importance of performing stabilized *J-V* measurements. The stabilized measurement results show that the FF plateaus slightly below a value of 0.8 which is good compared to reported values.[42–44] The J_{SC} and V_{OC} keep increasing with increasing perovskite layer thickness without the J_{SC} plateauing at high thicknesses like it did for the perovskite layers that were annealed

in N$_2$. This also causes P_{max} to keep increasing with increasing perovskite layer thickness and reaching the highest efficiency with the thickest perovskite layer of the series. The calculated PCE of the solar cell with a perovskite layer of 475 nm thick is 14.2% (Table 3.1). It must be noted here that while the maximum PCE was obtained with the thickest perovskite layer in the series, increasing the thickness further in subsequent experiments resulted in lower solar cell efficiencies due to a reduction in J_{SC}, V_{OC}, and FF.
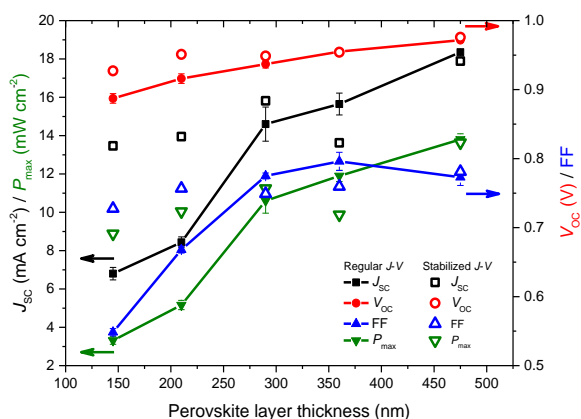
Figure 3.17 Graph displaying the short circuit current density (J_{SC}) in black squares, open circuit voltage (V_{OC}) in red dots, fill factor (FF) in blue upward facing triangles, and maximum power (P_{max}) in green downward facing triangles, obtained from regular (fast) J-V measurements (lines with solid symbols) and stabilized measurements (open symbols, no line) with different perovskite layer thicknesses that were annealed in air. Symbols are the average and error bars are the standard deviation over 4 cells on the same substrate.

Table 3.1 Stabilized J-V parameters of solar cells with perovskite layers of different thicknesses (d) that were annealed in air. The PCE is calculated by multiplying the V_{OC} and FF obtained from the stabilized J-V sweep with the J_{SC} obtained from the high illumination intensity (light-biased) EQE measurement.

d (nm)	$J_{SC, stab}$ (mA cm^{-2})	$V_{OC, stab}$ (V)	FF $_{stab}$	$P_{max, stab}$ (mW cm^{-2})	$J_{SC, SR}$ (mA cm^{-2})	$J_{SC, SR bias}$ (mA cm^{-2})	PCE (%)
145	13.5	0.93	0.73	8.9	15.0	14.4	9.7
209	13.9	0.95	0.76	10.0	16.2	15.8	11.9
290	15.8	0.95	0.75	11.2	18.0	17.8	12.6
361	13.6	0.95	0.76	9.9	18.5	18.2	13.2
475	17.9	0.98	0.78	13.6	19.1	18.7	14.2

3.6 Conclusions

In this chapter we have optimized methylammonium lead triiodide ($CH_3NH_3PbI_3$, $MAPbI_3$) perovskite layers for use in planar p-i-n solar cells with PEDOT:PSS and PCBM as hole and electron transporting layers respectively. By using multiple lead sources ($PbCl_2$ and $Pb(OAc)_2 \cdot 3H_2O$) in the precursor mixture, and changing the ratio between them, the crystallization process of the perovskite can be controlled. This allows fine-tuning of the crystallization speed and with that the size of the formed crystallites and the compactness of the perovskite layer, which are of great influence on the solar cell performance. Additionally, the use of this precursor solution composition results in an improved reproducibility compared to the "mixed halide" mixture. An optimal perovskite layer morphology was found at $PbCl_2$ and $Pb(OAc)_2 \cdot 3H_2O$ fractions of 0.2 and 0.8 respectively, employing a 3:1 MAI:total Pb ratio in DMF. The annealing time and temperature were also found to be critical parameters for the formation of the desired perovskite layer, where annealing too long or too hot leads to decomposition of the perovskite into PbI_2 and $MAI_{(g)}$, while annealing too short or too cold results in residual solvent or unreacted ions in the layer. Both of which were found to be detrimental for solar cell performance. The optimal annealing time and temperature that were found were 15 minutes and 90 °C respectively. The perovskite layer thickness was found to have a significant influence on mainly the current density that can be extracted from the solar cell, where an optimal layer thickness of 475nm was found to yield a J_{SC} of almost 18 mA cm^{-2}. Additionally, it was found that these high values of J_{SC} could only be obtained by annealing the perovskite layer in ambient conditions, since perovskite layers annealed in inert conditions suffer from strong sublinearity of the photocurrent with illumination intensity. The cause of the reduction in extracted photocurrent at high illumination intensities of solar cells annealed in N_2 and why this is solved by annealing in air is discussed in detail in chapter 4 of this dissertation. Finally, the optimized production procedure described in this chapter allows the reproducible production of perovskite solar cells with an efficiency of ~14%.

3.7 Experimental

Device fabrication:

Tin doped indium oxide (indium-tin oxide, ITO) coated and pre-patterned glass substrates (Naranjo substrates) were cleaned by sonication in acetone (Sigma Aldrich), scrubbing in a solution of sodium dodecyl sulfate (SDS, Acros, 99%) in filtered water (Milli-Q), rinsing in deionized water, sonication in 2-propanol (Sigma Aldrich) and 30 minutes of UV-ozone treatment right before use. Poly(3,4-ethylenedioxythiophene):poly(styrenesulfonate) (PEDOT:PSS, Heraeus Clevios PVP Al 4083) was filtered using a 0.45 µm PVDF filter and spin coated (40 sec, 3000 RPM) onto the cleaned and UV-ozone treated substrates. The PEDOT:PSS layer is then dried at 140 °C for 15 minutes in ambient conditions.

For the perovskite precursor solutions methylammonium iodide (MAI) (Dyesol), lead(II) chloride ($PbCl_2$) (Sigma Aldrich, 98%), lead(II) acetate trihydrate ($Pb(OAc)_2 \cdot 3H_2O$, Sigma Aldrich, 99.999% trace metal basis), and *N,N*-dimethylformamide (DMF, Sigma Aldrich, anhydrous, 99.8%) were used and the solutions were stirred at room temperature until completely dissolved. The perovskite precursor solution used in section 3.2 consisted of 450 mg mL^{-1} (MAI) and 233 mg mL^{-1} $PbCl_2$ in DMF and was spin coated at 3000 RPM for 120 seconds. The formed film was dried using ramp annealing which consisted of 1h at 25 °C, a ramp from 25 °C →100 °C at 1°C min^{-1} and 2 h at 100 °C in N_2. For the production of the perovskite precursor solutions used in section 3.3 two stock solutions were produced, one consisting of 450 mg mL^{-1} MAI and 232 mg mL^{-1} $PbCl_2$ in DMF (solution I) and the other consisting of 450 mg mL^{-1} MAI and 319 mg mL^{-1} $Pb(OAc)_2 \cdot 3H_2O$ in DMF (solution II). To make solutions with different ratios, the two stock solutions were mixed in (I:II) 1:9, 1:4, 3:7, 2:3, 1:1, 3:2, and 7:3 ratio for fractions of 0.1, 0.2, 0.3, 0.4, 0.5, 0.6, and 0.7 $PbCl_2$ respectively. All solutions were spin coated at 3000 RPM for 60 seconds. The formed films were annealed for 10 min at 130 °C in N_2. The perovskite precursor solution used in section 3.4 was produced in the same way as those used for section 3.3 (fraction $PbCl_2$ = 0.2) and was spin coated at 3000 RPM for 120 seconds. The formed films were annealed for 10 min at 70, 90, 110, and 130 °C, and for 30 min at 90 and 110 °C in N_2. The perovskite precursor solutions used in the first part (N_2 annealing) of section 3.5 consisted of 287, 383, 481, 574, and 670 mg mL^{-1} MAI; 34, 45, 54, 66, and 76 mg mL^{-1} $PbCl_2$; and 182, 243, 302, 364, and 425 mg mL^{-1} $Pb(OAc)_2 \cdot 3H_2O$ in DMF for perovskite layer thicknesses of 110, 180, 240, 290, and 360 nm respectively. The precursor solutions were spin coated at 5700 RPM for 120 seconds and the formed films were annealed for 10 min at

90 °C in N_2. The perovskite precursor solutions used in the second part (air annealing) of section 3.5 were diluted from a stock solution containing 952 mg mL^{-1} MAI, 110 mg mL^{-1} $PbCl_2$ and 609 mg mL^{-1} $Pb(OAc)_2 \cdot 3H_2O$ in DMF. From this stock solution, 50 μL was taken and 5.6, 12.5, 21.4, 33.3, and 50 μL of DMF was added for perovskite layer thicknesses of 475, 360, 290, 210 and 145 nm respectively. The precursor solutions were spin coated at 5700 RPM for 120 seconds and the formed films were annealed for 15 min at 90 °C in air.

For the electron transport layer (ETL), 24 mg mL^{-1} of [6,6]-phenyl-C_{61}-butyric acid methyl ester (PCBM, Solenne BV, 99%) was dissolved in a 50/50 mixture of chloroform (Biosolve, AR grade) and chlorobenzene (Sigma Aldrich, anhydrous 99.8%) and spin coated on top of the completed perovskite layer (60 s at 500 RPM) in the same atmosphere as where the cells are annealed. After that, the contact area was cleaned and LiF (1 nm) and Al (100 nm) were thermally evaporated under high vacuum (±3×10^{-7} mbar) as a back electrode.

Measurement methods:

Layer thicknesses were measured using a Veeco Dektak 150 profilometer.

J–V characteristics were measured in a nitrogen environment with a Keithley 2400 source meter under ±100 mW cm^{-2} white light illumination from a tungsten-halogen lamp filtered by a Schott GG385 UV filter and a Hoya LB120 daylight filter. The cells were masked with a 0.0676 cm^2 or 0.1296 cm^2 aperture (the physical overlap of the contacts is 0.09 cm^2 and 0.16 cm^2 respectively). Regular (fast) upwards and downwards *J–V* sweeps were performed between −0.5 and 1.5 V with a scan speed of 0.25 V s^{-1}. The stabilized *J-V* measurement protocol (section 2.3) used was defined by light soaking at V_{OC} for 10 minutes, followed by a downward sweep (V_{OC} + 0.05 V → −0.05 V) with a step size of 0.025 V.

Short-circuit currents under AM 1.5G conditions were determined by integrating the spectral response with the solar spectrum. Spectral response measurements were conducted under only probe light and 1 sun operating conditions by using a 530 nm high power LED (Thorlabs M530L3 driven by a DC4104 driver) for bias illumination. The device was kept in a nitrogen filled box behind a quartz window and a circular aperture with a 1 mm radius and irradiated with modulated monochromatic light, from a 50 W tungsten-halogen lamp (Philips focusline) and monochromator (Oriel, Cornerstone 130) with the use of a mechanical chopper (160 Hz). The response was recorded as a voltage from a preamplifier (SR570) using a lock-in amplifier (SR830). A calibrated silicon cell was used as reference (calibrated at the Energy research Centre of the Netherlands).

J_{SC} and V_{OC} vs light intensity measurements were performed using a Keithley 2400 source meter and 405 and 730 nm high power LEDs (Thorlabs M405L3 and M730L4 driven by a DC4104 driver) for illumination.

Scanning electron microscopy (SEM) was performed on a FEI Quanta 3D FEG.

J_{SC}, EQE, and V_{OC} vs light intensity measurements were performed using a Keithley 2400 source meter and 730 nm high power LEDs (Thorlabs M730L4 driven by a DC4104 driver) for illumination.

X-Ray Diffraction measurements were performed on a Bruker 2D Phaser using Cu Kα radiation with a wavelength of 0.15406 nm between 2θ angles of 10 to 60° using increments of 0.05° and a 2 second integration time. A 0.6 mm slit was used at the X-Ray source and a shield was positioned 0.5 mm above the sample surface. The sample rotated at a speed of 60 RPM during the measurement.

Optical Modeling

Optical modeling based on the TM method was performed using Setfos 4.3 (Fluxim). The solar cell stack used consisted of glass (100nm, incoherent), SiO_2 (20 nm), ITO (140 nm), PEDOT:PSS (40 nm) perovskite (variable thickness), PCBM (110 nm), LiF (1 nm), and Al (100 nm).

3.8 References

1   Q. Lin, A. Armin, R. C. R. Nagiri, P. L. Burn and P. Meredith, *Nat. Photonics*, 2014, **9**, 106–112.

2   N. G. Park, *Mater. Today*, 2015, **18**, 65–72.

3   C. Wehrenfennig, G. E. Eperon, M. B. Johnston, H. J. Snaith and L. M. Herz, *Adv. Mater.*, 2014, **26**, 1584–1589.

4   C.-S. Jiang, M. Yang, Y. Zhou, B. To, S. U. Nanayakkara, J. M. Luther, W. Zhou, J. J. Berry, J. van de Lagemaat, N. P. Padture, K. Zhu and M. M. Al-Jassim, *Nat. Commun.*, 2015, **6**, 8397.

5   V. D'Innocenzo, G. Grancini, M. J. P. Alcocer, A. R. S. Kandada, S. D. Stranks, M. M. Lee, G. Lanzani, H. J. Snaith and A. Petrozza, *Nat. Commun.*, 2014, **5**, 1–6.

6   G. E. Eperon, S. D. Stranks, C. Menelaou, M. B. Johnston, L. M. Herz and H. J. Snaith, *Energy Environ. Sci.*, 2014, **7**, 982.

7   G. E. Eperon, G. M. Paterno, R. J. Sutton, A. Zampetti, A. A. Haghighirad, F. Cacialli and H. J. Snaith, *J. Mater. Chem. A*, 2015, **3**, 19688–19695.

8   W. Zhang, M. Saliba, D. T. Moore, S. K. Pathak, M. T. Hörantner, T. Stergiopoulos, S. D. Stranks, G. E. Eperon, J. A. Alexander-Webber, A. Abate, A. Sadhanala, S. Yao, Y. Chen, R. H. Friend, L. A. Estroff, U. Wiesner and H. J. Snaith, *Nat. Commun.*, 2015, **6**, 6142.

9   N. J. Jeon, J. H. Noh, Y. C. Kim, W. S. Yang, S. Ryu and S. Il Seok, *Nat. Mater.*, 2014, **13**, 897–903.

10   N. K. Noel, S. N. Habisreutinger, B. Wenger, M. T. Klug, M. T. Hörantner, M. B. Johnston, R. J. Nicholas, D. T. Moore and H. J. Snaith, *Energy Environ. Sci.*, 2017, **10**, 145-152.

11   K. Hendriks, J. J. van Franeker, B. J. Bruijnaers, J. A. Anta, M. M. Wienk and R. A. J. Janssen, *J. Mater. Chem. A.*, 2017, **5**, 2346-2354.

12   W. Liao, D. Zhao, Y. Yu, N. Shrestha, K. Ghimire, C. R. Grice, C. Wang, Y. Xiao, A. J. Cimaroli, R. J. Ellingson, N. J. Podraza, K. Zhu, R.-G. Xiong and Y. Yan, *J. Am. Chem. Soc.*, 2016, **138**, 12360–12363.

13   H.-B. Kim, H. Choi, J. Jeong, S. Kim, B. Walker, S. Song and J. Y. Kim, *Nanoscale*, 2014, **6**, 6679-6683.

14   W. Qiu, T. Merckx, M. Jaysankar, C. Masse de la Huerta, L. Rakocevic, W. Zhang, U. W. Paetzold, R. Gehlhaar, L. Froyen, J. Poortmans, D. Cheyns, H. J. Snaith and P. Heremans, *Energy Environ. Sci.*, 2016, **9**, 484–489.

15   F. K. Aldibaja, L. Badia, E. Mas-Marzá, R. S. Sánchez, E. M. Barea and I. Mora-Sero, *J. Mater. Chem. A*, 2015, **3**, 9194–9200.

16   J. Qing, H.-T. Chandran, Y.-H. Cheng, X.-K. Liu, H.-W. Li, S.-W. Tsang, M.-F. Lo and C.-S. Lee, *Appl. Mater. Interfaces*, 2015, **7**, 23110–23116.

17   J. H. Heo, S. H. Im, J. H. Noh, T. N. Mandal, C.-S. Lim, J. A. Chang, Y. H. Lee, H. Kim, A. Sarkar, M. K. Nazeeruddin, M. Grätzel and S. Il Seok, *Nat. Photonics*, 2013, **7**, 486–491.

18   M. Liu, M. B. Johnston and H. J. Snaith, *Nature*, 2013, **501**, 395–398.

19   P.-W. Liang, C.-Y. Liao, C.-C. Chueh, F. Zuo, S. T. Williams, X.-K. Xin, J. Lin and A. K.-Y. Jen, *Adv. Mater.*, 2014, **26**, 3748–3754.

20   D. Liu and T. L. Kelly, *Nat. Photonics*, 2013, **8**, 133–138.

21   J. You, Z. Hong, Y. Yang, Q. Chen, M. Cai, T.-B. Song, C.-C. Chen, S. Lu, Y. Liu, H. Zhou and Y. Yang, *ACS Nano*, 2014, **8**, 1674–1680.

22   O. Malinkiewicz, A. Yella, Y. H. Lee, G. M. Espallargas, M. Graetzel, M. K. Nazeeruddin and H. J. Bolink, *Nat. Photonics*, 2014, **8**, 128–132.

23   Q. Chen, H. Zhou, Z. Hong, S. Luo, H.-S. Duan, H.-H. Wang, Y. Liu, G. Li and Y. Yang, *J. Am. Chem. Soc.*, 2013, **136**, 622–625.

24   V. Gonzalez-Pedro, E. J. Juarez-Perez, W.-S. Arsyad, E. M. Barea, F. Fabregat-Santiago, I. Mora-Sero and J. Bisquert, *Nano Lett.*, 2014, **14**, 888–893.

25   G. E. Eperon, V. M. Burlakov, A. Goriely and H. J. Snaith, *ACS Nano*, 2014, **8**, 591–598.

26   C. Roldán-Carmona, O. Malinkiewicz, A. Soriano, G. Mínguez Espallargas, A. Garcia, P. Reinecke, T. Kroyer, M. I. Dar, M. K. Nazeeruddin and H. J. Bolink, *Energy Environ. Sci.*, 2014, **7**, 994.

27   G. E. Eperon, V. M. Burlakov, P. Docampo, A. Goriely and H. J. Snaith, *Adv. Funct. Mater.*, 2014, **24**, 151–157.

28   S. D. Stranks, G. E. Eperon, G. Grancini, C. Menelaou, M. J. P. Alcocer, T. Leijtens, L. M. Herz, A. Petrozza and H. J. Snaith, *Science*, 2014, **342**, 341–344.

29   Q. Chen, H. Zhou, Y. Fang, A. Z. Stieg, T.-B. Song, H.-H. Wang, X. Xu, Y. Liu, S. Lu, J. You, P. Sun, J. McKay, M. S. Goorsky and Y. Yang, *Nat. Commun.*, 2015, **6**, 7269.

30   S. Colella, E. Mosconi, G. Pellegrino, A. Alberti, V. L. P. Guerra, S. Masi, A. Listorti, A. Rizzo, G. G. Condorelli, F. De Angelis and G. Gigli, *J. Phys. Chem. Lett.*, 2014, **5**, 3532–3538.

31   H. Yu, F. Wang, F. Xie, W. Li, J. Chen and N. Zhao, *Adv. Funct. Mater.*, 2014, **24**, 7102–7108.

32   S. Colella, E. Mosconi, P. Fedeli, A. Listorti, F. Gazza, F. Orlandi, P. Ferro, T. Besagni, A. Rizzo, G. Calestani, G. Gigli, F. De Angelis and R. Mosca, *Chem. Mater.*, 2013, **25**, 4613–4618.

33   T. A. Berhe, W.-N. Su, C.-H. Chen, C.-J. Pan, J.-H. Cheng, H.-M. Chen, M.-C. Tsai, L.-Y. Chen, A. A. Dubale and B.-J. Hwang, *Energy Environ. Sci.*, 2016, **9**, 323–356.

34   Takeo Oku, *Solar Cells - New Approaches and Reviews, chapter 3*, 2015.

35   S. Bae, J.-S. Park, I. K. Han, T. J. Shin and W. H. Jo, *Sol. Energy Mater. Sol. Cells*, 2017, **160**, 77–84.

36   P. Docampo, F. C. Hanusch, N. Giesbrecht, P. Angloher, A. Ivanova, T. Bein, *APL Mater.*, 2014, **2**, 81508.

37   B. J. Foley, J. Girard, B. A. Sorenson, A. Z. Chen, J. S. Niezgoda, M. R. Alpert, A. F. Harper, D.-M. Smilgies, P. Clancy, W. A. Saidi and J. J. Choi, *J. Mater. Chem. A*, 2017, **5**, 113–123.

38   A. Z. Chen, B. J. Foley, J. H. Ma, M. R. Alpert, J. S. Niezgoda and J. J. Choi, *J. Mater. Chem. A*, 2017, **5**, 7796–7800.

39   Q. Dong, Y. Yuan, Y. Shao, Y. Fang, Q. Wang and J. Huang, *Energy Environ. Sci.*, 2015, **8**, 2464–2470.

40   W. Zhu, C. Bao, B. Lv, F. Li, Y. Yi, Y. Wang, J. Yang, X. Wang, T. Yu and Z. Zou, *J. Mater. Chem. A*, 2016, **4**, 12535–12542.

41   M. M. Lee, J. Teuscher, T. Miyasaka, T. N. Murakami, H. J. Snaith, *Science*, 2012, **338**, 643-647

42   S. S. Mali and C. K. Hong, *Nanoscale*, 2016, **8**, 10528–10540.

43   C. Roldán-Carmona, O. Malinkiewicz, R. Betancur, G. Longo, C. Momblona, F. Jaramillo, L. Camacho and H. J. Bolink, *Energy Environ. Sci.*, 2014, **7**, 2968–2973.

44   P. Docampo, J. M. Ball, M. Darwich, G. E. Eperon and H. J. Snaith, *Nat. Commun.*, 2013, **4**, 2761.

45   S. S. Shin, W. S. Yang, J. H. Noh, J. H. Suk, N. J. Jeon, J. H. Park, J. S. Kim, W. M. Seong and S. Il Seok, *Nat. Commun.*, 2015, **6**, 7410.

46   J. H. Heo, M. H. Lee, H. J. Han, B. R. Patil, J. S. Yu and S. H. Im, *J. Mater. Chem. A*, 2016, **4**, 1572–1578.

Chapter 4

The effect of oxygen on the efficiency of planar p-i-n metal halide perovskite solar cells with a PEDOT:PSS hole transport layer*

Abstract

Poly(3,4-ethylenedioxythiophene):poly(styrenesulfonate)   (PEDOT:PSS)   is frequently used as hole transport layer in planar p-i-n perovskite solar cells. Here we show that the processing of a metal halide perovskite layer on top of PEDOT:PSS via spin coating of a precursor solution chemically reduces the oxidation state of PEDOT:PSS. This reduction leads to a lowering of the work function of the PEDOT:PSS and the perovskite layer on top of it. As a consequence, the solar cells display inferior performance with a reduced open-circuit voltage and a reduced short-circuit current density, which increases sublinearly with light intensity. The reduced PEDOT:PSS can be re-oxidized by thermal annealing of the PEDOT:PSS/perovskite layer stack in the presence of oxygen. As a consequence, thermal annealing of the perovskite layer in air provides solar cells with increased open-circuit voltage, short-circuit current density and high efficiency.

4.1 Introduction

Metal halide perovskite materials currently attract great interest for use in hybrid organic-inorganic solar cells. Methylammonium lead halides were first used in 2009 as light sensitizers of mesoporous titania (TiO_2) in photovoltaic cells comprising a liquid electrolyte, providing a power conversion efficiency (PCE) of 3.8%.[1] The introduction of a solid organic hole transport material efficiently solved the fast degradation of the liquid-electrolyte cells and led to stable photovoltaic cells with an optimized PCE of 9.7%.[2] The use of an insulating alumina (Al_2O_3) layer instead of the electron-transporting TiO_2 layer proved that the perovskite material itself is capable of free charge generation and very efficient ambipolar charge transport.[3] Recent advances have shown PCEs of over 22% for metal halide perovskites with optimized compositions and processing methods.[4,5]

Many desirable properties like strong absorption, low exciton binding energy for creating free charges[6–8] and high charge mobilities and lifetimes[9] characterize metal halide perovskite materials. The fact that they can be processed from solution with relative ease makes future roll-to-roll processing an attractive option.[10–12] Their versatility in composition and processing has allowed the usage of different solvents and precursor materials and even made it possible to tune the band gap of the material.[13–23]

Precursor and solvent combinations also allow changing of the morphology of the perovskite layer by influencing nucleation and crystal growth during the processing steps.[24–27] The versatility in processing has led to many different processing techniques ranging from single-step solution processing,[4,18] to multi-step solution processing with and without drying and anti-solvent treatments,[28–31] single and multi-step thermal evaporation and even combinations of solution processing and thermal evaporation.[32–36] After the deposition of the precursor materials, usually a (thermal) annealing step is used to convert the deposited layer into the desired perovskite phase and morphology.[37–41] By changing the composition of the precursor solution, the crystallization process can be retarded or sped up and by combining different lead salt precursors, the layer can even be tuned to achieve a favorable morphology and smoothness of the perovskite layer for the most efficient solar cells, which is especially important in planar device configurations.[24,26,42]

Here we investigate the influence of the processing atmosphere on the photovoltaic performance of planar *p-i-n* perovskite solar cells with poly(3,4-ethylenedioxythiophene):poly(styrenesulfonate) (PEDOT:PSS) as hole transport layer,

methylammonium lead triiodide as semiconductor and [6,6]-phenyl-C_{61}-butyric acid methyl ester (PCBM) as electron transport layer. To do so, a processing method that allows complete processing in ambient atmosphere was developed.

4.2 The effect of processing atmosphere on solar cell performance

The perovskite solar cell fabrication is based on a triple anion solution of methylammonium iodide (MAI), lead(II) chloride ($PbCl_2$) and lead(II) acetate trihydrate ($Pb(OAc)_2 \cdot 3H_2O$) in *N,N*-dimethylformamide (DMF). This solution is heated to 70 °C and spin coated dynamically onto a pre-heated (100 °C) glass substrate with patterned indium tin oxide (ITO), covered with PEDOT:PSS. By this hot-casting method the very hygroscopic precursor salts are already converted to the perovskite during deposition, as indicated by a pronounced color change from the yellow precursor to the brown perovskite. This allows the complete processing of the solar cell in ambient atmosphere. Even though perovskite crystals are already formed during casting, a short additional thermal annealing step, during which the color of the perovskite layer changes from light brown to dark brown, is required to maximize the efficiency.[42] The devices are completed by a PCBM electron transport layer and a LiF/Al top contact. Further details of the fabrication can be found in the experimental section.

Figure 4.1a shows the stabilized current density-voltage (*J–V*) measurements under simulated AM 1.5G (100 mW cm^{-2}) illumination of these *p-i-n* photovoltaic devices, when all processing steps are either done in ambient air or in an inert atmosphere. The corresponding photovoltaic parameters are summarized in Table 4.1. Strikingly, the efficiency of cells processed under inert conditions (N_2 atmosphere, < 1 ppm O_2 and < 1 ppm H_2O) is much lower than the PCE of the air-processed devices where both J_{SC} and V_{OC} are considerably enhanced.
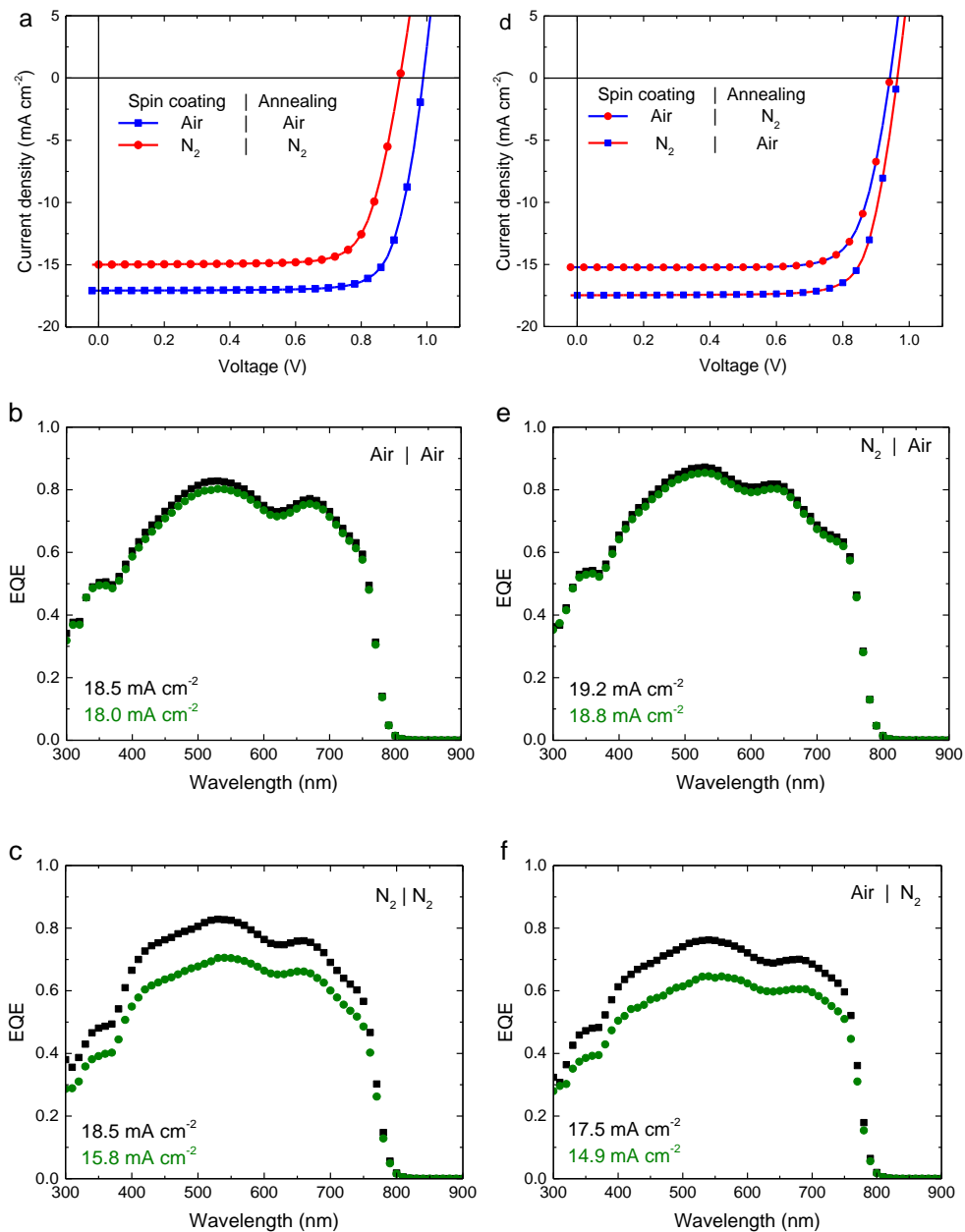
Figure 4.1 Stabilized current density-voltage (*J–V*) curves (a and d) under simulated AM 1.5G illumination and EQE spectra (b, c, e and f) of ITO/PEDOT:PSS/perovskite/PCBM/LiF/Al solar cells processed under different atmospheres as indicated in the legends. Black squares depict the EQE under low charge carrier density (*i.e.* without bias illumination), green circles depict the EQE at a charge carrier density similar to that of the cell under 1-sun light intensity (*i.e.* with bias illumination). The integrated current density is displayed in the graphs for both measurements.

To identify which processing step, deposition or annealing, is most critical, devices partially processed in air and N_2 have been measured (Figure 4.1d). For cells deposited in N_2 but annealed in air the performance is almost identical to the fully air processed device. In sharp contrast, cells cast in air but annealed in N_2, resemble the fully N_2-processed devices. This demonstrates that the annealing atmosphere, and not the casting atmosphere, has the largest impact on the performance.

The significantly lower J_{SC} for cells annealed in N_2 was confirmed by EQE measurements under appropriate 1-sun equivalent bias light (Figure 4.1b, 4.1c, 4.1e and 4.1f). Remarkably, in absence of bias light the magnitude of the EQEs of the N_2-annealed cells is much higher and similar to that of the air-annealed cells. Indicating that for the samples annealed in N_2 charge carrier collection is only reduced at higher charge carrier densities created by high illumination intensities.

Scanning electron microscopy (SEM) images of the top surface of the four differently processed perovskite layers (Figure 4.2) indicate that the largest morphological differences can be related to the casting atmosphere. Perovskite layers cast in air possess smaller crystallites compared to those cast in N_2. This could be related to a more efficient perovskite nucleation, probably due to the presence of moisture in the air.[43] The distinct difference in morphology, however, does not significantly affect the device performance. The X-Ray diffractograms (XRD) (Figure 4.3) of these four samples are very similar, showing the same degree of preferential orientation and the presence of a small PbI_2 peak for all samples.

Spin: air, anneal: air   Spin: air, anneal: N_2 Spin: N_2, anneal: air   Spin: N_2, anneal: N_2
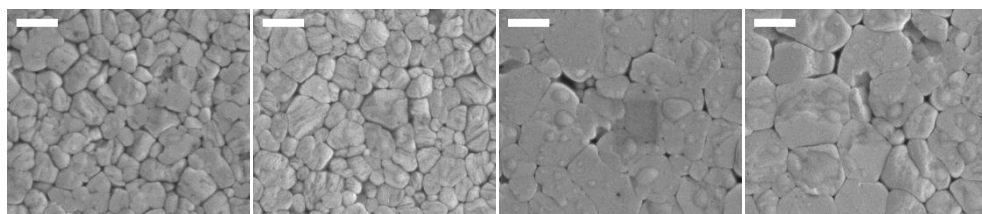
Figure 4.2 Scanning electron microscopy (SEM) top view images of perovskite layers spin coated in air or N_2 using the hot cast method and annealed in air or N_2 as indicated above the images (all scale bars are 1 µm).
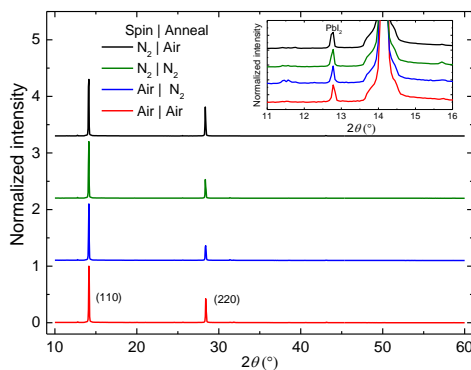
Figure 4.3 X-Ray diffractograms of perovskite layers spin coated in air or N_2 using the hot cast method and annealed in air or N_2. The inset is a zoom and shows the presence of a small PbI_2 peak at ~12.8°.

Experiments so far demonstrate that exposure to air during annealing of the perovskite layer is beneficial for the device performance. Besides N_2, ambient air contains oxygen and moisture, both of which have been shown to impact the properties of perovskite layers.[39,43–45] To identify which component is of importance here, experiments were conducted in which the perovskite annealing in dry air (*i.e.* exposure to O_2 but not to H_2O) was compared to annealing in humid N_2 (*i.e.* exposure to H_2O but not to O_2). Spin coating was done in N_2 in both cases since this provides more stability of the un-annealed samples over time when stored in N_2 after spin coating. The perovskite layer annealed in humid N_2 performs very similar to the one annealed in dry N_2, displaying both a low V_{OC} and J_{SC}, and a pronounced light intensity dependent EQE, indicating that water does not significantly influence the annealing process (Figure 4.4a and 4.4c). The perovskite layer annealed in dry air however, performs very similarly to layers annealed in ambient air, generating a high voltage and current, and a light-intensity independent EQE (Figure 4.4a and 4.4b). This demonstrates that the oxygen content of the air is the main reason for the performance increase. Table 4.1 summarizes the stabilized photovoltaic characteristics of these perovskite solar cells.
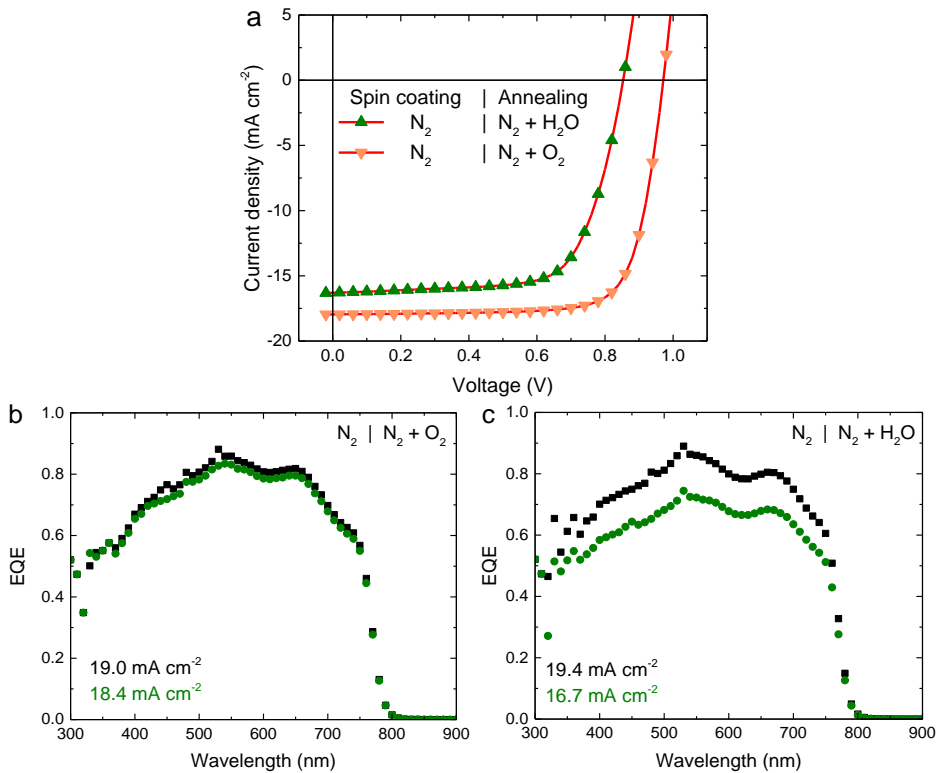
Figure 4.4 Stabilized current density-voltage (*J*–*V*) curves (a) under simulated AM 1.5G illumination, and EQE spectra (b and c) of ITO/PEDOT:PSS/perovskite/PCBM/LiF/Al solar cells spin coated in N_2 using the hot cast method and annealed in dry air and humid N_2 as indicated in the legends. Black squares depict the EQE under low charge carrier density (*i.e.* without bias illumination), green circles depict the EQE at a charge carrier density similar to that of the cell under 1-sun light intensity (*i.e.* with bias illumination). The integrated current density is displayed in the graphs for both measurements.

Table 4.1 Perovskite layer thickness and photovoltaic parameters of perovskite solar cells spin coated in air and N_2 using the hot cast method and annealed in air, N_2, dry air and humid N_2.

Spin coating atmosphere	Annealing atmosphere	Perovskite thickness (nm)	$J_{SC, J-V}$ (mA cm^{-2})	$J_{SC, SR}$ @ 1sun (mA cm^{-2})	V_{OC} (V)	FF	PCE[a] (%)
Air	Air	401	17.1	18.0	0.99	0.78	14.0
N_2	N_2	399	15.0	15.8	0.92	0.76	11.8
Air	N_2	409	15.2	14.9	0.94	0.77	10.9
N_2	Air	380	17.5	18.8	0.96	0.78	14.2
N_2	$N_2 + O_2$	368	18.0	18.4	0.97	0.76	13.7
N_2	$N_2 + H_2O$	377	16.3	16.7	0.85	0.70	9.9

[a] The PCE has been calculated with the photocurrent determined from integrating the EQE spectrum with the AM 1.5G spectrum ($J_{SC, SR}$ @ 1 sun).

Light intensity dependent J_{SC} measurements (Figure 4.5a) show that the current generation of the N_2-annealed samples is more sublinear ($J_{SC} \propto I^{\alpha}$, with $\alpha <$ 1) than that of air-annealed samples. Especially at higher light intensities the exponent α starts deviating from 1, consistent with the results from the EQE measurements. From the light intensity dependent V_{OC} measurement (Figure 4.5b), the ideality factor (η) is calculated by determining the slope of the V_{OC} versus the logarithm of the light intensity in the linear part of the graph,[46–48] where a slope equal to the thermal voltage (kT/q with k the Boltzmann constant, T the absolute temperature, and q the elementary charge) represents an ideality factor of 1. An ideality factor of η = 2 indicates dominant trap-assisted recombination in the bulk, an ideality factor of η = 1 indicates purely bimolecular recombination. The higher slope at low light intensities is caused by recombination over shunt paths.[48] The ideality factor determined using this method is about $\eta \approx 1.3$ for air-annealed cells, which would indicate a significant amount of trap-assisted (Shockley-Read-Hall (SRH)) recombination. The ideality factor of the N_2-annealed cells, however is about $\eta \approx 1$, which would suggest pure bimolecular recombination. However, the V_{OC} of this cell is lower than that of the air annealed cell, which should not be the case for an identical device with an ideality factor closer to unity. Strong surface recombination at a doped interface however, can reduce the ideality factor, making it appear to be closer to unity.[49] Additionally, V_{OC} vs light intensity measurements using different illumination wavelengths (405 nm absorbed predominantly in the first 100 nm of the active layer seen from the PEDOT:PSS layer and 730 nm absorbed more uniformly through the active layer) show that the charge carrier generation profile inside the perovskite layer does not strongly influence the V_{OC} or the ideality factor. Together, these results suggest that the PEDOT:PSS/perovskite interface is a source of significant surface recombination in the N_2-annealed perovskite cell at higher light intensities.[48,50,51]
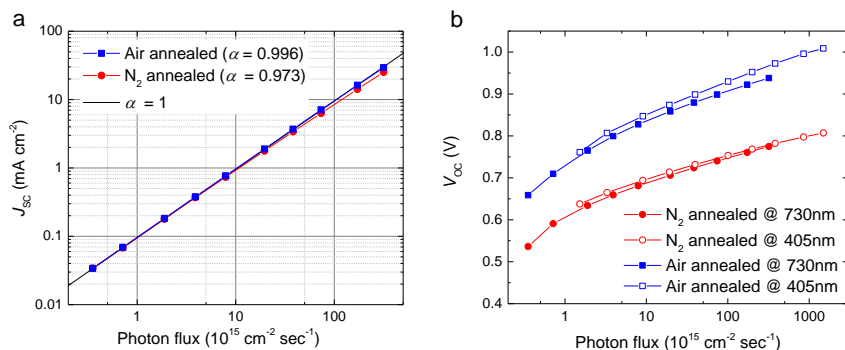
Figure 4.5 Light intensity dependent J_{SC} of air-annealed (blue solid squares) and N_2-annealed (red solid circles) perovskite solar cells (using an illumination wavelength of 730 nm) (a). A black line with an exponent α = 1 is added as a visual aid. Light intensity dependent V_{OC} of air annealed (blue squares) and N_2 annealed (red circles) perovskite solar cells measured using two different illumination wavelengths (730 nm solid symbols and 405 nm open symbols) (b). The ideality factors (η) calculated from the slopes of linear fit lines to the higher light intensity linear parts of the curves are $n \approx 1$ for N_2-annealed cells and $n \approx 1.3$ for air-annealed cells.

The hot casting procedure has proven to be very reliable and reproducible in our lab,[42] it is however a technique that has not found widespread use in other labs for the production of perovskite solar cells. Therefore, solar cells were also produced using the much more commonly used room temperature spin coating (cold casting). For this experiment, the same precursor mixture was used (at a 1.8× higher concentration in order to achieve the optimal perovskite layer thickness) which was spin coated with solution and substrate at room temperature in the regular fashion (solution is deposited before spinning of the substrate is started). Spin coating this precursor solution at room temperature in air results in rough perovskite layers with many pinholes after annealing, resulting in solar cells with low performance. Therefore, the cells for this experiment were spin coated in an N_2 atmosphere and annealed in either dry nitrogen or air.

Similar to the hot cast results, the solar cells produced in this experiment also show a significantly higher J_{SC} and V_{OC} for the cells annealed in air than those annealed in N_2 in the J–V characteristic (Figure 4.6a and Table 4.2). The EQE of the N_2-annealed cells also drops significantly under bias illumination (Figure 4.6c) while that of the air annealed cell remains high (Figure 4.6b). Showing that the decreased performance of N_2 annealed perovskite layers is not exclusive to the hot cast procedure. Top view SEM images of the layers are shown in Figure 4.7.
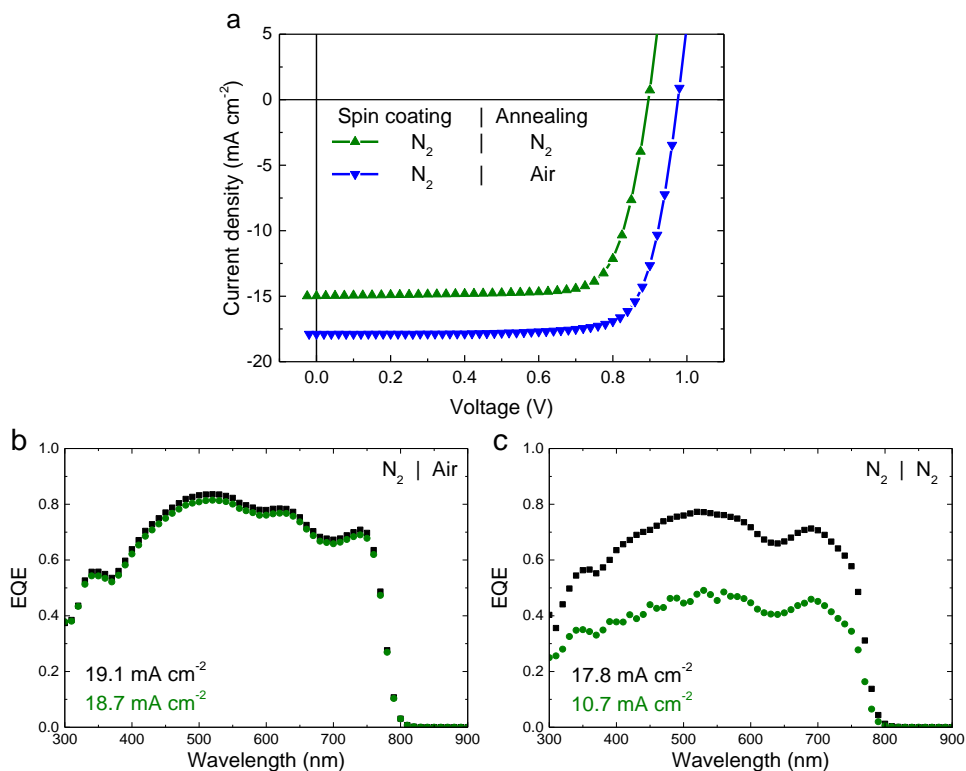
Figure 4.6 Stabilized current density-voltage (*J–V*) curves (a) under simulated AM1.5G illumination, and EQE spectra (b and c) of ITO/PEDOT:PSS/perovskite/PCBM/LiF/Al solar cells spin coated in N_2 using the cold cast method and annealed in air and N_2 as indicated in the legends. Black squares depict the EQE under low charge carrier density (*i.e.* without bias illumination), green circles depict the EQE at a charge carrier density similar to that of the cell under 1-sun light intensity (*i.e.* with bias illumination). The integrated current density is displayed in the graphs for both measurements.

Table 4.2 Photovoltaic parameters of perovskite solar cells spin coated in N_2 using the cold cast method and annealed in N_2 or air.

Spin coating atmosphere	Annealing atmosphere	Perovskite thickness (nm)	$J_{SC, J\text{-}V}$ (mA cm^{-2})	$J_{SC, SR}$ @ 1sun (mA cm^{-2})	V_{OC} (V)	FF	PCE[a] (%)
N_2	N_2	475	15.0	10.7	0.90	0.76	7.5
N_2	Air	362	17.9	18.7	0.98	0.78	14.3

[a] The PCE has been calculated with the photocurrent determined from integrating the EQE spectrum with the AM1.5G spectrum ($J_{SC, SR}$ @ 1 sun).

Spin: N$_2$, anneal: N$_2$ Spin: N$_2$, anneal: Air
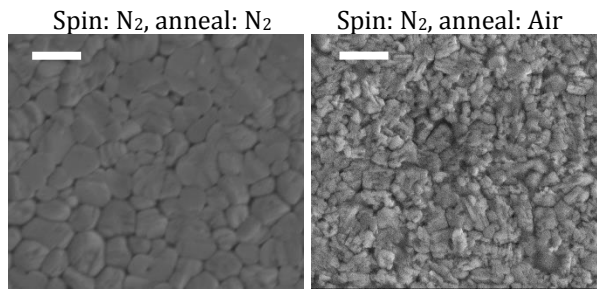
Figure 4.7 SEM top view images of perovskite layers spin coated in N$_2$ using the cold cast method and annealed in N$_2$ and air as indicated above the images (both scale bars are 1μm).

4.3 The effect of processing atmosphere on bulk properties of the perovskite layer

After establishing that it is the lack of oxygen that reduces the performance of perovskite layers annealed in N$_2$, the reason behind this performance reduction is investigated. To investigate the bulk properties of the perovskite layer, photoluminescence (PL) measurements on perovskite layers deposited on top of a non-quenching poly(4-styrenesulfonic acid) (PSSH) layer and annealed in nitrogen and air were conducted. These measurements show that at room temperature, the peak position and shape of the emission spectrum is similar for both samples (Figure 4.8a). Illumination intensity dependent measurements also show no significant difference between the two perovskite layers at both low and high illumination intensities (Figure 4.8b). A clear change from a slope of 1.5 for lower light intensities to a slope of 1 for high light intensities in a log-log plot is visible. This indicates a transition from dominant trap assisted (SRH) recombination (slope = 1.5) to dominant band-to band (free carrier) recombination (slope = 1) at a charge carrier density of about 1 sun AM 1.5 illumination intensity.[52–55] The PL spectrum does not change with increasing illumination intensity.
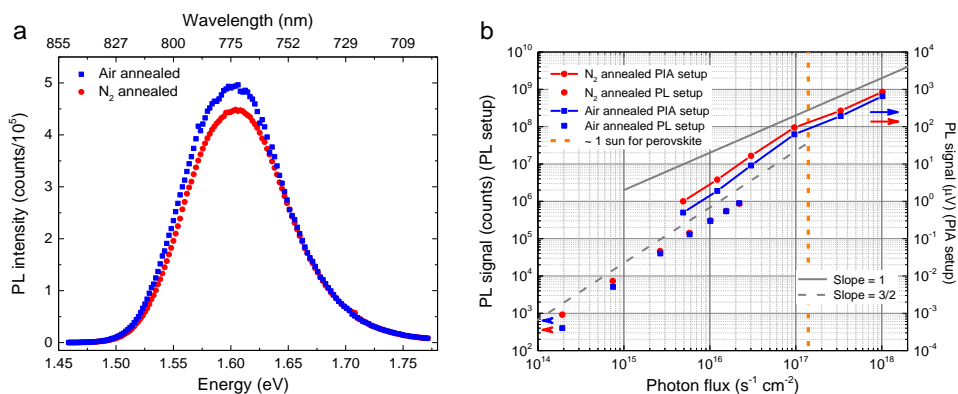
Figure 4.8 (a) Room temperature photoluminescence spectra of perovskite layers annealed in air (blue solid squares) and nitrogen (red solid circles). (b) Illumination intensity dependent photoluminescence of perovskite layers annealed in air (blue solid squares) and nitrogen (red solid circles) at room temperature measured in two different setups to cover a larger photon flux range including illumination intensities that generate charge carrier densities ≥ 1 sun AM1.5 illumination intensity. Lines with slopes of 1 and 3/2 (in a log-log plot) indicating different recombination mechanisms are also added. The wavelengths measured were the peak maxima in both setups.

Upon cooling to 70 K, the peak position and shape changes similarly for both samples through the range of temperatures (Figure 4.9) and similar as reported in literature.[52] At room temperature the PL is dominated by a band at 1.60 eV, while at 70 K the emission peaks at 1.66 eV together with a weak trap-related emission at 1.53 eV (Figure 4.10a). At 70 K there is no significant difference in peak shape and position at both medium and low illumination intensities and the relative intensity of the 1.53 eV defect emission does not seem to increase. In addition, a weak defect emission at 0.96 eV (~1300 nm)[56] is observed (Figure 4.10b), which shows a higher intensity for the N_2-annealed sample.
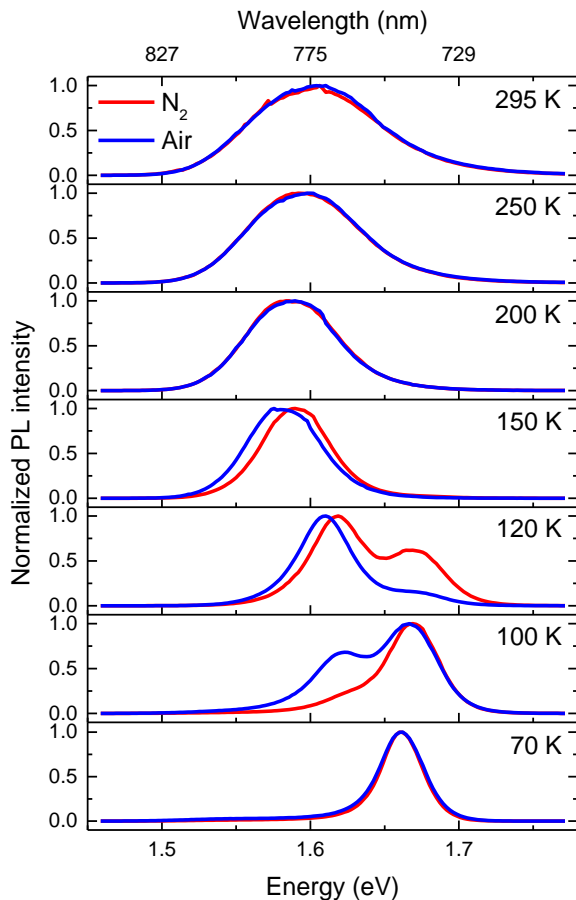
Figure 4.9 Normalized photoluminescence spectra of perovskite layers annealed in nitrogen (red) and air (blue) through a range of temperatures while cooling down from room temperature to 70 K.
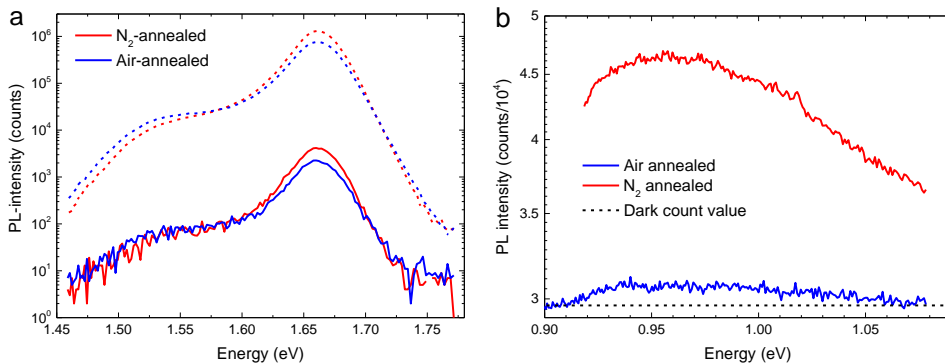
Figure 4.10 Photoluminescence spectra at 70 K of perovskite layers annealed in air (blue) and nitrogen (red) at high (dashed lines) and low (solid lines) illumination intensities.

The illumination intensity dependent photoluminescence at 70 K of the main emission peak (Figure 4.11a) looks very similar to the one measured at room temperature (Figure 4.8b low illumination intensity) again with a slope of 1.5 indicating trap assisted recombination. The slope is nearly 1 for both defect emissions (Figure 4.11b and 4.11c) and there is again no significant difference caused by the different annealing atmospheres.

These photoluminescence measurements combined indicate that the bulk physical properties of the perovskite layers are very similar and the only small difference that can be found is in the low energy (~1300 nm) defect.
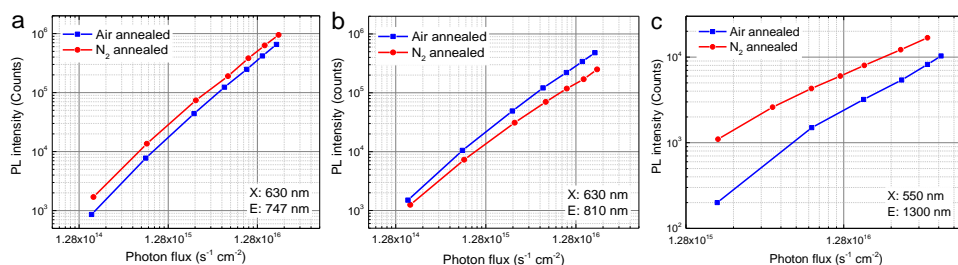
Figure 4.11 Illumination intensity dependent photoluminescence at 70 K of perovskite layers annealed in air (blue) and nitrogen (red) at three different wavelengths. Excitation (X) and emission (E) wavelengths are displayed in each graph. For the 1300 nm graph, the dark count was subtracted.

4.4 The effect of processing atmosphere on interface and electronic properties of the perovskite solar cell

Since the bulk properties of the perovskite layer are unaffected by the annealing atmosphere, the interface properties are investigated. To do so, electroluminescence (EL) measurements were conducted on air-annealed and N_2-annealed devices. If one of the interfaces is indeed defective, in contrast to the PL measurements, the EL measurements should show differences between the air- and N_2-annealed perovskite cells, when charges build up near the injecting charge transport layers.

In electroluminescence (EL) measurements at different voltages at room temperature and 70 K, again no significant differences can be found in peak shape and position (Figure 4.12). Due to the high sensitivity of the measured intensities to the alignment of the sample inside the cryostat in our setup, we are not able to make a firm conclusion about any differences in intensities that may be related to improvement of interfaces by air-annealing. We did notice, however, that especially at lower temperatures, the current running through the air-annealed samples was significantly lower than for the N_2-annealed samples for similar light intensities. Therefore, electroluminescence external quantum efficiency (EL-EQE) measurements were performed.
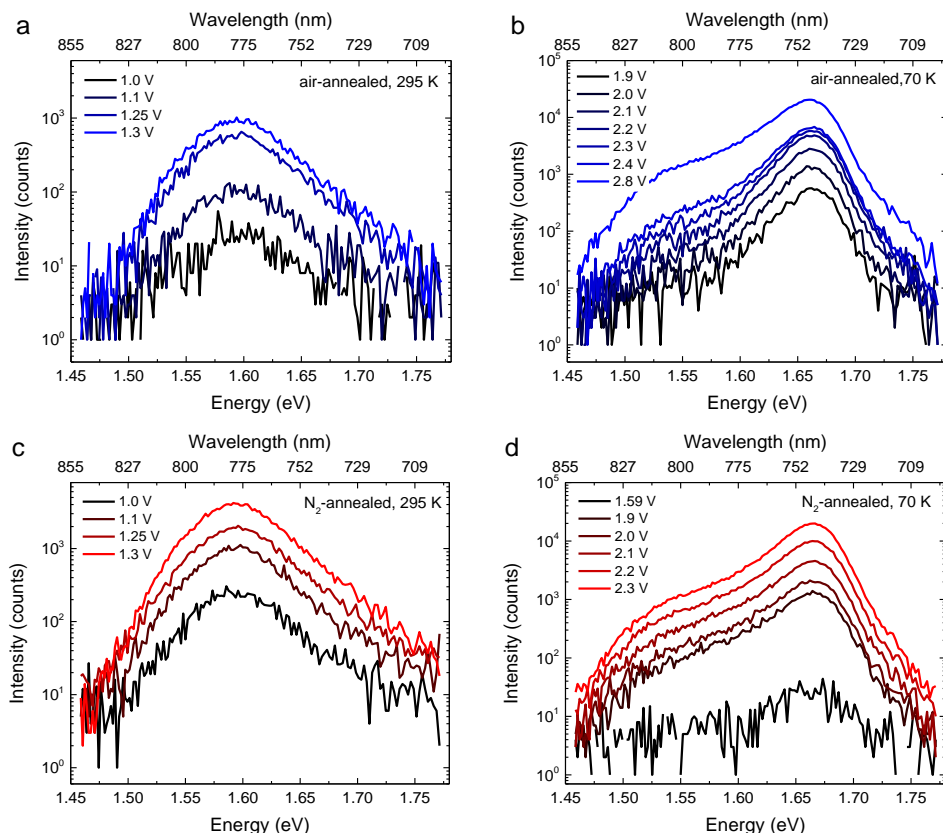
Figure 4.12 Electroluminescence (EL) spectra recorded at 295 K (a, c) and 70 K (b, d) at different voltages for air (a, b) and N_2 (c, d) annealed samples.

These EL-EQE measurements at room temperature show that the EL-EQE of perovskite layers annealed in air is higher than that of perovskite layers annealed in nitrogen (Figure 4.13a), which holds up to high current densities (>100 mA cm^{-2}). It can be seen that the current-voltage characteristics are similar (except for the ~0.1 V shifted onset, see Figure 4.13b) and that between 1.0 and 1.3 V, the light emitted by the air-annealed device is higher than for the N_2-annealed device. Because the current through the perovskite cells is similar for both annealing atmospheres (Fig 4.12b), this indicates that the air-annealed cells show electroluminescence at lower voltages, consistent with less traps that need to be filled before charges can recombine radiatively.

Combining the room- and low-temperature PL and the room temperature EL and V_{OC} vs light intensity results, we conclude that the improvement of the solar cell performance in the air-annealed perovskite layers is not primarily due to a change in the bulk properties of the perovskite layer but rather due to an improvement of the PEDOT:PSS / perovskite interface.
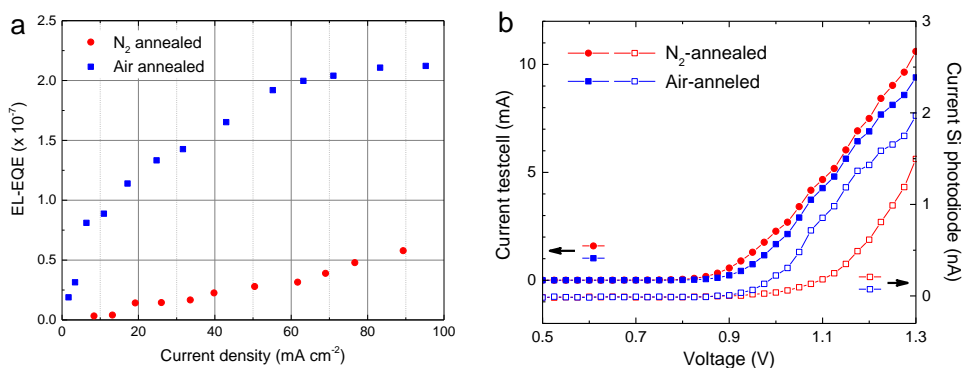
Figure 4.13 (a) EL-EQE measurements of solar cells with perovskite layers annealed in air (blue solid squares) and N_2 (red solid circles). (b) Current-voltage characteristics of the perovskite devices (solid symbols) and the simultaneously recorded photocurrent of a silicon photodiode placed on top during the EL-EQE measurements

4.5 The effect of processing atmosphere on the PEDOT:PSS / perovskite interface

We have shown that oxygen exposure during annealing is required for producing high performance solar cells and that likely the PEDOT:PSS/perovskite interface deteriorates when the perovskite layer is annealed in N_2. It has been reported that PEDOT:PSS can be reduced (electro)chemically by the application of a voltage[57] or by exposure to polyethylenimine (PEI)[58] and methylamine (MA)[59] vapor. In the latter case, the reduced PEDOT:PSS can be re-oxidized by exposure to oxygen.[59] To investigate this effect in more detail, PEDOT:PSS layers were spin coated onto glass slides and perovskite layers were hot cast onto the PEDOT:PSS layers in a N_2 atmosphere both using the same processing parameters as used for solar cell fabrication. The perovskite layers were then annealed, either in ambient air or in N_2 and subsequently the perovskite layers were washed off from the underlying PEDOT:PSS layers using pure DMF. The resulting PEDOT:PSS layers were analyzed and compared to fresh PEDOT:PSS layers using UV-vis-NIR spectroscopy (Figure 4.14). The spectra show that the polaron absorption at 900 nm of the PEDOT:PSS layer that was underneath the N_2-annealed perovskite layer, is higher than that of fresh PEDOT:PSS, and that the bipolaron band at wavelengths $\geq$ 1100 nm is lower in intensity (Figure 4.14a). These are two clear signatures of chemical de-doping of PEDOT.[59] In contrast, the UV-vis-NIR spectrum of the PEDOT:PSS layer that was underneath the air-annealed perovskite layer is very similar to the spectrum of the fresh PEDOT:PSS layer, apart from a narrow peak at 400 nm. The onset and peak position of the 400 nm absorption coincides with the absorbance of orthorhombic lead oxide (PbO)[60] and tri-iodide (I_3^-),[61] both of which could be present in the PEDOT:PSS film after deposition and washing off the perovskite layer. The presence of either of the two could however not be confirmed by XPS measurements.

To confirm that the de-doping of the PEDOT:PSS layer is reversible, the PEDOT:PSS layer that was underneath the N_2-annealed perovskite layer was exposed to air (Figure 4.14b). Air exposure of the de-doped PEDOT:PSS layer up to 180 minutes does indeed re-oxidize the PEDOT, evidenced by a reduced polaron absorption at 900 nm and an increased bipolaron absorption above 1100 nm. Annealing of the reduced PEDOT:PSS layer in air speeds up the re-oxidation reaction and prolonged air exposure almost completely re-oxidizes the PEDOT.
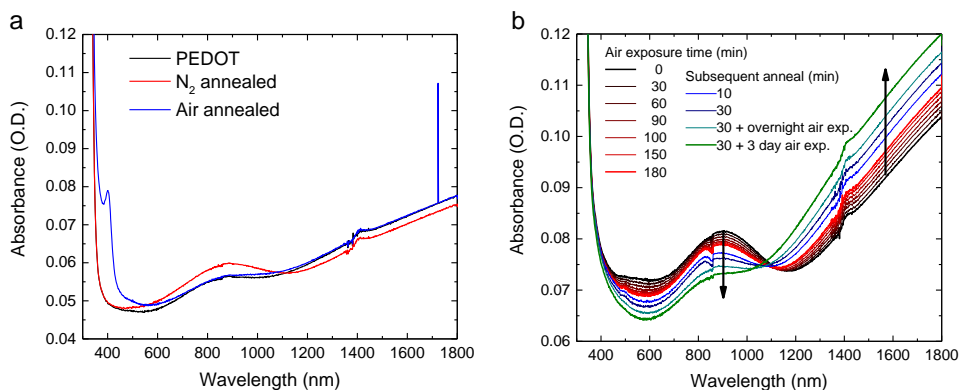
Figure 4.14 (a) UV-vis-NIR spectra of a fresh PEDOT:PSS layer and PEDOT:PSS layers on which perovskite layers were deposited, annealed and washed off again. (b) UV-vis-NIR spectra of the PEDOT:PSS layer that was underneath the N_2-annealed perovskite layer upon air exposure vs time.

Ultraviolet photoelectron spectroscopy (UPS) measurements were performed on air- and N_2-annealed perovskite layers and on the PEDOT:PSS layers that were underneath, after washing off the perovskite, to investigate the effect of the reduction and re-oxidation of the PEDOT:PSS layer on the electronic properties of the materials (Figure 4.15 and Table 4.3). By comparing to UPS results for PEDOT:PSS, and PEDOT:PSS that was treated with DMF (Table 4.3), we see that just casting hot DMF on top of PEDOT:PSS already reduces both the work function (WF, Fermi energy) and ionization potential (IP, valence band energy) of a PEDOT:PSS layer. By subsequent washing with DMF at room temperature, a further decrease can be seen. The striking result is that with spin coating the perovskite precursor on PEDOT:PSS, annealing and washing off of the perovskite layer from the PEDOT:PSS layer, the WF is equal to the IP. The other important observation is that the WF and IP of the PEDOT:PSS layer that was underneath a N_2-annealed perovskite film is lower compared to the PEDOT:PSS layer that was underneath an air-annealed perovskite layer. Looking at the results of the perovskite layers deposited on PEDOT:PSS, we see a similar difference with the N_2 annealed perovskite layer showing a lower WF than the air annealed one, while the IP of the two perovskite layers remains equal. This suggests that the WF of the perovskite layer is influenced by that of the PEDOT:PSS beneath it. It is worth to note that the difference between the WF of the PEDOT:PSS layer and that of the perovskite layer is similar (~0.5 eV) for both annealing atmospheres. The difference in the value of the WF of the perovskite layers results in a difference in the built-in voltage of the solar cells, allowing the V_{OC} of the air-annealed perovskite layer to exceed that of the

N_2-annealed cell. The difference in WF (~0.12 eV) is comparable to the difference in V_{OC} we measure in *J-V* sweeps (~0.07 V). The measured WFs and IPs for fresh PEDOT:PSS and the prepared perovskite layers are similar to previously reported values.[62,63]
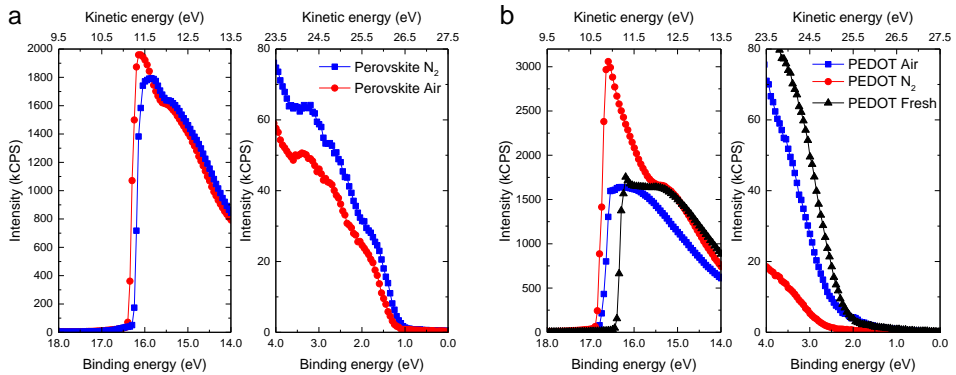
Figure 4.15 UPS results of measurements on the top of a perovskite layer deposited onto PEDOT:PSS and annealed in air or nitrogen (a) and a fresh PEDOT:PSS layer and PEDOT:PSS layers that had a N_2 or air annealed perovskite layer on top of them that has been washed off (b).

Table 4.3 UPS result summary of PEDOT:PSS and perovskite layers under different processing conditions.

Layer and processing	Work-function (eV)	Ionization potential (eV)
PEDOT:PSS	4.83	5.06
PEDOT:PSS | clean DMF hot cast	4.48	4.83
PEDOT:PSS | clean DMF hot cast | DMF wash	4.40	4.65
PEDOT:PSS | perovskite hot cast | anneal in N_2 | DMF wash	4.36	4.38
PEDOT:PSS | perovskite hot cast | anneal in air | DMF wash	4.48	4.47
PEDOT:PSS | perovskite hot cast | anneal in N_2	4.84	6.10

4.6 Conclusions

In this chapter we have shown that spin coating a perovskite precursor in DMF solution chemically reduces the oxidation state of the PEDOT:PSS hole transport layer on which it is deposited. The partial reduction of PEDOT:PSS from the highly oxidized bipolaron state to the polaron state, reduces the work function of the PEDOT:PSS whereby the work function becomes equal to the ionization potential. The reduction in the work function of the PEDOT:PSS also reduces the work function of the perovskite layer that is positioned on top of it. Exposure of the reduced PEDOT:PSS to

oxygen re-oxidizes the PEDOT:PSS. Even relatively short exposure (8 minutes) of the PEDOT:PSS layer during the annealing of the perovskite layer that is on top of it (partially) restores the oxidation state of the PEDOT and restores its functionality in the solar cell. The bulk properties of the perovskite layer do not seem to change by annealing in different atmospheres. Annealing the perovskite layers in an inert atmosphere therefore produces solar cells of inferior performance, displaying lower V_{OC} and a J_{SC} that is sublinear with light intensity compared to air-annealed devices.

4.7 Experimental

Device fabrication

Indium-tin oxide (ITO) coated and pre-patterned glass substrates (Naranjo substrates) were cleaned by sonication in acetone (Sigma Aldrich), scrubbing in a solution of sodium dodecyl sulfate (SDS, Acros, 99%) in filtered water (Milli-Q), rinsing in deionized water, sonication in 2-propanol (Sigma Aldrich) and 30 minutes of UV-ozone treatment right before use. Poly(3,4-ethylenedioxythiophene): polystyrene sulfonate (PEDOT:PSS, Heraeus Clevios PVP Al 4083) was filtered using a 0.45 µm PVDF filter and spin coated (60 s, 3000 RPM) onto the cleaned substrates.

For the hot casting method, the PEDOT:PSS coated substrate was heated for 1 minute at 100 °C right before use, for the cold casting method, the PEDOT:PSS coated substrates were dried at 140 °C for 15 minutes. For the electron transport layer, PCBM (Solenne BV, 99%) was dissolved in a 1:1 (v/v) mixture of chloroform (Biosolve, AR grade) and chlorobenzene (Sigma Aldrich, anhydrous 99.8%) at 20 mg mL^{-1}. The perovskite precursor solution for use with the hot casting method was prepared by weighing 476.9 mg of methylammonium iodide (Dyesol), 303.5 mg of lead(II) acetate trihydrate (Sigma Aldrich, 99.999% trace metal basis) and 55.6 mg of lead(II) chloride (Sigma Aldrich, 98%) in air and adding 1 mL of *N,N*-dimethylformamide (Sigma Aldrich, anhydrous, 99.8%). The mixture was stirred for 30 minutes at room temperature to completely dissolve all compounds and stirred at 70 °C for 30 minutes before use. The solution was then spin coated onto pre-heated (100 °C) PEDOT:PSS-covered substrates (60 µL, 20 s, 5700 RPM, dynamic) using a specially designed spin coating chuck that minimizes contact between the substrate and the chuck to avoid rapid cooling of the substrate. The perovskite layer was then annealed immediately (100 °C, 8 minutes) and after 1 minute of cooling, coated with PCBM (Solenne BV, 99%) (30 s, 1000 RPM). The device was then transferred into a glovebox, the contact

area was cleaned and LiF (1 nm) and Al (100 nm) were thermally evaporated under high vacuum (±3 × 10⁻⁷ mbar) as a back electrode.

The perovskite precursor solution for use with the cold casting method was made by weighing 858.4 mg of methylammonium iodide (Dyesol), 546.3 mg of lead(II) acetate trihydrate (Sigma Aldrich, 99.999% trace metal basis) and 100.1 mg of lead(II) chloride (Sigma Aldrich, 98%) and adding 1 mL of *N,N*-dimethylformamide (Sigma Aldrich, anhydrous, 99.8%). The mixture was stirred for 30 minutes at room temperature to completely dissolve all the compounds. The solution was then spin coated onto the cleaned, PEDOT:PSS-coated and dried substrates (60 μL, 120 s, 5700 RPM) using the same specially designed spin coating chuck. The perovskite layer was then annealed immediately (100 °C, 15 minutes) and coated with PCBM (Solenne BV, 99%) (30 s, 500 RPM). The device contact area was cleaned and LiF (1 nm) and Al (100 nm) were thermally evaporated under high vacuum (±3 × 10⁻⁷ mbar) as a back electrode.

To accurately control the temperature of the hotplate surfaces of different hotplates, aluminum slabs were used to achieve a homogeneous surface temperature and a surface temperature probe (Testo 0560 1109 mini surface thermometer) was used to measure the temperature. The mentioned temperatures are the temperatures set on the hotplate thermocouple. A set temperature of 100 °C corresponds to a temperature of 94 °C at the top of the aluminum slab measured with the surface probe.

Measurement methods

Layer thicknesses were measured using a Veeco Dektak 150 profilometer.

J–*V* characteristics were measured in a nitrogen environment with a Keithley 2400 source meter under ±100 mW cm⁻² white light illumination from a tungsten-halogen lamp filtered by a Schott GG385 UV filter and a Hoya LB120 daylight filter. The cells were masked with a 0.0676 cm² or 0.1296 cm² aperture (the physical overlap of the contacts is 0.09 cm² and 0.16 cm² respectively). The stabilized *J-V* measurement protocol used was defined by light soaking at V_{OC} for 5 minutes, followed by a downward sweep (V_{OC} + 0.04 V → −0.04 V) with a step size of 0.02 V. At each voltage the current density was recorded for 10 s and the final value was used for plotting the *J*–*V* curve. Fast upwards and downwards *J*–*V* sweeps were performed before and after the slow sweep measurement between −0.5 and 1.5 V with a scan speed of 0.25 V s⁻¹.

Short-circuit current densities under AM 1.5G conditions were determined by integrating the spectral response with the solar spectrum. Spectral response

measurements were conducted under only probe light and 1-sun equivalent operating conditions by using a 530 nm high power LED (Thorlabs M530L3 driven by a DC4104 driver) for bias illumination. The device was kept in a nitrogen filled box behind a quartz window and a circular aperture with a 1 mm radius and irradiated with modulated monochromatic light, from a 50 W tungsten-halogen lamp (Philips focusline) and monochromator (Oriel, Cornerstone 130) with the use of a mechanical chopper (160 Hz). The response was recorded as a voltage from a preamplifier (SR570) using a lock-in amplifier (SR830). A calibrated silicon cell was used as reference (calibrated at the Energy Research Centre of the Netherlands).

J_{SC} and V_{OC} vs light intensity measurements were performed using a Keithley 2400 source meter and 405 and 730 nm high power LEDs (Thorlabs M405L3 and M730L4 driven by a DC4104 driver) for illumination.

Scanning electron microscopy (SEM) was performed on a FEI Quanta 3D FEG.

X-Ray Diffraction measurements were performed on a Bruker 2D Phaser using Cu Kα radiation with a wavelength of 0.15406 nm between 2θ angles of 10 to 60° using increments of 0.05° and a 2 second integration time. A 0.6 mm slit was used at the X-Ray source and a shield was positioned 0.5 mm above the sample surface. The sample rotated at a speed of 60 RPM during the measurement.

Low intensity photoluminescence measurements were performed using an Edinburgh Instruments FLSP920 double-monochromator luminescence spectrometer equipped with a multialkali photomultiplier tube and a nitrogen-cooled near IR sensitive photomultiplier (Hamamatsu). The substrate was positioned inside an Oxford Optistat cryostat under a dynamic vacuum. Cryogenic temperatures were achieved by indirectly cooling the substrate. The photoluminescence spectrometer has an internal uncalibrated photodetector to monitor the intensity of excitation beam of which the output is in counts per second. We have used a calibrated Si solar cell to calibrate the reference detector. The light from a Xenon light source is monochromated to specific wavelengths for the PL measurements.

High intensity photoluminescence measurements were performed using a 532 nm laser (B&W tek inc. BWN-532-20E/56486) excitation that was chopped using a mechanical chopper (277 Hz). The sample was located in an Oxford Optistat cryostat under dynamic vacuum. The signal was measured using a monochromator (Oriel 77700 at 775 nm) and a Si diode linked to a lock-in amplifier (SR830DSP). The

illumination intensity was varied using a double optical density filter wheel (New Focus 5215) and was calibrated at different OD settings using a Si photodiode. The

illumination area of the laser beam was determined at different optical densities using a Gentec Beamage 3.0 beam diagnostic tool ($1/e^2$ value was used).

Electroluminescence measurements were performed in a nitrogen environment using a reference Si cell and two Keithley 2400 source meters to control the voltage and record the current flowing through the test cell and record the current flow out of the Si reference cell. Dividing the two current flows results in a crude electroluminescence external quantum efficiency value that is not absolute but can be used to compare samples measured in the same setup.

UPS measurements were performed in a multi-chamber ESCALAB II system using 6 V bias and the HeI line at 21.22 eV. The Fermi level reference was established on an in situ sputter-cleaned Au film. The ionization potential and the work function are derived from the energy difference between the secondary electron edge and, respectively, the valence band edge or the position of the Fermi energy. Samples were transferred from gloveboxes to the measurement equipment completely in an N_2 atmosphere to avoid any effects of oxygen exposure.

4.8 References

1   A. Kojima, K. Teshima, Y. Shirai and T. Miyasaka, *J. Am. Chem. Soc.*, 2009, **131**, 6050–6051.

2   H.-S. Kim, C.-R. Lee, J.-H. Im, K.-B. Lee, T. Moehl, A. Marchioro, S.-J. Moon, R. Humphry-Baker, J.-H. Yum, J. E. Moser, M. Grätzel and N.-G. Park, *Sci. Rep.*, 2012, **2**, 591.

3   M. M. Lee, J. Teuscher, T. Miyasaka, T. N. Murakami and H. J. Snaith, *Science*, 2012, **338**, 643–648.

4   M. Saliba, T. Matsui, J.-Y. Seo, K. Domanski, J.-P. Correa-Baena, M. K. Nazeeruddin, S. M. Zakeeruddin, W. Tress, A. Abate, A. Hagfeldt and M. Grätzel, *Energy Environ. Sci.*, 2016, **9**, 1989–1997.

5   W. S. Yang, B.-W. Park, E. H. Jung, N. J. Jeon, Y. C. Kim, D. U. Lee, S. S. Shin, J. Seo, E. K. Kim, J. H. Noh and S. Il Seok, *Science.*, 2017, **356**, 1376–1379.

6   V. D'Innocenzo, G. Grancini, M. J. P. Alcocer, A. R. S. Kandada, S. D. Stranks, M. M. Lee, G. Lanzani, H. J. Snaith and A. Petrozza, *Nat. Commun.*, 2014, **5**, 3586.

7   L. M. Pazos-Outón, M. Szumilo, R. Lamboll, J. M. Richter, M. Crespo-Quesada, M. Abdi-Jalebi, H. J. Beeson, M. Vrućinić, M. Alsari, H. J. Snaith, B. Ehrler, R. H. Friend and F. Deschler1, *Science.*, 2016, **351**, 1430-1433.

8   C.-S. Jiang, M. Yang, Y. Zhou, B. To, S. U. Nanayakkara, J. M. Luther, W. Zhou, J. J. Berry, J. Van De Lagemaat, N. P. Padture, K. Zhu and M. M. Al-jassim, *Nat. Commun.*, 2015, **6**, 8397.

9   C. Wehrenfennig, G. E. Eperon, M. B. Johnston, H. J. Snaith and L. M. Herz, *Adv. Mater.*, 2014, **26**, 1584–1589.

10   T. M. Schmidt, T. T. Larsen-Olsen, J. E. Carlé, D. Angmo and F. C. Krebs, *Adv. Energy Mater.*, 2015, **5**, 1500569

11   K. Hwang, Y.-S. Jung, Y.-J. Heo, F. H. Scholes, S. E. Watkins, J. Subbiah, D. J. Jones, D.-Y. Kim and D. Vak, *Adv. Mater.*, 2015, **27**, 1241–1247.

12   Y. Galagan, E. W. C. Coenen, W. J. H. Verhees and R. Andriessen, *J. Mater. Chem. A*, 2016, **4**, 5700–5705.

13   G. E. Eperon, S. D. Stranks, C. Menelaou, M. B. Johnston, L. M. Herz and H. J. Snaith, *Energy Environ. Sci.*, 2014, **7**, 982-988.

14   G. E. Eperon, G. M. Paternò, R. J. Sutton, A. Zampetti, A. A. Haghighirad, F. Cacialli and H. J. Snaith, *J. Mater. Chem. A.*, 2015, **3**, 19688–19695.

15   W. Liao, D. Zhao, Y. Yu, N. Shrestha, K. Ghimire, C. R. Grice, C. Wang, Y. Xiao, A. J. Cimaroli, R. J. Ellingson, N. J. Podraza, K. Zhu, R. G. Xiong and Y. Yan, *J. Am. Chem. Soc.*, 2016, **138**, 12360–12363.

16   J. H. Heo, D. H. Song, H. J. Han, S. Y. Kim, J. H. Kim, D. Kim, H. W. Shin, T. K. Ahn, C. Wolf, T. W. Lee and S. H. Im, *Adv. Mater.*, 2015, **27**, 3424–3430.

17   C.-C. Chueh, C.-Y Liao, F. Zuo, S. T. Williams, P.-W. Liang and A. K.-Y. Jen, *J. Mater. Chem. A*, 2015, **3**, 9058–9062.

18   W. Zhang, M. Saliba, D. T. Moore, S. K. Pathak, M. T. Hörantner, T. Stergiopoulos, S. D. Stranks, G. E. Eperon, J. A. Alexander-Webber, A. Abate, A. Sadhanala, S. Yao, Y. Chen, R. H. Friend, L. A. Estroff, U. Wiesner and H. J. Snaith, *Nat Commun*, 2015, **6**, 6142.

19   K. L. Gardner, J. G. Tait, T. Merckx, W. Qiu, U. W. Paetzold, L. Kootstra, M. Jaysankar, R. Gehlhaar, D. Cheyns, P. Heremans and J. Poortmans, *Adv. Energy Mater.*, 2016, **6**, 1600386.

20   K. H. Hendriks, J. J. van Franeker, B. J. Bruijnaers, J. A. Anta, M. M. Wienk and R. A. J. Janssen, *J. Mater. Chem. A.*, 2017, **5**, 2346.

21   S. Bae, S. J. Han, T. J. Shin and W. H. Jo, *J. Mater. Chem. A*, 2015, **3**, 23964–23972.

22   N. Ahn, D.-Y. Son, I.-H. Jang, S. M. Kang, M. Choi and N.-G. Park, *J. Am. Chem. Soc.*, 2015, **137**, 8696–8699.

23   N. K. Noel, S. N. Habisreutinger, B. Wenger, M. T. Klug, M. T. Hörantner, M. B. Johnston, R. J. Nicholas, D. T. Moore and H. J. Snaith, *Energy Environ. Sci.*, 2017, **10**, 145-152.

24   F. K. Aldibaja, L. Badia, E. Mas-Marzá, R. S. Sánchez, E. M. Barea and I. Mora-Sero, *J. Mater. Chem. A*, 2015, **3**, 9194–9200.

25   G. Li, T. Zhang and Y. Zhao, *J. Mater. Chem. A.*, 2015, **3**, 19674–19678.

26   W. Qiu, T. Merckx, M. Jaysankar, C. Masse de la Huerta, L. Rakocevic, W. Zhang, U. W. Paetzold, R. Gehlhaar, L. Froyen, J. Poortmans, D. Cheyns, H. J. Snaith and P. Heremans, *Energy Environ. Sci.*, 2016, **9**, 484-489.

27   J. Qing, H.-T. Chandran, Y.-H. Cheng, X.-K. Liu, H.-W. Li, S.-W. Tsang, M.-F. Lo and C.-S. Lee, *ACS Appl. Mater. Interfaces*, 2015, **7**, 23110–23116.

28   Z. Zhang, D. Wei, B. Xie, X. Yue, M. Li, D. Song and Y. Li, *Sol. Energy*, 2015, **122**, 97–103.

29   B. Conings, A. Babayigit, M. T. Klug, S. Bai, N. Gauquelin, N. Sakai, J. T.-W. Wang, J. Verbeeck, H.-G. Boyen and H. J. Snaith, *Adv. Mater.*, 2016, **28**, 10701–10709.

30   N. J. Jeon, J. H. Noh, Y. C. Kim, W. S. Yang, S. Ryu and S. Il Seok, *Nat. Mater.*, 2014, **13**, 897–903.

31   J. Xiong, B. Yang, R. Wu, C. Caoa, Y. Huanga, C. Liu, Z. Hu, H. Huang, Y. Gao and J. Yang, *Org. Electron.*, 2015, **24**, 106–112.

32   M. Liu, M. B. Johnston and H. J. Snaith, *Nature*, 2013, **501**, 395–398.

33   L. K. Ono, M. R. Leyden, S. Wang and Y. Qi, *J. Mater. Chem. A*, 2016, **4**, 6693–6713.

34   Q. Chen, H. Zhou, Z. Hong, S. Luo, H.-S. Duan, H.-H. Wang, Y. Liu, G. Li and Y. Yang, *J. Am. Chem. Soc.*, 2014, **136**, 622–625.

35   C. Wehrenfennig, M. Liu, H. J. Snaith, M. B. Johnston and L. M. Herz, *Energy Environ. Sci.*, 2014, **7**, 2269.

36   M. M. Tavakoli, L. Gu, Y. Gao, C. Reckmeier, J. He, A. L. Rogach, Y. Yao and Z. Fan, *Sci. Rep.*, 2015, **5**, 14083.

37   M. Saliba, K. W. Tan, H. Sai, D. T. Moore, T. Scott, W. Zhang, L. A. Estro, U. Wiesner and H. J. Snaith, *J. Phys. Chem. C*, 2014, **118**, 17171–17177.

38   Y. Chen, Y. Zhao and Z. Liang, *Chem. Mater.*, 2015, **27**, 1448–1451.

39   S. R. Raga, M.-C. Jung, M. V. Lee, M. R. Leyden, Y. Kato and Y. Qi, *Chem. Mater.*, 2015, **27**, 1597–1603.

40   A. Dualeh, N. Tétreault, T. Moehl, P. Gao, M. K. Nazeeruddin and M. Grätzel, *Adv. Funct. Mater.*, 2014, **24**, 3250–3258.

41   Z. Xiao, Q. Dong, C. Bi, Y. Shao, Y. Yuan and J. Huang, *Adv. Mater.*, 2014, **26**, 6503–6509.

42   J. J. van Franeker, K. H. Hendriks, B. J. Bruijnaers, M. W. G. M. Verhoeven, M. M. Wienk and R. A. J. Janssen, *Adv. Energy Mater.*, 2017, **7**, 1601822.

43   G. E. Eperon, S. N. Habisreutinger, T. Leijtens, B. J. Bruijnaers, J. J. van Franeker, D. W. deQuilettes, S. Pathak, R. J. Sutton, G. Grancini, D. S. Ginger, R. A. J. Janssen, A. Petrozza, and H. J. Snaith, 2015, **9**, 9380–9393.

44   C.-G. Wu, C.-H. Chiang, Z.-L. Tseng, M. K. Nazeeruddin, A. Hagfeldt and M. Grätzel, *Energy Environ. Sci.*, 2015, **8**, 2725–2733.

45   S. Pathak, A. Sepe, A. Sadhanala, F. Deschler, A. Haghighirad, N. Sakai, K. C. Goedel, S. D. Stranks, N. Noel, M. Price, S. Hüttner, N. A. Hawkins, R. H. Friend, U. Steiner and H. J. Snaith, *ACS Nano*, 2015, **9**, 2311–2320.

46   L. J. A. Koster, V. D. Mihailetchi, R. Ramaker and P. W. M. Blom, *Appl. Phys. Lett.*, 2005, **86**, 1–3.

47   S. R. Cowan, A. Roy and A. J. Heeger, *Phys. Rev. B*, 2010, **82**, 245207.

48   K. Tvingstedt, L. Gil-Escrig, C. Momblona, P. Rieder, D. Kiermasch, M. Sessolo, A. Baumann, H. J. Bolink and V. Dyakonov, *ACS Energy Lett.*, 2017, **2**, 424–430.

49   K. Tvingstedt and C. Deibel, *Adv. Energy Mater.*, 2016, **6**, 1502230.

50   O. Malinkiewicz, A. Yella, Y. H. Lee, G. M. Espallargas, M. Graetzel, M. K. Nazeeruddin and H. J. Bolink, *Nat. Photonics*, 2014, **8**, 128–132.

51   O. Bubnova, Z. U. Khan, H. Wang, S. Braun, D. R. Evans, M. Fabretto, P. Hojati-Talemi, D. Dagnelund, J.-B. Arlin, Y. H. Geerts, S. Desbief, D. W. Breiby, J. W. Andreasen, R. Lazzaroni, W. M. Chen, I. Zozoulenko, M. Fahlman, P. J. Murphy, M. Berggren and X. Crispin, *Nat. Mater.*, 2013, **13**, 190–194.

52   H.-H. Fang, R. Raissa, M. Abdu-Aguye, S. Adjokatse, G. R. Blake, J. Even and M. A. Loi, *Adv. Funct. Mater.*, 2015, **25**, 2378–2385.

53   T. Schmidt and K. Lischka, *Phys. Rev. B*, 1992, **45**, 8989–8994.

54   H. A. Klasens, *J. Phys. Chem. Solids*, 1958, **7**, 175–200.

55   X. Wen, Y. Feng, S. Huang, F. Huang, Y.-B. Cheng, M. Green and A. Ho-Baillie, *J. Mater. Chem. C*, 2016, **4**, 793–800.

56   X. Wu, M. T. Trinh, D. Niesner, H. Zhu, Z. Norman, J. S. Owen, O. Yaffe, B. J. Kudisch and X.-Y. Zhu, *J. Am. Chem. Soc.*, 2015, **137**, 2089–2096.

57   P. M. Beaujuge and J. R. Reynolds, *Chem. Rev.*, 2010, **110**, 268–320.

58   S. Fabiano, S. Braun, X. Liu, E. Weverberghs, P. Gerbaux, M. Fahlman, M. Berggren and X. Crispin, *Adv. Mater.*, 2014, **26**, 6000–6006.

59   T. Liu, F. Jiang, J. Tong, F. Qin, W. Meng, Y. Jiang, Z. Li and Y. Zhou, *J. Mater. Chem. A*, 2016, **4**, 4305–4311.

60   R. C. Keezer, D. L. Bowman and J. H. Becker, *J. Appl. Phys.*, 1968, **39**, 2062–2066.

61   N. Li, L. Shi, X. Wang, F. Guo and C. Yan, *Int. J. Anal. Chem.*, 2011, 130102.

62   P. Schulz, E. Edri, S. Kirmayer, G. Hodes, D. Cahen and A. Kahn, *Energy Environ. Sci.*, 2014, **7**, 1377.

63   S. Olthof and K. Meerholz, *Sci. Rep.*, 2017, **7**, 40267.

Chapter 5

Vapor assisted solution processing of lead halide perovskite solar cells

Abstract

In this chapter we explore the conversion of solution deposited metal halide layers to perovskite by exposing them to the organic material in the vapor phase. At first, this is done using a commercial thermal gradient sublimer tube oven that is heated at one end and cooled at the other, which shows that it is possible to convert solution-processed lead(II) iodide (PbI_2) layers with gas-phase methylammonium iodide (MAI) to perovskite. The temperature at the position of both the organic material and the pre-deposited PbI_2 layers, the deposition time, and the physical transport distance of the organic vapor are identified as the most important parameters in the deposition process. With this knowledge, a dedicated reactor for vapor assisted solution processing (VASP) is designed and built and with this reactor the influence of several parameters on the deposition profile of the MAI is investigated and optimized using deposition on top of cleaned glass slides. Subsequently, PbI_2 covered glass substrates were used and converted into perovskite. This requires some re-optimization since it is found that substantial MAI deposition is undesirable and a fair balance between the physical deposition and the conversion reaction is more important. The production of solar cells using this reactor follows next, which shows that next to the critical parameters that are identified using the thermal sublimer, the flow rate of the carrier gas (N_2) is vital for optimal conversion of the PbI_2 layers into perovskite. Optimized solar cell efficiencies close to 12% were achieved using this production method.

5.1 Introduction

Currently, the vast majority of perovskite solar cells are being produced using solution deposition methods. Using solution deposition, already significant progress has been made towards large scale production. The explored large scale deposition techniques range from blade coating, roll-to-roll processing and slot dye coating, to covered deposition.[1–7] In an attempt to gain more control over the layer morphology, several sequential deposition techniques have been applied where the precursor components are deposited sequentially instead of using a "one pot" precursor mixture. In sequential processing, the metal halide (usually lead(II) iodide, PbI_2) is deposited first, after which it is exposed to the organic material (often methylammonium iodide, MAI). The potential advantage of this method is that it separates the crystallization process of the metal halide from the conversion process to perovskite. The deposition of the metal halide is usually done from solution and the exposure to the organic component can be done with various methods. Solution processing of the organic compound on top of the finished metal halide layer, the dipping of the metal halide layer into a solution containing the organic compound or exposure of the metal halide layer to the organic material in the gas phase are commonly used techniques.[8–30] Optimization of the metal halide layer to improve intercalation of the organic compound is commonly done by using different solvents and post deposition annealing techniques.[17–21,27–35] To optimize the completed perovskite layer, various annealing techniques have been implemented.[36–46] Perovskite layers produced completely from the vapor phase have also been explored.[8,47–50]

Here we explore the conversion of solution deposited metal halide (PbI_2) layers to perovskite by exposing them to the organic material (MAI) in the vapor phase. We identify the most critical parameters during the deposition and optimize the perovskite layers for use in solar cells. A dedicated vapor assisted solution processing (VASP) reactor is built and after optimization, a maximum solar cell efficiency of close to 12% is reached.

5.2 Exploring VASP with thermal gradient sublimer

After experimenting with sequential solution processing, it was found that the main issue for producing high quality and dense perovskite layers is the incomplete conversion of PbI_2 into perovskite. Due to the lack of surface area in the compact PbI_2 layers used for planar *p-i-n* perovskite solar cells, complete conversion generally takes too long. In the case of sequential spin coating, the exposure time of the PbI_2 to the MAI solution is not sufficient, even with the use of loading time in which the MAI solution is left on top of the PbI_2 layer for a certain amount of time before spinning is initiated. This results in only partial conversion of thick PbI_2 layers (>150 nm) or complete conversion of PbI_2 layers that are too thin to absorb sufficient light. By using the sequential dipping method, the exposure time can be increased, however, long dipping times generally lead to (partial) dissolution of the PEDOT:PSS/perovskite stack in the MAI solution. When porous PbI_2 layers are produced by adding additives (*e.g.* 4-*tert*-butylpyridine (TBP)) to the PbI_2 solution that is spin coated, the PbI_2 surface area and with that the conversion speed can be increased. Although the perovskite layer thickness can be sufficient using the dipping method, residual MAI crystallites always appear on top of the perovskite layer, which cannot be washed off completely and reduce the solar cell performance. Since it was not possible to produce high performance solar cells using the sequential solution processing methods, the idea arose to introduce the MAI to the PbI_2 from the vapor phase.[11] To test the feasibility of this method, a thermal gradient sublimer (which is typically used for the purification of low molecular weight materials and the growing of large crystals) was used. A schematic diagram of the used apparatus is displayed in Figure 5.1.
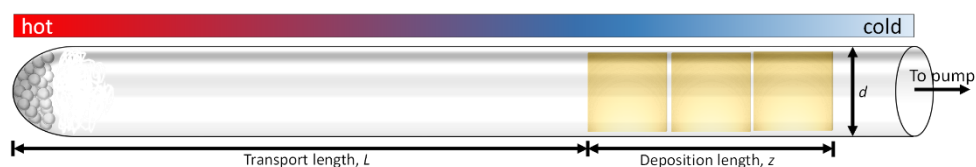
Figure 5.1 Schematic depiction of the evaporation process in the thermal gradient sublimer.

It consists of a glass tube that is under dynamic vacuum (~0.5 mbar). The tube is placed inside the thermal gradient oven and is heated at one end and cooled over its total length by a counter flow of cooling water. This creates a temperature gradient over the length of the tube which can be influenced by the heating temperature and the cooling water flow rate. Inside the glass tube, the MAI is placed at the heated end behind some glass fiber wadding and PbI_2 covered substrates are positioned along the colder part of the tube. At the hot part of the tube, the MAI evaporates and diffuses down the tube towards the PbI_2 covered substrates. The evaporation rate of MAI depends on the chamber pressure (P_h) and the temperature of the tube at the location of the MAI according to equation 5.1.[51, 52]

$$\Gamma = 5.834 \times 10^{-2} \sqrt{\frac{M}{T_c}} (P_e - P_h) \qquad 5.1$$

Where Γ is the mass evaporation rate of MAI in g cm^{-2} s^{-1}, M is the molecular weight of MAI, T_c is the temperature of the evaporation source (crucible), P_e is the vapor pressure of MAI (equilibrium pressure in Torr) at temperature T_c, and P_h is the pressure inside the chamber (hydrostatic pressure in Torr). At a set chamber pressure (P_h), the evaporation rate is therefore governed by the source temperature which determines P_e. The evaporated MAI subsequently diffuses through the chamber. The diffusion constant of a dilute gas is given by equation 5.2.[53]

$$D_g \propto \frac{T^{3/2}}{P} \qquad 5.2$$

In which D_g is the gas phase diffusion constant, T is the absolute temperature and P is the pressure. At a certain point in the tube, the lower temperature causes the MAI vapor to deposit onto the substrates placed there and the wall of the tube. When the deposition occurs onto the PbI_2 covered substrates and the conditions are right, MAI can intercalate into the PbI_2 layer and the PbI_2 can be converted to perovskite, evidenced by the gradual color change from yellow to dark brown. In this process, the temperature dependent solid diffusion coefficient can often be described by equation 5.3.[53]

$$D_s = D_0 \exp\left[-\frac{Q}{kT}\right] \qquad 5.3$$

Where D_s is the gas diffusion constant, D_0 the pre-exponential (frequency) factor, Q is an activation energy, and k is Boltzmann's constant. The reaction mechanism to form perovskite ($CH_3NH_3PbI_3$) from the PbI_2 and MAI (CH_3NH_3I) precursors is given by equation 5.4. The reaction rate of perovskite formation (v) is dependent on the concentration of both precursors ($[CH_3NH_3I]$ and $[PbI_2]$) and is given by equation 5.5 with n and m being the partial orders of the reaction (not necessarily equal to the stoichiometric coefficients of the reaction). The temperature dependent rate constant κ is given by the Arrhenius equation 5.6 with A a constant and E_a the activation energy.

$$PbI_{2\,(s)} + CH_3NH_3I_{(g)} \rightleftarrows CH_3NH_3PbI_{3\,(s)} \qquad 5.4$$
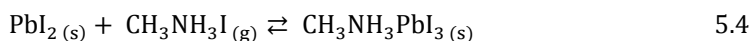
$$v = \kappa\,[CH_3NH_3I]^n\,[PbI_2]^m \qquad 5.5$$

$$\kappa = A \exp\left[\frac{-E_a}{kT}\right] \qquad 5.6$$

When the pre-deposited PbI_2 crystals are converted into perovskite crystals by the intercalation of MAI, the crystallites undergo an expansion. The density and unit cell volume of trigonal PbI_2 have been reported to be 6.16 g cm^{-3} and 125.7 Å^3 respectively while those of the tetragonal methylammonium lead triiodide (MAPbI$_3$) are 4.22 g cm^{-3} and 249.5 Å^3.[55] Therefore, the theoretically calculated volume expansion factor (δ) should be ~2.0. When assuming no expansion in the plane due to the compact nature of the PbI_2 layer, the increase in the thickness of the PbI_2 layer upon conversion can also be expected to be a factor ~2.0.

In the initial experiments with the thermal gradient sublimer, the temperature of the heater of the tube was varied to find a suitable temperature for the evaporation of MAI and deposition onto the ~140 nm thick PbI_2 covered substrates. Here it was found that with a too high temperature of the heater (~160 to ~180 °C) the deposition of MAI on top of the PbI_2 coated substrates is too harsh. Creating MAI crystallites on top of the PbI_2 layer with hardly any conversion of the PbI_2 layer to perovskite resulting in non-functional solar cells (Figure 5.2). At these heater temperatures, the temperature of the tube at the location of the samples is ~110 °C.
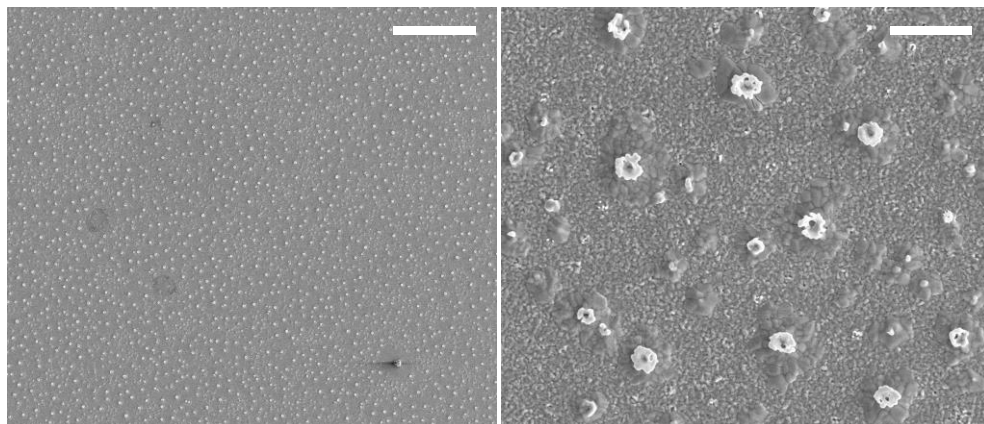
Figure 5.2 Top view SEM images of perovskite films with excess MAI crystallites deposited on top of the PbI$_2$ layer. Samples were fabricated with the thermal gradient sublimer at a heater temperature of 180 °C and a deposition time of 20 minutes. Scale bars are 50 µm (left) and 5 µm (right)

Lowering the heater temperature to ∼140 °C reduces the MAI deposition rate sufficiently to produce reasonable perovskite layers. Using this heater temperature, the tube at the position of the 3rd sample is ∼90 °C. In Figure 5.3 an example of the samples before and after the deposition of MAI is displayed. From this example it is seen that the samples that are closest to the MAI during the deposition are converted to perovskite first. However, an excess of MAI is deposited on top of these samples upon prolonged deposition. The samples farthest from the crucible remain almost completely unconverted, because the MAI vapor does reach the far end of the tube sufficiently as can been seen from the absence of the white MAI crystals deposited on the inside of the glass tube. The result is that only one or two of the PbI$_2$ layers are converted sufficiently to perovskite without having excess MAI on top of them and only these few produced perovskite layers perform well in a solar cell.

Porous PbI$_2$ layers (∼140 nm) were produced by adding TBP to the PbI$_2$ solution (120 or 240 µl TBP mL^{-1} DMF) (Figure 5.4) and it was found that the easier intercalation of MAI into the more porous PbI$_2$ layer results in a larger number of substrates that are converted sufficiently while not having excess MAI on top of the perovskite layer (Figure 5.5). However still, only one or two of the perovskite layers perform well in a solar cell. In Tables 5.1 and 5.2 the highest achieved efficiencies using both the compact and porous PbI$_2$ layers after optimization of the complete evaporation process (deposition time and temperature, post deposition annealing, and PbI$_2$ layer thickness) are displayed, where substrate #1 is closest to the MAI.
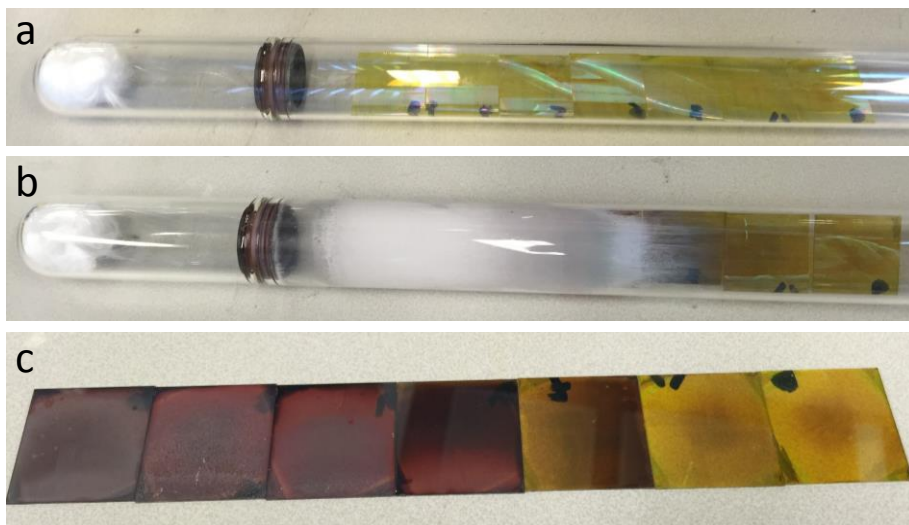
Figure 5.3 Example of the MAI crystals covered by wadding and PbI$_2$ covered substrates inside the glass tube before deposition (a) after 80 min. of deposition (b) and the finished layers after the complete 100 min. deposition process outside of the tube (c).
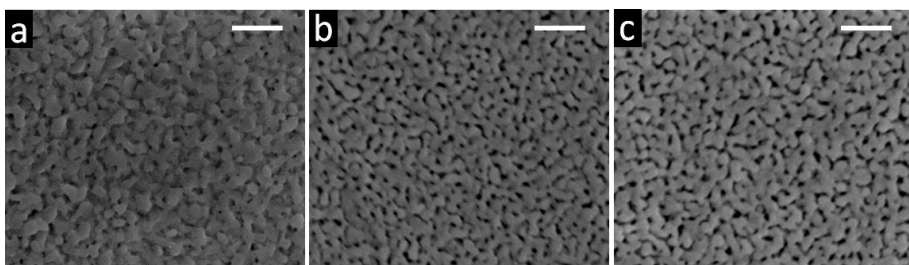
Figure 5.4 Top view SEM images of compact (a) and porous PbI$_2$ layers (b) 120 and (c) 240 μl TBP mL^{-1} DMF. Scale bars are 500 μm.

Figure 5.5 Example of the MAI crystals covered by wadding and porous PbI$_2$ (120 μl TBP mL^{-1} DMF) covered substrates inside the glass tube before deposition (a) and the finished layers after the complete 100 min. deposition process (b).

Table 5.1 Regular (fast) *J-V* characteristics of solar cells produced in the thermal gradient sublimer using the optimal settings for the compact PbI$_2$ layers. Values are averages and standard deviation of 4 cells on one substrate.

Substrate No.	J_{SC} (mA cm^{-2})	V_{OC} (V)	FF	P_{max} (%)
1	2.8 ± 2.4	0.88 ± 0.07	0.61 ± 0.06	1.4 ± 0.9
2	4.1 ± 2.5	0.95 ± 0.02	0.61 ± 0.05	2.3 ± 1.2
3	8.8 ± 1.9	0.96 ± 0.02	0.55 ± 0.19	4.9 ± 2.7
4	1.4 ± 0.2	0.73 ± 0.03	0.37 ± 0.04	0.4 ± 0.1
Record device	10.7	0.98	0.73	7.7

Table 5.2 Regular (fast) *J-V* characteristics of solar cells produced in the thermal gradient sublimer using the optimal settings for the porous PbI$_2$ layers. Values are averages and standard deviation of 4 cells on one substrate.

Substrate No.	J_{SC} (mA cm^{-2})	V_{OC} (V)	FF	P_{max} (%)
1	2.3 ± 0.6	0.84 ± 0.06	0.62 ± 0.14	1.3 ± 0.5
2	8.3 ± 1.4	0.87 ± 0.02	0.74 ± 0.03	5.4 ± 1.2
3	10.2 ± 1.4	0.70 ± 0.03	0.39 ± 0.06	2.8 ± 0.6
4	3.7 ± 0.5	0.33 ± 0.03	0.29 ± 0.00	0.4 ± 0.1
Record device	9.3	0.89	0.78	6.5

These exploratory experiments using the thermal gradient sublimer have shown that PbI$_2$ layers can be converted to perovskite with exposure to MAI vapor at moderate temperatures and pressures. Although the solar cell efficiency that can be achieved using the thermal gradient sublimation equipment is reasonable, the large variation in the solar cell performance on one substrate and between substrates due to the strong deposition gradient along the tube axis makes the equipment unsuitable for reproducible and reliable experiments with a larger number of samples per batch. In order to produce vapor assisted solution processed (VASP) perovskite solar cells on larger scale (up to 9 substrates per batch) a VASP reactor was designed and produced, based on the information gathered in the experiments using the thermal gradient sublimer. The design of this reactor is discussed in section 5.3.

5.3 Design of the VASP reactor

In the exploratory vapor assisted solution processing (VASP) experiments using the thermal gradient sublimer (section 5.2) it was found that the most critical parameters in the vapor deposition process were the (difference between the) temperatures at the position of the PbI_2 samples and the MAI source, the deposition time, and physical transport distance of the vapor. In order to gain more control over the vapor deposition process and to be able to produce larger batches of samples, a VASP reactor was designed and built. The reactor is schematically displayed in Figure 5.6.

Figure 5.6 Schematic representation of the designed VASP reactor with the temperature controlled sample stage on the right and the crucible on the left inside a Pyrex tube with stainless steel end caps. It must be noted here that the crucible shown here was changed for a much smaller ceramic piece.

In order to accommodate a larger number of substrates per batch, the VASP reactor consists of a 52 cm long, large diameter (d = 10.4 cm) Pyrex tube with tapered ends that improve sealing. The tube is capped with two rail mounted, moveable end caps, onto one of which the crucible for MAI powder is attached while on the other the sample stage is connected (Figure 5.6). Both stainless steel end caps have rubber O-rings that provide a seal between the caps and the tapered ends of the glass tube. The tapered aluminum oxide ceramic crucible for MAI powder has a diameter of 25 and 23 mm for the top and bottom respectively, a wall thickness of 1 mm and depth of 31 mm and resides inside an electric heating coil. The bottom of the crucible rests on top of a thermocouple to be able to accurately determine and control the temperature of the crucible using a digital PID temperature controller (West Control Solutions 6100). The sample stage consists of a 9 cm × 9 cm stainless steel plate on which the samples can be placed (up to nine 3 cm × 3 cm samples per batch). The sample stage is located on

top of stainless steel tubing that is filled with silicon oil. The oil is used for the cooling and heating of the sample stage. In order to do so, the oil is circulated by means of a home built high temperature resistant electrically driven pump that pumps the oil from a reservoir that contains a 250 Watt electrical heating element, through the lines underneath the sample stage, after which the oil is cooled by traveling through a set of radiators equipped with electrical cooling fans. After the oil is cooled down inside the radiators, it travels back into the reservoir in order to be heated back up to the required temperature. The whole system is designed to run as a so called "open" cooling system, meaning that there is always an opening to the atmosphere in the system. This way, there is no pressure increase in the system because of the expansion of the oil due to its heating, avoiding any pressure build-up in the system and reducing the risk of leakage of hot oil. On the underside of the sample plate a thermocouple is mounted to accurately measure and control the temperature of the sample plate, again using a digital PID temperature controller (West Control Solutions 6100). The digital PID temperature controller controls the heating element located inside the oil reservoir, the electric radiator fans rotate at a set speed during the experiment (different speeds can be selected). To avoid the deposition of MAI onto the inner wall of the Pyrex tube as was seen in the experiments with the thermal gradient sublimer (Figure 5.3b), three 4 cm wide, 700 Watt heating rings (Rokoma DH 400) are attached on the outside of the Pyrex tube. These three heating rings are used to heat the tube sufficiently and are controlled by three separate digital PID temperature controllers (West Control Solutions 6100). To improve the temperature homogeneity of the Pyrex tube wall, the whole tube, including the heating rings, is wrapped in thermally insulating material and aluminum foil. Both stainless steel end caps have one additional connector providing the possibility to connect a vacuum pump to the cap at the side of the sample stage and to supply a carrier gas at the side of the crucible.

This design aims to provide accurate control of the parameters that were identified as the most important for VASP in the experiments with the thermal gradient sublimer. The accurate temperature control of the crucible should provide excellent control of the evaporation rate of the MAI. The oil circulation system should provide adequate temperature control of the sample stage whereby the physical vapor deposition and conversion rate of the PbI_2 layer to perovskite should be controlled. With the heating rings on the outside of the glass tube, vapor deposition onto the tube wall should be avoidable. The possibility to introduce a carrier gas can provide additional physical vapor transport towards the substrates and with the vacuum system the pressure inside the reactor is be controllable.

5.4 Exploratory experiments with the VASP reactor

Temperature verification

The first experiment that was conducted with the VASP reactor aimed at visualizing the stability and accuracy of the temperatures that can be set with the five different digital PID temperature controllers. Five thermocouples were placed inside the glass tube at different locations as indicated in Figure 5.7 to measure the actual temperature while the different heating elements were set to several different temperatures. Figure 5.8 shows the resulting temperature measurements.
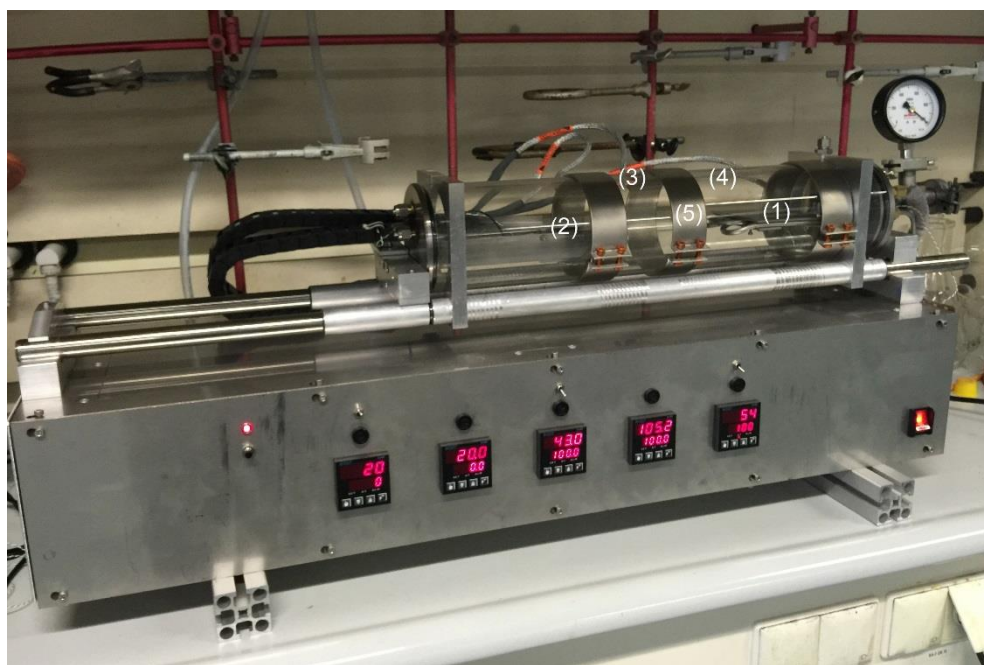
Figure 5.7 Photograph of the VASP reactor without the thermal insulation, with the locations of the thermocouples indicated. The positions of the three heating rings can be varied and ultimately, the most homogeneous heating was attained with the rings evenly spaced over the whole tube.
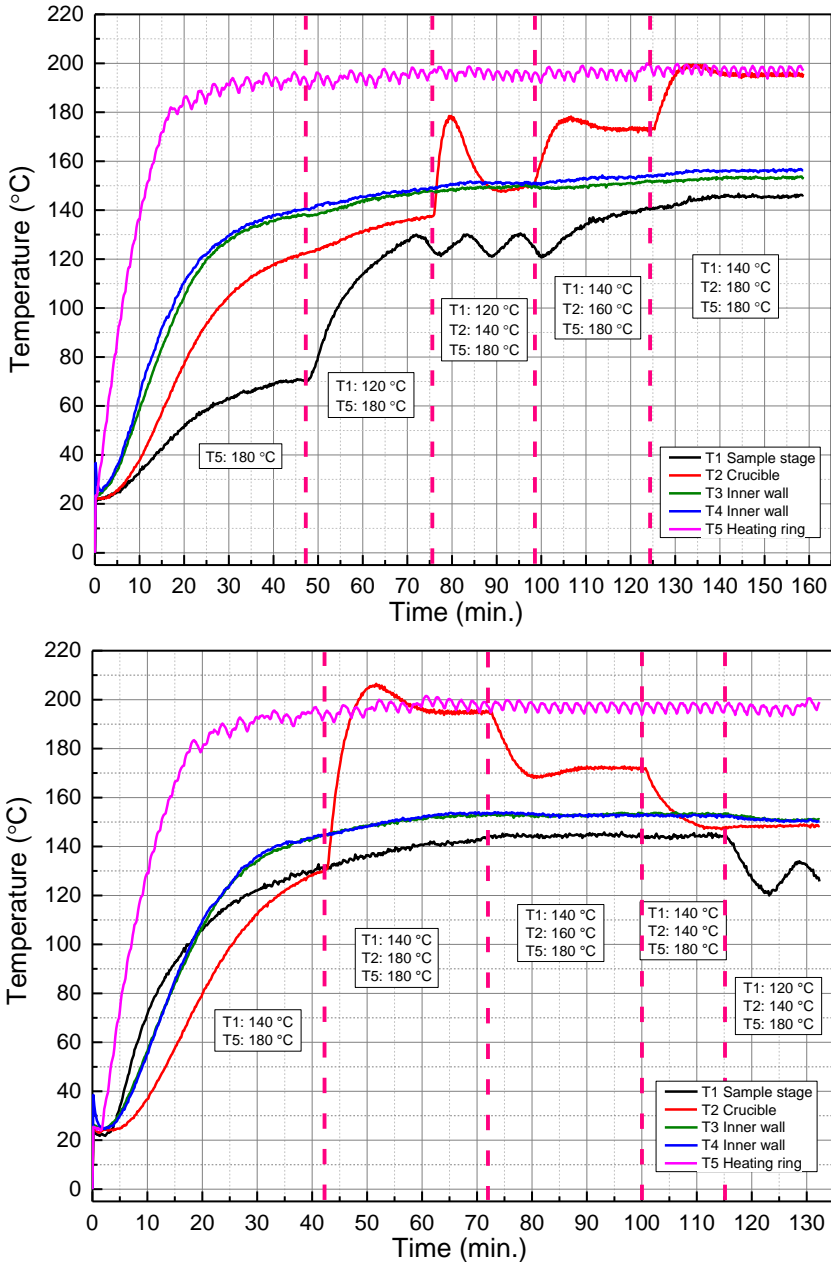
Figure 5.8 Time dependent temperature measurements at different locations inside the VASP reactor as indicated by Figure 5.7 (1 = top of sample stage, 2 = inside crucible, 3 = tube wall in between heating rings 1 and 2, 4 = tube wall in between heating rings 2 and 3, and 5 = at the position of heating ring 2). Set temperature values are displayed in the rectangles.

From the first measurements, we see that the temperature at the position of the heating ring stabilizes within 30 minutes to ~10 °C above the set value of 180 °C. We also see that during this time, the crucible and sample holder also start heating up to ~120 and ~70 °C respectively. When the sample stage is set to 120 °C, it stabilizes within 20 minutes and from that point on keeps fluctuating between ~120 °C and ~130 °C. The heating of the sample stage also slightly increases the rate at which the crucible heats up, going up to ~135 °C in 20 minutes. These temperature measurements were, however, carried out with the tube at atmospheric pressure because it could not be evacuated due to the thermocouple wires that are running through a hole in one of the end caps. Since the VASP experiments will be performed in vacuum, it is expected that the heat transfer between components inside the tube is much less because at vacuum there is (almost) no transport medium inside the tube and heat transfer will depend on only radiative heat transfer instead of radiation and convection at atmospheric pressure. Upon activating the crucible heating (set to 120 °C), there is a quite severe overshoot of the temperature to ~180 °C after which it stabilizes quickly (< 10 min.) at ~30 °C above the set temperature. This offset in temperature decreases to ~15 °C upon further increasing the crucible temperature to 160 °C and 180 °C. Also here there is probably quite significant heat transfer from the hot tube wall and sample stage at 180 °C and 120 °C respectively.

From the second experiment we confirm the quick heating and stabilization of the temperature at the position of the heating ring at ~10 °C above the set temperature. Furthermore, when the sample stage is set to 140 °C, it remains quite stable at ~145 °C even when the temperatures of the other heat sources are varied. In this experiment, again the crucible temperature overshoots but stabilizes quickly to between ~5 and ~15 °C above the set temperature (depending on the set temperature).

Finally, the temperature in between the heating rings stabilizes equally fast as that at the position of the heating rings at a temperature of ~25 °C below the set temperature of the heating rings in both experiments. Without the thermal insulating material covering the glass tube, this temperature difference can be as large as 80 °C.

Summarizing, the temperature at the position of the heating rings is stable and ~10 °C higher than the set value while that in between the heating rings also stable but ~25 °C lower than the set value. The temperature of the sample stage is very stable and ~5 °C higher than the set value and the crucible temperature stabilizes quickly to a temperature of ~10 °C above the set value after an initial overshoot. The

temperatures that will be mentioned throughout the remainder of this chapter are the set temperatures.

The pressure at which the apparatus can be operated was also tested, in this experiment it was found that the minimal pressure that can be achieved inside the reactor is slightly below 2 mbar under dynamic vacuum (the pump is able to reach values in the range of $P = {\sim}10^{-2}$ mbar). Furthermore, upon closing off of the vacuum source, the pressure inside the chamber increases slowly, reaching a pressure of $\sim$29 mbar after more than 60 minutes, indicating some slow leakage paths in the setup that limit the minimal operating pressure (Figure 5.9).
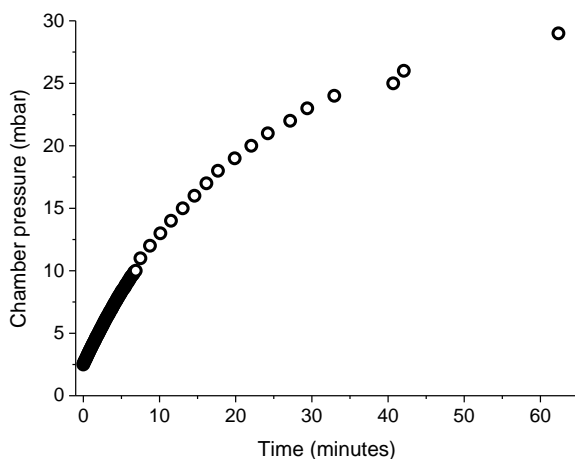
Figure 5.9 Pressure inside the evaporation chamber versus time upon switching off of the vacuum pump at $t = 0$.

Methylammonium iodide deposition

With the accuracy of the set temperatures and the minimal operating pressure of the reactor known, the basic dynamics of the deposition were investigated. According to the experiments with the thermal gradient sublimer and equation 5.1, the crucible temperature (T_c) is the most influential on the rate of MAI evaporation (Γ) at a given tube pressure (P_h). Where an increase in the crucible temperature results in increased MAI evaporation rate because the vapor pressure increases with temperature. On the other hand, the temperature of the substrates determines the deposition rate on top of the substrate surface. A decrease in the sample stage temperature should result in stronger MAI deposition onto the samples since there is a larger temperature difference (ΔT). Therefore, several experiments were conducted in which the temperatures of the crucible and sample stage were

varied and the MAI was evaporated onto clean glass slides. In these experiments the tube wall temperature (T_w) was kept at 20 °C above the crucible temperature (T_c) to avoid significant heat transfer from the tube walls to the crucible or sample stage. The deposition duration was kept constant at 30 minutes. MAI is too soft to perform thickness measurements with a surface profiler but MAI deposition can be assessed visually from the appearance of white deposits. With the crucible temperature set to T_c = 140 °C and the sample stage temperature set to T_s = 100 °C, it was observed that MAI was only deposited on the substrates closest to the evaporation source and a strong deposition gradient was observed (Figure 5.10b). It appears that the temperature drop (ΔT) of 40 °C between the crucible and the sample stage is too large, causing the MAI vapor to deposit strongly as soon as it comes into contact with the "cold" substrates. Another possible explanation is that the rate of MAI evaporation is too low and diffusion is not sufficient to supply the required amount of MAI to the substrates. Subsequent experiments in which the crucible temperature was varied from T_c = 130 to 180 °C in steps of 10 °C, while the sample stage temperature was kept at T_s = 80 °C, showed that a larger substrate coverage was achieved at crucible temperatures of $T_c \geq$ 170 °C. Nevertheless, the deposition profile still showed strong deposition and a very sharp gradient (Figure 5.10c), confirming that the abundant MAI deposition is a result of a large temperature drop and that the surface coverage is strongly dependent on the amount of MAI vapor supplied. Figure 5.10 schematically shows a template of the samples on top of the sample stage (a) and the deposition profiles that were obtained with the different parameter settings as discussed above and indicated in the figure (b, c). In the images displayed throughout this chapter, the location of the crucible is downward of the displayed sample stage, meaning the direction in which the MAI vapor is traveling over the sample stage is upward as indicated by the arrow in the figure.
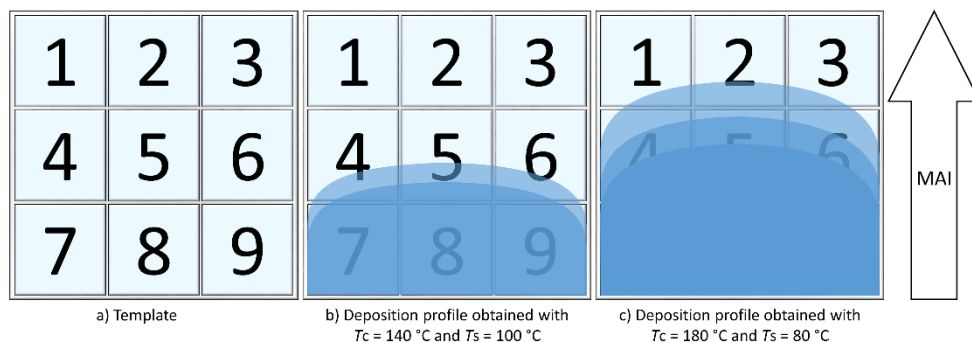
Figure 5.10 Influence of crucible and substrate temperatures on the obtained deposition profile where a darker color represents a thicker MAI layer.

Since a moderate and sufficiently homogeneous deposition profile could not be obtained by varying only the crucible and sample stage temperatures, a flow of nitrogen (N_2) carrier gas was introduced. N_2 was supplied via a pressure regulator and needle valve to the end cap that holds the crucible. The reactor was evacuated to a pressure of ~3.5 mbar and the pressure inside the tube was increased by opening the N_2 supply and regulated using the needle valve. The crucible and substrate temperatures were set to 170 and 100 °C respectively and the deposition was performed for 60 minutes at tube pressures of ~10, ~20, and ~50 mbar. Increasing the tube pressure lowers the MAI evaporation rate and gas phase diffusion constant according to equations 5.1 and 5.2, but the introduction of the carrier gas improves the vapor flow towards the sample stage. At a tube pressure of ~10 mbar, a relatively uniform deposition across all nine substrates was achieved (Figure 5.11 a). A uniform deposition was not achieved with the higher operating pressures (Figure 5.11b and 5.11c). Noteworthy is the fact that in all cases, the left side area is largely not covered with MAI. This corresponds to the location of the opening from which the tube is evacuated (Figure 5.12), and will therefore probably experience the highest gas flow rates. These high flow rates of cold N_2 gas might be hindering deposition onto the substrates due to cooling of the sample stage. Additionally, with the use of the N_2 carrier gas, a large quantity of MAI was deposited on the walls of the tube as powder, probably caused by deposition of the MAI vapor upon contact with the cold N_2 carrier gas. Therefore, a copper tube that is immersed in an oil bath that is kept at 70 °C was added to the reactor in order to pre-heat the N_2 carrier gas to a temperature of ~70 °C before it enters the deposition chamber. The experiment at a chamber pressure of ~10 mbar was repeated, leading to a very similar deposition profile but without the deposition of MAI powder on the inside of the tube. From these experiments, it is seen

that the most homogeneous deposition profile is achieved using a high crucible temperature in combination with moderate sample stage temperature, a relatively low chamber pressure and (a low) pre-heated N_2 flow (rate).

Figure 5.11 Influence of chamber pressure as regulated by introducing N_2 gas on the obtained deposition profile where a darker color equals a thicker MAI layer.

Figure 5.12 Pictures showing the position of the chambers' exhaust (red circle) with respect to the sample stage.

Methylammonium iodide deposition onto PbI$_2$

With the use of a relatively low pressure (~10 mbar) and a pre-heated N_2 flow, the most homogeneous MAI deposition pattern was achieved on cleaned glass slides. Therefore, these parameters were used to deposit MAI onto glass slides coated with ~100 nm thick PbI$_2$ layers using a 60 min. deposition time. Now, we are not primarily looking for strong deposition of MAI onto the PbI$_2$ layers, but rather a fair balance between the physical deposition rate and the reaction rate of PbI$_2$ to perovskite (equation 5.4). For this purpose, the sample stage temperature plays a dual role, where it should firstly provide an adequate temperature drop to ensure sufficient deposition of MAI onto the PbI$_2$ layers, while simultaneously providing sufficient

thermal energy to provide the activation energy for reaction of PbI_2 with MAI to perovskite.[56, 57] The resulting deposition and conversion profile showed that the area in which the MAI deposition is very small, has turned into a nice dark brown perovskite color (Figure 5.12 right). The area in which the MAI deposition is strongest on the other hand, has turned into a red phase, which quickly turns white or transparent after exposure to atmospheric conditions, indicating a strong instability of the created material. Also post deposition annealing does not influence the appearance of the red layer. A similar red color was observed on the samples that were closest to the MAI source in the experiments with the thermal gradient sublimer (Figures 5.3c and 5.5b). Indicating that the physical MAI deposition onto these substrates is too strong and there is an imbalance in the deposition and conversion processes, hindering the formation of the desired brown perovskite phase. X-ray diffraction (XRD) measurements of the red and brown perovskite layers were performed, showing firstly that the brown phase is indeed the desired perovskite phase, displaying the characteristic (110) and (220) perovskite peaks at angles of 14.2° and 28.6° respectively, along with a small PbI_2 peak at 12.6° (Figure 5.13).[58, 59] The red phase does not show the characteristic perovskite peaks and the large peak at 11.4° could not be identified with the perovskite or any of the precursor materials.
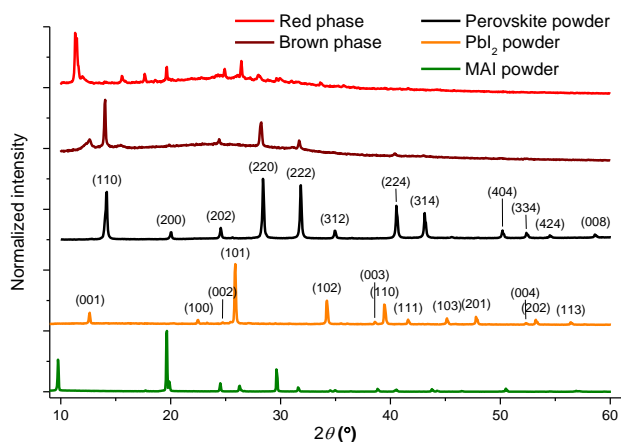
Figure 5.13 Normalized X-ray diffraction patterns of the red and brown phases produced using the VASP reactor along with powder references of the perovskite and precursor materials.

Since the deposition appears to be too strong, in the subsequent experiment, the crucible temperature was lowered to 150 °C to reduce the MAI evaporation rate, while all other parameters were kept consistent with the previous experiment. This resulted in a widened brown phase area, but still leaving a significant red phase area (Figure 5.14a). Therefore, the crucible temperature was lowered further to T_c = 130 °C while the sample stage temperature was also lowered to T_s = 90 °C to ensure a sufficient temperature drop. This led to a significant reduction in the area of the red phase but left a large area of unreacted PbI_2 at the far end of the sample stage (Figure 5.14b). This implies that either the MAI vapor did not reach these samples due to the strong deposition on the other samples, or the conversion reaction is too slow due to a substrate temperature that is too low. The small area in between the unreacted PbI_2 and the red phase however looks like the desired dark brown perovskite phase. To increase the conversion reaction speed, the sample stage temperature was increased to T_s = 110 °C in the subsequent experiment. This had the desired effect and resulted in very homogeneous deposition and conversion, without any red phase formation and only very slight yellow PbI_2 color at the very edge of the sample stage (Figure 5.14c). Thus resulting in the production of nine perovskite layers that visually resemble each other very closely.
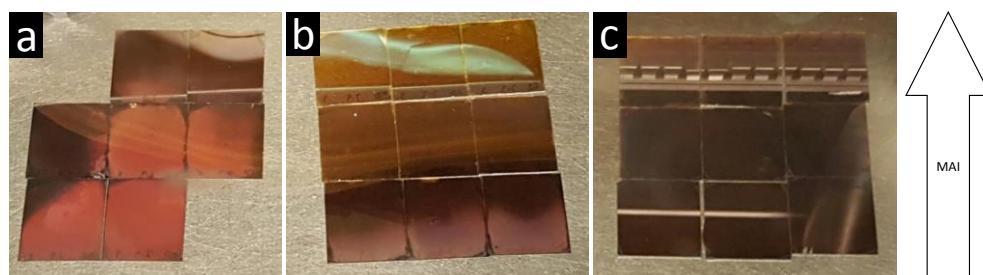
Figure 5.14 Influence of sample stage and crucible temperature (T_s and T_c respectively) on the deposition and conversion profile. a): T_s = 100 °C, T_c = 150 °C, b): T_s = 90 °C, T_c = 130 °C, and c): T_s = 110 °C, T_c = 130 °C. The arrow represents the direction of MAI flow over the sample stage.

As a final experiment with PbI_2 layers on glass slides, the deposition time was increased from 1 to 5.5 hours to see the effect of deposition time on the deposition profile and crystallinity of the material. Visually, the deposition profile and color of the produced perovskite layers is very similar for both deposition times. XRD measurements however show that the longer deposition time results in a higher peak intensity in XRD (Figure 5.15), suggesting a stronger preferred orientation of the perovskite crystals.
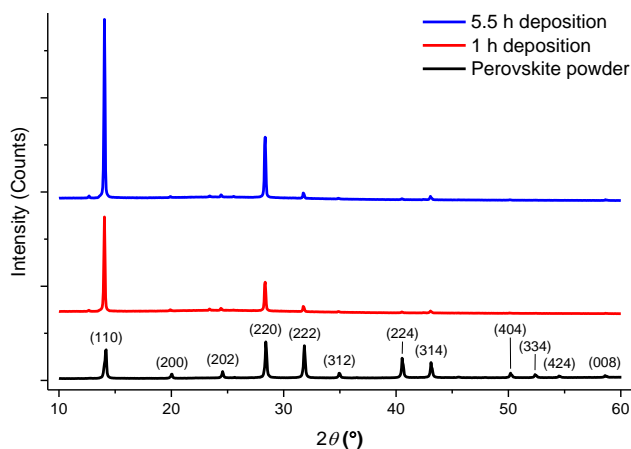
Figure 5.15 XRD traces of the perovskite layers of samples from the middle row (sample #6 for 1 h deposition and sample #5 for 5.5 h deposition as indicated in Figure 5.11a). A trace of $CH_3NH_3PbI_3$ perovskite powder is added for reference of peak identification.

5.5 Solar cells with home-built VASP reactor

With sufficient understanding of the functioning of the home-built vapor assisted solution processing (VASP) reactor and rudimentary optimization of the deposition process for the formation of perovskite layers, the advance was made to fabricate solar cells using the VASP reactor. For the fabrication of solar cells, poly(3,4-ethylenedioxythiophene):poly(styrenesulfonate) (PEDOT:PSS) (40 nm) is spin coated onto cleaned glass substrates with patterned indium tin oxide (ITO) electrodes. On top of this, a ~150 nm thick layer of PbI_2 is spin coated from a hot solution in inert conditions after which the substrate is annealed for 20 minutes at 70 °C under inert conditions to achieve the desired crystallinity of the PbI_2 layer (Figure 5.4a).

For the deposition of MAI in the first batch of solar cells, the optimized deposition conditions determined in section 5.4 were used (T_c = 130 °C, T_s = 110 °C, T_w = 150 °C, P_h = 10 mbar, and a deposition duration of 5.5 hours). This resulted in the incomplete conversion to perovskite of the top two rows of samples as evidenced by the yellow color of the majority of the samples in Figure 5.16.

Nevertheless, the solar cells were completed by spin coating a ~60 nm thick layer of [6,6]-phenyl-C_{61}-butyric acid methyl ester (PCBM) and after cleaning the device contact area, thermally evaporating 1 nm of lithium fluoride (LiF) and 100 nm of aluminum (Al) under high vacuum as the back electrode. Current density-voltage (*J-V*) measurements of the four cells on all nine substrates reveal low efficiencies in

136

general, with a slightly higher efficiency for the darker samples. Although the V_{OC} of the cells is reasonable, the J_{SC} and FF are very low, pointing towards incomplete conversion. The average solar cell parameters of regular (fast) J-V measurements are displayed in Figure 5.17.
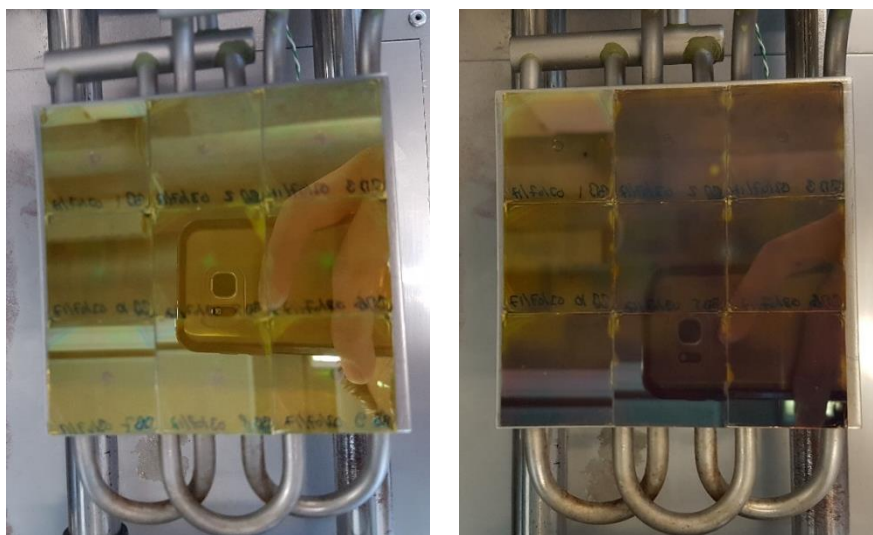
Figure 5.16 Top view photographs of the PbI$_2$ covered substrates before (left) and after a deposition time of 5.5 h (right).

J_{SC}			V_{OC}			
2.0	4.9	3.8	0.72	0.76	0.74	**highest**
3.1	5.9	4.4	0.77	0.80	0.75	
4.8	7.2	8.1	0.77	0.85	0.89	
FF			P_{max}			
0.39	0.35	0.37	0.5	1.3	1.0	
0.39	0.35	0.36	0.9	1.6	1.2	
0.36	0.39	0.40	1.3	2.4	3.0	**lowest**
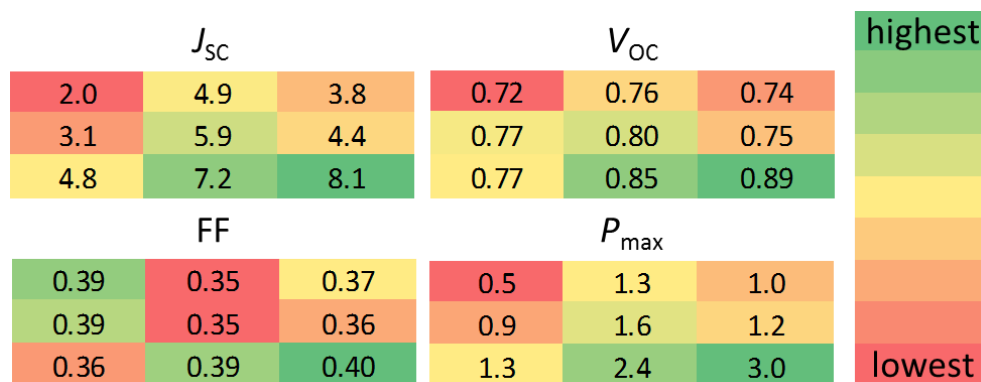
Figure 5.17 Average J-V parameters from 4 cells on the same substrate from regular (fast) downward measurements on solar cells produced with the home built VASP reactor. The layout is the same as the one shown in Figure 5.11a, the values are color coded for easy recognition of the lowest and highest values according to the color coding displayed in the scale bar on the right.

XRD measurements on the darkest and highest performing device (sample 9) and the most yellow and worst performing device (sample 1) confirm the incomplete conversion of the PbI_2 layers by showing very large PbI_2 peaks and only very small perovskite peaks in both cases (Figure 5.18). Indicating that in both samples, the conversion is very small. Additionally, the appearance of selected PbI_2 diffraction peaks ((001) and (003)) suggests that the PbI_2 layer has some preferential orientation. Thickness measurements of the perovskite layers confirm the low conversion with expansion factors of δ = 1.2 and 1.6 for substrates 1 and 9 respectively.
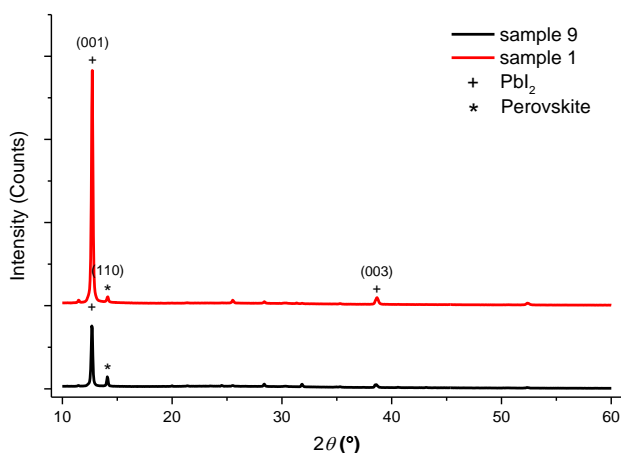
Figure 5.18 XRD traces of solar cells 1 and 9 produced using the VASP reactor, characteristic $CH_3NH_3PbI_3$ and PbI_2 peaks are indicated with an asterisk and plus sign respectively.

After varying the deposition parameters in several subsequent experiments, it was found that the pressure inside the chamber has a large effect on the deposition and conversion rate. Figure 5.19 shows several photographs that were taken during the deposition process. After only 30 minutes of deposition, the samples have already turned very faintly brown (Figure 5.19a). The color of the sample does however not get much darker upon prolonged deposition up to 205 minutes (Figure 5.19b). Lowering the chamber pressure from 10 mbar to 6 mbar, resulted in significantly darker samples after only 40 minutes of additional deposition (Figure 5.19c). An additional 110 minutes of deposition in which the pressure was varied between 2 and 6 mbar resulted in very dark perovskite layers (Figure 5.19d). Additionally, with this variation of chamber pressure it was observed that when the chamber pressure is reduced below ~4 mbar, deposition of MAI powder on top of the perovskite layers

starts occurring. Upon increasing the chamber pressure, this deposited powder is removed again very slowly. This MAI deposition is probably caused by the low amount of N_2 that is flowing through the chamber at these low pressures. It must be noted here that the perovskite layers look quite different since in this experiment, the morphology of the PbI_2 layer was also varied.
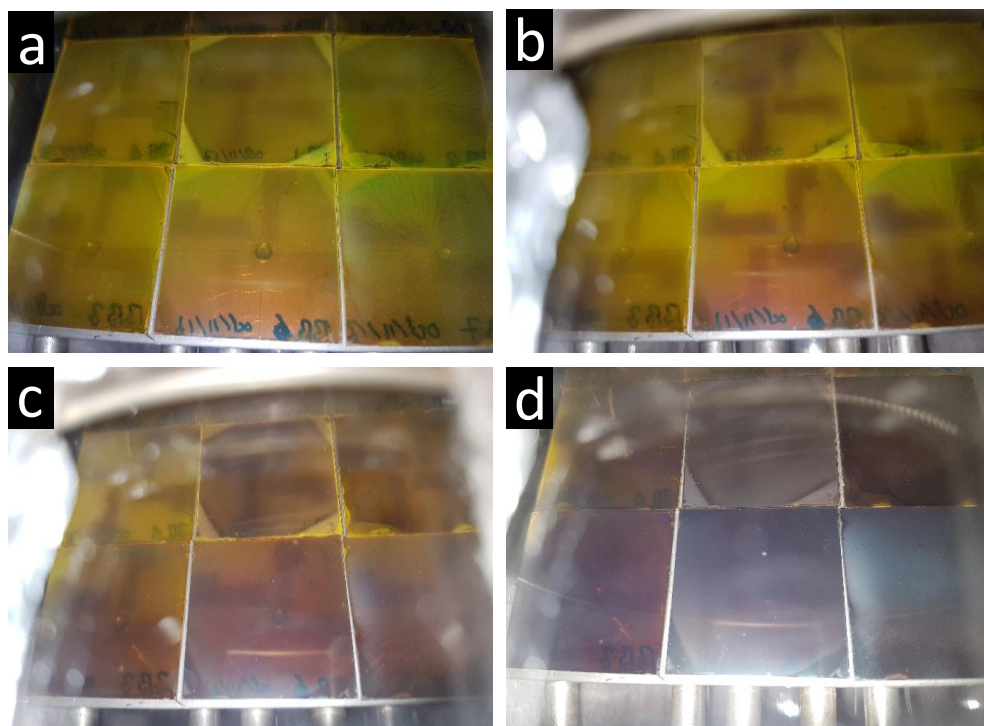
Figure 5.19 Photographs of the bottom rows of the sample stage during deposition, a) after 30 min. at P_h = 10 mbar, b) after 205 min. at P_h = 10 mbar, c) after 205 min. at P_h = 10 mbar plus 40 min. at P_h = 6 mbar, and d) after 205 min. at P_h = 10 mbar plus 150 min. at P_h = 2 - 6 mbar.

A chamber pressure of 6 mbar was used for the subsequent deposition experiments since it provided ample MAI deposition and conversion while avoiding the deposition of MAI powder on top of the layers. To investigate the influence of the PbI_2 source that is used on the conversion reaction and solar cell performance, three lead sources with different purity ratings were used in the same experiment. PbI_2 powder batches were ordered from Sigma-Aldrich (99%) and TCI Chemicals (99.99% trace metals basis) along with PbI_2 beads from Alfa Aesar (ultra-dry, 99.999% trace metals basis) (up to this point PbI_2 from TCI Chemicals was used). The solutions that were prepared for spin coating the PbI_2 layers had to be slightly less concentrated to

ensure the complete dissolution of all three lead iodide materials (300 mg mL^{-1} is used here where 400 mg mL^{-1} was the standard up to this point) resulting in thinner PbI$_2$ layers (~110 nm). Furthermore, in this batch one layer of each lead iodide source was cast at room temperature while two layers were cast at the standard solution temperature of 70 °C. All PbI$_2$ layers were annealed for 20 minutes at 70 °C as usual. The PbI$_2$ layers that were cast at room temperature appear a bit hazier (top row in Figure 5.20 left). All deposition parameters were kept identical apart from a slightly shorter deposition time of 4.5 hours. After the deposition of MAI, the formed perovskite layers all appear similar, very dark brown, and smooth (Figure 5.20 right).
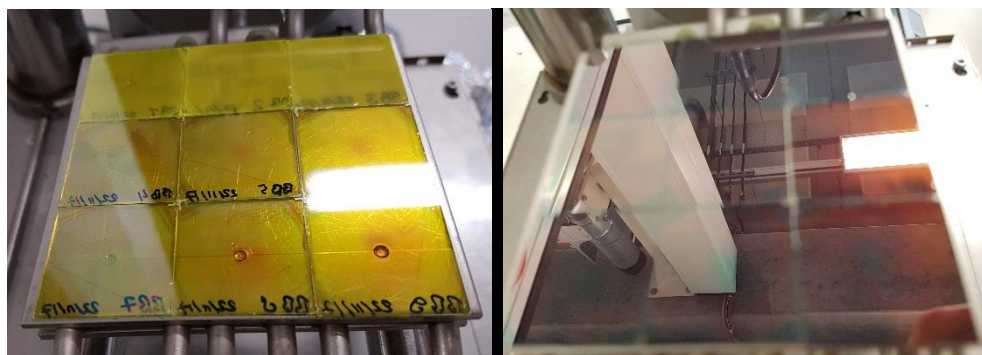
Figure 5.20 Photographs of the PbI$_2$ layers before (left) and after (right) 4.5 hours of MAI deposition.

After completing the devices and measuring *J-V* characteristics, it is obvious that the devices produced from PbI$_2$ solutions cast at room temperature do not perform well. Also, the devices produced from the Sigma-Aldrich lead iodide source perform worse than those produced from the two other lead sources (Figure 5.21). The performance of the cells produced with PbI$_2$ from TCI chemicals and the "ultra-dry" beads from Alfa Aesar is very similar. All produced layers appear to be converted quite well, which is confirmed with thickness measurements of the perovskite layers resulting in an expansion factor of $\delta = 1.8$ for the Sigma Aldrich and TCI Chemicals PbI$_2$ materials and $\delta = 1.9$ for the Alfa Aesar PbI$_2$ beads. For subsequent experiments the TCI Chemicals PbI$_2$ source was used and the production of 9 identical samples using ~110 nm thick PbI$_2$ layers and identical deposition parameters of the previous experiment results in 9 visually identical perovskite layers (Figure 5.22) that also perform very similar in *J-V* measurements (Figure 5.23), showing reasonable J_{SC}, V_{OC} and FF values compared to the solution processed devices described in Chapters 3 and 4.

	Sigma	TCI	Alfa	Sigma	TCI	Alfa	
		J_{SC}			V_{OC}		highest
Cast at RT	13.8	0.5	15.7	0.79	0.07	0.27	
	10.1	16.3	14.9	0.71	0.87	0.89	
	14.5	16.8	16.5	0.79	0.87	0.88	
		FF			P_{max}		
Cast at RT	0.63	0.25	0.40	6.9	0.0	1.7	
	0.46	0.72	0.70	3.6	10.2	9.3	
	0.64	0.75	0.73	7.3	10.9	10.6	lowest

Figure 5.21 Average *J-V* parameters from 4 cells on the same substrate from regular (fast) downward measurements on solar cells produced with the home built VASP reactor from different PbI₂ sources. The layout is the same as the one shown in Figure 5.11a, the values are color coded for easy recognition of the lowest and highest values according to the color coding displayed in the scale bar on the right.
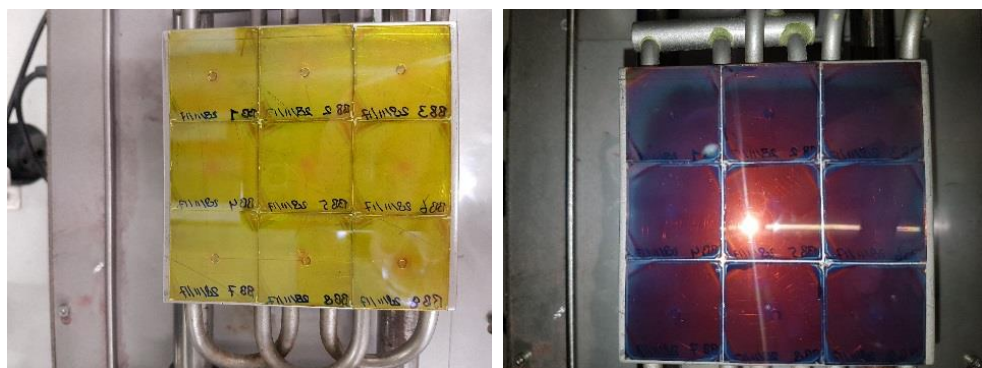
Figure 5.22 Photographs of the PbI₂ layers before (left) and after (right) 5.5 hours of MAI deposition.

	J_{SC}			V_{OC}		
15.6	16.1	16.1	0.91	0.90	0.91	highest
15.4	15.2	15.3	0.87	0.85	0.86	
15.3	15.1	15.5	0.84	0.82	0.83	
	FF			P_{max}		
0.72	0.74	0.75	10.2	10.7	10.9	
0.70	0.72	0.73	9.3	9.3	9.7	
0.73	0.74	0.75	9.4	9.1	9.6	lowest

Figure 5.23 Average *J-V* parameters from 4 cells on the same substrate from regular (fast) downward measurements on 9 identical solar cells produced with the home built VASP reactor using TCI chemical PbI₂. The layout is the same as the one shown in Figure 5.11a, the values are color coded for easy recognition of the lowest and highest values according to the color coding displayed in the scale bar on the right.

Surprisingly, thickness measurements show that the expansion factor for samples 2, 5, and 8 is δ = 1.7, 2.0, and 2.0 respectively. Indicating the best performing cell is not yet fully expanded. X-Ray diffraction analysis of these three samples however shows that they are almost completely identical, clearly showing the characteristic (110) and (220) $CH_3NH_3PbI_3$ perovskite peaks (Figure 5.24). Compared to the solution processed perovskite layers described in the other sections of this dissertation, there seems to be less strong preferential orientation of the perovskite crystals in the sequentially produced layers, as suggested by the larger number of diffraction peaks appearing in the XRD trace. The main difference in the trace shape is in the contribution of the PbI_2 peak that is slightly larger for sample 2, confirming that the top row of samples is converted slightly less (inset Figure 5.24). The EQE spectra and integrated J_{SC} of all 9 samples are very similar with all of the spectra showing only very small light intensity dependence (Figure 5.25).
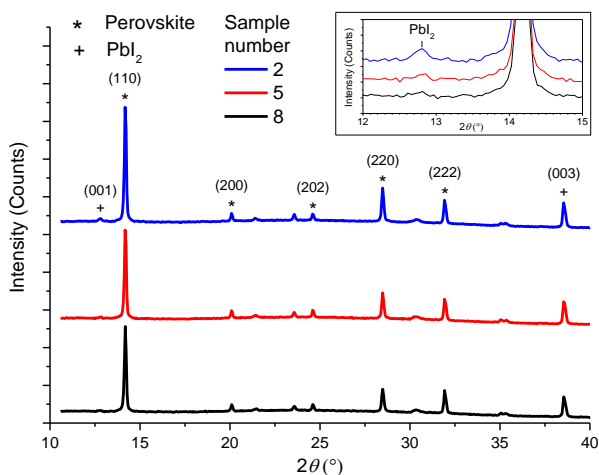
Figure 5.24 X-Ray diffraction (XRD) patterns of the perovskite solar cells produced in the middle column on the sample stage, deposited using the VASP reactor.
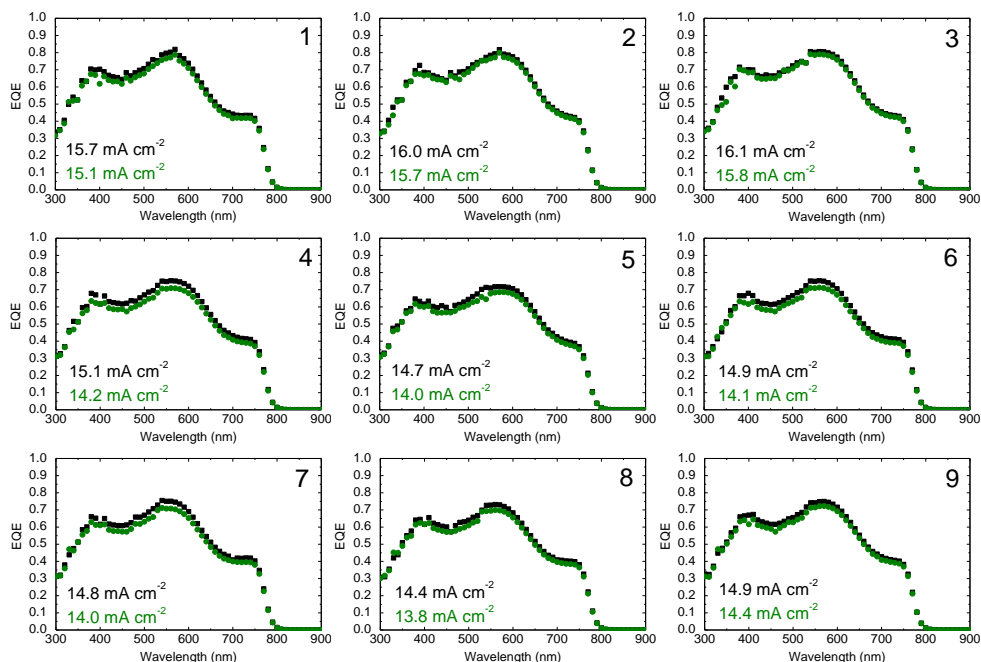
Figure 5.25 External quantum efficiency (EQE) plots of perovskite solar cells produced using the VASP reactor, measured under low- (black squares) and high- (green dots) illumination intensity. The integrated current density is displayed in the graphs for both measurements in black and green for the low- and high illumination intensity measurements respectively.

This experiment shows that the production of identical solar cells on 9 substrates (= 36 solar cells) via VASP is possible using the home built reactor with the correctly set deposition parameters (T_c = 130 °C, T_s = 110 °C, T_w = 150 °C, P_h = 6 mbar, and a deposition duration of 5.5 hours). The average J-V parameters with the standard deviation over 36 solar cells is displayed in Table 5.3, along with those of the best performing device in this series. The power conversion efficiency (PCE) is calculated with the photocurrent determined from integrating the EQE spectrum with the AM 1.5G spectrum ($J_{SC,\ SR\ @\ 1\ sun}$). Stabilized measurements were not performed on these cells, however the fast upward and downward scans of all these cells are almost identical.

Table 5.3 Regular (fast) downward *J-V* characteristics of nine identical solar cells produced in the home built VASP reactor. Values are averages and standard deviation of all 36 cells produced. Bottom row shows the parameters of the best performing device.

Substrate No.	J_{SC}	$J_{SC, SR @ 1 sun}$	V_{OC}	FF	PCE[α]
	(mA cm^{-2})	(mA cm^{-2})	(V)		(%)
Average	15.5 ± 0.4	14.6 ± 0.7	0.86 ± 0.03	0.73 ± 0.02	9.2 ± 0.9
Record device	16.1	15.8	0.91	0.75	10.7

[α] The PCE has been calculated with the photocurrent determined from integrating the EQE spectrum with the AM 1.5G spectrum ($J_{SC, SR @ 1 sun}$)

Although the achieved efficiencies are already quite good, the EQE spectra of the solar cells produced using these parameters show a reduced contribution at wavelengths above 650 nm (Figure 5.25). This evidences that light absorbance of the perovskite layer is not optimal and the perovskite layer thickness should be increased in order to improve the EQE at wavelengths > 650 nm as was already discussed in section 3.5, Figure 3.13. Since XRD measurements and the calculated expansion factors suggest that almost all of the PbI$_2$ is converted into perovskite in these layers, it should be possible to increase the PbI$_2$ layer thickness and enhance the performance of these solar cells. In order to do so, the spin coating speed for PbI$_2$ deposition was lowered from 2200 to 1000 and 500 RPM in the next experiment. This resulted in PbI$_2$ layer thicknesses of ~90 nm (2200 RPM, substrates 1, 4, and 7), ~130 nm (1000 RPM, substrates 2, 5, and 8), and ~210 nm (500 RPM, substrates 3, 6, and 9). Spin coating speeds <1000 RPM were, however, found to be too low since it resulted in very large thickness variations on one substrate. After the conversion process was performed using identical parameters to the previous experiments, the solar cell EQE was measured. This indeed showed an increase of the EQE at wavelengths > 650 nm for the thicker layers, even though most solar cells suffer from moderate light intensity dependence in the EQE (Figure 5.26).
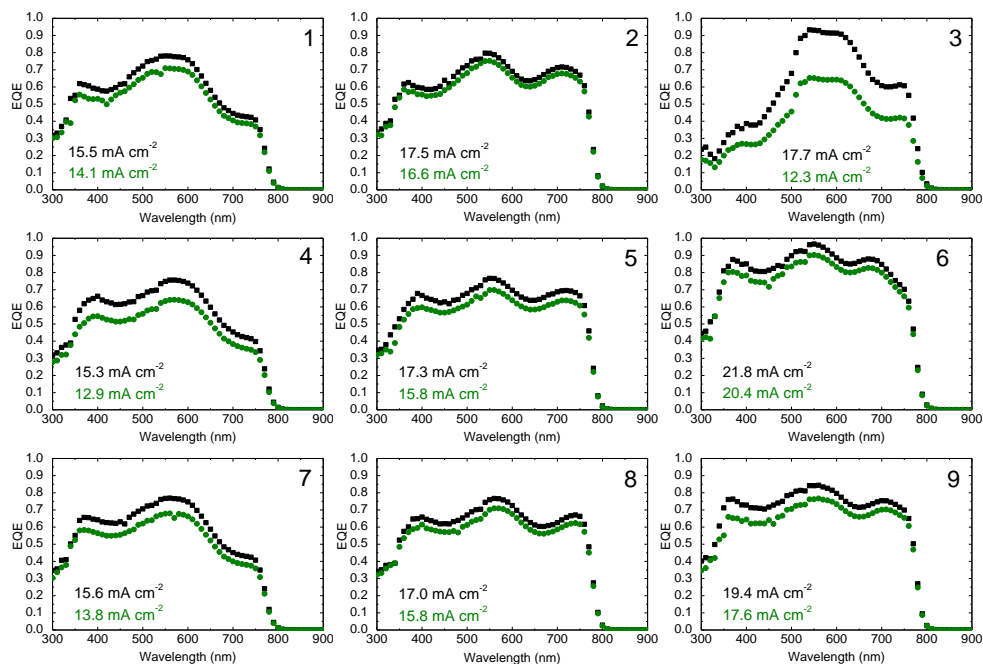
Figure 5.26 External quantum efficiency (EQE) plots of perovskite solar cells produced using the VASP reactor, measured under low (black squares) and high (green dots) illumination intensity. The integrated current density is displayed in the graphs for both measurements in black and green for the low and high illumination intensity measurements respectively.

From XRD analysis on the top and bottom row of substrates, the bottom row of substrates seem to be completely converted, while plenty of PbI_2 remains in the substrates on the top row (Figure 5.27). However, this residual PbI_2 apparently does not have a negative influence on the device performance. Additionally, the thicker PbI_2 layers appear to have more unconverted PbI_2 looking at the perovskite to PbI_2 peak height ratio. There is no difference in the perovskite peak intensity for the samples on the bottom row, even though the thickness measurements indicate the perovskite layer thicknesses are different (~210, ~310, and ~410 nm for substrates 7, 8, and 9 respectively) and the calculated expansion factors: δ = 2.3 (#7), δ = 2.3 (#8), and δ =1.9 (#9) indicate substantial conversion in all cases. The XRD results again show a preferential orientation in the PbI_2 layers and lower preferential orientation in the perovskite layers compared to their solution processed counterparts.

The solar cell characteristics show that the performance of the reference cells is somewhat lower due to the slightly thinner PbI₂ layer, but the thickest perovskite layers do not perform well at all (Figure 5.28). This is most likely related to the large variation in thickness of these PbI₂ layers. The large difference between the determined J_{SC} in EQE and J-V measurements however cannot be explained.
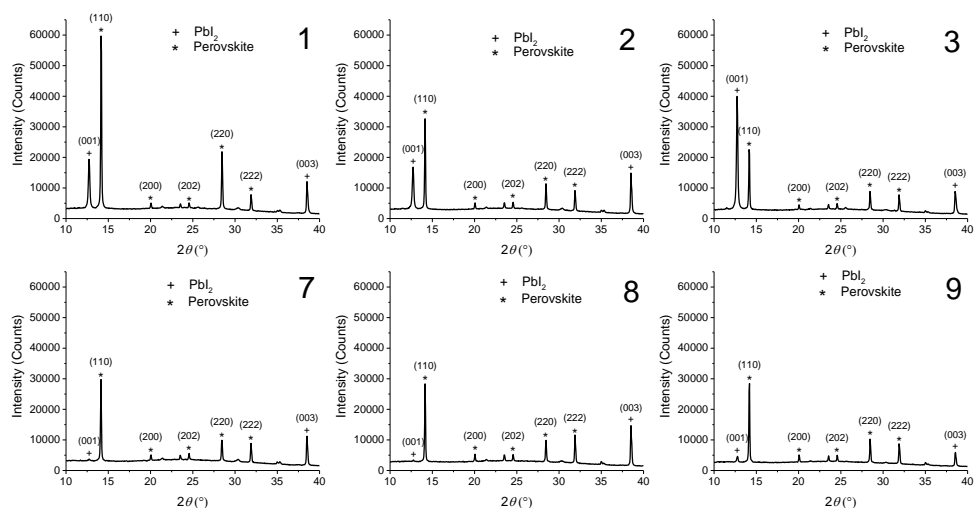
Figure 5.27 X-Ray diffraction (XRD) traces of the perovskite solar cells produced on the top and bottom row of the sample stage using the VASP reactor.

PbI₂ thickness (nm)			PbI₂ thickness (nm)			
90	130	210	90	130	210	
	J_{SC}			V_{OC}		highest
13.1	14.6	5.9	0.94	0.94	0.34	
13.0	15.5	9.6	0.89	0.88	0.25	
13.0	14.3	7.4	0.85	0.84	0.24	
	FF			P_{max}		
0.68	0.66	0.33	8.3	9.1	1.6	
0.68	0.71	0.34	7.8	9.7	1.0	
0.69	0.71	0.32	7.6	8.6	0.6	lowest

Figure 5.28 Average J-V parameters from 4 cells on the same substrate from regular (fast) downward measurements on solar cells produced with the home built VASP setup. The layout is the same as the one shown in Figure 5.11a, the values are color coded for easy recognition of the lowest and highest values according to the color coding displayed in the scale bar on the right.

Alternative attempts to increase the thickness of the PbI_2 layer by increasing the solution concentration yielded similar results. PbI_2 layer thicknesses of ~150, ~230, and ~390 nm were produced by spin coating (1000 RPM) 300, 400, and 500 mg mL^{-1} solutions respectively. After conversion, the perovskite layer thicknesses were ~290 nm (δ = 1.9), ~410 nm (δ = 1.8), and ~540 nm (δ = 1.4) indicating significant conversion except for the 390 nm thick PbI_2 layers. *J-V* measurements show similar performance for the 290 and 410 nm thick perovskite layers and very low performance for the 540 nm perovskite layers (Figure 5.29).

PbI$_2$ thickness (nm)				PbI$_2$ thickness (nm)			
150	230	390		150	230	390	
	J_{SC}				V_{OC}		highest
10.0	12.2	10.7		0.94	0.93	0.50	
16.7	16.2	13.7		0.87	0.90	0.58	
17.9	18.3	15.5		0.89	0.86	0.50	
	FF				P_{max}		
0.48	0.41	0.38		4.5	4.8	1.9	
0.64	0.64	0.42		9.2	9.2	3.2	
0.75	0.73	0.49		11.9	11.5	3.9	lowest
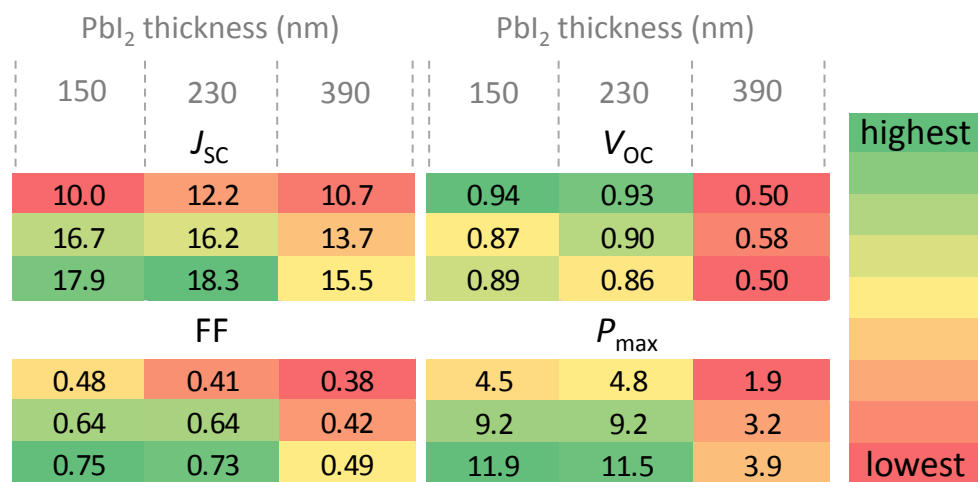
Figure 5.29 Average *J-V* parameters from 4 cells on the same substrate from regular (fast) downward measurements on solar cells produced with the VASP reactor. The layout is the same as the one shown in Figure 5.11a, the values are color coded for easy recognition of the lowest and highest values according to the color coding displayed in the scale bar on the right.

EQE measurement results also show very similar profiles with little light intensity dependence for the bottom row ~290 and ~410 nm thick perovskite layers (Figure 5.30). The ~540 nm thick perovskite layers show a low EQE with large light intensity dependence. It is remarkable that the EQE profile of the 410 nm thick perovskite layer is so similar to that of the much thinner ~290 nm perovskite layer, even though the expansion factor indicates almost complete conversion. Attempts were made to improve the conversion of these thicker layers by increasing the porosity of the PbI_2 layers with the addition of TBP to the PbI_2 solution. This however had no significant effect on conversion of the PbI_2 layer or the device performance. Therefore, the ~140 nm thick PbI_2 layer (300 mg mL^{-1}, 1000 RPM) gives the best device performance and was used for subsequent experiments.
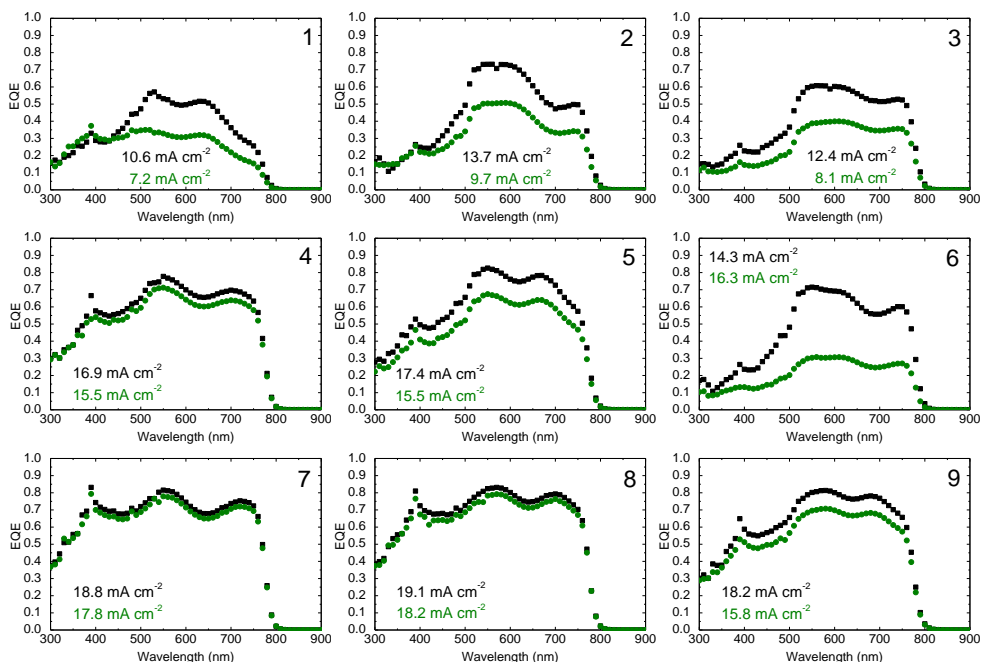
Figure 5.30 External quantum efficiency (EQE) plots of perovskite solar cells produced using the VASP reactor, measured under low- (black squares) and high- (green dots) illumination intensity. The integrated current density is displayed in the graphs for both measurements in black and green for the low- and high illumination intensity measurements respectively.

Earlier experiments have shown that the combined pressure and N_2 flow rate inside the tube during the deposition process have a large effect on the efficiency of the produced solar cells (compare Figure 5.17 with P_h = 10 mbar to Figure 5.23 with P_h = 6 mbar). To identify if it is the chamber pressure (P_h) or the N_2 flow speed inside the tube that is so influential, the setup was slightly modified. The setup was equipped with a gas flow meter that shows the amount of N_2 flowing into the tube in liters per minute (LPM). Initial testing revealed that the N_2 flow rate is ~2.5 and ~4.5 LPM when the reactor is operated at 6 mbar and 10 mbar respectively. Additionally, a needle valve was added between the tube and the pump to be able to leak air into the pump and thereby artificially lower the pump capacity, resulting in an increase in the pressure inside the reactor chamber. Using these modifications, an experiment was performed in which 9 identical substrates (TCI Chemical PbI_2, ~140 nm thick) were used and the deposition was done using a N_2 flow rate of ~2.5 LPM and a tube pressure of 10 mbar.

Photographs of the samples again show nine visually identical PbI_2 and perovskite layers before and after the deposition process respectively (Figure 5.31).
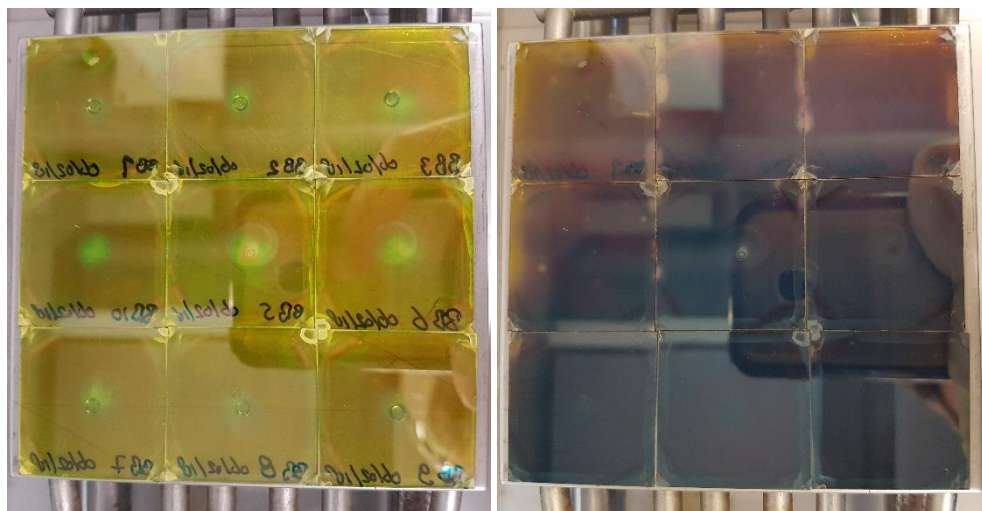
Figure 5.31 Photographs of the PbI$_2$ layers before (left) and after (right) 5.5 hours of MAI deposition.

The results from *J-V* measurements however show that the top row samples (1, 2, and 3) perform very poor, while the bottom row of samples (7, 8, and 9) perform very well (Figure 5.32). The EQE measurements reflect the same trend, with high EQEs and virtually no light intensity dependence for the bottom row of samples and aberrant profiles with large light intensity dependence for the top row (Figure 5.33). From thickness measurements we calculate an expansion factors of δ = 1.3, 2.1, 2.3 for samples 2, 5, and 8 respectively. Indicating the conversion of the top row of samples is far from complete. XRD measurements confirm this incomplete conversion of samples 2 and 5, showing PbI$_2$ peaks next to the characteristic perovskite peaks while the PbI$_2$ peak is absent in the XRD trace of sample 8 (Figure 5.34). Again a preferential orientation in the PbI$_2$ layers and a lower preferential orientation of the perovskite layers compared to the solution processed perovskite layers are seen.

J_{SC}			V_{OC}		
11.0	12.6	12.8	1.02	1.00	1.00
14.7	16.9	16.7	0.95	0.86	0.88
17.5	17.8	18.1	0.92	0.93	0.93

FF			P_{max}		
0.53	0.51	0.53	5.9	6.4	6.8
0.67	0.70	0.70	9.4	10.1	10.3
0.74	0.76	0.76	11.7	12.5	12.8

highest

lowest

Figure 5.32 Average *J-V* parameters from 4 cells on the same substrate from regular (fast) downward measurements on 9 solar cells produced with the VASP reactor operating with a N₂ flow rate of 2.5 LPM and a chamber pressure of P_h = 10 mbar. The layout is the same as the one shown in Figure 5.11a, the values are color coded for easy recognition of the lowest and highest values according to the color coding displayed in the scale bar on the tight.
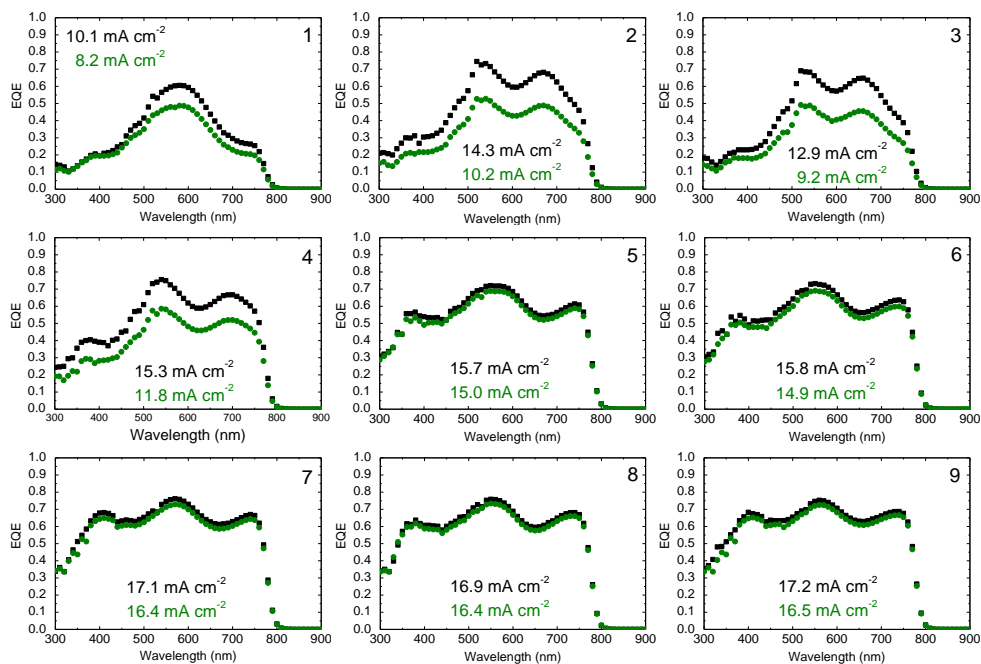
Figure 5.33 External quantum efficiency (EQE) plots of perovskite solar cells produced using the VASP reactor operating with a N₂ flow rate of 2.5 LPM and a chamber pressure of P_h = 10 mbar. Measured under low- (black squares) and high- (green dots) illumination intensity. The integrated current density is displayed in the graphs for both measurements in black and green for the low- and high illumination intensity measurements respectively.
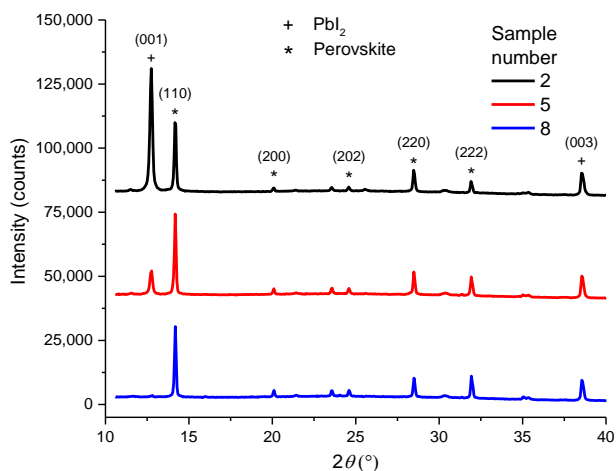
Figure 5.34 X-Ray diffraction (XRD) spectra of the perovskite solar cells produced in the middle column on the sample stage using the VASP reactor with 2.5 LPM N_2 flow and 10 mbar chamber pressure.

Top view SEM images of perovskite layers 2 and 8 produced in this experiment show identical, very compact perovskite layers, even though the XRD of sample 2 showed that it is not fully converted into perovskite (Figure 5.35). The similarity is probably caused by the top of the PbI_2 layer being converted first in the VASP reactor. Compared to the solution processed perovskite layers described in sections 3.5 and 4.2, the crystallites produced using the VASP method appear smaller and more irregularly shaped.
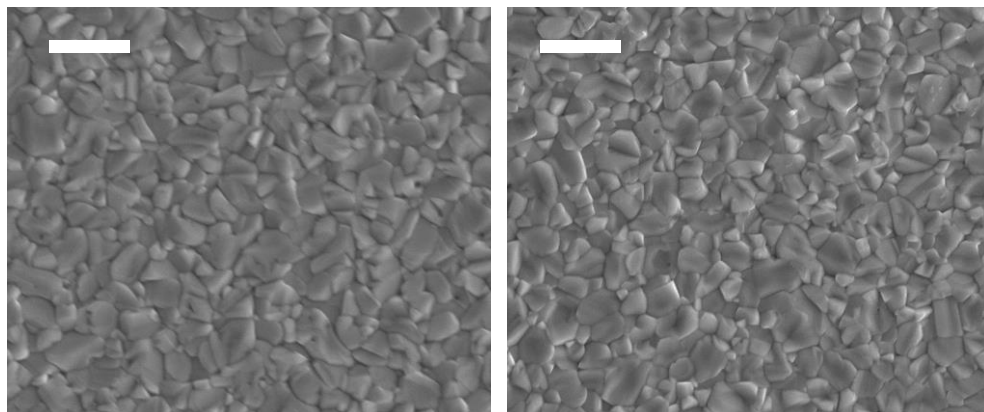
Figure 5.35 Top view SEM images of the perovskite layers of samples 2 (left) and 8 (right). Scale bars are 1 µm.

From these results we conclude that a low N_2 flow rate is essential for the slow deposition of MAI vapor onto the PbI_2 substrates, enabling the proper balance between deposition and conversion to be established. The pressure inside the chamber mainly influences the deposition profile, obtaining very similar results as were found in the experiments on glass slides in section 5.4, Figure 5.11. Stabilized measurements performed on these cells confirm the superior performance of the samples on the bottom row (Figure 5.36). Indicating that even longer deposition times might be required to achieve completely homogeneous conversion for this combination of N_2 flow rate and chamber pressure. With the results from these measurements and the EQE measurements the power conversion efficiency (PCE) is calculated. Table 5.4 shows the stabilized *J-V* parameters and calculated PCE where substrate #9 is the best performing solar cell produced using the home-built VASP reactor.
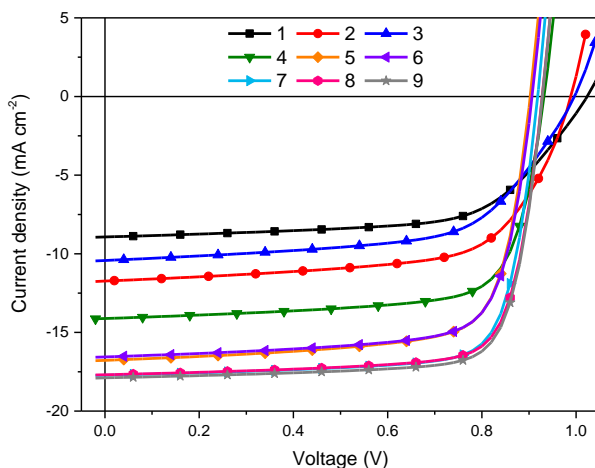
Figure 5.36 Stabilized *J-V* sweeps of the solar cells produced with the VASP reactor operating with a N_2 flow rate of 2.5 LPM and a chamber pressure of P_h = 10 mbar.

Table 5.4 Stabilized *J-V* characteristics of nine solar cells produced with the VASP reactor operating with a N$_2$ flow rate of 2.5 LPM and a chamber pressure of P_h = 10 mbar.

Substrate No.	J_{SC} (mA cm^{-2})	$J_{SC, SR @ 1 sun}$ (mA cm^{-2})	V_{OC} (V)	FF	PCE[α] (%)
1	8.9	8.2	1.02	0.63	4.6
2	11.7	10.2	0.99	0.65	5.8
3	10.4	9.2	1.00	0.61	4.8
4	14.1	11.8	0.93	0.73	7.2
5	16.8	15.0	0.90	0.74	9.4
6	16.6	14.9	0.91	0.74	9.6
7	17.7	16.4	0.92	0.77	11.3
8	17.7	16.4	0.93	0.77	11.4
9	17.9	16.5	0.93	0.78	11.7

[α] The PCE has been calculated with the photocurrent determined from integrating the EQE spectrum with the AM 1.5G spectrum ($J_{SC, SR @ 1 sun}$)

5.6 Conclusions

Using a thermal gradient sublimer we have shown that it is possible to convert solution deposited PbI$_2$ layers into perovskite layers. We were also able to determine a number of critical parameters for the deposition process like the temperature of both crucible and substrate, the distance between the crucible and the substrates, and the deposition time. This allowed the design and fabrication of a home-built reactor for vapor assisted solution processing (VASP) of perovskite layers. With this reactor, we were able to identify one more critical parameter in the process, the flow speed of the heated carrier gas. The flow rate is critical for achieving a proper balance between the deposition of MAI from the vapor phase onto the substrates and the chemical reaction to form the perovskite. By separating the crystallization and conversion processes with this sequential deposition method, the resulting perovskite layer has less strong preferential orientation compared to "one pot" solution processed samples. This is evidenced by a larger number of perovskite diffraction peaks appearing in the XRD traces of the sequentially processed perovskite films. With the optimized deposition procedure, 9 very similar perovskite layers can be produced giving us 36 almost identical solar cells. The highest achieved solar cell efficiency using this reactor was 11.7%, which is significantly lower than the solution processed perovskite solar cells described in other sections of this dissertation. The lower performance is most likely related to the smaller size and less strong preferential

orientation of the perovskite crystals in the solar cells produced using the VASP reactor. Furthermore, a gradient in the conversion and with that the solar cell performance is often seen along the axis of the tube. This is most likely related to the combination of set temperatures, flow speed and deposition time and can most likely be removed by further optimization of the deposition process.

The efficiency of the solar cells produced using this VASP setup can surely be increased further and come close to that of its solution processed counterparts with further optimization of the production process and the reactor itself. Even the production of 36 identical high efficiency solar cells is probably possible using this equipment. However, the production process is lengthy and with further optimization the reaction time might even exceed the 5.5 hours that were used here. Although the reproducibility of the method is good, this will still result in only 9 substrates (36 solar cells) per produced batch of solar cells. Furthermore, the solar cell performance will probably still suffer from the lower degree of preferred orientation of the perovskite crystals compared to that of the solution processed solar cells, potentially limiting the device performance even after full optimization. Therefore, although we have learned from the experiments working with this VASP reactor, the possibilities of using this setup for larger scale production of highly efficient solar cells is not without challenges. It does however show the opportunity of upscaling for this method and is helpful towards the development of large scale VASP production processes.

5.7 Experimental

Glass slides were cleaned by scrubbing in a solution of sodium dodecyl sulfate (SDS, Acros, 99%) in filtered water (Milli-Q), rinsing in deionized water, sonication in 2-propanol (Sigma Aldrich) and 30 minutes of UV-ozone treatment right before use.

For the experiments with the thermal gradient sublimer (Esoteric Chemicals AB), 400 mg mL^{-1} PbI$_2$ (Sigma Aldrich, 99,%) in *N,N*-dimethylformamide (DMF) (Sigma Aldrich, anhydrous, 99.8%) was spin coated at 4000 RPM in an inert atmosphere followed by drying at 70 °C for 20 min. For the porous PbI$_2$ films 4-*tert*-butylpyridine (TBP) was added to the PbI$_2$ solution (120 or 240 µl TBP mL^{-1} DMF). MAI deposition times and temperatures are mentioned in the main text.

The glass slides used in the initial experiments with the home-built VASP reactor were cleaned with the above mentioned procedure. For the following experiments, a ~ 100 nm thick PbI$_2$ layer was produced by spin coating a solution of 400 mg PbI$_2$ (Sigma Alrdich, 99%) per mL DMF (Sigma Aldrich, anhydrous, 99.8%) at 5600 RPM with the solution at 70 °C in an inert atmosphere onto cleaned glass slides. The PbI$_2$ layer was subsequently annealed for 20 min. at 70 °C.

Device fabrication

For the production of solar cells with the VASP reactor, indium-tin oxide (ITO) coated and pre-patterned glass substrates (Naranjo substrates) were cleaned by sonication in acetone (Sigma Aldrich), scrubbing in a solution of sodium dodecyl sulfate (SDS, Acros, 99%) in filtered water (Milli-Q), rinsing in deionized water, sonication in 2-propanol (Sigma Aldrich) and 30 minutes of UV-ozone treatment right before use. Poly(3,4-ethylenedioxythiophene):polystyrene sulfonate (PEDOT:PSS, Heraeus Clevios PVP Al 4083) was filtered using a 0.45 µm PVDF filter and spin coated (60 s, 3000 RPM) onto the cleaned substrates. PbI$_2$ (TCI Chemicals, 99.99% trace metals basis, unless stated otherwise) was spin cast onto the PEDOT:PSS covered substrates at various speeds and concentrations throughout the chapter. (First batch (~150 nm PbI$_2$): 400 mg mL^{-1}, 2200 RPM, different PbI$_2$ sources and 9 identical TCI PbI$_2$ layers (~110 nm PbI$_2$): 300 mg mL^{-1}, 2200 RPM, and 2.5 LPM N$_2$ flow with 10 mbar pressure (~140 nm PbI$_2$): 300 mg mL^{-1}, 1000 RPM. For the other experiments, spin speeds and solution concentrations are given in the main text. For the MAI deposition from the vapor phase using the VASP reactor, all parameters are mentioned in the main text. After the formation of the perovskite layers, the devices are completed by spin coating a ~60 nm thick PCBM (Solenne BV, 99%) layer. The

device contact area is cleaned and LiF (1 nm) and Al (100 nm) are thermally evaporated under high vacuum ($\pm 3 \times 10^{-7}$ mbar) as the back electrode.

Measurement methods

Layer thicknesses were measured using a Veeco Dektak 150 profilometer.

J–V characteristics were measured in a nitrogen environment with a Keithley 2400 source meter under ± 100 mW cm^{-2} white light illumination from a tungsten-halogen lamp filtered by a Schott GG385 UV filter and a Hoya LB120 daylight filter. The cells were masked with a 0.0676 cm^2 or 0.1296 cm^2 aperture (the physical overlap of the contacts is 0.09 cm^2 and 0.16 cm^2 respectively). The stabilized J-V measurement protocol used was defined by light soaking at V_{OC} for 5 minutes, followed by a downward sweep (V_{OC} + 0.04 V $\rightarrow$ −0.04 V) with a step size of 0.02 V. At each voltage the current density was recorded for 10 s and the final value was used for plotting the J–V curve. Fast upwards and downwards J–V sweeps were performed before and after the slow sweep measurement between −0.5 and 1.5 V with a scan speed of 0.25 V s^{-1}.

Short-circuit current densities under AM 1.5G conditions were determined by integrating the spectral response with the solar spectrum. Spectral response measurements were conducted under only probe light and 1-sun equivalent operating conditions by using a 530 nm high power LED (Thorlabs M530L3 driven by a DC4104 driver) for bias illumination. The device was kept in a nitrogen filled box behind a quartz window and a circular aperture with a 1 mm radius and irradiated with modulated monochromatic light, from a 50 W tungsten-halogen lamp (Philips focusline) and monochromator (Oriel, Cornerstone 130) with the use of a mechanical chopper (160 Hz). The response was recorded as a voltage from a preamplifier (SR570) using a lock-in amplifier (SR830). A calibrated silicon cell was used as reference (calibrated at the Energy Research Centre of the Netherlands).

Scanning electron microscopy (SEM) was performed on a FEI Quanta 3D FEG.

X-Ray Diffraction measurements were performed on a Bruker 2D Phaser using Cu Kα radiation with a wavelength of 0.15406 nm between 2θ angles of 10 to 60° using increments of 0.05° and a 2 second integration time. A 0.6 mm slit was used at the X-ray source and a shield was positioned 0.5 mm above the sample surface. The sample rotated at a speed of 60 RPM during the measurement.

5.8 References

1   Y. Deng, Q. Dong, C. Bi, Y. Yuan and J. Huang, *Adv. Energy Mater.*, 2016, **6**, 1600372.

2   K. Hwang, Y.-S. Jung, Y.-J. Heo, F. H. Scholes, S. E. Watkins, J. Subbiah, D. J. Jones, D.-Y. Kim and D. Vak, *Adv. Mater.*, 2015, **27**, 1241–1247.

3   H. Chen, F. Ye, W. Tang, J. He, M. Yin, Y. Wang, F. Xie, E. Bi, X. Yang, M. Grätzel and L. Han, *Nature*, 2017, **550**, 92–95.

4   Z. Gu, L. Zuo, T. T. Larsen-Olsen, T. Ye, G. Wu, F. C. Krebs and H. Chen, *J. Mater. Chem. A*, 2015, **3**, 24254–24260.

5   T. M. Schmidt, T. T. Larsen-Olsen, J. E. Carlé, D. Angmo and F. C. Krebs, *Adv. Energy Mater.*, 2015, **5**, 1500569.

6   F. Ye, H. Chen, F. Xie, W. Tang, M. Yin, J. He, E. Bi, Y. Wang, X. Yang and L. Han, *Energy Environ. Sci.*, 2016, **9**, 2295–2301.

7   Y. Galagan, E. W. C. Coenen, W. J. H. Verhees and R. Andriessen, *J. Mater. Chem. A*, 2016, **4**, 5700–5705.

8   L. K. Ono, M. R. Leyden, S. Wang and Y. Qi, *J. Mater. Chem. A*, 2016, **4**, 6693–6713.

9   M. M. Tavakoli, L. Gu, Y. Gao, C. Reckmeier, J. He, A. L. Rogach, Y. Yao and Z. Fan, *Sci. Rep.*, 2015, **5**, 14083.

10 F. Huang, Y. Dkhissi, W. Huang, M. Xiao, I. Benesperi, S. Rubanov, Y. Zhu, X. Lin, L. Jiang, Y. Zhou, A. Gray-Weale, J. Etheridge, C. R. McNeill, R. A. Caruso, U. Bach, L. Spiccia and Y.-B. Cheng, *Nano Energy*, 2014, **10**, 10–18.

11 Q. Chen, H. Zhou, Z. Hong, S. Luo, H.-S. Duan, H.-H. Wang, Y. Liu, G. Li and Y. Yang, *J. Am. Chem. Soc.*, 2014, **136**, 622–625.

12 Y. Jin and G. Chumanov, *Chem. Lett.*, 2014, **43**, 1722–1724.

13 D. Liu and T. L. Kelly, *Nat. Photonics*, 2014, **8**, 133–138.

14 T. Zhang, M. Yang, Y. Zhao and K. Zhu, *Nano Lett.*, 2015, **15**, 3959–3963.

15 J. Burschka, N. Pellet, S.-J. Moon, R. Humphry-Baker, P. Gao, M. K. Nazeeruddin and M. Grätzel, *Nature*, 2013, **499**, 316–319.

16 K. Liang, D. B. Mitzi and M. T. Prikas, *Chem. Mater.*, 1998, **10**, 403–411.

17 Y. Xie, F. Shao, Y. Wang, T. Xu, D. Wang and F. Huang, *ACS Appl. Mater. Interfaces*, 2015, **7**, 12937–12942.

18 Y. H. Lee, J. Luo, R. Humphry-Baker, P. Gao, M. Grätzel and M. K. Nazeeruddin, *Adv. Funct. Mater.*, 2015, **25**, 3925–3933.

19 W. Li, H. Dong, L. Wang, N. Li, X. Guo, J. Li and Y. Qiu, *J. Mater. Chem. A*, 2014, **2**, 13587–13592.

20 H. Zhang, J. Mao, H. He, D. Zhang, H. L. Zhu, F. Xie, K. S. Wong, M. Grätzel and W. C. H. Choy, *Adv. Energy Mater.*, 2015, **5**, 1501354.

21 Y. Wu, A. Islam, X. Yang, C. Qin, J. Liu, K. Zhang, W. Peng and L. Han, *Energy Environ. Sci.*, 2014, **7**, 2934–2938.

22   P. Docampo, F. C. Hanusch, S. D. Stranks, M. Döblinger, J. M. Feckl, M. Ehrensperger, N. K. Minar, M. B. Johnston, H. J. Snaith and T. Bein, *Adv. Energy Mater.*, 2014, **4**, 1400355.

23   Y. Li, W. Sun, W. Yan, S. Ye, H. Peng, Z. Liu, Z. Bian and C. Huang, *Adv. Funct. Mater.*, 2015, **25**, 4867–4873.

24   Q. Dong, Y. Yuan, Y. Shao, Y. Fang, Q. Wang and J. Huang, *Energy Environ. Sci.*, 2015, **8**, 2464–2470.

25   X. Huang, K. Wang, C. Yi, T. Meng and X. Gong, *Adv. Energy Mater.*, 2016, **6**, 1501773.

26   C.-H. Chiang, Z.-L. Tseng and C.-G. Wu, *J. Mater. Chem. A*, 2014, **2**, 15897–15903.

27   Y. Zhou, M. Yang, A. L. Vasiliev, H. F. Garces, Y. Zhao, D. Wang, S. Pang, K. Zhu and N. P. Padture, *J. Mater. Chem. A*, 2015, **3**, 9249–9256.

28   K. Wang, C. Liu, C. Yi, L. Chen, J. Zhu, R. A. Weiss and X. Gong, *Adv. Funct. Mater.*, 2015, **25**, 6875–6884.

29   Z. Zhang, D. Wei, B. Xie, X. Yue, M. Li, D. Song and Y. Li, *Sol. Energy*, 2015, **122**, 97–103.

30   W. Li, J. Fan, J. Li, Y. Mai and L. Wang, *J. Am. Chem. Soc.*, 2015, **137**, 10399–10405.

31   H. Miyamae, Y. Numahata and M. Nagata, *Chem. Lett.*, 1980, 663–664.

32   A. Wakamiya, M. Endo, T. Sasamori, N. Tokitoh, Y. Ogomi, S. Hayase and Y. Murata, *Chem. Lett.*, 2014, **43**, 711–713.

33   B. J. Foley, J. Girard, B. A. Sorenson, A. Z. Chen, J. Scott Niezgoda, M. R. Alpert, A. F. Harper, D.-M. Smilgies, P. Clancy, W. A. Saidi and J. J. Choi, *J. Mater. Chem. A*, 2017, **5**, 113–123.

34   J. W. Lee, H.-S. Kim and N.-G. Park, *Acc. Chem. Res.*, 2016, **49**, 311–319.

35   Y. Jo, K. S. Oh, M. Kim, K.-H. Kim, H. Lee, C.-W. Lee and D. S. Kim, *Adv. Mater. Interfaces*, 2016, **3**, 1500768.

36   A. Dualeh, N. Tétreault, T. Moehl, P. Gao, M. K. Nazeeruddin and M. Grätzel, *Adv. Funct. Mater.*, 2014, **24**, 3250–3258.

37   W. Zhang, M. Saliba, D. T. Moore, S. K. Pathak, M. T. Hörantner, T. Stergiopoulos, S. D. Stranks, G. E. Eperon, J. A. Alexander-Webber, A. Abate, A. Sadhanala, S. Yao, Y. Chen, R. H. Friend, L. A. Estroff, U. Wiesner and H. J. Snaith, *Nat. Commun.*, 2015, **6**, 6142.

38   S. R. Raga, M.-C. Jung, M. V. Lee, M. R. Leyden, Y. Kato and Y. Qi, *Chem. Mater.*, 2015, **27**, 1597–1603.

39   M.-F. Xu, H. Zhang, S. Zhang, H. L. Zhu, H.-M. Su, J. Liu, K. S. Wong, L.-S. Liao and W. C. H. Choy, *J. Mater. Chem. A*, 2015, **3**, 14424–14430.

40   B. Conings, A. Babayigit, M. T. Klug, S. Bai, N. Gauquelin, N. Sakai, J. T.-W. Wang, J. Verbeeck, H.-G. Boyen and H. J. Snaith, *Adv. Mater.*, 2016, **28**, 10701–10709.

41   Z. Zhou, Z. Wang, Y. Zhou, S. Pang, D. Wang, H. Xu, Z. Liu, N. P. Padture and G. Cui, *Angew. Chemie Int. Ed.*, 2015, **54**, 9705–9709.

42   Z. Xiao, Q. Dong, C. Bi, Y. Shao, Y. Yuan and J. Huang, *Adv. Mater.*, 2014, **26**, 6503–6509.

43   J. Liu, C. Gao, X. He, Q. Ye, L. Ouyang, D. Zhuang, C. Liao, J. Mei and W. Lau, *ACS Appl. Mater. Interfaces*, 2015, **7**, 24008–24015.

44   H. Yu, X. Liu, Y. Xia, Q. Dong, K. Zhang, Z. Wang, Y. Zhou, B. Song and Y. Li, *J. Mater. Chem. A*, 2016, **4**, 321–326.

45   Q. Liang, J. Liu, Z. Cheng, Y. Li, L. Chen, R. Zhang, J. Zhang and Y. Han, *J. Mater. Chem. A*, 2016, **4**, 223–232.

46   Y. Chen, Y. Zhao and Z. Liang, *Chem. Mater.*, 2015, **27**, 1448–1451.

47   P. Fan, D. Gu, G.-X. Liang, J.-T. Luo, J.-L. Chen, Z.-H. Zheng and D.-P. Zhang, *Sci. Rep.*, 2016, **6**, 29910.

48   O. Malinkiewicz, A. Yella, Y. H. Lee, G. M. Espallargas, M. Graetzel, M. K. Nazeeruddin and H. J. Bolink, *Nat. Photonics*, 2014, **8**, 128–132.

49   C. Roldán-Carmona, O. Malinkiewicz, A. Soriano, G. Mínguez Espallargas, A. Garcia, P. Reinecke, T. Kroyer, M. I. Dar, M. K. Nazeeruddin and H. J. Bolink, *Energy Environ. Sci.*, 2014, **7**, 994-997.

50   M. Liu, M. B. Johnston and H. J. Snaith, *Nature*, 2013, **501**, 395–398.

51   Y. Peng, G. Jing and T. Cui, *J. Mater. Chem. A*, 2015, **3**, 12436-12442.

52   M Ohring, *Materials Science of Thin Films 2nd edidion*, Academic Press, 2002.

53   M. R. Leyden, L. K. Ono, S. R. Raga, Y. Kato, S. Wang and Y. Qi, *J. Mater. Chem. A*, 2014, **2**, 18742-18745.

54   Chemical Kinetics (The Rates of Chemical Ractions), http://cbc.chem.arizona.edu/~salzmanr/480a/480ants/chemkine.html, (accessed 17 February 2018)

55   H. A. Harms, N. Tétreault, N. Pellet, M. Bensimon and M. Grätzel, *Faraday Discuss.*, 2014, **176**, 251-269.

56   J. S. Manser, M. I. Saidaminov, J. A. Christmas, O. M. Bakr and P. V. Kamat, *Acc. Chem. Res.*, 2016, **49**, 330–338.

57   H. Zhang, D. Li, J. Cheng, F. Lin, J. Mao, A.-K. Yen, M. Grätzel and W. C. H. Choy, *J. Mater. Chem. A*, 2017, **5**, 3599-3608.

58   InTech, *Solar Cells - New Approaches and Reviews*, 2015, **Chapter 3**.

59   D. Acuña, B. Krishnan, S. Shaji, S. Sepúlveda and J. L. Menchaca, *Bull. Mater. Sci.*, 2016, **39**, 1453–1460.

Epilogue

The research described in this thesis was conducted during a time period in which the perovskite solar cell research field experienced rapid development. This has led to an unprecedented rate in efficiency increase, but especially in the early years a lack of understanding on how to correctly perform and interpret characterization methods. The work on the correct characterization of perovskite solar cells described in this thesis has helped to determine the true efficiency of this type of solar cell and the methods described (and variations thereof) have found widespread use.

Control over the crystallization behavior of the perovskite material is vital for the optimization of solar cell performance and the production of dense, pinhole free layers with large crystals. This thesis has demonstrated that the desired $CH_3NH_3PbI_3$ ($MAPbI_3$) perovskite material can be produced using alternative lead sources to PbI_2, whereby the residual counter ions are not incorporated into the perovskite structure, but are removed from the layer by evaporation during annealing. Furthermore, we demonstrated that the evaporation rate of these counter ions strongly influences the crystallization speed and the quality of the formed perovskite layer, which has helped to increase control over layer quality and improve solar cell efficiency.

The chemical reduction of the oxidation state of PEDOT:PSS and subsequent reduction in solar cell efficiency by the application of the perovskite precursor solution described in this work has illustrated that not only the perovskite layer deserves attention, but that the other layers in the solar cell stack also require optimization. The fact that annealing the PEDOT:PSS/perovskite stack in ambient conditions re-oxidizes the PEDOT:PSS, not only recovers the perovskite solar cell performance, but also allows processing of the complete ITO/PEDOT:PSS/perovskite/PCBM stack in air. Allowing large scale processing of these devices without the need of an inert atmosphere.

The vapor assisted solution processing (VASP) has shown that it is possible to convert solution processed PbI_2 layers into perovskite by exposure to MAI in the vapor phase. Not only have we identified the most crucial deposition parameters, we have also scaled production capacity up to nine substrates with four solar cells per substrates and a total deposition area of $81cm^2$. Although this method still only allows batch to batch production and the reaction time is lengthy, it does show the possibility of large scale application of this production method. It however still needs to be seen if the efficiencies achieved using this method can eventually equal those of the solution

processed counterparts that show a higher degree of preferred orientation of the perovskite crystals.

In general, the field of perovskite solar cell research has come a long way in the past four years, achieving efficiencies that are close to that of the industrial crystalline silicon technology while still tolerating changes to composition and production methods. This tolerance is also one of the main reasons for the rapid development of the technology and the steep increase of efficiencies reported in the past years. Although the efficiency and processability of the technology seem promising, the long term stability of the material under operating conditions and the use of toxic lead to make the best performing solar cells are still issues that need to be solved in the near future. Perovskite solar cells probably will not replace crystalline silicon solar cells as market leader for both private and industrial application soon, due to the large price drop of the crystalline silicon technology. Perovskite solar cells do however hold a bright future in other aspects. The development of tandem solar cells in which they are combined with silicon solar cells or even a perovskite-perovskite tandem solar cell have the potential to increase the efficiency of the cells without increasing the total installation and operation costs much (since they consist of mainly land and installation costs). Furthermore, the application of perovskite solar cells needs to be found in niche markets like flexible solar cells, where traditional crystalline silicon is not a competitor.

Summary

Lead Halide Perovskite Solar Cells

Today's global population and economic growth is accompanied with a large increase in energy consumption. Satisfying this energy demand by generating energy using traditional sources like fossil fuels has a large negative impact on our environment. Therefore the generation of energy using renewable sources is of great importance to mitigate climate change. Photovoltaic (PV) devices are an elegant way of generating energy since they directly convert the only form of energy that reaches the earth (sunlight) into usable power. Currently, crystalline silicon solar cells are dominant in the commercial and private PV market. The efficiency of these devices is high (>25%). Compared to thin film PV technologies however, these solar cells are thick, heavy and rigid. Thin film photovoltaics have already been applied in niche markets like extraterrestrial solar panels. However, highly efficient (>20%) thin film solar cells often use highly toxic or very costly materials. Recently, metal halide perovskites have emerged as a promising new thin film PV technology. Characterized by an incredible increase in efficiency in only a few years after discovery of the technology, the current record devices reach efficiencies of over 22%. Besides this high efficiency and the ability to produce thin, lightweight and potentially flexible solar cells, the material's solution processability makes low cost large scale production an interesting possibility. The material's tolerance towards compositional changes allows tuning of the material properties towards specific applications. The toxicity of lead (Pb), that is required for the highest efficiency devices, and the long term stability of the material under operational conditions are currently the main challenges for this new technology.

An introduction into the working principles of solar cells and the necessity of using solar power are discussed in **Chapter 1**, followed by a detailed description of perovskite solar cells by first giving an overview of the historic development of this relatively new technology, after which the possibilities with the variation in composition of the perovskite semiconductor are presented. Solar cell architectures and processing methods are explained and advantages and challenges of the technology are discussed. At the end of this chapter, the aim and outline of this thesis are described.

The composition of the perovskite semiconductor is different from the well understood inorganic crystalline silicon or organic solar cells. Therefore, characterization of these solar cells is notoriously sensitive to the applied method and pre-conditioning, with atypical response of perovskite solar cells to conventional characterization methods reported widely. Especially sub-optimal perovskite solar cells seem to display atypical behavior, resulting in misleading measurement results and potentially incorrect interpretation. Therefore, the correct way to characterize perovskite solar cells with most conventional measurement methods is discussed in **Chapter 2**.

Reproducible production of (highly efficient) perovskite solar cells is of utmost importance. Solution processing of planar p-i-n solar cells using the widely reported "mixed halide" precursor mixture consisting of lead(II) chloride ($PbCl_2$) and methylammonium iodide (MAI) in *N,N*-dimethylformamide (DMF) proved to be very irreproducible due to the formation of a rough perovskite layer with large voids in between large crystals. The crystallization behavior of the perovskite layer can however be significantly modified with variation of the lead source in the precursor mixture. **Chapter 3** describes the optimization of perovskite layer crystallization for obtaining maximal solar cell efficiency. This is achieved by mixing different lead sources ($PbCl_2$ and lead(II) acetate trihydrate ($Pb(OAc)_2 \cdot 3H_2O$)) in various ratios. Optimization of spin coating and annealing procedures results in reproducible production of solar cells with a power conversion efficiency (PCE) of around 14%.

In **Chapter 4**, the influence of processing the metal halide perovskite layer on top of the frequently used poly(3,4-ethylenedioxythiophene):poly(styrenesulfonate) (PEDOT:PSS) hole transport material is discussed. It is shown that deposition of the precursor mixture via spin coating chemically reduces the oxidation state of the PEDOT:PSS, leading to a lowering of its work function, and consequently that of the perovskite layer on top of it. As a consequence, the solar cell performance is inferior with a reduced open-circuit voltage (V_{OC}) and a reduced short-circuit current density (J_{SC}) which increases sublinearly with light intensity. Furthermore it is demonstrated that annealing the perovskite layer in the presence of oxygen (O_2) can re-oxidize the PEDOT:PSS layer. Resulting in solar cells with increased open-circuit voltage, short-circuit current density and high efficiency.

Apart from the completely solution processed devices described in the previous sections, the conversion of solution deposited lead(II) iodide (PbI_2) layers to perovskite by exposure to MAI in the vapor phase is explored. Using a commercial thermal gradient sublimer it is shown that the conversion is indeed possible. A vapor

assisted solution processing (VASP) reactor was designed and built, based on the information gathered in these experiments. Subsequently, the deposition process was optimized firstly by deposition of MAI on glass slides followed by deposition onto PbI_2 layers. After re-optimization of this process, solar cells are produced using the reactor and reproducible efficiencies close to 12% are achieved. These experiments and the design process of the reactor are described in **Chapter 5**.

The impact of the work is described in the epilogue.

Samenvatting

Lood Halogenide Perovskiet Zonnecellen

De huidige bevolkings- en economische groei gaat gepaard met een grote toename in energieconsumptie. Het voldoen aan deze enorme vraag naar energie, gebruikmakend van het verbranden van fossiele brandstoffen, heeft een grootschalige negatieve invloed op ons milieu. Het opwekken van energie vanuit duurzame bronnen is van groot belang om klimaatverandering tegen te gaan. Het gebruik van zonnecellen is een elegante manier om duurzame energie op te wekken omdat deze technologie de enige vorm van energie die onze aarde bereikt (zonlicht) direct om kan zetten in bruikbare energie (elektriciteit). Op dit moment vormen kristallijn silicium zonnecellen de meest gebruikte fotovoltaïsche technologie in zowel de commerciële als de particuliere markt, en is hun efficiëntie hoog (>25%). Vergeleken met dunne-film fotovoltaïsche technologieën zijn deze zonnecellen echter erg dik, zwaar en rigide. Dunne-film fotovoltaïsche cellen worden al gebruikt in nichemarkten zoals voor satellieten en ruimtestations. De dunne-film zonnecellen met een hoge efficiëntie (>20%) maken echter vaak gebruik van giftige of zeer kostbare materialen. Recent is er een nieuwe, veelbelovende klasse materialen voor dunne-film technologie ontdekt, de metaal halogenide perovskieten. Deze technologie wordt gekenmerkt door een enorm snelle ontwikkeling en toename van efficiëntie, waarbij de tot op heden hoogst behaalde efficiënties meer dan 22% zijn. Naast deze hoge efficiëntie en de mogelijkheid om dunne, lichtgewicht en potentieel flexibele zonnecellen te produceren, is door de verwerkbaarheid uit oplossing van het materiaal, grootschalige productie een interessante optie. De tolerantie van het materiaal ten opzichte van veranderingen in compositie maakt het afstemmen van de materiaaleigenschappen voor specifieke toepassingen mogelijk. De giftigheid van lood (Pb) dat gebruikt wordt in de meest efficiënte perovskiet zonnecellen en de langdurige stabiliteit van het materiaal onder bedrijfsomstandigheden zijn momenteel de grootste uitdagingen voor deze nieuwe technologie.

In **Hoofdstuk 1** wordt de werking van zonnecellen besproken en wordt de noodzakelijkheid van het gebruik van zonne-energie bediscussieerd. Dit wordt gevolgd door een beschrijving van de historische ontwikkeling van de perovskiet zonneceltechnologie en een gedetailleerde samenvatting van de effecten die veranderingen in de compositie van het materiaal hebben op de

materiaaleigenschappen. De meest gebruikte zonnecelarchitecturen en productiemethoden en de voordelen en uitdagingen van de perovskiettechnologie worden toegelicht. Aan het eind van dit hoofdstuk wordt het doel en een overzicht van de thesis beschreven.

De structuur van de perovskiet halfgeleider is anders dan die van de bekende anorganische silicium of organische zonnecellen. Daardoor is de karakterisatie van perovskiet zonnecellen gevoelig voor de gebruikte methode en voorbehandeling, waarbij een atypische reactie van de cellen op conventionele meetmethoden veelvuldig gerapporteerd is. Vooral cellen die suboptimaal zijn, tonen vaak deze atypische respons waardoor de metingen en resultaten misleidend kunnen zijn en het correct interpreteren hiervan moeilijk is. Daarom wordt er in **Hoofdstuk 2** uitgelegd hoe deze cellen correct gekarakteriseerd dienen te worden.

De reproduceerbare productie van (efficiënte) perovskiet zonnecellen is van groot belang. Het produceren van planaire p-i-n zonnecellen uit oplossing waarbij gebruik gemaakt wordt van het "mixed halide" mengsel dat bestaat uit lood(II) chloride ($PbCl_2$) en methylammonium jodide (MAI) in *N,N*-dimethylformamide (DMF) bleek zeer on-reproduceerbaar door de vorming van een ruwe laag met grote gaten tussen de grote perovskietkristallen. Door de loodbron die gebruikt wordt in dit mengsel te veranderen kan het kristallisatiegedrag echter sterk worden beïnvloedt. In **Hoofdstuk 3** wordt de optimalisatie van het kristallisatieproces van het perovskiet materiaal beschreven, strevend naar een maximale zonneelefficiëntie. Dit wordt bereikt door het combineren van twee verschillende loodbronnen ($PbCl_2$ en lood(II) acetaat ($Pb(OAc)_2 \cdot 3H_2O$)) in verschillende mengverhoudingen. Na optimalisatie van het productieproces leidt dit tot de reproduceerbare productie van zonnecellen met een efficiëntie van ruwweg 14%.

In **Hoofdstuk 4** wordt de invloed van het aanbrengen van een perovskietlaag bovenop het veel gebruikte gaten transport materiaal poly(3,4-ethyleendioxythiofeen):poly(styreensulfonaat) (PEDOT:PSS) besproken. Dit laat zien dat het aanbrengen van het perovskiet precursor mengsel door middel van spin coaten zorgt voor een chemische reductie van de oxidatietoestand van de PEDOT:PSS laag. Dit resulteert in een verlaging van de werkfunctie van de PEDOT:PSS en die van het perovskiet, wat leidt tot een gereduceerde zonneelefficiëntie. De openklemspanning (V_{OC}) en kortsluitstroomdichtheid (J_{SC}) worden gereduceerd waarbij de J_{SC} sublineair toeneemt met de belichtingsintensiteit. Verder wordt aangetoond dat het temperen van de perovskietlaag in de aanwezigheid van zuurstof

(O_2) de PEDOT:PSS kan re-oxideren, waardoor de zonnecelefficiëntie wordt hersteld en de J_{SC} weer lineair toeneemt met de belichtingsintensiteit.

Naast uit oplossing geproduceerde perovskiet zonnecellen is de conversie van een uit oplossing geproduceerde lood(II) jodide (PbI_2) laag naar perovskiet door blootstelling aan MAI in de dampfase onderzocht. Gebruikmakend van een commerciële sublimatie-oven wordt aangetoond dat deze conversie daadwerkelijk mogelijk is. Naar aanleiding van de ervaringen met deze sublimatie-oven is een nieuwe oven gebouwd die ontworpen is voor het converteren van PbI_2 lagen naar perovskiet met MAI uit de dampfase. Hiermee is het depositieproces geoptimaliseerd, gebruikmakend van depositie op glazen substraten. Gevolgd door optimalisatie van het conversieproces met PbI_2 lagen op glazen substraten. Na verdere optimalisatie zijn met deze opstelling zonnecellen geproduceerd met reproduceerbare efficiëntie van bijna 12%. Deze experimenten en het ontwerp van de reactor staan beschreven in **Hoofdstuk 5**.

De impact van het uitgevoerde werk staat beschreven in de epiloog.

Curriculum Vitae

Bardo Bruijnaers was born on November 4th, 1987 in Weert, the Netherlands. After finishing high school (HAVO) at the Philips van Horne scholengemeenschap in Weert, he studied Chemistry (BSc Applied Science) at Fontys Hogescholen in Eindhoven. After an internship at the Eindhoven University of Technology where he studied the influence of domain size in thermoplastic vulcanizates and a graduation project at Lapinus Fibres (Rockwool B.V.) Roermond where he studied the influence of continuous fibers on the performance of brake pads, he graduated in August 2009. From October 2009 to July 2011 he was employed full time as a quality control laboratory scientist (BSc level) at Interchemie werken de Adelaar in Venray. In September 2011 he started the master program Chemical Engineering at the Eindhoven University of Technology, specializing in the material sciences track "Polymers and Composites". After his graduation project on directing light in luminescent solar concentrators in the Functional Organic Materials and Devices group chaired by Prof. dr. Dick Broer and Prof. dr. Albert Schenning at the Eindhoven University of Technology, he graduated "with great appreciation" in February 2014. In April 2014 he started his PhD project at the Eindhoven University of Technology in the Molecular Materials and Nanosystems group chaired by Prof. dr. ir. René Janssen on the topic of lead halide perovskite solar cells, of which the most significant results are described in this thesis.

Publications related to this work

G. E. Eperon, S. N. Habisreutinger, T. Leijtens, <u>B. J. Bruijnaers</u>, J. J. Van Franeker, D. W. Dequilettes, S. Pathak, R. J. Sutton, G. Grancini, D. S. Ginger, R. A. J. Janssen, A. Petrozza, and H. J. Snaith, "The Importance of Moisture in Hybrid Lead Halide Perovskite Thin Film Fabrication," *ACS Nano*, 2015, **vol. 9**, no. 9, 9380–9393.

K. H. Hendriks, J. J. van Franeker, <u>B. J. Bruijnaers</u>, J. A. Anta, M. M. Wienk, and R. A. J. Janssen, "2-Methoxyethanol as a new solvent for processing methylammonium lead halide perovskite solar cells," *J. Mater. Chem. A*, 2017, **vol. 5**, no. 5, 2346–2354.

J. J. van Franeker, K. H. Hendriks, <u>B. J. Bruijnaers</u>, M. W. G. M. Verhoeven, M. M. Wienk, and R. A. J. Janssen, "Monitoring Thermal Annealing of Perovskite Solar Cells with In Situ Photoluminescence," *Adv. Energy Mater.*, 2017, **vol. 7**, no. 7, 1601822.

<u>B. J. Bruijnaers</u>, E. Schiepers, C. H. L. Weijtens, S. C. J. Meskers M. M. Wienk and R. A. J. Janssen, "The effect of oxygen on the efficiency of planar p-i-n metal halide perovskite solar cells with a PEDOT:PSS hole transport layer", *J. Mat. Chem. A*, 2018, **6**, 6882-6890.

F. Di Giacomo, S. Shanmugam, H. Fledderus, <u>B. J. Bruijnaers</u>, W. J. H. Verhees, M. S. Dorenkamper, S. C. Veenstra, W. Qiu, R. Gehlhaar, T. Merckx, T. Aernouts, R. Andriessen and Y. Galagan, "Up-scalable sheet-to-sheet production of high efficiency perovskite module and solar cells on 6-in. substrate using slot die coating," *Sol. Energy Mater Sol. Cells*, 2018, **181**, 53-59.

In preparation

W. M. J. Franssen, <u>B. J. Bruijnaers</u>, V. H. L Portengen, R. A. J. Janssen and A. P. M. Kentgens, "Evidence of unintentional dimethylammonium incorporation in lead acetate based perovskite solar cells".

Not related to this work

B. J. Bruijnaers, A. P. H. J. Schenning, and M. G. Debije, "Capture and concentration of light to a spot in plastic lightguides by circular luminophore arrangements," *Adv. Opt. Mater.*, 2015, **vol. 3**, no. 2, pp. 257–262.

C. Duan, R. E. M. Willems, J. J. van Franeker, B. J. Bruijnaers, M. M. Wienk, and R. A. J. Janssen, "Effect of side chain length on the charge transport, morphology, and photovoltaic performance of conjugated polymers in bulk heterojunction solar cells," *J. Mater. Chem. A*, 2016, **vol. 4**, no. 5, pp. 1855–1866.

Q. (Mike) Wang, J. J. van Franeker, B. J. Bruijnaers, M. M. Wienk, and R. A. J. Janssen, "Structure–property relationships for bis-diketopyrrolopyrrole molecules in organic photovoltaics," *J. Mater. Chem. A*, 2016, **vol. 4**, no. 27, pp. 10532–10541.

P. Verstappen, J. Kesters, L. D'Olieslaeger, J. Drijkoningen, I. Cardinaletti, T. Vangerven, B. J. Bruijnaers, R. E. M. Willems, J. D'Haen, J. V. Manca, L. Lutsen, D. J. M. Vanderzande, and W. Maes, "Simultaneous Enhancement of Solar Cell Efficiency and Stability by Reducing the Side Chain Density on Fluorinated PCPDTQx Copolymers," *Macromolecules*, 2015, **vol. 48**, no. 12, pp. 3873–3882.

International Conference Contributions

In-situ observation of perovskite film formation

B. J. Bruijnaers, J. J. van Franeker, M. M. Wienk, and R. A. J. Janssen, *Winterschool: Organic Photovoltaics*, **2015**, Hassel, Belguim, **Oral Contribution**.

In-situ monitoring of absorbance during perovskite annealing

B. J. Bruijnaers, J. J. van Franeker, B. van Gorkom, M. M. Wienk and R. A. J. Janssen, *International Conference on Hybrid and Organic Photovoltaics (HOPV)*, **2015**, Rome, Italy, **Poster Presentation**.

Influence of Processing Atmosphere on Perovskite Solar Cell Performance

B. J. Bruijnaers, J. J. van Franeker, M. M. Wienk and R. A. J. Janssen, *International Conference on Hybrid and Organic Photovoltaics (HOPV)*, **2016**, Swansea, Great Britain, **Poster Presentation**.

Efficient charge extraction by oxygen exposure of perovskite solar cells

B. J. Bruijnaers, E. Schiepers, S. C. J. Meskers, M. M. Wienk and R. A. J. Janssen, *International Conference on Hybrid and Organic Photovoltaics (HOPV)*, **2017**, Lausanne, Switzerland, **Poster Presentation (awarded with the Journal of Materials Chemistry A Poster Prize)**.

The importance of oxygen exposure of perovskite solar cells with a PEDOT:PSS hole transport layer

B. J. Bruijnaers, E. Schiepers, C. H. L. Weijtens, S. C. J. Meskers, M. M. Wienk and R. A. J. Janssen, *International Conference on Hybrid and Organic Photovoltaics (HOPV)*, **2018**, Benidorm, Spain, **Oral Contribution**.

Dankwoord

Na 50 maanden, zes labjournalen en 4460 zonnecellen is het einde in zicht. Mijn boekje is af en de datum van de verdediging staat vast. In de afgelopen vier jaar heb ik enorm veel geleerd en genoten van het fantastische werk dat ik heb mogen doen en de vrijheid die ik heb gekregen om mijn eigen onderzoek uit te voeren. Uiteraard was al het werk dat beschreven is in deze thesis (en al het werk dat de thesis niet gehaald heeft) niet mogelijk geweest zonder de hulp van een groot aantal mensen.

De eerste persoon die ik graag wil bedanken is René. Bedankt voor de kans om in jouw groep aan mijn promotieonderzoek te beginnen. Naast ons twee-wekelijkse gesprek en de perovskiet meeting, ben je ook nog altijd bereid om me op andere tijdstippen te woord te staan, dit waardeer ik enorm. Ook de vrijheid die jij je promovendi geeft om hun onderzoek in te richten komt de positieve sfeer in de groep zeker ten goede. Ik ben zeer onder de indruk van je inzicht en lange termijn visie, waar ik bezig was met mijn eigen onderzoek dacht jij al ver vooruit over nieuwe projecten en de verdere mogelijkheden met onze perovskieten. Als laatste wil ik je nog om een gunst vragen: neem alsjeblieft nooit meer een Ajacied aan als promovendus. Want met nog 4 jaar zonder schaal houden we dat sterretje voorsprong op PSV wellicht niet in stand.

Ook mijn copromotor Martijn wil ik natuurlijk graag bedanken. Jouw advies tijdens de twee wekelijkse gesprekken, de perovskiet meetings en daar tussendoor was onmisbaar. Vooral jouw kritische blik op het ontwerpen van experimenten en het interpreteren van de gegenereerde data is van grote waarde. Dat dit vaak meer vragen dan antwoorden opleverde kwam het onderzoek alleen maar ten goede en ik ben er dan ook van overtuigd dat door jou de kwaliteit van het geleverde werk en de gepresenteerde resultaten hoog is en ook zal blijven.

I would also like to take this opportunity to thank Maria, Arno, Adriana, Erik and Yulia for participating in my PhD committee. Thank you for your suggestions and improvements, which have increased the quality of the work, and for approving my thesis.

Verder heb ik tijdens mijn eigen promotie een heel aantal studenten mogen begeleiden tijdens hun bachelor of master afstudeerproject. Deze wil ik natuurlijk ook hartelijk danken voor hun inzet en het geleverde werk. Bas, jij was de eerste student die ik (samen met Hans) heb begeleid. Jij hebt hard gewerkt aan het bestuderen en

karakteriseren van de perovskiet formatie uit het "mixed halide" recept dat we toen nog gebruiktem. Zoals beschreven staat in de thesis hebben we dat recept nooit echt goed aan de praat gekregen maar desondanks hebben we tijdens jouw project veel geleerd over dit recept. Je hebt tijdens je bachelor afstudeerproject duidelijk je weg in de groep gevonden en bent dan ook voor je master afstudeerproject bij ons terug gekomen. Waarin je hebt gewerkt aan de verbetering van het PCBM contact d.m.v. doping van deze laag. We kwamen uiteindelijk tot de conclusie dat de PCBM laag die we standaard maken al erg goed functioneert en dat het dopen van deze laag vooral negatieve gevolgen heeft. Desalniettemin hebben we in dit project veel geleerd over de mogelijkheden om deze lagen te dopen en vooral dat we voor een verbetering van de zonnecel efficiëntie beter elders kunnen gaan zoeken. Verder heb ik uit betrouwbare bron vernomen dat je het in onze groep nog niet beu bent en dat je ook in onze groep zult gaan promoveren. Ik wil je bedanken voor al het geleverde werk en heel veel succes wensen met je eigen promotieonderzoek. Tim, jouw project waarin je "toluene dripping" gebruikte om de kristallisatie van de perovskiet laag te versnellen heeft geresulteerd in zonnecellen met hele aardige efficiëntie. We hebben in dit project dan ook veel geleerd over deze productiemethode en een vergelijkbare methode wordt nu gebruikt om "inverted" perovskiet cellen te maken. Bedankt voor je harde werk en succes met het afronden van je studie. Junke, you came to us to do a project in which you were supposed to produce solar cells using the designed vapor assisted solution processing method. Unfortunately, building the equipment took (a lot) longer than anticipated and you were only able to use it for a few weeks at the end of your project. Nevertheless, you spent your time researching the sequential solution processing from which we learned a lot about controlling the porosity of the PbI_2 layer. Also your initial work with the thermal gradient sublimer was very useful, and both have found their way into the thesis. That automatically brings me to Kunal, who continued the work with the VASP equipment. Your work identified the usable parameter space of the setup and has contributed to the development of efficient solar cells using this method. Your combined work makes up a substantial portion of Chapter 5 of this thesis. Furthermore, both of you are still active in the group, doing your own PhD research. I want to thank you both for your hard work and I wish you the best of luck with your research. Edoardo, even though your experiments often looked chaotic and you often changed multiple cell production parameters at once, you managed to make some quite efficient planar n-i-p perovskite solar cells (albeit with substantial hysteresis). Thank you for your work and the best of luck with your job and project on the all carbon battery. Last but not least, Erik, jouw project waarin

je naar de fotoluminescentie van de perovskiet lagen ge-annealed in lucht en stikstof hebt gekeken heeft ons veel duidelijkheid gegeven over de bulkeigenschappen van deze lagen. Uiteindelijk heeft dit dan ook een grote bijdrage geleverd aan een publicatie in Journal of Materials Chemistry A en Hoofdstuk 4 van deze thesis. Dank voor je inzet en veel succes in je verdere carrière.

Nog even verder gaand op dit project over fotoluminescentie wil ik ook Stefan hartelijk danken voor alle nuttige discussies en de hulp bij het doen van, en het analyseren van de fotoluminescentie en electroluminescentie data die ook veel hebben bijgedragen aan de hiervoor genoemde publicatie en Hoofdstuk 4 van deze thesis. Ook Christ mag niet ontbreken in dit dankwoord. Mede door jouw expertise op het gebied van UPS en XPS metingen hebben we eindelijk duidelijkheid gevonden over de oorzaak van de verlaagde efficiëntie van perovskiet zonnecellen ge-annealed in stikstof. Bedankt voor het uitvoeren van alle metingen, het interpreteren van de resultaten en alle nuttige discussies die we hierover hebben gevoerd. Jouw werk heeft ook een grote bijdrage geleverd aan de bovengenoemde publicatie en Hoofdstuk 4 van deze thesis.

Marco en Wijnand (oftewel WiMa design), ook al duurde het bouwen van de "oven" langer dan ieder van ons had verwacht, uiteindelijk is het een pareltje geworden. We kunnen met voldoende precisie alle belangrijke parameters controleren tijdens de depositie. Zonder jullie inzet bij het ontwerpen en bouwen van de reactor was Hoofdstuk 5 er niet geweest. Bedankt hiervoor, maar ook vooral voor de leuke praatjes tussen de bedrijven door.

Margot, Carla en Martina, als secretaresses van SMO hebben jullie de bijna ondoenlijke taak om alles wat de professoren, assistent professoren, promovendi en studenten (zouden moeten) doen in goede banen te leiden. Bedankt voor al jullie hulp. Margot, als secretaresse (amateur psychologe en tweede moeder) van onze M2N groep wil ik jou speciaal bedanken. Jij zorgt altijd dat alles op tijd in orde komt en bent altijd in voor een praatje waarin doorgaans erg veel wordt gelachen. Ook zorgde je goed voor me als ik verkouden was door je "vloeibare cocaïne druppels" in mijn thee te mengen.

Henk, Bas en Jeroen, vanaf de eerste dag van mijn promotie zijn wij met een kopje koffie en een goed gesprek de dag begonnen. Dit is inmiddels uitgegroeid tot een heus ochtendritueel waarbij ook ons groepje uitgebreid is met Bas, Robin, Margot en zo nu en dan Carla en René. Dit leuke onderonsje aan het begin van de werkdag zal ik enorm missen. Bedankt voor de gezellige uurtjes en het uitgebreide aanbod aan fantastische anekdotes (en Henk: bedankt voor de koffie).

Natuurlijk wil ik mijn sportmaatjes Jeroen en Tom niet overslaan. Door jullie is de kickboks training op dinsdagmiddag waar we de laatste maanden steevast bij aanwezig zijn en de fitness op vrijdag iets waar ik naar uitkijk.

Hans Damen wil ik bedanken voor (de discussies over) het bestellen van alle chemicaliën en apparatuur.

Dan volgen natuurlijk nog de (ex-)collega promovendi en post-docs. Koen, jij hebt me in de eerste werken wegwijs gemaakt in het device lab en geholpen met mijn eerste experimenten in de wereld van zonnecellen en perovskieten. Jouw inbreng in de verschillende bijeenkomsten en inzicht in de experimenten waren van grote waarde. Ik ben dan ook blij dat je na een kort uitstapje in de VS weer terug bent in Eindhoven waar je ons alles kunt leren over flow-batteries. Hans, we hebben veel samengewerkt aan experimenten waarin we onder andere perovskiet hebben ge-bladecoat, opdampers hebben ingeregeld en het hot-cast recept hebben ontwikkeld. Daarbovenop mocht ik ook nog je paranimf zijn, een enorme eer. Obviously, my (former) office mates cannot be forgotten in this acknowledgement. Serkan, Chunhui, Mike, Robin and Anna, I really enjoyed sharing an office with you. Especially the non-work related chats were always enjoyable, we've had a lot of fun together, thank you. Also a big thank you to all the (former) M2N chemistry group members with whom I have had the pleasure to work and laugh, Alice, Gijs, Andreanne, Sandra, Gael, Fallon, Ruurd, Bart, Matt, Haijun, Pieter, Benjamin, MengMeng, Dario, and Miriam, thanks for everything.

Jeroen, je bent al een aantal keren verschenen in dit dankwoord maar toch wil ik je alsnog een stukje tekst aan jou wijden. Wij hebben samen niet alleen de verkorte masteropleiding doorlopen, wij zijn zelfs tegelijkertijd op dezelfde afdeling afgestudeerd en zijn ook min of meer simultaan aan onze promoties begonnen. Je bent dan ook niet voor niets mijn paranimf. Jij bent inmiddels al een aantal weken doctor en ik hoop je spoedig te vergezellen. Bedankt voor alle dagelijkse koffie, praatjes en algemene pret die we samen gehad hebben en heel veel succes met je bedrijf "LUSOCO".

Verder wil ik nog alle promovendi en medewerkers van SMO bedanken voor de leuke tijd die ik gehad heb in deze grote groep.

Dan kan ich noow eindelijk oover op det Limburgs van os. As ierste wil ich mien kammeroaj bedanke, neet allein vur de aafgelaupe veer joar mer natuurlijk auch vur hiel vul joare doaveur. Met uch allemoal heb ich vul meijgemaaktj, van ut waekelijkse stappe inne Madeira tot BBQs, het bezeuke van festivals en vakanties noa Hongarije, Kroatië, Spanje en Portugal. Jullie zeen der altied um vur de nuudige

onstpanning te zurge, veural in de weekende. Ich hoop dan auch det we allemoal nog lang beejein oover de vloer kinne koome vur nog mier spaß en plezeer. Koen, Sas, Koen, Lynn, Mark, Fanny, Hubert, Tim, Inge, Roy, Reneé, Siem en Claudia bedanktj vur al ut plezeer det we al gedaeldj hebbe en det der nog vul mier schoen herrineringe beej mooge koome. Dennis wil ich nog ff speciaal bedanke, veural umdejje miene paranimf wiltj zeen en het feit det ich met uch bekans dekker op vakantie bin gewaesj as met Manon zeet deenk ich al zat oover oos vreendjschap.

Ich maak nog ffkes un uutstapje noa mien schoenoajers. Wim en Gerthy, vanaaf de ierste daag det ich beej uch oover de vloer kwoom heb ich mich thoes geveuldj beej uch. Auch wae hebbe in de aafgelaupe 10 joar unne haup met ein meijgemaaktj, van un dikke lup oppe viever (nog bedanktj Wim), tot ut miest recente fiestje, het slaage van Manon. Bedanktj vur de gooi zurg door de joare haer en det auch wae saame nog un hiel dael pilskes meister mooge maake (al dan neet oppe viever).

Pap en Mam, gae hetj mich altied gesteundj in alle keuzes die ich gemaaktj heb. Of ut noow ging um ut goan studeere aan de universiteit, ut kaupe van un amerikaans oad barrel (he mam) of ut haale van ut motorrijbewies. Gea woortj ut der misschien neet altied met ins, mer toch kos ich altied op uch twie terugvalle. Auch as ich hulp noedig heb met ut sleutele aan de auto (of wat angers) dan stiet pap altied kloar, daag en nacht (want soms waerdje un klusje van "un half eurke" bijna nachtwerk). Auch as ich weer us 's oavus laat opgehaaldj mot waere (in Eindhoven of Remunj) dan hoof ich mam mer te belle. Bedanktj vur alles waat dejje mich gegaeve hetj en hetj loate doon. Ich weit dejje hiel gruuts op mich zultj zeen as ich de doctorstitel heb bereiktj, mer deeze is auch vur un groet dael van uch.

Luca, wie we nog klein woore koste we neet met mer auch zeker neet zonger ein. Det giet noow al allebei stukke baeter, en door oos gezamelijke hobbys (die oaj barrels, ut motorrije en aaf en tow un concertje) zeen we nog vul met elkaar (en met os pap) bezig. Binnekort goajje saamewoene met Lesley en doabeej wil ich Lesley hiel vul sterkdje weense. Ut giet uch allebei good en wae zeen os.

En dan, as aller leste, mien maegdje, Manon. Op ein of anger manier hulst dich ut al mier as 10 joar uut met "dae drukdjemaaker uut Ni-jwiert". De bist pas begonne aan dien ierste baan as dierenarts en ich bin super trots op dich. We hebbe elkaar dek lang motte misse tiedens dien studie in Utrecht mer ut waas ut allemoal waerd. Ich wil dich bedanke umdesse der altied vur mich bist en ich hoop dan auch det wae saame hiel oad mooge waere. Ich bin bang det ich det kliere noets zal verliere en det zal dan auch veural vur dich un hiel opgaaf waere. Lieve schat ich hoaj van dich!